Reactions of Heme Proteins in Solutions and Crystals

Thesis by

Faik Akif Tezcan

In Partial Fulfillment of the Requirements

For the Degree of

Doctor of Philosophy

California Institute of Technology

Pasadena, California

2001

(Submitted April 11, 2001)

Acknowledgements

When I first came to Caltech, I was quite clueless about many things (see Young Turk). One could say that I still am, but that would be discrediting the conscious and unconscious efforts of several people who have been influential in my life as a grad student.

I was the sixth and last student to join Harry's group my first year and feel extremely lucky to have caught the train. Harry is a very gracious person who cares, smiles and inspires. He is a great scientist and advisor, but it is his warm personality and sense of humor that make his intelligence and wisdom so easily accessible. Being his student has been a pleasure and I thank him for his generosity and instilling some confidence in me.

Another thing that's nice about the Gray group is that you have Jay as your second advisor. I wouldn't be exaggerating if I said that almost everything scientific that I've learned is the result of the three-a-day visits to Jay's office. I thank him for being patient with me, patching up all the scientific holes in my brain, showing me the way out (not out of his door) when I got stuck and having a few laughs with me at the same time.

Living in the Cats during my first year was a huge blessing. That's where I became good friends with Derek, Kevin, Ivan, Bob and others who were passing by while we were grilling. The 930 E. Leslie Dr.-period that I shared with them and nine others (Maggie, Liz, Isaac, Rob, Ken, Adam, Grace, Jane and Abbie) over three years is certainly one of the most memorable in my life (probably also for tens or hundreds of other people who saw Derek in a woman's swimsuit).

I feel very fortunate to have Adrian and Jim as friends. I have met few people as genuine as AP and Jethro, whom I could always talk to openly about pretty much anything. I additionally thank AP for being open-minded about my musical taste and accompanying me to many shows that he didn't have any idea about. I also thank Xenia here for the same and not minding me making faces at her in the hallway.

I thank several people for their guidance and putting up with my endless questions: Jason Telford, who taught me to work quickly in lab so that I can (also ☺) have fun outside; Jeff Rack for early morning chats over a cup of coffee; Don Low and Gary Mines, who have provided a lot of guidance early on; Jon Wilker for being my

scuba buddy and his mentorship during early morning drives to the Ventura Harbor; Brian Crane for his never-ending enthusiasm and encouragement, and him and Alex Bilwes for their help with crystallography.

My life at Caltech would not have been the same (I mean it in a good way) without my classmates in the Gray group, Liz, Ivan, Mike M. (thanks for the Architectural Digest supplies), Cindy Q. (as in queso), and Lila. While most people chose to move to BI over the years, some just remained within the friendly confines of Noyes: I thank Alex M., Kevin, Angelo, Julia and especially Will for making life interesting on the 3rd floor. I am very grateful to Pat Anderson for all her help and welcoming smile. I should apologize here to everyone (mostly John Bercaw) for playing "Akif's music" loudly (it was the one thing that kept me going in the morning).

I have shared many fun times with the BI bunch. Corinna and Jenn, in particular, have been good friends whose mood swings can rival mine. I wish we could synchronize the highs and the lows a little better. Mike G., who is a funny, interesting (in a chin-scratching way) and certainly agreeable guy, and I have had so many lunches and dinners this past year that "Ace and Gary" analogies have been made. Randy has persistently kept me updated about upcoming Melvins concerts. Alex Dunn and I had many enjoyable random talks about science and music.

Whenever I had to physically or mentally get away from Pasadena, my high school and college friends and my cousins in FL have always been around. I thank them for keeping me sane.

I feel so lucky to have my family; I wish I had them closer. Words cannot describe my gratitude to my mom for her love and support. I dedicate my thesis to her.

Abstract

To assess the effects of heme solvation and iron ligation on reduction potentials in *c*-type cytochromes, we have examined the redox and ligand-binding properties of microperoxidase-8 (MP8). Methionine-, histidine- and amine-coordination to MP8 were found to account for 130, –40 and –10-mV shifts in the Fe(III/II)-potential, respectively. Our finding that reduction potentials increase with decreasing heme-surface exposure suggests that the protein matrix can further tune the reduction potential by 500 mV through water exclusion from the heme pocket.

The 410-mV upshift in the cytochrome *c* (cyt *c*) potential as the heme cofactor is moved from a highly-solvated environment to the protein interior signals a 10-kcal/mol greater stability of the reduced form. Consequently, there exists a range of denaturant concentrations where Fe(II)-cyt *c* is folded and Fe(III)-cyt *c* is unfolded. Electron injection into the oxidized protein in this range triggers the folding reaction. Using NADH as a redox photosensitizer, cyt *c* folding can be initiated within 100 μs. Our results suggest that the folding of cyt *c* is rate-limited by ligand-substitution events on the iron center.

Due to an increased barrier to ligand substitution, folding of Co(III)-substituted cyt *c* is 5 orders of magnitude slower than Fe-cyt *c*. The slow folding kinetics of Co(III)-cyt *c* have allowed the convenient study of protein dynamics with a variety of spectroscopic techniques, revealing previously unresolved folding pathways involving Lys- and His-misligated populations of the unfolded molecule and extremely long-lived folding intermediates.

Factors that control electron flow *between* proteins are not well understood, owing to uncertainties in the relative orientations and structures of the reactants during the short time that tunneling occurs. To circumvent this ambiguity, we have measured the kinetics of electron transfer (ET) between native and Zn-substituted tuna cyt *c* molecules in crystals of known structure. ET rates (320 s^{-1} for *Zn-cyt *c* → Fe(III)-cyt *c*; 2000 s^{-1} for Fe(II)-cyt *c* → Zn-cyt c^{+}) over a Zn-Fe distance of 24.1 Å closely match those for intraprotein ET over similar donor-acceptor separations. Our results indicate that van der Waals interactions and water mediated H-bonds provide effective electronic coupling across a protein-protein interface.

Table of Contents

Chapter 1. Effects of Folding and Ligation on the Reduction Potentials of Heme Proteins 1

List of Tables and Figures

Chapter 1

<u>Chapter 2</u>

<u>Chapter 3</u>

Chapter 4

Appendix A

Appendix B

Appendix C

Chapter 1

Effects of Folding and Ligation on the Reduction Potentials of Heme Proteins*

* Adapted from Tezcan, F. A.; Winkler, J. R.; Gray, H. B. *J. Am. Chem. Soc.* **1998**, *120*, 13383-13388.

Introduction

The reactivity and function of a redox protein are strongly dependent on its reduction potential. Because there are relatively few redox cofactors available in nature, proteins have evolved to accommodate a range of potentials for a given cofactor. Notably, the reduction potential of the heme group spans over 800 mV, depending on its protein environment (Figure 1.1). There is great interest in elucidating how such a large range in heme potentials is achieved.

The reduction potential of a heme protein (or any metalloprotein) is coupled to the folding free energies of its oxidized and reduced forms (Figure 1.2).[1-3] An upshift in the potential as a redox cofactor is moved from aqueous solution to the interior of a protein signals a greater driving force for folding the reduced form. Several factors, especially changes in cofactor inner-sphere coordination and solvation, cause the shift in potential.[1-5]

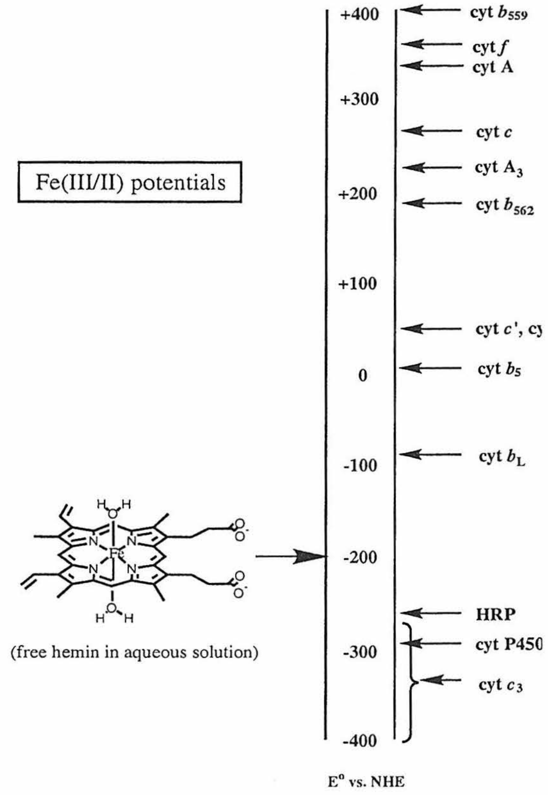

Figure 1.1. Fe(III/II) potentials of free hemin and heme containing proteins. The potential for hemin (Fe-protoporphyrin IX), which is known to exist in aqueous solution as a mixture of monomers and μ-oxo dimers, is estimated to be ~ –200 mV.

Ferrocytochrome *c* (Fe(II)cyt *c*) is ~10 kcal/mol more stable toward unfolding than its ferric form.[6-8] This difference makes it possible to unfold the ferric protein under conditions where the ferrous protein remains folded (see Chapter 2).

Electrochemical measurements demonstrate that the difference between the reduction potentials of the folded (~ 260 mV) and unfolded forms (~ –150 mV) of cyt *c* (ΔE_f) corresponds closely to the 10 kcal/mol higher stability of Fe(II)cyt *c*.[2,6,7,9] In the unfolded state of cyt *c*, the iron center is axially ligated by His 18, and another nitrogenous base, which replaces the native axial ligand, Met 80.[10] As it will be addressed in detail in Chapters 2 and 3, this nitrogenous base is His 26, His 33 or a lysine. Evidently, the heme in the unfolded protein is highly solvent exposed, as the reduction potential of unfolded cyt *c* is very similar to that of bis-imidazole-ligated iron-porphyrin species in aqueous solution (~ –200 mV).[11,12] The folding process involves the burial of the heme and the restoration of Met 80 axial ligation.

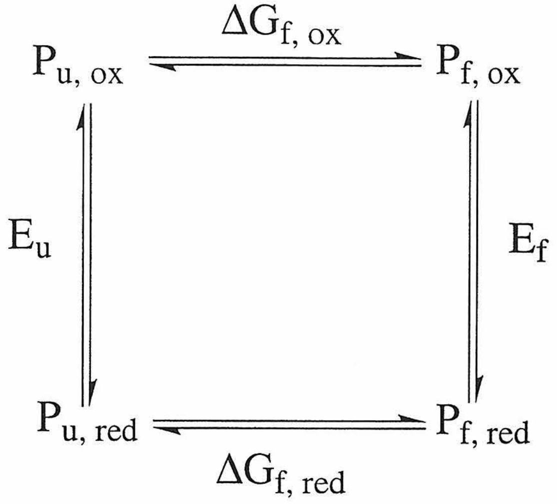

$$\Delta G_{f,ox} - \Delta G_{f,\,red} = -nF(E_u - E_f)$$

Figure 1.2. Thermodynamic cycle illustrating the relationship between the folding free energy and the reduction potential for a redox protein (P, protein; f, folded; u, unfolded; ox, oxidized; red, reduced). The difference between the folding free energies of the reduced and the oxidized protein corresponds to the difference between the reduction potentials of the folded and unfolded protein.

In order to assess the contributions of heme solvation and iron ligation to ΔE_f in cyt *c*, we have examined the redox and ligand-binding properties of microperoxidase-8 (MP8), a proteolytic fragment of cyt *c* containing the heme group and amino acids 14-21 (Figure 1.3). The MP8 heme is bound to the peptide backbone through thioether links to Cys 14 and Cys 17, and the iron is coordinated to the imidazole sidechain of His 18. The sixth coordination site of iron is occupied by a water or a hydroxide molecule that can be readily exchanged with other ligands. Thus, MP8 offers a great flexibility in modeling 6-coordinate active sites in heme proteins, which commonly have at least one histidine as an axial ligand. A great advantage of MP8 as a heme mimic is its high water solubility. Yet, MP8 can aggregate at micromolar concentrations by π-stacking or dimerization through N-terminus-iron coordination.[13,14] N-terminal acetylation of MP8 (AcMP8) at Cys 14 inhibits these aggregation processes that can complicate ligand-binding equilibria.[13,14]

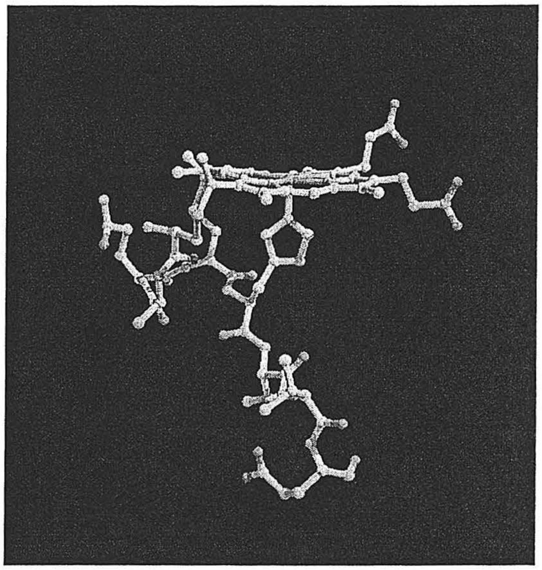

Figure 1.3. A static view of microperoxidase 8. The C-terminal tail portion of MP8 was shown to be quite fluxional by paramagnetic NMR studies.[15] The coordinates are from the horse heart cyt *c* crystal structure (PDB ID: 1HRC). The sixth coordination site of Fe(III)MP8 is known to be occupied by a water or a hydroxide molecule. MP8 consists of the heme group and (starting with the N-terminal Cys 14) Cys, Ala, Gln, Cys, His, Thr, Val, Glu.

We have investigated the binding of N-acetyl-methionine (AcMet), imidazole and alanine (Ala) to AcMP8, and the spectral features of resulting complexes. Absorption and resonance Raman (RR) spectra indicate that AcMet-, imidazole- and Ala- adducts of Fe(II)- and Fe(III)AcMP8 are good models for heme proteins with His-Met, His-His and His-amine axial coordination, respectively. Especially noteworthy is the significant increase in the AcMet affinity for iron upon reduction, which corresponds to a large upshift in heme potential (~ 130 mV). By accurately quantitating the affinity of AcMP8 for different ligands, we have been able to normalize of the reduction potentials of several *c*-type cytochromes with varying axial coordination. Our finding that reduction potentials increase with decreasing heme-surface exposure for these proteins suggests that by excluding water from the heme environment E_f can be further tuned by 500 mV.

Materials and Methods

General

All protein and peptide solutions were prepared with purified water (Millipore Nanopure system) and buffered to pH 7.0 with 50 mM sodium phosphate unless otherwise noted. Acetonitrile (omni-solve grade) and trifluoroacetic acid (TFA) used during MP8 purification were obtained from EM Science; acetic anhydride used for MP8 acetylation was from Aldrich. N-acetyl-methionine (AcMet) (Sigma), N-acetyl-L-valine (AcVal) (Sigma), DL-alanine (Ala) (Sigma) and imidazole (Aldrich) were used as received. Horse heart cyt *c* (Type VI from Sigma) (hh cyt *c*) was oxidized with K[Co(EDTA)] and purified by FPLC (Mono S) before use. Trypsin and pepsin were obtained from Sigma; trypsin was treated with TPCK or DPCC to inhibit chymotrypsin activity. All UV-visible spectra were collected with a Hewlett Packard 8452A unless otherwise noted. Mass analyses were done by Dr. Gary Hathaway in the Beckman Institute Peptide and Protein Analytical Laboratory using matrix assisted laser desorption (MALDI) spectroscopy.

Preparation and purification of MP8

MP8 was prepared and purified as previously reported[14] and described in great detail.[15] The majority of MP8 used in this study was made with help from Dr. Don Low and Grace Yang. In a typical preparation, 200 mg of hh cyt *c* was dissolved in 8 ml water; enough 1M HCl was added to adjust the pH to 2. Following the addition of 5.5 mg pepsin (previously dissolved in 100 μl water), the solution was stirred for 30 min at room temperature (RT). Subsequently, another 5.5 mg of pepsin was added, and the solution was stirred overnight at RT. The pH was then adjusted to 8 by the addition of 30% ammonium hydroxide, followed by the addition of 8 mg of trypsin. After 10 h of stirring at RT, the volume was brought up to 30 ml with water. Excess ammonium sulfate (> 10 g) was added to crash MP8 out of solution, which was collected as a solid by centrifugation at 5000 rpm. The supernatant was discarded. The peptide was redissolved in 45 ml water, and ammonium sulfate was removed by repeated filtration and dilution in an Amicon stirred cell using a YM1 membrane. MP8 was then exchanged into water containing 0.1% (v:v) TFA (Buffer A) using the same Amicon setup. For purification, we used the standard FPLC protocol developed by Dr. Don Low, with a 60% acetonitrile, 40% water, 0.1% TFA mixture as Buffer B. The crude MP8 solution in Buffer A was applied to a reverse-phase PepRPC column (16/10), followed by a wash with 50 ml 20% Buffer B (10 min at a flow rate of 5 ml/min). A gradient to 100% Buffer B over 300 ml (60 min) afforded the elution of MP8 at 45% Buffer B as the major product. MP8 was characterized by MALDI mass spectroscopy (MW = 1506 amu) and UV-vis spectroscopy ($\varepsilon_{396\text{ nm}} = 1.57\ \text{mM}^{-1}\text{cm}^{-1}$).

Preparation and purification of AcMP8

Purified MP8 was dissolved in 0.1 M potassium bicarbonate buffer (pH 9) to give a concentration of > 1 mM (~10 ml total volume). A total of 500-fold excess acetic anhydride was added in 10 portions over 1 hour with constant stirring at RT. Small amounts of NaOH were added to maintain a pH of 9. After 30 more min of stirring, the solution was exchanged into buffer A (see previous section) by repeated concentration and dilution with an Amicon stirred cell (YM1 membrane). The previously described FPLC protocol was used for purification. AcMP8 elutes at ~ 55% Buffer B (Figure 1.4).

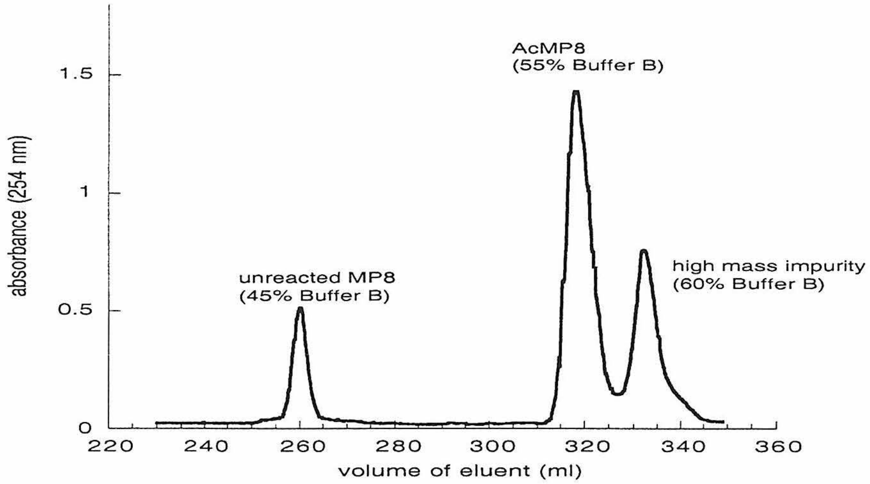

Figure 1.4. FPLC trace for AcMP8 purification. The third peak is due to an unidentified (heme-containing) reaction byproduct with MW = 1946 amu.

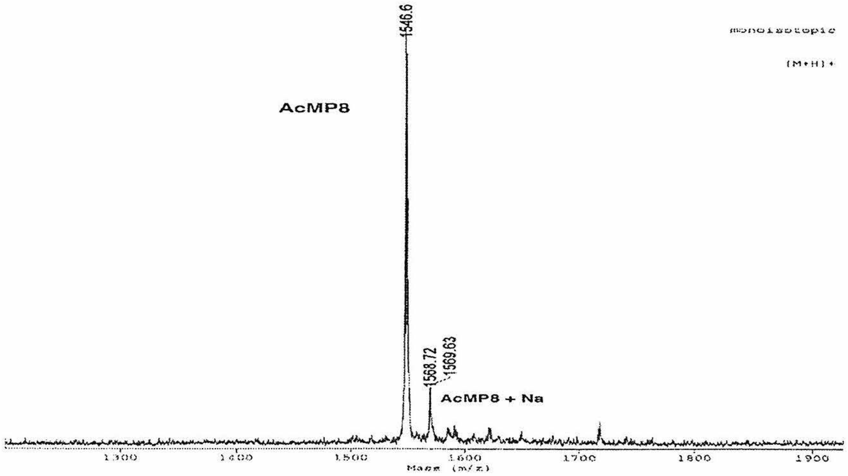

Figure 1.5. MALDI mass spectrum of FPLC purified AcMP8.

We have always observed some amount of unreacted MP8, which can be reduced by increasing the peptide concentration in the reaction solution. AcMP8 was characterized by MALDI mass spectrometry (MW = 1549 amu) (Figure 1.5).

Ligand binding

Ligand binding experiments with Fe(III)AcMP8 were performed under aerobic conditions at RT. 4 - 5 ml of a concentrated stock solution for each ligand (> 2 M) was initially prepared in 50 mM sodium phosphate (pH 7). These stock solutions were then used to prepare solutions of lower ligand concentrations at pH 7. Equal-volume aliquots (0.5 – 1 ml) from these ligand solutions were added equal volumes of concentrated AcMP8 for each data point on a titration curve. Each solution contained 4 - 7 μM AcMP8 and up to 1.98 M AcMet, 1.68 M Ala or 1M imidazole. Ala and imidazole titrations were done in 200 mM phosphate buffer at pH 8 for the former and pH 7 and 8 for the latter. Samples were allowed to equilibrate ~ 30 min before spectroscopic measurements.

Samples for Fe(II)AcMP8 titrations were initially deaerated by Ar-bubbling for 5-7 min prior to the addition of aliquots from a deaerated sodium dithionite (Mallinckrodt) stock solution. They were kept in a cuvette sealed with a rubber septum. Each solution contained 4 - 7 μM peptide and up to 80 mM AcMet, 1.68 M Ala or 1 M imidazole. The final concentration of dithionite in the samples was adjusted to an absorbance of 1.5 - 2.0 at 314 nm. Solutions were equilibrated for 10 min before recording absorption spectra (HP-8452 and Cary-14 spectrophotometers).

Titration data were fit using Equation 1

$$A_{\lambda} = A_{\lambda(\mathrm{AcMP8})} - \left[\frac{\dfrac{[\mathrm{AcMP8}]}{K_d}[\mathrm{L}]}{1 + \dfrac{[\mathrm{L}]}{K_d}} \right] \left(\varepsilon_{\lambda(\mathrm{AcMP8})} - \varepsilon_{\lambda(\mathrm{L\text{-}AcMP8})} \right) \qquad (1)$$

where A_{λ} is the absorbance at a given wavelength, L is the added ligand and $\varepsilon_{\lambda(\text{AcMP8})}$ and $\varepsilon_{\lambda(\text{L-AcMP8})}$ are the extinction coefficients of water- and ligand-bound AcMP8 at that wavelength. Fitting was optimized by adjusting $\varepsilon_{\lambda(\text{L-AcMP8})}$ values. The $\varepsilon_{\lambda(\text{AcMet-AcMP8})}$ values that resulted in the best fits were used to calculate the spectra of 100%-AcMet-bound Fe(II)- and Fe(III)AcMP8. Data at several wavelengths were used to calculate dissociation constants and standard deviations.

Resonance Raman spectroscopy

Samples for resonance Raman (RR) spectroscopy contained 5-10 μM AcMP8 and sufficiently high concentrations of ligands to ensure a large population of bound species. The 413.0-nm RR-excitation was generated by a Lambda-Physik FL3002 dye laser (PBBO dye) pumped by a Lambda-Physik LPX 210I XeCl excimer laser. The probe light was cleaned using a 1200 groves/mm-diffraction grating and passage through a 20 μm slit to reject off-axis light. RR spectra were recorded at RT using a 0.75 m spectrograph (Spex 750) and a liquid nitrogen cooled CCD detector (Princeton Instruments) interfaced to a PC running WinSpec data collection software. Data were collected at a 90°-geometry. Extra care was taken to prevent room light from reaching the monochromator slit. To this end, the sample and data collection optics were covered as much as possible without blocking the excitation beam. The fluorescence from a concentrated solution of $Ru(bpy)_3^{2+}$ was used for the alignment of light collection optics in order to optimize the Raman signal. The excitation energy was 1 - 1.5 mJ at the sample and data acquisition times ranged from 40 to 600 s at a 10 Hz repetition rate. Raman shifts were calibrated using known emission lines from an Ar spectral calibration lamp (Oriel).

Electrochemistry

Solutions for electrochemical measurements contained 75 μM AcMP8 and 100 mM $NaClO_4$ as supporting electrolyte in addition to 50 mM phosphate buffer (pH 7) and varying concentrations of AcMet (≤ 700 mM) or 100 mM imidazole. Solutions were thoroughly deaerated after the addition of each aliquot of AcMet. Measurements were conducted at RT with a CH Instruments 660 electrochemical workstation. A polished and sonicated 3 mm-diameter glassy carbon electrode (BAS) and a platinum wire were used as working- and counter-electrodes, and the reference electrode was Ag/AgCl. Cyclic voltammograms for every sample remained unchanged with repetitive scans (at scan rates up to 100 mV/s); in a typical experiment 2 - 4 scans were recorded and the final scan was used for analysis. The anodic-cathodic peak separation (ΔE_p) was 75 mV for the imidazole complex and did not change with scan rate. Peak currents varied linearly with (scan rate)$^{1/2}$. In the methionine titration experiment, ΔE_p ranged between 80 and 120 mV depending on the methionine concentration. At low methionine concentrations, peak currents were linearly dependent on (scan rate)$^{1/2}$; at high concentrations, accurate current readings could not be obtained at a sufficient number of scan rates due to the dilution of AcMP8.

Calculation of heme exposure to solvent

Solvent-exposed heme surface areas were calculated using MS[16] (with help from Dr. Brian Crane) with a probe radius of 1.4 Å and a Z-factor of 10 dots/Å^2. The following

PDB structures were used: 1YCC (cyt *c*), 256B (cyt b_{562}), 1CYO (cyt b_5), 2C2C (cyt c_2), 2CDV (cyt c_3), 1CC5 (cyt c_5), 351C (cyt c_{551}), 1CYI (cyt c_6), 1CTM (cyt *f*), 4MBN (metmyoglobin), and 1DVH (cyt c_{553}). All were from crystal structure analyses with the exception of cyt c_{553}, for which 11 randomly selected NMR structures out of the listed 36 were used. Only monomers were considered in cases where a protein crystallized as an oligomer. A slight modification in MS was also undertaken to exclude the C_β, C_γ, O_1, and O_2 atoms of the heme propionates and the β-carbons of the vinyl substituents from calculations by evaluating them as separate residues from the heme.

Results

Absorption spectroscopy

Absorption spectroscopy of Fe(III)AcMP8 has been examined previously in great detail.[13,17] The spectrum features a Soret band at 397 nm, broad absorption around 500 nm, and a porphyrin(π) → iron(dπ) charge-transfer (CT) band at 622 nm, which are typical of a mixed spin ferric heme system (S=5/2 ↔ 1/2 or 5/2 ↔ 3/2) (Figure 2.6).[18,19] There are far fewer investigations on Fe(II)MP8, as dithionite, which is commonly used as a reductant, has been reported to degrade the porphyrin ring even under the most carefully controlled anaerobic conditions.[20] Under the conditions mentioned in the Materials section, we found the Fe(II)AcMP8 to be relatively stable. The spectrum of Fe(II)AcMP8 exhibits a broad Soret absorption peaking at 410 nm with a shoulder at 422 nm, and Q-bands at 516 and 546 nm (Figure 1.6). A comparable Soret absorption profile in the spectrum of semisynthetic Met80Ala-Fe(II)cyt *c* (maximum at 411 nm and shoulder at 434 nm) has been interpreted in terms of a mixture of five-coordinate, high-

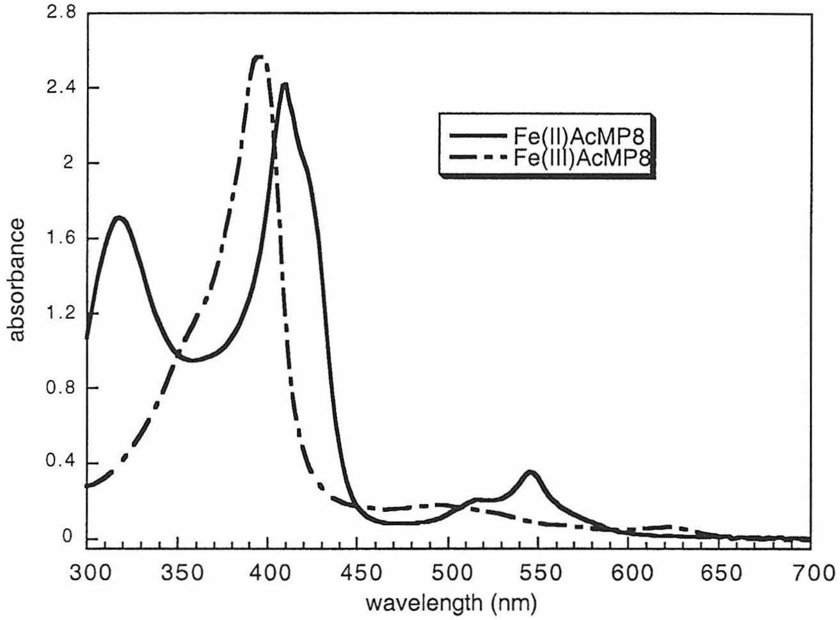

Figure 1.6. UV-vis spectra of oxidized (**broken line**) and reduced (**solid line**) AcMP8. The large absorption band centered at 314 nm is due to dithionite.

spin and six-coordinate, low-spin iron species.[21] Similarly, the absorption spectrum of Fe(II)MP8 with an unblocked N-terminus exhibits features (Soret at 414 nm, shoulder at 430 nm, and Q-bands at 521 and 549 nm) that indicate a mixture of low- and high-spin species.[22] The low-spin component of this spectrum is possibly due to the coordination of the terminal amine group to iron. In the case of AcMP8, it is likely that a water-bound low-spin iron is in equilibrium with a five-coordinate high-spin species.

In order to determine the range of concentrations where AcMP8 is monomeric and can thus be used for ligand titrations, we have investigated the concentration dependence of its absorption spectrum. It has been reported that in Fe(III)AcMP8 solutions intermolecular N-terminus → Fe ligation results in a red-shifted Soret band around 404 nm,[23] and that π–π stacking of the heme groups causes hypochromism of the Soret band and the appearance of a shoulder at ~ 360 nm.[14] In both oxidation states, the intensities of absorption bands in the AcMP8 spectrum are linearly dependent on concentration, indicating that AcMP8 is monomeric at the concentrations used in this study (Figure 1.7). This is further confirmed by the fact that the spectral features of AcMP8 do not change upon the addition of methanol (10% v:v), which is known to inhibit aggregation by disrupting π–π stacking.

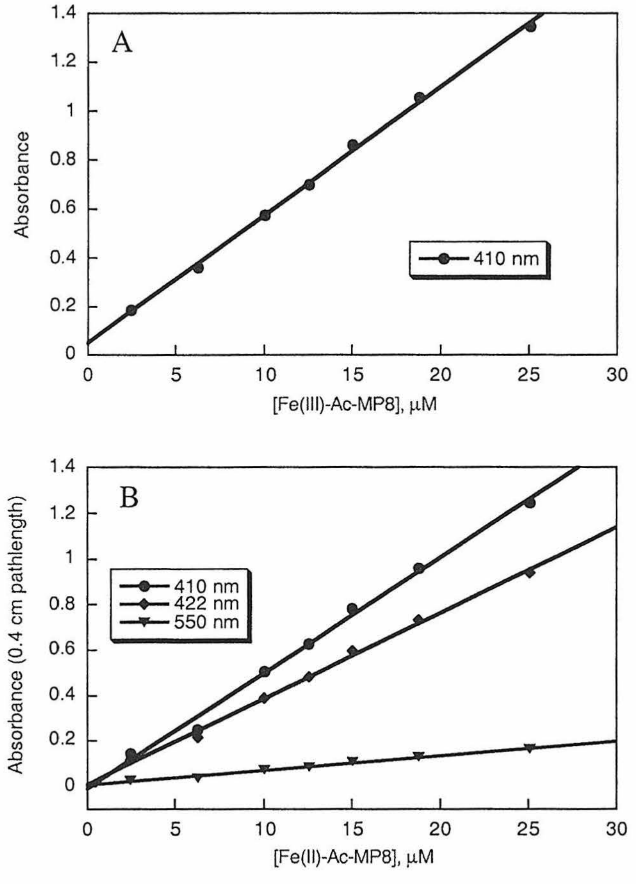

Figure 1.7. Concentration dependence of oxidized (**A**) and reduced (**B**) AcMP8 absorption intensities. The linear dependence indicates that AcMP8 is monomeric in the 0 –25 μM range used for ligand titrations.

Ligand binding

Upon the addition of AcMet, the spectrum of Fe(III)AcMP8 undergoes changes that are consistent with a high- to low-spin transition (Figure 1.8): the Soret band red-shifts, a Q-band emerges at 526 nm with a shoulder at 560 nm, and the 622-nm absorption intensity drops. Further evidence for methionine S-atom (S(AcMet)) coordination is provided by the presence of a band at 695 nm.[24] The isosbestic point at 404 nm implies a two-state conversion as the water is replaced by S(AcMet).

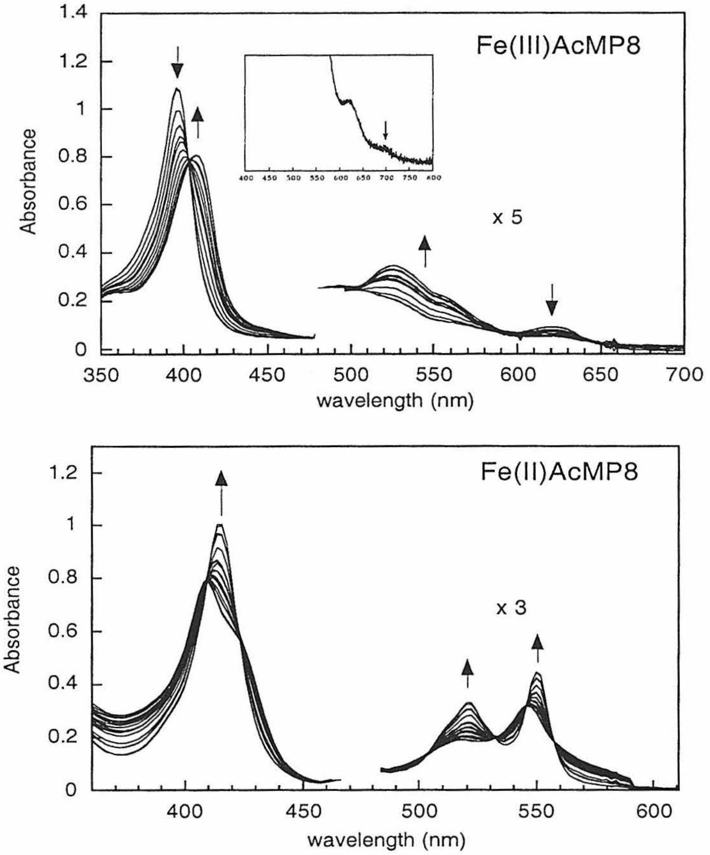

Figure 1.8. Changes in the absorption spectra of oxidized (**top**) and reduced (**bottom**) AcMP8 upon AcMet addition. [AcMet]-range is 0 – 1.98 M for Fe(III)AcMP8, and 0 – 80 mM for Fe(II)AcMP8). The inset in the upper spectrum shows the 695-nm band indicative of S(Met)-AcMP8 coordination.

Munro and Marques have previously demonstrated that increasing ionic strength results in the aggregation of AcMP8.[14] The finding that the spectrum of AcMP8 remains unchanged in the presence of 1.2 M AcVal indicates that aggregation does not take place in our titrations, and that carboxylate binding is not responsible for the AcMet-induced spin change.

Similar to its oxidized counterpart, Fe(II)AcMP8 also undergoes a high- to low-spin transition upon AcMet coordination (Figure 1.8). The Soret band sharpens at 415 nm and the shoulder at 422 nm disappears. The Q-bands also become more distinct, with maxima at 520 and 550 nm, very similar to those observed in the spectrum of Fe(II)cyt *c*. Isosbestic points are evident at 410, 424, 504, 532, 546 and 558 nm. As expected from previous observations that the reduction potential of AcMP8 increases upon AcMet coordination,[25] the affinity of Fe(II)AcMP8 for AcMet is considerably higher than that of

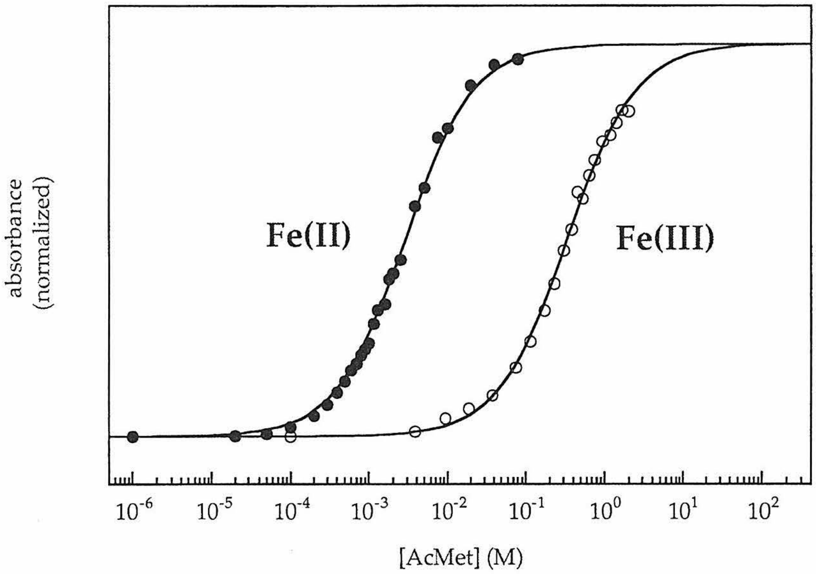

Figure 1.9. AcMet titration curves for oxidized and reduced AcMP8. Absorbances were monitored at 408 and 416 nm, respectively. $K_d = 2.4 \times 10^{-3}$ M (Fe(II)), 3.8×10^{-1} M (Fe(III)).

the oxidized peptide (Figure 1.9). Assuming a two-state equilibrium, we calculate the AcMet-dissociation constants to be 2.4 ± 0.2 mM for Fe(II)AcMP8 and 380 ± 40 mM for Fe(III)AcMP8, and that AcMet binding increases the heme reduction potential by 130 ± 15 mV (Figure 1.10).

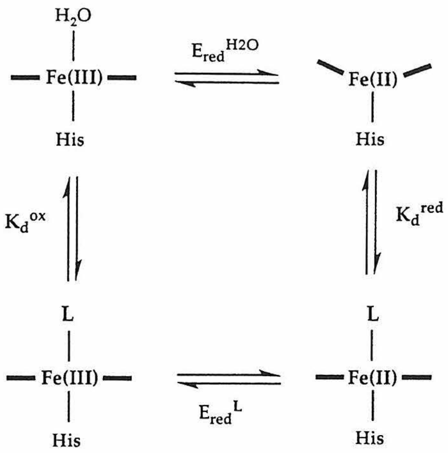

$$E_{red}^{L} - E_{red}^{H2O} = (RT/F) * \ln(K_d^{ox} / K_d^{red})$$

Figure 1.10. Thermodynamic cycle illustrating the relationship between ligand (**L**) binding affinities (or dissociation constants) and reduction potentials for MP8.

Ligation of imidazole (Figure 1.11) or the N-terminus of DL-alanine

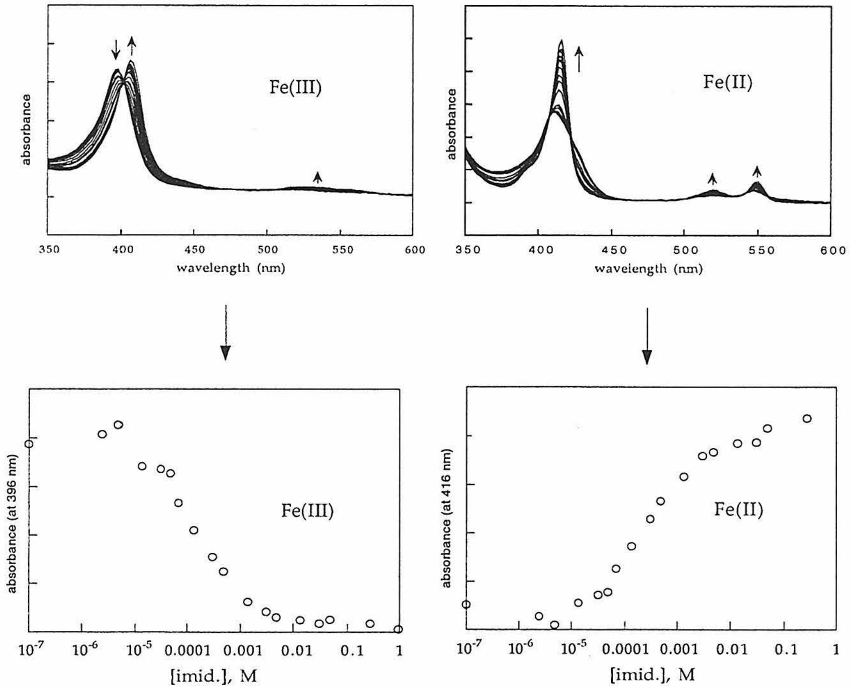

Figure 1.11. Changes in the absorption spectrum of oxidized and reduced AcMP8 upon imidazole addition (at pH 8) and the corresponding titration curves. [Imid] = 0 — 950 mM. $K_d = 3.9 \times 10^{-4}$ M (Fe(II)), 2.5×10^{-4} M (Fe(III)).

(Figure 1.12) to AcMP8 at pH 8 similarly results in high- to low-spin conversion, with Soret bands peaking at 406 or 405 nm for Fe(III)AcMP8 and 416 or 414 nm for

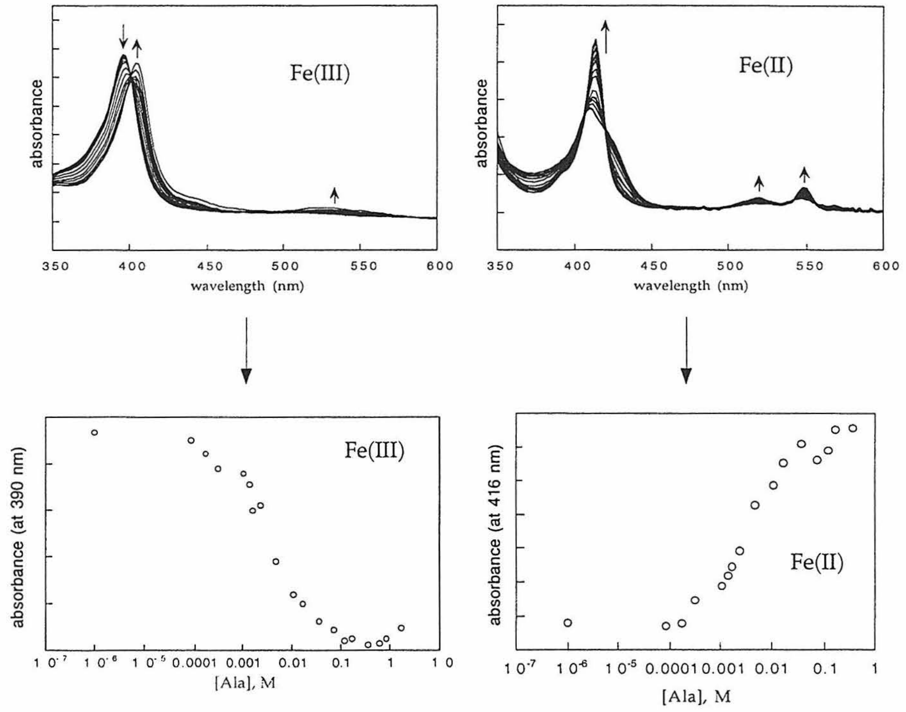

Figure 1.12. Changes in the absorption spectrum of oxidized and reduced AcMP8 upon DL-alanine addition (at pH 8) and corresponding titration curves. [Ala] = 0 — 1.68 M. $K_d = 4.3 \times 10^{-3}$ M (Fe(II)), 3.8×10^{-3} M (Fe(III)).

Fe(II)AcMP8, respectively. Fe(III)AcMP8 adducts of these σ-donating ligands are only slightly more stable than those of Fe(II)AcMP8 (Table 1.1), giving rise to a small downshift in potential (~ 10 mV) .

Titration data were used to generate the absorption spectra of the AcMet complexes of ferric and ferrous AcMP8 (Figure 1.13). All features in these two spectra, including the maxima and the isosbestic points, agree well with those of ferric and ferrous cyt *c*. Residual absorption at 622 nm signals the presence of a small population of a high-spin species in the ferric AcMP8 complex. On the basis of magnetic

Table 1.1. Dissociation constants (M) of thioether, imidazole, and amine complexes.

	Fe(II)AcMP8	Fe(III)AcMP8[a]	Ru(II)$(NH_3)_5$[b]	Ru(III)$(NH_3)_5$[b]
Ac-methionine	2.4×10^{-3}	3.8×10^{-1}	$\leq 1 \times 10^{-5}$	$\leq 6.3 \times 10^{1}$
imidazole	3.9×10^{-4}[c]	2.5×10^{-4}[c]	3.5×10^{-7}	5.3×10^{-7}
alanine	4.3×10^{-3}[c]	3.8×10^{-3}[c]	2.8×10^{-5}	6.3×10^{-6}

[a] An extensive list of binding constants for Fe(III)MP8 ligands is given in Chapter 20 of Ref. 4. [b] From Ref. 38. Corresponding entries for Ac-methionine and alanine are $(CH_3)_2S$ and NH_3. [c] At pH 8. Dissociation constants for the imidazole adduct of AcMP8 at pH 7 are 5.8 and 3.4×10^{-4} M for Fe(II) and Fe(III) forms, respectively, in accordance with a $pK_a \sim 7$ of free imidazole.

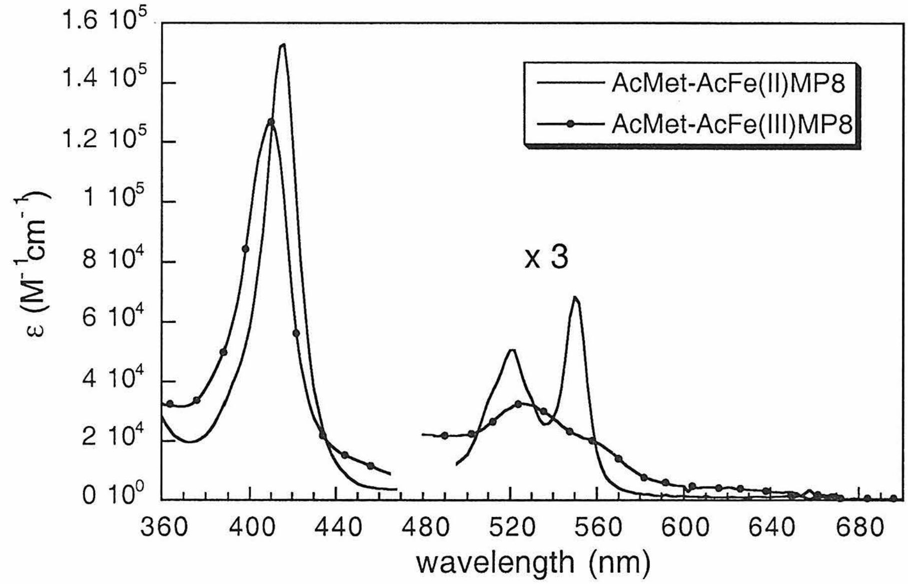

Figure 1.13. Calculated UV-visible absorption spectra for the AcMet complexes of Fe(II)AcMP8 (straight line) and Fe(III)AcMP8 (dotted line). The Q-band region was magnified three-fold. The absorption maxima exactly match those of Fe(II)- and Fe(III)-cyt *c*.

measurements, Yang and Sauer also concluded that (AcMet)Fe(III)AcMP8 exists in a thermal spin equilibrium that is dominated by the low-spin form at room temperature.[26]

Resonance Raman spectroscopy

High-frequency (1300 - 1650 cm^{-1}) RR spectra (Soret excitation) of heme proteins depend strongly on the oxidation state, spin state, and coordination of the metal center.[27,28] The spectrum of Fe(III)AcMP8 (Figure 1.14) exhibits an oxidation-state marker band, ν_4, at 1370 cm^{-1}, typical of a six-coordinate Fe(III).[19,29] The porphyrin core-size marker bands (ν_3 and ν_2, centered at 1490 and 1575 cm^{-1}) are broad, owing to contributions from both high- and low-spin species. AcMet coordination to

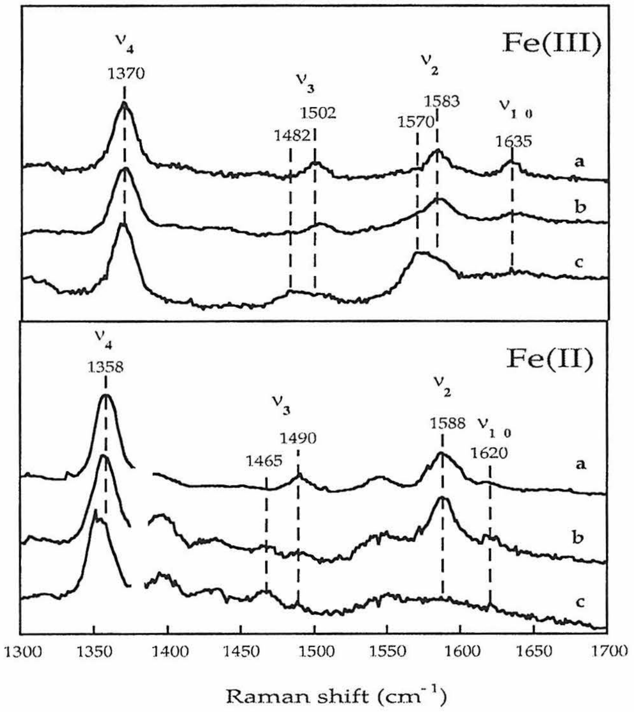

Figure 1.14. High-frequency RR spectra of AcMP8 and cytochrome *c*. **(Top)** Fe(III) species (a) Fe(III)cyt *c* (b) Fe(III)AcMP8 in the presence of 1 M AcMet (~70% bound) (c) Fe(III)AcMP8. **(Bottom)** Fe(II) species. The spectra were magnified by 150% in the range 1380 - 1700 cm^{-1} (a) Fe(II)cyt *c* (b) Fe(II)AcMP8 in the presence of 100 mM AcMet (~97% bound) (c) Fe(II)AcMP8.

Fe(III)AcMP8 shifts ν_3 and ν_2 to 1502 and 1583 cm^{-1}, indicative of a low-spin iron center. The breadth of these bands relative to those of low-spin Fe(III)cyt *c* is most likely due to the presence of AcMet-free Fe(III)AcMP8, because at the AcMet concentration used to record the spectrum in Figure 1.14 (1 M), the ratio of high- to low-spin species should be approximately 1 : 3 (K_d = 380 mM). The small high-spin population that exists even in the completely AcMet-bound AcMP8 (see Ligand Binding) should broaden the core-size marker bands as well. Due to the preservation of six-coordinate iron, the ν_4 band in (AcMet)Fe(III)AcMP8 remains at 1370 cm^{-1}. The emergence of the ν_{10}-mode at 1635 cm^{-1} further supports the presence of a low-spin, six-coordinate iron.

Fe(II)AcMP8 also appears to be an equilibrium mixture of high- and low-spin iron species, dominated by the former (Figure 1.14). The ν_4 band, at 1353 cm^{-1}, is red-shifted by 5 cm^{-1} from the frequency expected for a low-spin Fe(II), consistent with observations made on high-spin, five-coordinate species such as deoxyhemoglobin.[27] The ν_3 band is split into two peaks, indicative of high- (1465 cm^{-1}) and low-spin (1490 cm^{-1}) forms of Fe(II). The spin-state sensitive ν_{10} and ν_2 modes are too weak to be discerned, but the broad feature centered at ~1575 cm^{-1} is evidence for a spin equilibrium. Hence, the RR spectra suggest that Fe(II)AcMP8 is a mixture of a high-spin, five-coordinate and low-spin, water-bound species at room temperature. As AcMet is added, ν_{10} and ν_2 bands can be resolved, and the oxidation-state marker blue-shifts to 1357 cm^{-1}, consistent with a high- to low-spin transition. Increases in intensity at 1490 and 1588 cm^{-1} and a decrease at 1465 cm^{-1} also indicate the appearance of a low-spin species. Yet, even at an AcMet concentration of 100 mM, where the fraction of AcMet-bound AcMP8 should be greater than 97% (see Ligand Binding), there is still considerable intensity at 1465 cm^{-1}. Some high-spin component also is present in the imidazole complex of Fe(II)AcMP8, which exhibits essentially the same RR spectrum (1.15). It would appear that the protein fold imposes structural constraints on Fe-S(Met) coordination, since both Fe(II)- and Fe(III)cyt *c* have low-spin ground states.

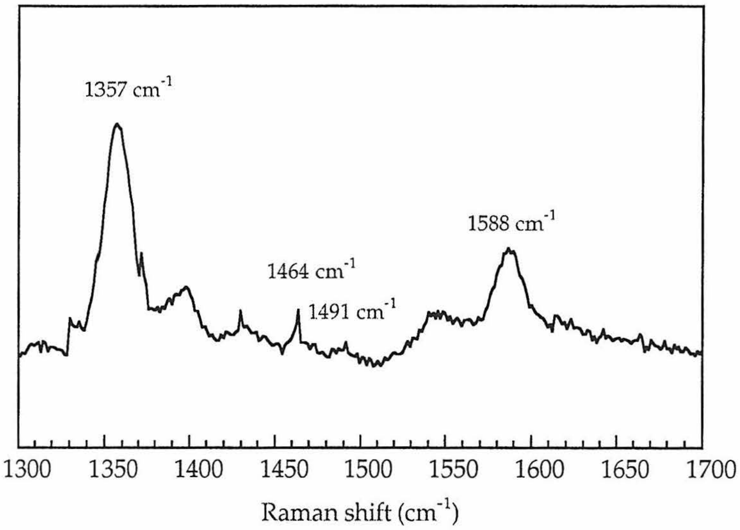

Figure 1.15. High-frequency region of the resonance Raman spectrum of Fe(II)AcMP8 in the presence of 100 mM imidazole (pH7, 413 nm excitation). The ν_3-band is visible (at 1464 cm^{-1} under a spectral glitch), indicating the presence of some high-spin component even in the fully imidazole-bound AcMP8.

Electrochemistry

Cyclic- and square-wave voltammograms of AcMP8 in the presence of various concentrations of AcMet are consistent with binding-constant measurements. The reduction potential of AcMP8 increases by approximately 110 mV when [AcMet] = 700 mM (Figure 1.16), whereas it remains unchanged upon the addition of up to 500 mM

AcVal. Hence, S(AcMet) ligation appears to be responsible for the upshift in potential. At the concentrations that these measurements (75 - 100 μM) were performed, however, heme aggregation is apparent, as indicated by absorption spectra (not shown). Thus, the electrochemistry is complicated by the monomer/dimer equilibrium. Nevertheless, the ΔE measured electrochemically is quite close to that determined spectrophotometrically.

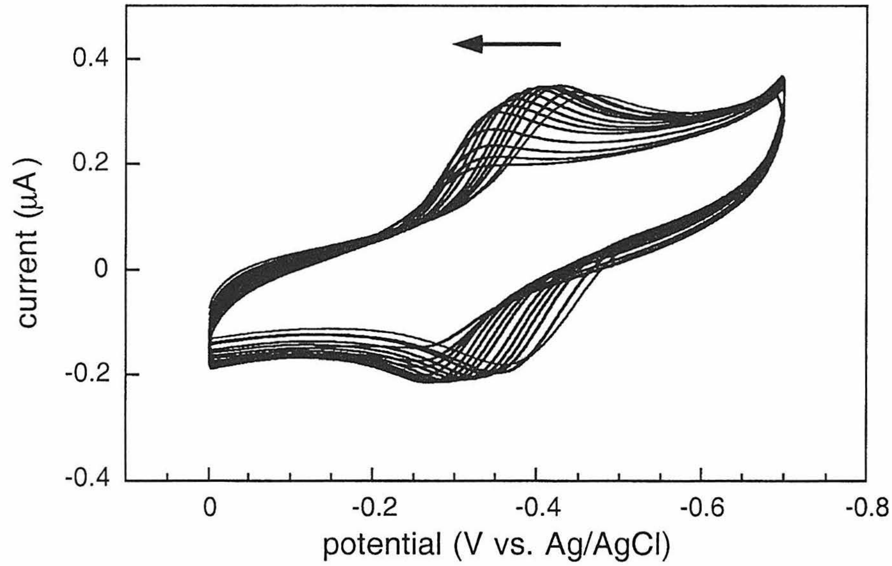

Figure 1.16. Changes in the cyclic voltammogram of AcMP8 upon successive additions of AcMet. [AcMet] = 0 - 700 mM. The voltammograms are not corrected for the dilution of AcMP8 due to the addition of AcMet aliquots. The anodic-cathodic peak separation (ΔE_p) ranged between 80 and 120 mV. At low AcMet concentrations, peak currents were linearly dependent on (scan rate)$^{1/2}$, indicating quasi-reversibility. At high AcMet concentrations, accurate current readings could not be obtained at a sufficient number of scan rates due to the dilution of AcMP8.

Cyclic voltammetry of the AcMP8-imidazole complex ([imidazole] = 100 mM, pH 7) indicates a reduction potential 40 mV lower than that of AcMP8 (Figure 1.17), in agreement with our titration data and a previous report on the electrochemistry of MP11 (MP8 + residues 11-13).[11]

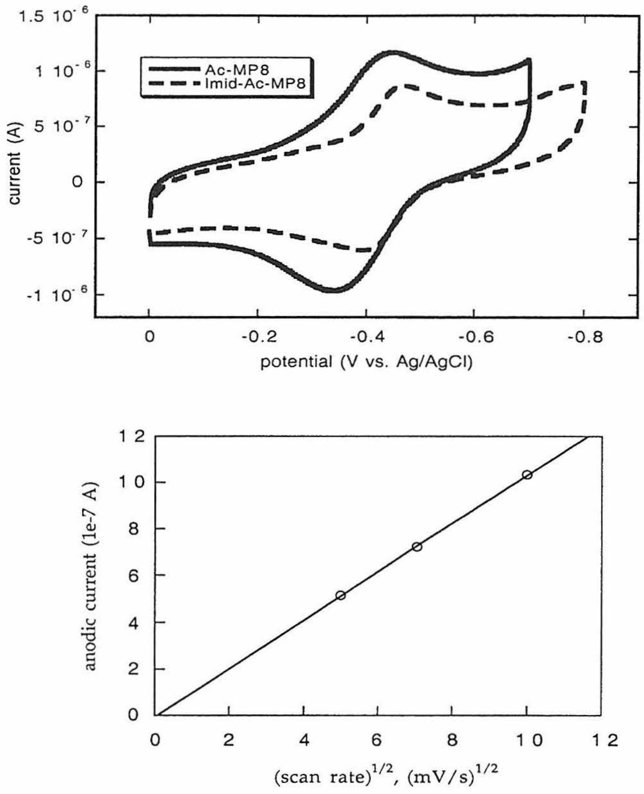

Figure 1.17. Electrochemistry of the imidazole-AcMP8 complex. **(Top)** Cyclic voltammogram (CV) of the complex. CV of AcMP8 (solid line) was also included to illustrate the 40-mV downshift in the AcMP8 potential upon imidazole coordination. The anodic-cathodic peak separation (ΔE_p) was 75 mV and did not change with scan rate. **(Bottom)** Linear dependence of the anodic peak current on (scan rate)$^{1/2}$ for (imid)AcMP8, indicating reversible electrochemistry.

Discussion

Cyt *c* folding involves the collapse of the polypeptide chain around the solvent-exposed heme and changes in the axial ligation of iron.[10,30-33] Burial of the heme in the hydrophobic protein matrix stabilizes the neutral Fe(II)-species relative to the cationic Fe(III)-form, and the reduction potential of the heme increases. The polarity of the cofactor environment has a large influence on the potential of a redox-active protein;[1,3,34-37] thus, it is not surprising that heme encapsulation provides a major portion of the 410-meV driving force for the folding of Fe(II)cyt *c*. Although the exact contribution of heme encapsulation in cyt *c* is difficult to quantify experimentally, the effects of axial ligation can be measured readily by using models such as AcMP8. A previous potentiometric measurement of the (AcMet)MP8 reduction potential suggested an upshift of ~160 mV over that of imidazole-bound MP8.[25] At the AcMet concentrations employed in this study (≤ 2 M),[25] however, MP8 exists as a mixture of AcMet- and water-bound species. Indeed, it is very challenging to measure directly the reduction potential of (AcMet)MP8, due to the fact that 2 M is close to the solubility limit of AcMet. Moreover, MP8 aggregation complicates ligand-binding equilibria. Determination of the reduction-potential shift based on dissociation constants of (AcMet)Fe(II)- and (AcMet)Fe(III)AcMP8 circumvents the complications associated with direct electrochemical measurements.

Our spectrophotometric titrations confirm that AcMet has substantially greater affinity for Fe(II) than for Fe(III). A similar pattern was observed for the binding of thioether ligands to ruthenium-ammine complexes (Table 1.1).[38] The difference in affinity between Fe(II)- and Fe(III)AcMP8 for AcMet corresponds to a 130-mV increase in the heme reduction potential. Wilgus et al. reported that methionine binding affinities of several heme-containing cyt *c* fragments were up to two orders of magnitude greater for the ferrous derivatives, and they were pH dependent between pH 3.1 and 7.0, at least in part due to competitive ligation by histidines present in these protein fragments.[39] Binding affinities for both oxidation states were only reported at pH 4.8, where they were 99 and 3.9 M^{-1} for the ferrous and ferric forms, respectively, corresponding to a reduction potential increase of ~ 80 mV.

Imidazole ligation to MP8 causes a 40-mV downshift in the potential; thus, replacing imidazole with AcMet should result in an upshift of 170 mV, in good agreement with the findings of Harbury et al.[25] and Marchon et al.,[34] who observed a 168-mV upshift with a synthetic heme model system. This value indicates that encapsulation of the heme by the protein raises the cyt *c* potential by ~ 240 mV.

Tuning the Fe(III/II) potential in heme proteins is critical for function. It has been a continuing challenge for theory and experiment to understand how the protein structure regulates this potential.[40-43] Site-directed mutagenesis experiments have revealed the roles of individual amino acid side chains in this regulation,[44-53] and theoretical calculations have focused on the electrostatic heme-protein and heme-solvent interactions in an attempt to account for the potential shifts caused by heme encapsulation.[1,54-56] In an analysis of eight structurally characterized *c*-type cytochromes, we have found that the reduction potential increases with decreasing heme exposure to solvent (Figure 1.18).

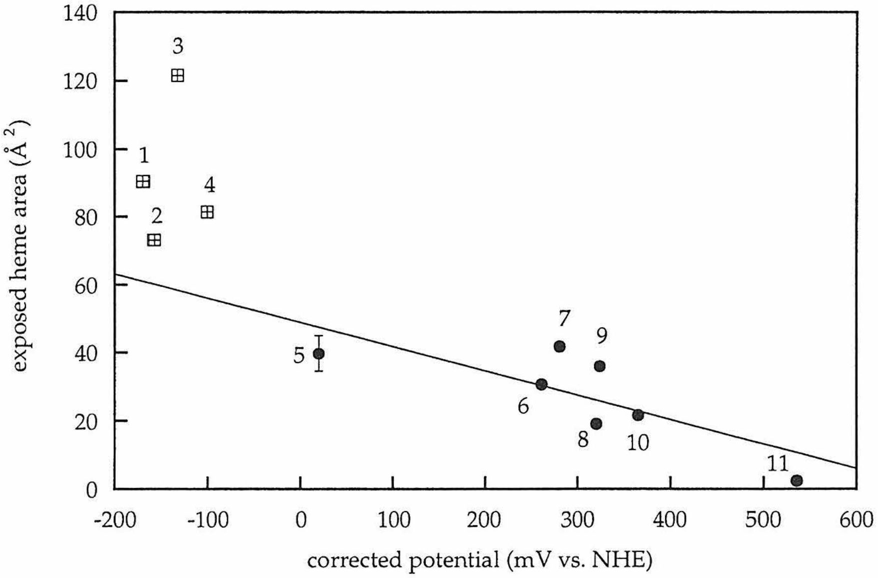

Figure 1.18. Solvent-exposed heme area vs. corrected reduction potential. (1)-(4) Hemes 4-1, cyt c_3 (*D.vulgaris* Miyazaki F),[59] (5) cyt c_{553} (*D. vulgaris*, average of 11 solution structures),[60] (6) cyt *c* (*S. cerevisiae*),[5] (7) cyt c_{551} (*P. aeruginosa*),[61] (8) cyt c_5 (*A. vinelandii*),[62] (9) cyt c_2 (*R. rubrum*),[61] (10) cyt c_6 (*C. reinhardtii*),[63] (11) cyt *f* (turnip).[64] Heme exposures were calculated using MS (Connolly, M. *Science* **1983**, *221*, 709-713) using a 1.4 Å probe radius.

The C_β, C_γ, O_1, and O_2 atoms of the heme propionates and the β-carbons of the vinyl groups were excluded from the solvent-exposed surface-area calculations in order to limit the analysis to the conjugated porphyrin ring system and atoms within one σ-bond from the ring. Heme potentials were corrected by converting His-His (hemes 1-4 and 10) and His-amine (heme 11) ligated hemes to His-Met coordination through the addition of 170 mV to the reported values. In a similar analysis, Stellwagen (*Nature* **1978**, *275*, 73-74) examined the reduction potentials of 6 structurally characterized *b*- and *c*-type heme proteins without correcting for axial ligation effects. He concluded that the principal determinant of reduction potential is heme exposure to solvent.

According to Figure 1.18, the potentials of the four hemes of cyt c_3 (hemes 1-4), which were not included in the correlation, lie significantly higher than a linear potential/exposure model would predict. These hemes are more exposed to the solvent environment than are the cofactors in most other proteins, owing to the relatively small size of cyt c_3 (107 amino acids). It would appear that the downshift of the potential with increasing heme exposure reaches a limit somewhere in the 60-100 $Å^2$ range. Further evidence for this limit are the high potentials of hemes in MP8, unfolded cyt *c*, and the alkaline form of cyt *c* (all ca. -50 mV after ligand correction),[57] which are presumably solvent-exposed to a great extent.

Cyt *f* is at the high-potential end of the correlation; its heme has a solvent exposure very close to zero (2.5 $Å^2$) and a corrected potential of 535 mV, significantly higher than the next set of potentials (hemes 6-10). When the heme propionates and the vinyl β-carbons are included in the calculations, the solvent exposure of the cyt *f* heme (51 $Å^2$) is not significantly lower than those of hemes 6-10. Apparently, by burying the conjugated portion of the porphyrin ring almost completely, the protein is able to achieve a very high reduction potential. We believe that 600 mV should be close to the maximum attainable potential of a His-Met ligated protein.

According to our examination, reduction potentials of *c*-type cytochromes can be tuned by roughly 500 mV through variations in the heme exposure to solvent. Several investigations have shown that electrostatic interactions other than those between the heme and the solvent also play a role in tuning the potentials,[40-43] which is evidenced by the scatter in Figure 1.18. Since changes in axial ligation have been shown to shift the potential by as much as 650 mV,[58] a protein can cover a 1-V range by proper adjustment of the heme environment within its folded structure.

References

(1) Churg, A. K.; Warshel, A. *Biochemistry* **1986**, *25*, 1675-1681.

(2) Bixler, J.; Bakker, G.; McLendon, G. *J. Am. Chem. Soc.* **1992**, *114*, 6938-6939.

(3) Winkler, J. R.; Wittung-Stafshede, P.; Leckner, J.; Malmström, B. G.; Gray, H. B. *Proc. Natl. Acad. Sci. USA* **1997**, *94*, 4246-4249.

(4) Gunner, M. R.; Honig, B. In *Cytochrome c: A Multidisciplinary Approach*; Scott, R. A., Mauk, A. G., Eds.; University Science Books: Sausalito, 1996; pp 347-372.

(5) Moore, G. R.; Pettigrew, G. W. In *Cytochrome c. Evolutionary, Structural and Physicochemical Aspects*; Springer Verlag: Heidelberg, 1990; pp 309-362.

(6) Pascher, T.; Chesick, J. P.; Winkler, J. R.; Gray, H. B. *Science* **1996**, *271*, 1558-1560.

(7) Mines, G. A.; Pascher, T.; Lee, S. C.; Winkler, J. R.; Gray, H. B. *Chem. Biol.* **1996**, *3*, 491-497.

(8) Cohen, D. S.; Pielak, G. J. *J. Am. Chem. Soc.* **1995**, *117*, 1675-1677.

(9) Hilgen-Willis, S.; Bowden, E. F.; Pielak, G. J. *J. Inorg. Biochem.* **1993**, *51*, 649-653.

(10) Elöve, G. A.; Bhuyan, A. K.; Roder, H. *Biochemistry* **1994**, *33*, 6925-6935.

(11) Santucci, R.; Reinhard, H.; Brunori, M. *J. Am. Chem. Soc.* **1988**, *110*, 8536-8537.

(12) Chattopadhyay, K.; Mazumdar, S. *Curr. Sci.* **1997**, *73*, 65-68.

(13) Munro, O. Q.; Marques, H. M. *Inorg. Chem.* **1996**, *35*, 3752-3767.

(14) Low, D. W.; Winkler, J. R.; Gray, H. B. *J. Am. Chem. Soc.* **1996**, *118*, 117-120.

(15) Low, D. W. Ph.D., California Institute of Technology, 1997.

(16) Connolly, M. L. *Science* **1983**, *221*, 709-713.

(17) Wang, J.-S.; Tsai, A.-L.; Heldt, J.; Palmer, G.; Van Wart, H. E. *J. Biol. Chem.* **1992**, *267*, 15310-15318.

(18) Huang, Y.-P.; Kassner, R. J. *J. Am. Chem. Soc.* **1981**, *103*, 4927-4932.

(19) Wang, J.-S.; Van Wart, H. E. *J. Phys. Chem.* **1989**, *93*, 7925-7931.

(20) Adams, P. A.; Baldwin, D. A.; Marques, H. M. In *Cytochrome c- A multidisciplinary approach*; Scott, R. A., Mauk, A. G., Eds.; University Science Books: Sausalito, 1995.

(21) Bren, K. L. Ph.D., California Institute of Technology, 1996.

(22) Othman, S.; Le Lirzin, A.; Desbois, A. *Biochemistry* **1993**, *32*, 9781-9791.

(23) Urry, D. W.; Pettegrew, J. W. *J. Am. Chem. Soc.* **1967**, *89*, 5276-5283.

(24) Moore, G. R.; Pettigrew, G. W. In *Cytochrome c. Evolutionary, Structural and Physicochemical Aspects*; Springer Verlag: Heidelberg, 1990; pp 27-113.

(25) Harbury, H. A.; Cronin, J. R.; Fanger, M. W.; Hettinger, T. P.; Murphy, A. J.; Myer, Y. P.; Vinogradov, S. N. *Proc. Natl. Acad. Sci. USA* **1965**, *54*, 1658-1664.

(26) Yang, E. K.; Sauer, K. In *Electron Transport and Oxygen Utilization*; Ho, C., Ed.; Elsevier Biomedical: New York, Amsterdam, Oxford, 1982.

(27) Spiro, T. G.; Strekas, T. C. *J. Am. Chem. Soc.* **1974**, *96*, 338-345.

(28) Spiro, T. G. In *Biological Applications of Raman Spectroscopy*; Spiro, T. G., Ed.; John Wiley & Sons: New York, 1987; Vol. 3.

(29) Othman, S.; Le Lirzin, A.; Desbois, A. *Biochemistry* **1994**, *33*, 15437-15448.

(30) Sosnick, T. R.; Mayne, L.; Englander, S. W. *Proteins* **1996**, *24*, 413-426.

(31) Pierce, M. M.; Nall, B. T. *Protein Sci.* **1997**, *6*, 618-627.

(32) Takahashi, S.; Yeh, S.-R.; Das, T. K.; Chan, C.-K.; Gottfried, D. S.; Rousseau, D. L. *Nature Struct. Biol.* **1997**, *4*, 44-56.

(33) Telford, J. R.; Wittung-Stafshede, P.; Gray, H. B.; Winkler, J. R. *Acc. Chem. Res.* **1998**, *31*, 755-763.

(34) Marchon, J.-C.; Mashiko, T.; Reed, C. A. In *Electron Transport and Oxygen Utilization*; Ho, C., Ed.; Elsevier Biomedical: New York, Amsterdam, Oxford, 1982.

(35) Stephens, P. J.; Jollie, D. R.; Warshel, A. *Chem. Rev* **1996**, *96*, 2491-2513.

(36) Kassner, R. J. *Proc. Natl. Acad. Sci. USA* **1972**, *69*, 2263-2267.

(37) Kassner, R. J. *J. Am. Chem. Soc.* **1973**, *95*, 2674-2677.

(38) Kuehn, C. G.; Taube, H. *J. Am. Chem. Soc.* **1976**, *98*, 689-702.

(39) Wilgus, H.; Ranweiler, J. S.; Wilson, G. S.; Stellwagen, E. *J. Biol. Chem.* **1978**, *253*, 3265-3272.

(40) Zhou, H.-X. *JBIC* **1997**, *2*, 109-113.

(41) Mauk, A. G.; Moore, G. R. *JBIC* **1997**, *2*, 119-125.

(42) Gunner, M. R.; Alexov, E.; Torres, E.; Lipovaca, S. *JBIC* **1997**, *2*, 126-134.

(43) Warshel, A.; Papazyan, A.; Muegge, I. *JBIC* **1997**, *2*, 143-152.

(44) Varadarajan, R.; Zewert, T. E.; Gray, H. B.; Boxer, S. G. *Science* **1989**, *243*, 69-72.

(45) Lloyd, E.; King, B. C.; Hawkridge, F. M.; Mauk, A. G. *Inorg. Chem.* **1998**, *37*, 2888-2892.

(46) Davies, A. M.; Guillemette, J. G.; Smith, M.; Greenwood, C.; Thurgood, A. G. P.; Mauk, A. G.; Moore, G. R. *Biochemistry* **1993**, *32*, 5431-5435.

(47) Cutler, R. L.; Davies, A. M.; Creighton, S.; Warshel, A.; Moore, G. R.; Smith, M.; Mauk, A. G. *Biochemistry* **1989**, *28*, 3188-3197.

(48) Whitford, D.; Gao, Y.; Pielak, G. J.; Williams, R. J. P.; McLendon, G. L.; Sherman, F. *Eur. J. Biochem.* **1991**, *200*, 359-367.

(49) Rafferty, S. P.; Pearce, L. L.; Barker, P. D.; Guillemette, J. G.; Kay, C. M.; Smith, M.; Mauk, A. G. *Biochemistry* **1990**, *29*, 9365-9369.

(50) Louie, G. V.; Pielak, G. J.; Smith, M.; Brayer, G. D. *Biochemistry* **1988**, *27*, 7870-7876.

(51) Rodgers, K. K.; Sligar, S. G. *J. Am. Chem. Soc.* **1991**, *113*, 9419-9421.

(52) Guillemette, J. G.; Barker, P. D.; Eltis, L. D.; Lo, T. P.; Smith, M.; Brayer, G. D.; Mauk, A. G. *Biochimie* **1994**, *76*, 592-604.

(53) Rivera, M.; Seetharaman, R.; Girdhar, D.; Wirtz, M.; Zhang, X.; Wang, X.; White, S. *Biochemistry* **1998**, *37*, 1485-1494.

(54) Langen, R.; Brayer, G. D.; Berghuis, A. M.; McLendon, G.; Sherman, F.; Warshel, A. *J. Mol. Biol.* **1992**, *224*, 589-600.

(55) Gunner, M. R.; Honig, B. *Proc. Natl. Acad. Sci. USA* **1991**, *88*, 9151-9155.

(56) Zhou, H.-X. *J. Am. Chem. Soc.* **1994**, *116*, 10362-10375.

(57) Barker, P. D.; Mauk, A. G. *J. Am. Chem. Soc.* **1992**, *114*, 3619-3624.

(58) This value is from work on position-80 mutants of cyt *c* (Raphael, A. L.; Gray, H. B. *J. Am. Chem. Soc.* **1991**, *113*, 1038-1040).

(59) The four microscopic (interaction-decoupled) heme potentials in cyt c_3 were reported by Fan et al. (Fan, K.; Akutsu, H.; Kyogoku, Y.; Niki, K. *Biochemistry* **1990**, *29*, 2257-2263). The assignment of these potentials to individual hemes was made by Park et al. (Park, J.-S.; Kano, K.; Niki, K.; Akutsu, H. *FEBS Lett.* **1991**, *285*, 149-151).

(60) Blackledge, M. J.; Guerlesquin, F.; Marion, D. *Proteins* **1996**, *24*, 178-194.

(61) Taniguchi, V. T.; Sailasuta-Scott, N.; Anson, F. C.; Gray, H. B. *Pure Appl. Chem.* **1980**, *52*, 2275-2281.

(62) Mathews, F. S. *Prog. Biophys. Mol. Biol.* **1984**, *45*, 1-56.

(63) Kerfeld, C. A.; Anwar, H. P.; Interrante, R.; Merchant, S.; Yeates, T. O. *J. Mol. Biol.* **1995**, *250*, 627-647.

(64) Cramer, W. A.; Whitmarsh, J. *Annu. Rev. Plant Physiol.* **1977**, *28*, 133-172.

Chapter 2

Cytochrome *c* Folding Triggered by Electron Transfer. The Role of Ligand Substitution in Ferrocytochrome *c* Folding*

* Adapted from Telford, J. R.; Gray, H. B.; Tezcan, F. A.; Winkler, J. R. *Biochemistry* **1999**, *38*, 1944-1949. This work was done in collaboration with Dr. Jason Telford, who carried out most of the experiments on folding kinetics.

Introduction

Understanding how a singular protein structure is formed from a large ensemble of only slightly destabilized molecules is a continuing challenge for theory [1-6] and experiment.[7-14] For experiment, an important goal is to develop fast folding triggers that allow the monitoring of rapid protein motions and short-lived folding intermediates. Stopped-flow mixing techniques coupled with optical or NMR detection have been instrumental in our current understanding of protein folding.[15-21] These techniques, however, are typically limited by a time resolution of a few milliseconds and do not permit the monitoring of fast collapse events observed during the folding of some proteins.[22-26] Triggering methods employing laser excitation, such as rapid temperature jumps or photolysis of molecules that affect protein stability, have recently extended the time-resolution limit to microseconds.[7,27-29]

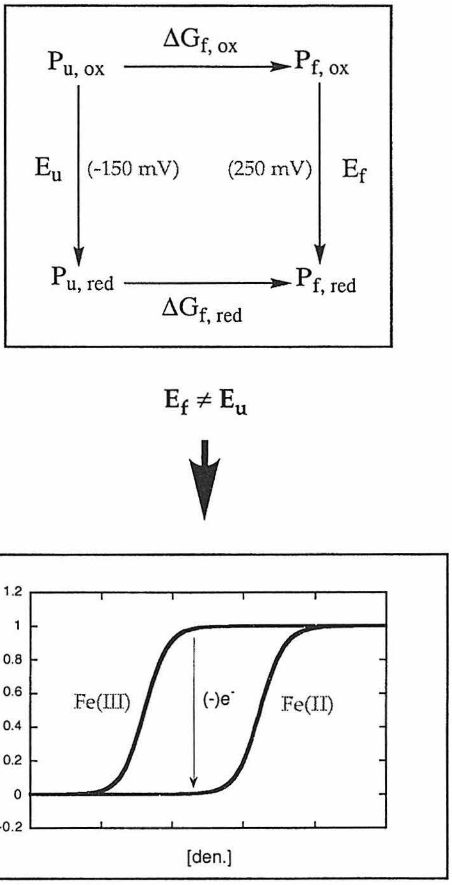

Figure 2.1. Thermodynamic basis for ET-triggered protein (cyt *c*) folding (P, protein; f, folded; u, unfolded; ox, oxidized; red, reduced).

Our approach to rapid triggering is based on photo-initiated electron transfer (ET). As we have seen in Chapter 1, the reduction potential of the heme group in aqueous solution can be markedly different (generally lower) from that inside a protein (Figure 1.1). Consequently, the folding free energies of the oxidized and reduced forms of the protein differ by a corresponding amount, giving rise to a denaturant concentration range where one oxidation state is unfolded and the other is folded (Figure 2.1). Injection or abstraction of an electron in this regime can effect the folding or unfolding of the protein.

Cytochrome *c* folding

Our initial efforts on ET-triggered folding have focused on cytochrome *c* (cyt *c*) (Figure 2.2). In the folded protein, the heme potential (260 mV) is ~ 400 mV higher than that in the unfolded protein. As predicted from this potential shift, Fe(II)cyt *c* is ~ 10 kcal/mol more stable towards unfolding than Fe(III)cyt *c* (Figure 2.3). Thus, photoinduced ET into unfolded Fe(III)cyt *c* triggers the folding Fe(II)cyt *c*.

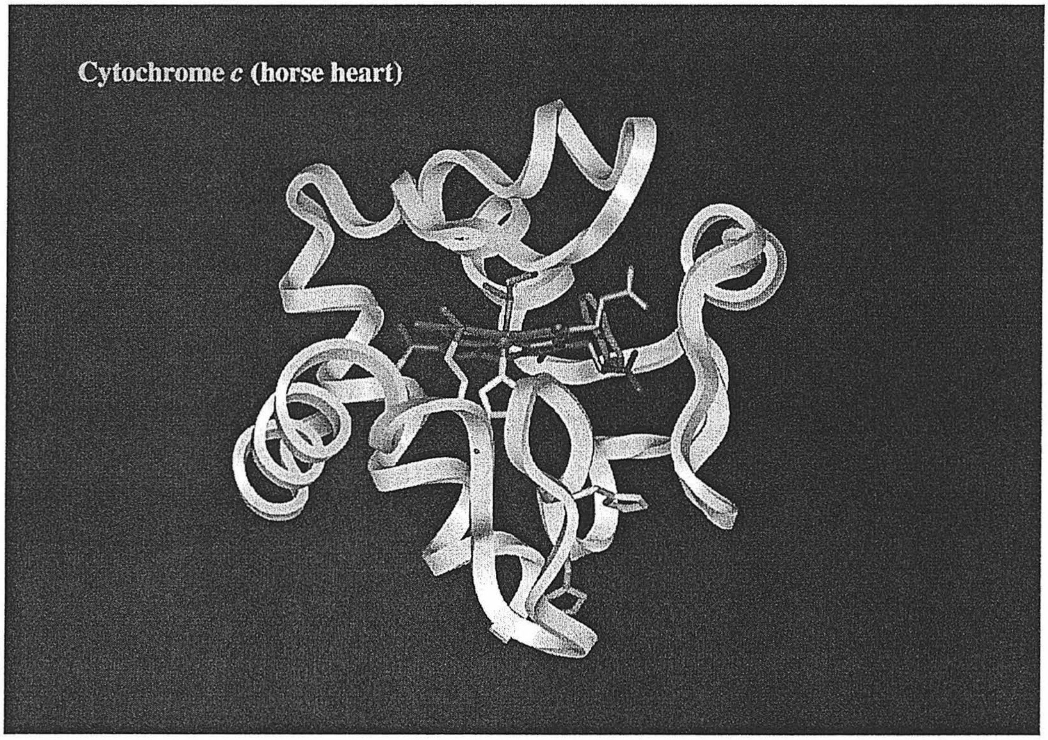

Figure 2.2. Crystal structure of horse heart cyt *c* (PDB ID: 1HRC). Heme, red; Met 80 and Cys 14 (back) &17 (front), green; His 18 (top), His 26 (middle) and His 33 (bottom), yellow; Trp 59, magenta.

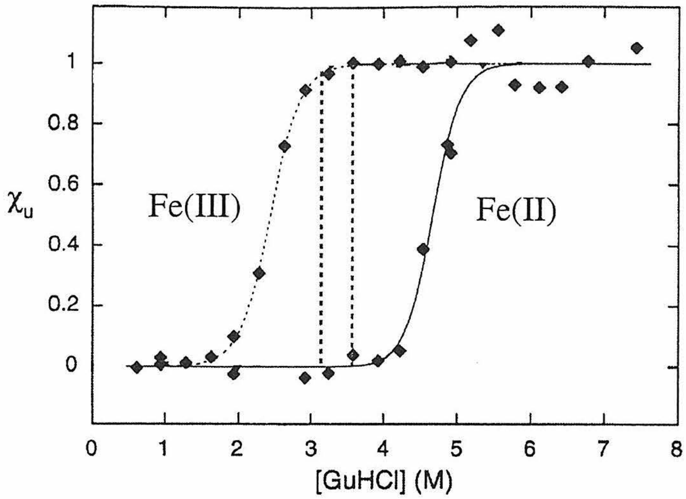

Figure 2.3. Guanidine hydrochloride (GuHCl) denaturation curves for oxidized and reduced horse heart cyt *c* (adapted from the Ph.D. thesis of Gary Mines); χ_u: fraction unfolded. Denaturation midpoints are 2.8 M (Fe(III)) and 5.3 M (Fe(II)) GuHCl. Folding experiments described in this study were typically conducted at 3.2-3.5 M GuHCl.

The kinetics of cyt *c* folding have been investigated in many laboratories.[7,30-37] The structure and stability of cyt *c* is intimately linked to the heme group and iron coordination. For example, metal-free cyt *c* is significantly destabilized compared to the native protein; apo-cyt *c*, in which the whole heme group has been removed, is devoid of any secondary or tertiary structure.[38-40] The heme iron in the folded protein is coordinated to two axial ligands, an imidazole nitrogen from His18 and a thioether sulfur from Met80 (Figure 2.2).[41] When Fe(III)cyt *c* is denatured by guanidine hydrochloride (GuHCl) at neutral pH, far-UV circular dichroism (CD) measurements reveal a cooperative unfolding transition with a midpoint at 2.7 M GuHCl.[39,42] The CD spectra suggest that all secondary structure is lost above 3.5 M GuHCl.[39,42] Small-angle X-ray scattering measurements (SAXS) of the Fe(III)cyt *c* radius of gyration (R_g) also show a cooperative unfolding transition with a midpoint at 2.6 M GuHCl; the value of R_g increases from 13.8 ± 0.3 to 30.3 ± 0.1 Å as the protein unfolds.[43] Consistent with this finding is the increase in Trp 59 fluorescence (> 2.0 M GuHCl; unfolding midpoint=2.8 M), which is quenched in the native protein due to energy transfer to the heme group (Figure 2.2).[44] Kratky plots of the SAXS data were interpreted in terms of two ensembles of unfolded protein; the dominant ensemble at 2.8 M GuHCl is not globular, but retains some residual structure. Above 3.5 M GuHCl, the SAXS data suggest that Fe(III)cyt *c* is a random coil.[43] It is likely that there are many unfolded states of the protein; the two ensembles identified in the SAXS analysis represent averages corresponding to the different denaturing conditions.[43] In addition to peptide conformational changes, GuHCl also induces replacement of the Met80 axial ligand by a nitrogenous base. In the equine protein, both His26 and His33 (Figure 2.2) have been implicated as ligands in the unfolded protein, although His33 is thought to dominate.[45] Several groups, including us (see Chapter 3), have recently reported that lysines or the N-terminal amine group (in yeast cyt *c*) can act as axial ligands as well.[46-48] Under acidic denaturing conditions, one or both of the axial ligands can be replaced by water. It is clear, then, that cyt c folding requires not just the arrangement of a polypeptide into a discrete three-dimensional structure, but also heme ligand substitution processes.[8,30,32,34,35,49-53]

The HisX (X = 26, 33) ligands present in unfolded Fe(III)cyt *c* at neutral pH lead to kinetic traps as the polypeptide tries to fold. Time-resolved resonance Raman studies suggest that HisX is not replaced directly by Met80; instead, formation of the folded protein involves an intermediate with His18/H_2O axial ligation.[35,50,53] At neutral pH, it is generally agreed that the unfolded peptide collapses around the heme prior to the replacement of Met80 for HisX, but there is considerable disagreement about the time scale. At lower pH, where the HisX traps are not formed, there is debate about whether peptide folding and ligand substitution are sequential or concerted processes.[51,53,54]

There have been relatively few investigations of Fe(II)cyt *c* folding. Given that metal-ligand binding constants and substitution rates are dependent on the metal oxidation state, it is possible that key steps in the folding of the reduced protein could differ markedly from those of Fe(III)cyt *c*. Indeed, in a study of folding initiated by photochemical dissociation of CO from the unfolded carbonmonoxy form of Fe(II)cyt *c*, a 40-μs time constant for Met80 binding was reported.[7,55,56] This rate is about 100 times higher than that of Met80 binding during the folding of the oxidized protein at low pH.[9]

It has been shown previously in Gray laboratories that photoinduced electron injection into unfolded Fe(III)cyt *c* triggers the folding of the reduced protein.[36,37] Electronically excited $Ru(bpy)_3^{2+}$ (bpy = 2,2'-bipyridine) is a powerful reductant (Figure 2.4), and its 600-ns lifetime makes it an excellent reagent for initiating folding on the

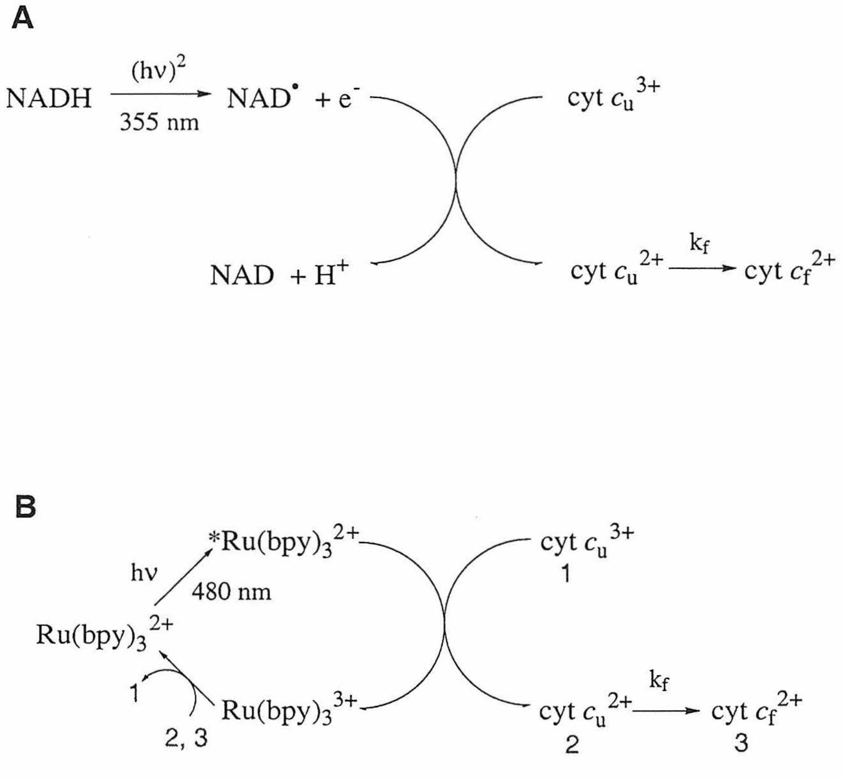

Figure 2.4. Schemes for the photoreduction of cyt *c* by NADH **(A)** and $Ru(bpy)_3^{2+}$ **(B)** (f, folded; u, unfolded).

microsecond time scale. We demonstrate here that NADH can also be a useful photoreductant:[57-59] two-photon excitation (355 nm) of NADH produces a proton and two powerful reducing species, a solvated electron and NAD· (Figure 2.4).[60,61] Both reductants can irreversibly reduce unfolded Fe(III)cyt *c* in less than 100 μs.

We have employed transient absorption spectroscopy to probe the kinetics of the heme-ligand substitution events that accompany the folding of Fe(II)cyt *c* following photoinduced electron transfer (ET) to unfolded ferricytochrome *c*. We could not prepare at a suitable denaturant concentration all of the possible axial-ligand adducts of unfolded cyt *c*. Instead, we have used the N-acetylated heme octapeptide from cyt *c* (AcMP8), and its axial-ligand adducts (see Chapter 1), to model the spectra of possible transient intermediates formed during Fe(II)cyt *c* folding. Our results are consistent with a mechanism in which HisX ligation at neutral pH leads to a kinetic trap. The importance of this trap is diminished at low pH, where folding is limited by the rate of formation of the Fe-S(Met80) bond.

Material and Methods

General

Type VI horse heart cytochrome *c* (Sigma) was used without further purification. $[Ru(bpy)_3]Cl_2.6H_2O$ and nicotinamide adenine dinucleotide (NADH) were obtained from Aldrich and Sigma, respectively. Guanidine hydrochloride (GuHCl) (United States Biochemical, Ultrapure Grade) concentrations were determined by measuring the refractive index of the solution.[62] Microperoxidase-8 (MP8), the heme octapeptide obtained by enzymatic digestion of horse cytochrome *c*, and N-terminal acetylated MP8

(AcMP8), which is less prone to aggregation, were prepared according to published procedures (see Chapter 1 for details). Steady-state absorption spectra were recorded with a Hewlett Packard 8452 diode array spectrophotometer.

pH titrations

The pH-induced ligand dissociation of (HisX)(His18)Fe(III/II)cyt$_u$ *c* was monitored by changes in Soret absorbance. All titrations were performed at 22 ± 1 °C in degassed buffer solutions, which were ~ 10 - 15 μM protein. The titration of Fe(III)cyt$_u$ *c* was performed in 50 mM phosphate buffer and 3.2 M GuHCl. The Fe(II)cyt$_u$ *c* titration was performed in 50 mM phosphate buffer and 5.5 M GuHCl in the presence of excess dithionite to ensure complete reduction of the protein. The change in intensity at 398 nm (Fe(III)cyt$_u$ *c*) or 524 nm (Fe(II)cyt$_u$ *c*) was plotted against pH to determine the pK$_a$ of the histidine bound to the heme. The pH was adjusted by the addition of small volumes of 1 M NaOH or 1 M HCl to the denatured protein stock solutions. The pH was measured with a calibrated microelectrode (Orion model 9826). No correction was applied for high [GuHCl]. The data were fit by nonlinear least squares methods using Kaleidagraph to the equation:

$$Abs_{pH} = \frac{Abs_{pH3.5} + Abs_{pH7.5}n(pK_a - pH)}{1 + 10^{n(pK_a - pH)}}$$

where n is the number of protons involved and pK$_a$ is the midpoint of the transition.

Kinetics measurements

Samples for transient absorption (TA) measurements were excited with pulses (480 nm, 1 - 4 mJ, 25 ns pulse) from an excimer-(Lambda Physik LPX210I, 308 nm) pumped dye laser (Lambda Physik FL 3002, Coumarin 480 dye) for experiments using Ru(bpy)$_3^{2+}$, or the third harmonic (355 nm, ≤ 10 mJ, 4 ns pulsewidth) from a Q-switched Nd:YAG laser (Quanta Ray DCR1) for experiments utilizing NADH as a photoreductant. When needed, the laser light was attenuated using cross polarizers (for dye laser excitation) or by adjusting the Q-switch delay. Laser shot selection was performed using a leading edge peak trigger linked to a discriminator (Phillips Scientific 6930).

Single-wavelength transients were recorded using a 75-W continuous-wave arc lamp (PTI A1010) as the probe light source that propagated colinearly with the excitation beam. The probe light was focused onto the aperture of an ISA monochromator (0.1 m) coupled to a 7-stage Hamamatsu (R928) photomultiplier tube (PMT). The PMT output was amplified by a 100 MHz current-to-voltage amplifier built at Brookhaven National Laboratories for time bases of 1μs - 1ms, or a slow amplifier from PSD Corp. for times > 1 ms. The signal was digitized (Sony/Tektronix digitizer RTD 710) and processed on a PC. Data were collected at various Soret-band wavelengths, where spectral changes due to reduction and folding are optimal (Figure 2.5).

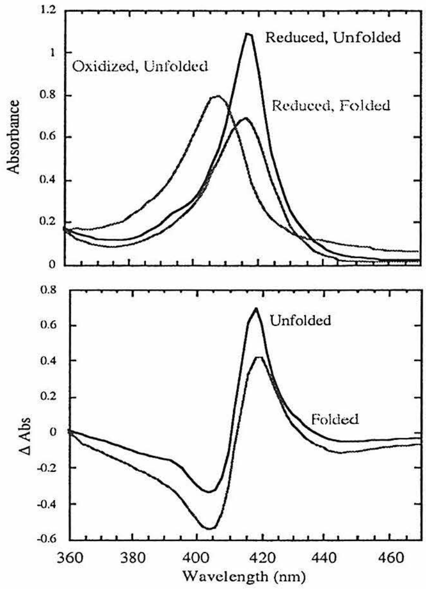

Figure 2.5. Absorption spectra (Soret region) of cyt *c* species (**upper**) and difference spectra relevant to ET-triggered folding (**lower**; folded: cyt $c_{\mathrm{folded,\ reduced}}$– cyt $c_{\mathrm{unfolded,\ oxidized}}$; unfolded: cyt $c_{\mathrm{unfolded,\ reduced}}$– cyt $c_{\mathrm{unfolded,\ oxi}}$

The data were fit using a nonlinear least-squares fitting program (Kinfit) written by Dr. Jay Winkler.

For multi-wavelength TA experiments, a microsecond flash lamp was used as the probe light source. The time resolution of measurements was adjusted by delaying the probe light relative to the excitation light using a digital gate-delay generator (EG&G D9650). Probe light was passed through a beam-splitter; the reflected light was sent directly to a spectrograph (Acto Research Corp. SpectraPro 275), while the transmitted light was first sent through the sample before the spectrograph. Intensities of the probe and the excitation beams were determined by a diode array detector (Princeton Instruments DPDA-1024) interfaced to a PC running commercial data processing software (WinSpec). The diode array wavelengths were calibrated using known emission lines from an argon lamp (Oriel).

Samples for TA kinetics were deoxygenated by repeated evacuation/argon-fill cycles on a Schlenk line (at least 30 cycles), using sealed quartz cuvettes (1-mm pathlength). All samples were prepared in 50 mM sodium phosphate buffer (pH 7). Protein concentrations were typically 100 μM unfolded in 3.2-3.5 M GuHCl. For measurements from 1 μs to 5 ms, $Ru(bpy)_3^{2+}$ (250 μM) was used as the photoreductant. For longer time scales (100 μs-1 s), NADH (100 μM) was used to deliver electrons. During NADH-experiments, one shot-cycles (1 Hz) were used; between each shot the sample was moved slightly in order to expose a different part of the sample to the excitation beam where NADH was not depleted. The pH of each of the samples containing NADH was checked before and after laser experiments to ensure that no change occurred. If necessary, the pH was adjusted by addition of 0.1 M HCl or 0.1 M

KOH. A stock solution ([Im] = 0.99 M) was used to prepare samples containing imidazole.

Results and Discussion

Spectra of model compounds: (Im)AcMP8 and (Met)AcMP8

Absorption in the Soret region (375-450 nm) is a sensitive probe of the oxidation and spin states of the AcMP8 heme (Figure 2.6): $(H_2O)(His18)Fe(III)AcMP8$ is a mixed-spin, six-coordinate complex, with water or hydroxide occupying the sixth ligand site (λ_{max} = 396 nm); imidazole (Im) readily replaces the aquo ligand (log K = 4.5), generating

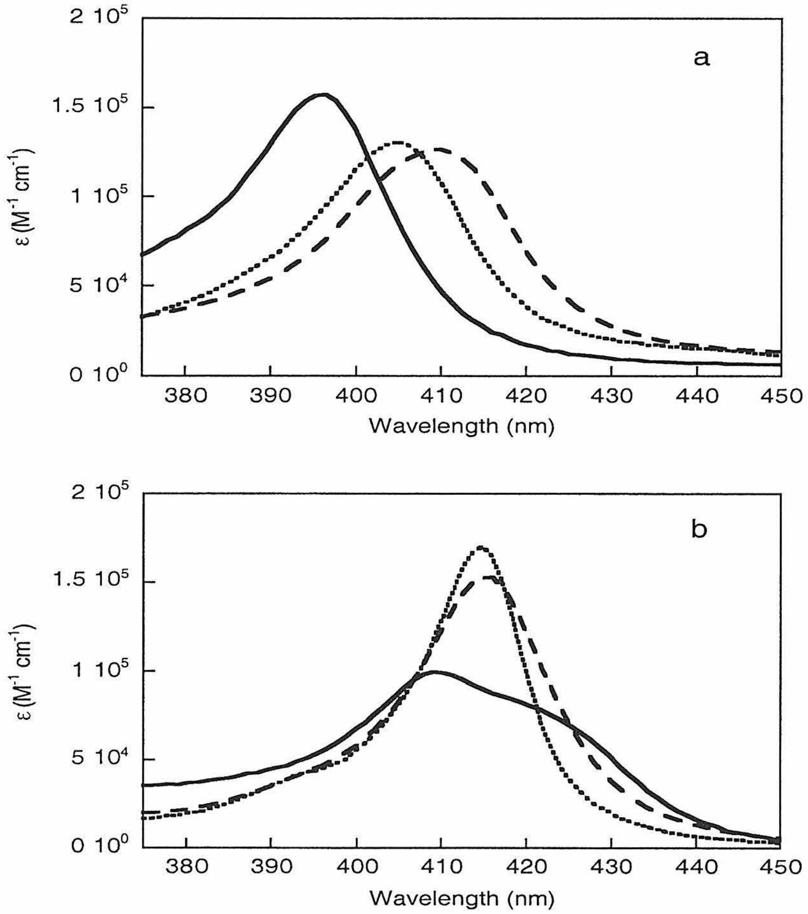

Figure 2.6. Absorption spectra (Soret region) of AcMP8 model species. **(a)** oxidized and **(b)** reduced AcMP8: no exogenous ligand (—); axial imidazole (· · · ·); axial methionine (----).

low-spin (Im)(His18)Fe(III)AcMP8 (λ_{max} = 404 nm).[63] The spectrum of this adduct is nearly identical with that of unfolded ferricytochrome *c*, (HisX)(His18)Fe(III)cyt$_u$ *c* (Figure 2.5). Since the formation constant for the methionine adduct of Fe(III)AcMP8 is quite small (log K ≈ 0.4), only partial methionine binding is seen even at Met concentrations > 1 M.[64] Hence, the spectrum of (Met)(His18)Fe(III)AcMP8 (λ_{max} = 410 nm) was determined using the projected extinction coefficients obtained by fitting the Met-titration curve of Fe(III)AcMP8 (Chapter 1).

The (His18)Fe(II)AcMP8 spectrum (λ_{max} = 409 nm) (pH 7) is similar to the spectrum of the Met80Ala mutant of Fe(II)cyt *c*, which has been interpreted in terms of an equilibrium mixture of high-spin, five-coordinate and low-spin, six-coordinate heme species.[65-67] Resonance Raman spectra suggest that the dominant form of (His18)Fe(II)AcMP8 is high-spin.[64] Both (Im)(His18)Fe(II)AcMP8 (λ_{max} = 413 nm) and (Met)(His18)Fe(II)AcMP8 (λ_{max} = 416 nm) exhibit spectra characteristic of six-coordinate, low-spin ferrohemes.

pH titrations of unfolded cyt *c*

In unfolded horse cyt *c* at pH 7, the Met80 ligand is replaced by HisX (X = 26 or 33).[45] Absorption changes indicate that acidification of (HisX)(His18)Fe(III)cyt$_u$ *c* and (HisX)(His18)Fe(II)cyt$_u$ *c* solutions converts the heme from a low-spin state, consistent with two axial ligands, to a mixed-spin or high-spin species, indicating the loss of one of the histidines (Figures 2.7 and 2.8).[30] The AcMP8 model spectra were used to assign the species present during the acid titrations. The misligated axial histidine is replaced by water in Fe(III)cyt$_u$ *c*; in contrast, the heme appears to remain five-coordinate after dissociation of the nonnative ligand in Fe(II)cyt$_u$ *c*.

The pK_a values for the protonation and dissociation of the nonnative axial histidine ligand are 5.3(2) (Fe(III)cyt$_u$ *c*) and 5.5(2) (Fe(II)cyt$_u$ *c*) (Figures 2.7 and 2.8).

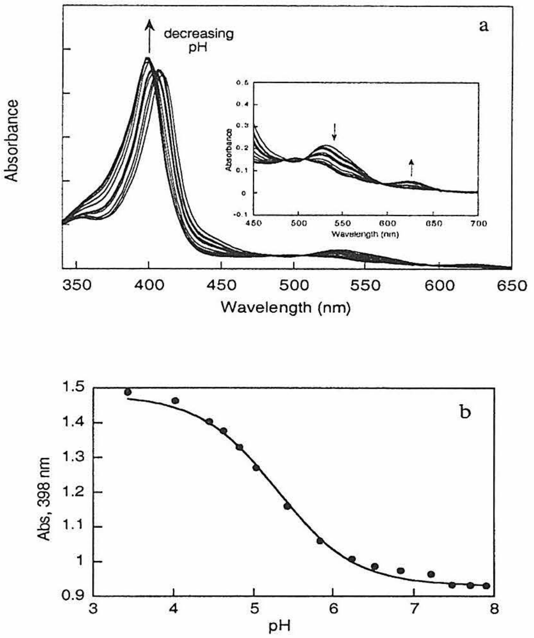

Figure 2.7. pH titration of unfolded Fe(III)-cyt *c* (3.2 M GuHCl). **(a)** Spectral changes observed during the pH titration. All changes are consistent with a low-to-high-spin conversion. **(b)** Absorbance (398 nm) vs. pH data and the calculated curve for a single protonation step ($pK_a = 5.3$).

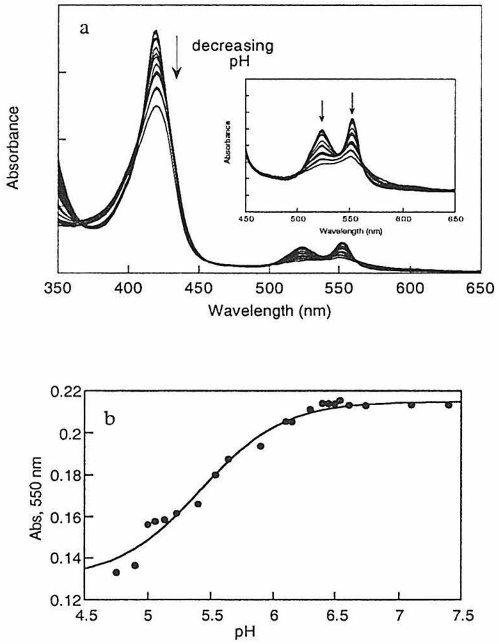

Figure 2.8. pH titration of unfolded Fe(II)-cyt *c* (5.5 M GuHCl). **(a)** Spectral changes observed during the pH titration. All changes are consistent with a low-to-high-spin conversion. **(b)** Absorbance (550 nm) vs. pH data and the calculated curve for a single protonation step ($pK_a = 5.5$).

The titration curves for both oxidized and reduced forms of (HisX)(His18)Fe cyt$_u$ *c* are well described by a model involving a single protonation step. The higher pK_a for Fe(II)cyt$_u$ *c* indicates that the misligated histidine is bound less strongly to the reduced heme. Consistent with this observation is the –40-mV shift in the Fe(III/II) reduction potential upon binding imidazole to (H_2O)(His18)Fe(III)AcMP8 (Chapter 1).[64] Our results are in reasonable agreement with other values (pK_a = 5.7,[45] 5.1[68]) reported for the acid-induced transition of unfolded Fe(III)cyt *c*. The native histidine ligand, His18, is strongly bound to the heme (pK_a ~ 2.8 for Fe(III)cyt *c*; ~ 3.8 for Fe(II)cyt *c*) by virtue of its position in the polypeptide chain (adjacent to Cys17, which forms a thioether linkage with the porphyrin).[69]

Transient spectra of AcMP8

In the ET-triggered experiments, the dominant form in the initial state is (HisX)(His18)Fe(III)cyt$_u$ *c* at pH 7 or (H_2O)(His18)Fe(III)cyt$_u$ *c* at pH 4.5. In order to distinguish the changes in spectra associated with folding from those arising from the folding trigger, we have studied transient spectra of (H_2O)(His18)Fe(III)AcMP8 and (Im)(His18)Fe(III)AcMP8 following photochemical reduction. Immediately after reduction by $^*Ru(bpy)_3^{2+}$ ($t > 5$ μs), the transient spectrum of AcMP8 closely matches the steady-state (His18)Fe(II)AcMP8 spectrum (Figure 2.9), indicating that loss of the axial water ligand to give a five-coordinate, high-spin heme is relatively rapid. (Note: There is also a secondary reduction phase by Ru(I)-species, which is generated by the disproportionation of $^*Ru(bpy)_3^{2+}$; for details see Appendix A). Photochemical reduction of (Im)(His18)Fe(III)AcMP8 (pH 7) produces a six-coordinate, low-spin heme (Figure 2.9). The transient difference spectrum of this species can be reproduced by the steady-state difference spectrum of (Im)Fe(III/II)AcMP8 without any contribution from five-coordinate Fe(II)AcMP8. The only process observed after the reduction of (His18)Fe(II)AcMP8 or (Im)(His18)Fe(II)AcMP8 is their reoxidation by Ru(bpy)$_3^{3+}$.

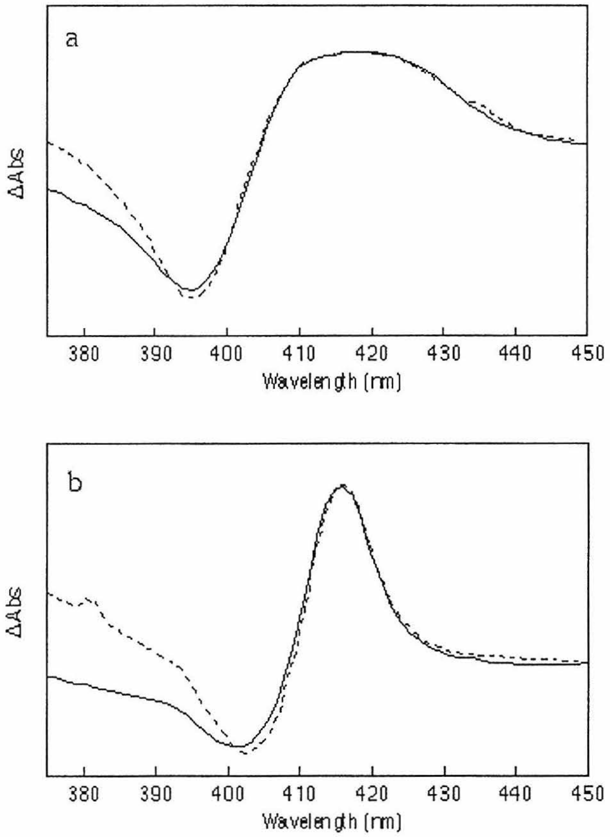

Figure 2.9. Multi-wavelength transient absorption spectra following AcMP8 reduction. **(a)** Time-resolved difference spectrum of AcMP8 (3.2 M [GuHCl]) at 100 μs following photoreduction (· · · ·) is shown with the steady-state difference spectrum Fe(II) - Fe(III)(His18)AcMP8 (—). **(b)** Time-resolved difference spectrum of Fe(III)(Im)(His18)AcMP8 (3.2 M [GuHCl]) at 100 μs following photoreduction (· · · ·) is shown with the steady-state difference spectrum Fe(II)-Fe(III)(Im)(His18)AcMP8 (—).

Fe(II)cyt *c* folding, pH 7

At neutral pH (3.2 M [GuHCl]), there is a rapid change in the heme absorbance following electron injection from *Ru(bpy)$_3^{2+}$ into (HisX)(His18)Fe(III)cyt$_u$ *c*. The transient difference spectrum recorded 5 μs after the laser flash is essentially identical with the spectrum observed following reduction of (Im)(His18)Fe(III)AcMP8, suggesting formation of (HisX)(His18)Fe(II)cyt$_u$ *c* (Figure 2.10). The only discernable process in the μs - ms time range (besides the secondary reduction phase, Appendix A) is the reoxidation of (HisX)(His18)Fe(II)cyt$_u$ *c* by Ru(bpy)$_3^{3+}$; there is no evidence for ligand substitution during this time period.

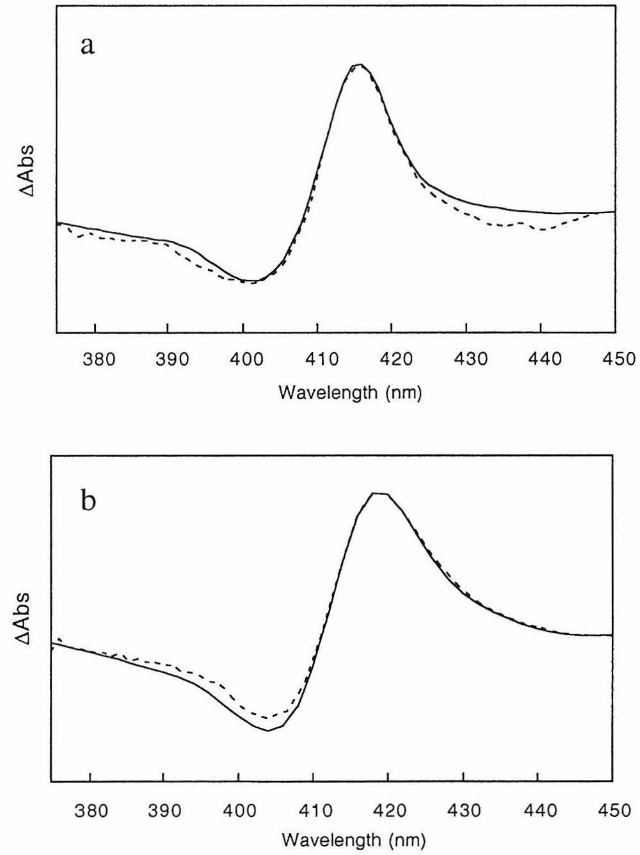

Figure 2.10. Multi-wavelength transient absorption spectra following cyt *c* photoreduction. **(a)** Time-resolved difference spectrum of cyt *c* (3.2 M [GuHCl]) at 100 μs following reduction (· · · ·) is shown with the steady-state difference spectrum Fe(II) - Fe(III)(Im)(His18)AcMP8 (—). **(b)** Time-resolved difference spectrum of cyt *c* (3.2 M [GuHCl]) at 500 ms following NADH photoreduction (· · · ·) is shown with the steady-state difference spectrum Fe(II)cyt$_f$ *c* - Fe(III)cyt$_u$ *c* (—).

We employed NADH as a photoreductant to study Fe(II)cyt *c* folding between 100 μs and 1 s. Since the photolysis of NADH produces reducing equivalents and no other species (reoxidation of the protein does not occur), folding can be monitored on much longer time scales (Figure 2.11). Significant changes in Soret absorbance appear 50-100 ms after electron injection. By 400 ms following the laser flash, the transient difference spectrum of Fe(II)cyt *c* closely matches that expected for (Met80)(His18)Fe(II)cyt$_f$ *c* (Figure 2.10). Thus, the substitution reaction that restores the Met80 ligand to Fe(II)cyt *c* takes place in the 50 - 400 ms time interval. There is no

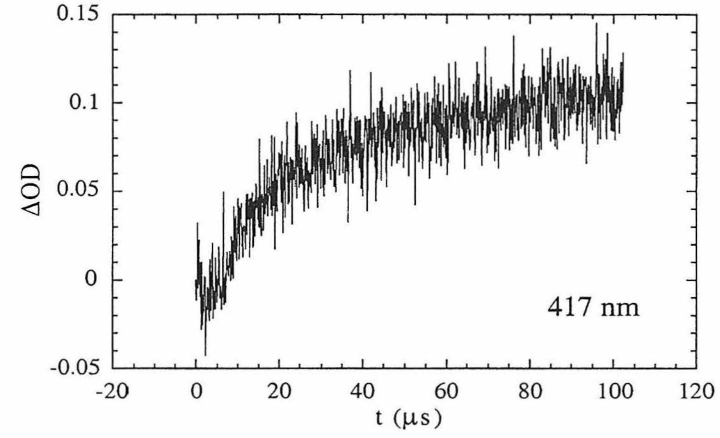

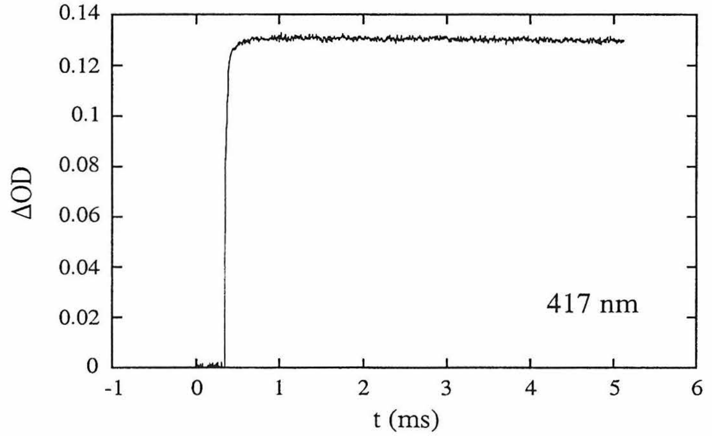

Figure 2.11. Transient absorption kinetics (417 nm) of cyt *c* (folded) photoreduction by NADH. **(Upper)** 100 μs timescale; **(Lower)** 5 ms timescale. As seen in the bottom trace, cyt *c* remains reduced after long times, indicating the irreversibility of reduction by NADH.

indication that a high-spin (i.e., five-coordinate) intermediate is formed during the folding of Fe(II)cyt *c* at pH 7. Instead, the kinetics of Fe(II)cyt *c* folding (pH 7) are adequately modeled by a single exponential phase.

Fe(II)cyt *c* folding in the presence of imidazole, pH 7

The addition of a large excess of imidazole (> 10 mM) converts (HisX)(His18)Fe(III)cyt$_u$ *c* to (Im)(His18)Fe(III)cyt$_u$ *c*. Although the addition of imidazole increases the rate of folding of Fe(III)cyt *c*,[52] it slows the binding of Met80 to the heme in the reduced protein.

The kinetics and Soret absorbance changes that accompany folding of Fe(II)cyt$_u$ *c* ([GuHCl] = 3.2 M) were monitored as a function of added imidazole (Figure 2.12). The

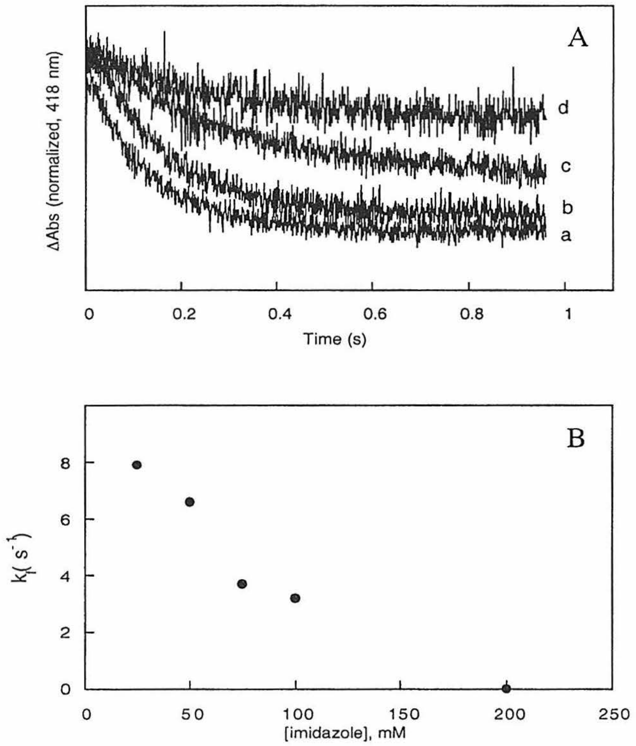

Figure 2.12. Dependence of cyt *c* folding kinetics on imidazole concentration. **(A)** Transient absorption kinetics traces (418 nm) at [imidazole] values of **a)** 25 mM; **b)** 50 mM; **c)** 75 mM; **d)** 100 mM. As [imidazole] increases, both the rate of formation and yield of folded protein are diminished. **(B)** Dependence of the (Met80)(His18)Fe(II)cyt *c* formation rate on [imidazole] in 3.2 M GuHCl.

rate of (Met80)(His18)Fe(II)cyt *c* formation decreases with increasing imidazole concentration; at very high [Im] (>100 mM), there is no sign of (Met80)(His18)Fe(II)cyt$_f$ *c*, even five seconds after electron injection. The data do not necessarily show that Fe(II)cyt *c* does not fold in the presence of imidazole. The major changes in the Soret absorbance report on the heme ligation state; the optical changes associated with polypeptide folding are likely to be small. In the presence of a large excess of imidazole, either the protein does not fold, or it folds around the misligated heme. The latter explanation is plausible, since it is known that imidazole will bind to the folded oxidized protein, although some reorganization of the heme pocket is required.[70]

Fe(II)cyt *c* folding, pH < 5

At lower pH, nonnative histidine-heme ligation in unfolded Fe(III)cyt *c* is disfavored and the axial coordination sites are occupied by water and His18, giving rise to a mixed-spin ferric heme. Under these conditions, folding is markedly faster than at neutral pH and a single kinetics phase is observed in stopped-flow studies using Trp fluorescence or S(Met80)Fe(III) charge-transfer absorption as a probe.[8,52]

In the unfolded oxidized and reduced proteins, the pK_a values of the two axial histidine ligands are so similar that there is no pH where His18 is bound but HisX is completely dissociated. Our studies of the ET-triggered folding kinetics of Fe(II)cyt$_u$ *c* cover the pH range 8.0 to 5.0, where His18 is bound, and the fraction of the population with HisX bound decreases from 100% to 33% (100% to 24%) for the oxidized (reduced) unfolded protein.

Distinct changes in the folding kinetics of Fe(II)cyt_u *c* are seen at lower pH. Between pH 8 and 5.5, the kinetics of Fe(II)cyt_f *c* formation are monoexponential, the rate increasing only slightly as the pH is lowered. Below pH 5.5, the kinetics are distinctly biphasic (Figure 2.13). The rate constant for the faster process is sensitive to pH, increasing by an order of magnitude as the pH is lowered from 5.5 to 4.5. The rate constant for the slower process is independent of pH, remaining constant within error at 16(5) s^{-1}.

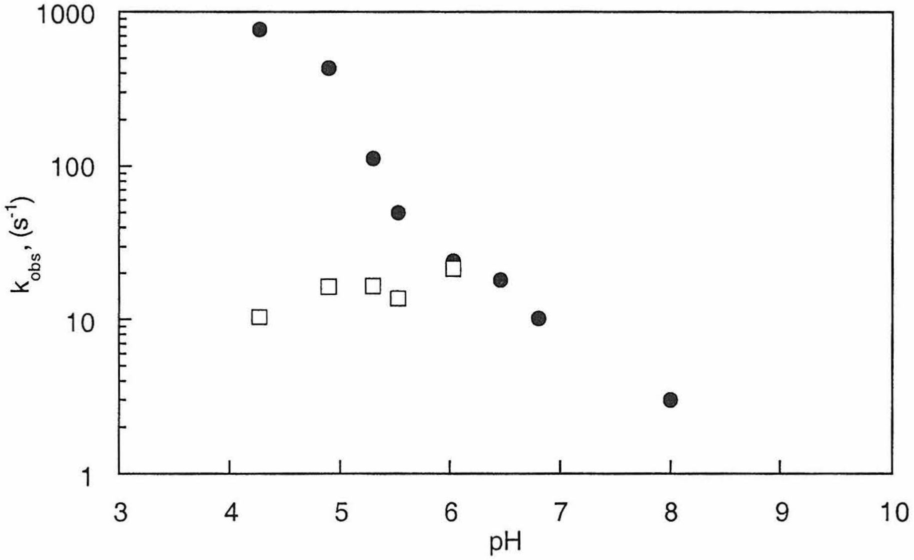

Figure 2.13. Dependence of cyt *c* folding rate constants on pH. Above pH 6, a single phase is observed (•); at lower pH values, kinetics are biexponential (•, fast phase; ❑, slow phase).

At pH 5, the oxidized unfolded protein is 67% mixed-spin (H_2O)(His18)Fe(III)cyt_u *c* and 33% low-spin (HisX)(His18)Fe(III)cyt_u *c*. The reduced unfolded protein, with an apparent pK_a ~ 5.5, has an equilibrium population of 24% (HisX)(His18)Fe(II)cyt_u *c* at pH 5. The fast process observed below pH 5.5 can be attributed to the approach to the equilibrium ligation state of the reduced heme. The transient spectrum measured 1 ms after reduction (pH 5.0) can be modeled by two absorbing heme species, with the majority fraction (65%) being a high-spin ferroheme. On the basis of its similarity to the spectrum of (His18)Fe(II)AcMP8, this intermediate is assigned as a five-coordinate heme. The minority fraction is attributed to six-coordinate (HisX)(His18)Fe(II)cyt$_u$ *c*.

The changes in absorbance associated with the slower process are consistent with conversion of five-coordinate, high-spin (His18)Fe(II)cyt$_u$ *c* to six-coordinate, low-spin (Met80)(His18)Fe(II)cyt$_f$ *c*. Thus, the rate of intramolecular methionine binding to Fe(II)cyt *c* is 16(5) s^{-1} at pH 5, 3.2 M GuHCl. The rate of this step contrasts sharply with the rapid Met binding ($k \sim 2.5 \times 10^4$ s^{-1}) when folding is initiated by CO photolysis in unfolded carbonmonoxy ferrocytochrome *c*.[7] The difference in Met80 binding rates is likely due to differences in the unfolded proteins. The initial state for ET-triggered folding is (H_2O)(His18)Fe(III)cyt$_u$ *c*; for folding initiated by CO dissociation, (CO)(His18)Fe(II)cyt$_u$ *c* is the starting point. The positive charge on the heme in Fe(III)cyt *c* destabilizes the folded protein more than the CO binding in (CO)(His18)Fe(II)cyt *c*,[7,36] and it is likely that the structures of the unfolded forms differ as well.

Kinetics model

A three-state kinetics model accounts for our results:

$$(\mathrm{His})_2\mathrm{Fe(II)cyt}\ c \xrightleftharpoons[k_{+\mathrm{His}}]{k_{-\mathrm{His}}} (\mathrm{His})\mathrm{Fe(II)cyt}\ c \xrightleftharpoons{k_{+\mathrm{Met}}} (\mathrm{His})(\mathrm{Met})\mathrm{Fe(II)cyt}\ c$$

The general solution to the rate law for this model predicts biphasic kinetics. However, above pH 5.5, ferrocytochrome *c* folding is slow and monophasic ($k_{obsd} = 1\text{-}20\ \mathrm{s}^{-1}$; [GuHCl] = 3.1 - 4.8 M). Since we observe only (HisX)(His18)Fe(II)cyt$_u$ *c* and (Met80)(His18)Fe(II)cyt$_f$ *c*, we can invoke the steady-state approximation for the concentration of (His18)Fe(II)cyt *c*. In this limit, the kinetics will be exponential with an observed rate constant given by:

$$k_{obsd} = \frac{k_{-His}k_{+Met}}{k_{+His} + k_{+Met}}$$

At high pH, folding is limited either by Met80 binding ($k_{+His} >> k_{+Met}$; $k_{\mathrm{obsd}} \approx \mathrm{K}_{His}k_{+Met}$, $K_{His} = k_{-His}/k_{+His}$) or by HisX dissociation ($k_{+Met} >> k_{+His}$; $k_{\mathrm{obsd}} \approx \mathrm{k}_{-His}$). The observed inhibition of Fe(II)cyt *c* folding by imidazole (as monitored by heme absorbance) is consistent with the kinetics model, because increasing the imidazole concentration effectively increases k_{+His}.

Below pH 5.5, the folding kinetics are biphasic and all three ligation states of the reduced heme are detected. Under these conditions, the steady-state approximation is no longer valid. The faster kinetics phase reflects the equilibration between (HisX)(His18)Fe(II)cyt$_u$ *c* and (His18)Fe(II)cyt$_u$ *c*, with a pH-dependent rate constant given by $k_{+His} + k_{-His}$. The rate for the slower step is pH independent, and represents k_{+Met}. This assignment is confirmed by transient absorption spectroscopy. Since k_{+Met} does not vary substantially with pH, it is likely that k_{-His} limits ferrocytochrome *c* folding above pH 6.

We have found that k_{obsd} (~ k_{-His}) at pH 7 depends on the folding driving force (rather than absolute denaturant concentration); similar folding rates are found for ferrocytochromes *c* from horse and yeast (with just 40% sequence homology) when the folding free energies are the same.[37,57] The fact that heme ligand substitution rates correlate with the overall folding free energy suggests that in the final step of Fe(II)cyt *c* folding the barrier does not arise solely from replacing an imidazole ligand by thioether on a ferroheme. Further support for this idea comes from the ET-triggered folding of cytochrome b_{562} (cyt b_{562}). The ferriheme of cyt b_{562} is not trapped by misligated His residues in the unfolded protein and, following photochemical electron injection, the low-spin, (His)(Met)-ligated ferroheme forms about 30 times faster than Met80 binding in the folding of Fe(II)cyt *c* (pH 5) at a comparable driving force.[58] This comparison suggests that the folding energy landscape[1,71-73] for cyt *c* is more rugged than that for formation of the four-helix bundle in cyt b_{562}.[57]

References

(1) Bryngelson, J. D.; Onuchic, J. N.; Socci, N. D.; Wolynes, P. G. *Proteins* **1995**, *21*, 167-195.

(2) Dill, K. A.; Chan, H. S. *Nat. Struct. Biol.* **1997**, *4*, 10-19.

(3) Shakhnovich, E. I. *Curr. Opin. Struct. Biol.* **1997**, *7*, 29-40.

(4) Lazaridis, T.; Karplus, M. *Science* **1997**, *278*, 1928-1931.

(5) Onuchic, J. N.; LutheySchulten, Z.; Wolynes, P. G. *Annu. Rev. Phys. Chem.* **1997**, *48*, 545-600.

(6) Karplus, M.; Weaver, D. L. *Protein Sci.* **1994**, *3*, 650-668.

(7) Jones, C. M.; Henry, E. R.; Hu, Y.; Chan, C. K.; Luck, S. D.; Bhuyan, A.; Roder, H.; Hofrichter, J.; Eaton, W. A. *Proc. Natl. Acad. Sci. USA.* **1993**, *90*, 11860-11864.

(8) Elöve, G. A.; Bhuyan, A. K.; Roder, H. *Biochemistry* **1994**, *33*, 6925-6935.

(9) Sosnick, T. R.; Mayne, L.; Hiller, R.; Englander, S. W. *Nat. Struct. Biol.* **1994**, *1*, 149-156.

(10) Baldwin, R. L. *Bioessays* **1994**, *16*, 207-210.

(11) Fersht, A. R. *Curr. Opin. Struct. Biol.* **1995**, *5*, 79-84.

(12) Ptitsyn, O. B. In *Advances in Protein Chemistry, Vol. 47*, 1995; Vol. 47, pp 83-229.

(13) Englander, S. W.; Mayne, L. *Annu. Rev. Biophys. Biomolec. Struct.* **1992**, *21*, 243-265.

(14) Plaxco, K. W.; Dobson, C. M. *Curr. Opin. Struct. Biol.* **1996**, *6*, 630-636.

(15) Kuwajima, K.; Yamaya, H.; Miwa, S.; Sugai, S.; Nagamura, T. *FEBS Lett.* **1987**, *221*, 115-118.

(16) Milla, M. E.; Brown, B. M.; Waldburger, C. D.; Sauer, R. T. *Biochemistry* **1995**, *34*, 13914-13919.

(17) Villegas, V.; Azuaga, A.; Catasus, L.; Reverter, D.; Mateo, P. L.; Aviles, F. X.; Serrano, L. *Biochemistry* **1995**, *34*, 15105-15110.

(18) Hooke, S. D.; Radford, S. E.; Dobson, C. M. *Biochemistry* **1994**, *33*, 5867-5876.

(19) Kragelund, B. B.; Robinson, C. V.; Knudsen, J.; Dobson, C. M.; Poulsen, F. M. *Biochemistry* **1995**, *34*, 7217-7224.

(20) Woodward, C. K. *Curr. Opin. Struct. Biol.* **1994**, *4*, 112-116.

(21) Plaxco, K. W.; Spitzfaden, C.; Campbell, I. D.; Dobson, C. M. *Proc. Natl. Acad. Sci. USA.* **1996**, *93*, 10703-10706.

(22) Elöve, G. A.; Chaffotte, A. F.; Roder, H.; Goldberg, M. *Biochemistry* **1992**, *31*, 6876-6883.

(23) Houry, W. A.; Rothwarf, D. M.; Scheraga, H. A. *Biochemistry* **1996**, *35*, 10125-10133.

(24) Arai, M.; Kuwajima, K. *Fold. Des.* **1996**, *1*, 275-287.

(25) Yamasaki, K.; Ogasahara, K.; Yutani, K.; Oobatake, M.; Kanaya, S. *Biochemistry* **1995**, *34*, 16552-16562.

(26) Jones, B. E.; Beechem, J. M.; Matthews, C. R. *Biochemistry* **1995**, *34*, 1867-1877.

(27) Ballew, R. M.; Sabelko, J.; Gruebele, M. *Proc. Natl. Acad. Sci. USA.* **1996**, *93*, 5759-5764.

(28) Woodruff, W. H.; Dyer, R. B.; Callender, R. H.; Paige, K.; Causgrove, T. *Biophys. J.* **1994**, *66*, A397-A397.

(29) Phillips, C. M.; Mizutani, Y.; Hochstrasser, R. M. *Proc. Natl. Acad. Sci. USA.* **1995**, *92*, 7292-7296.

(30) Babul, J.; Stellwagen, E. *Biochemistry* **1972**, *11*, 1195-1200.

(31) Bixler, J.; Bakker, G.; McLendon, G. *J. Am. Chem. Soc.* **1992**, *114*, 6938-6939.

(32) Colon, W.; Elöve, G. A.; Wakem, L. P.; Sherman, F.; Roder, H. *Biochemistry* **1996**, *35*, 5538-5549.

(33) Nall, B. T.; Landers, T. A. *Biochemistry* **1981**, *20*, 5403-5411.

(34) Pierce, M. M.; Nall, B. T. *Protein Sci.* **1997**, *6*, 618-627.

(35) Yeh, S. R.; Rousseau, D. L. *Nat. Struct. Biol.* **1998**, *5*, 222-228.

(36) Pascher, T.; Chesick, J. P.; Winkler, J. R.; Gray, H. B. *Science* **1996**, *271*, 1558-1560.

(37) Mines, G. A.; Pascher, T.; Lee, S. C.; Winkler, J. R.; Gray, H. B. *Chem. Biol.* **1996**, *3*, 491-497.

(38) Fisher, W. R.; Taniuchi, H.; Anfinsen, C. *J. Biol. Chem.* **1973**, *248*, 3188-3195.

(39) Hamada, D.; Kuroda, Y.; Kataoka, M.; Aimoto, S.; Yoshimura, T.; Goto, Y. *J. Mol. Biol.* **1996**, *256*, 172-186.

(40) Kang, X. S.; Carey, J. *Biochemistry* **1999**, *38*, 15944-15951.

(41) Bushnell, G. W.; Louie, G. V.; Brayer, G. D. *J. Mol. Biol.* **1990**, *214*, 585-595.

(42) Tsong, T. Y. *J. Biol. Chem.* **1974**, *249*, 1988-1990.

(43) Segel, D. J.; Fink, A. L.; Hodgson, K. O.; Doniach, S. *Biochemistry* **1998**, *37*, 12443-12451.

(44) Tsong, T. Y. *Biochemistry* **1976**, *15*, 5467-5470.

(45) Colon, W.; Wakem, L. P.; Sherman, F.; Roder, H. *Biochemistry* **1997**, *36*, 12535-12541.

(46) Russell, B. S.; Melenkivitz, R.; Bren, K. L. *Proc. Natl. Acad. Sci. USA.* **2000**, *97*, 8312-8317.

(47) Hammack, B.; Godbole, S.; Bowler, B. E. *J. Mol. Biol.* **1998**, *275*, 719-724.

(48) Tezcan, F. A.; Winkler, J. R.; Gray, H. B. *J. Am. Chem. Soc* **1999**, *121*, 11918-11919.

(49) Bai, Y. W.; Sosnick, T. R.; Mayne, L.; Englander, S. W. *Science* **1995**, *269*, 192-197.

(50) Chan, C.-K.; Hu, Y.; Takahashi, S.; Rousseau, D. L.; Eaton, W. A.; Hofrichter, J. *Proc. Natl. Acad. Sci. USA* **1997**, *94*, 8845-8850.

(51) Sosnick, T. R.; Mayne, L.; Englander, S. W. *Proteins* **1996**, *24*, 413-426.

(52) Brems, D. N.; Stellwagen, E. *J. Biol. Chem.* **1983**, *258*, 3655-3660.

(53) Yeh, S. R.; Takahashi, S.; Fan, B. C.; Rousseau, D. L. *Nat. Struct. Biol.* **1997**, *4*, 51-56.

(54) Shastry, M. C. R.; Roder, H. *Nat. Struct. Biol.* **1998**, *5*, 385-392.

(55) Hagen, S. J.; Hofrichter, J.; Szabo, A.; Eaton, W. A. *Proc. Natl. Acad. Sci. USA* **1996**, *93*.

(56) Hagen, S. J.; Hofrichter, J.; Eaton, W. A. *J. Phys. Chem. B* **1997**, *101*, 2352-2365.

(57) Telford, J. R.; Wittung-Stafshede, P.; Gray, H. B.; Winkler, J. R. *Accounts Chem. Res.* **1998**, *31*, 755-763.

(58) WittungStafshede, P.; Gray, H. B.; Winkler, J. R. *J. Am. Chem. Soc.* **1997**, *119*, 9562-9563.

(59) Wittung-Stafshede, P.; Malmstrom, B. G.; Winkler, J. R.; Gray, H. B. *J. Phys. Chem. A* **1998**, *102*, 5599-5601.

(60) Lindqvist, L.; Czochralska, B.; Grigorov, I. *Chem. Phys. Lett.* **1985**, *119*, 494-498.

(61) Orii, Y. *Biochemistry* **1993**, *32*, 11910-11914.

(62) Pace, N. C.; Shirley, B. A.; Thomson, A. J. In *Protein Structure: A Practical Approach*; Creighton, T. F., Ed.; IRL Press: Oxford, 1990; pp 311-330.

(63) Baldwin, D. A.; Marques, H. M.; Pratt, J. M. *J. Inorg. Biochem.* **1986**, *27*, 245-254.

(64) Tezcan, F. A.; Winkler, J. R.; Gray, H. B. *J. Am. Chem. Soc.* **1998**, *120*, 13383-13388.

(65) Lu, Y.; Casimiro, D. R.; Bren, K. L.; Richards, J. H.; Gray, H. B. *Proc. Natl. Acad. Sci. USA.* **1993**, *90*, 11456-11459.

(66) Bren, K. L.; Gray, H. B. *J. Am. Chem. Soc.* **1993**, *115*, 10382-10383.

(67) Bren, K. L. Ph.D., California Institute of Technology, 1996.

(68) Tsong, T. Y. *Biochemistry* **1975**, *14*, 1542-1547.

(69) Adams, P. A.; Baldwin, D. A.; Marques, H. M. In *Cytochrome c- A multidisciplinary approach*; Scott, R. A., Mauk, A. G., Eds.; University Science Books: Sausalito, 1995; pp 635-692.

(70) Shao, W. P.; Sun, H. Z.; Yao, Y. M.; Tang, W. X. *Inorg. Chem.* **1995**, *34*, 680-687.

(71) Socci, N. D.; Onuchic, J. N.; Wolynes, P. G. *J. Chem. Phys.* **1996**, *104*, 5860-5868.

(72) Onuchic, J. N.; Wolynes, P. G.; Lutheyschulten, Z.; Socci, N. D. *Proc. Natl. Acad. Sci. USA.* **1995**, *92*, 3626-3630.

(73) Wolynes, P. G. *Proc. Natl. Acad. Sci. USA.* **1996**, *93*, 14249-14255.

Chapter 3

Probing Protein Folding with Substitution-Inert Metal Ions. Folding Kinetics of Co(III)-cytochrome *c**

---

* Adapted from Tezcan, F. A.; Winkler, J. R.; Gray, H. B. *J. Am. Chem. Soc.* **1999**, *121*, 11918-11919. Work on methylisourea-modified Co-cyt *c* was done in collaboration with William Findley. Crystallographic characterization of tuna Co-cyt *c* and NMR-experiments were carried out with help from Drs. Brian Crane and Scott Ross, respectively.

Introduction

Cytochrome *c* (cyt *c*) folding is a heterogeneous process that involves peptide dynamics ranging from microseconds to seconds.[1-10] We have seen in the preceding chapter that the backbone movements in the final stages of cyt *c* folding are strongly coupled to (and limited by) ligand substitution processes at the iron center. When cyt *c* is unfolded with guanidine hydrochloride (GuHCl) at pH 7, one of the axial ligands (Met 80) is replaced by a nitrogenous base from an amino acid residue; this misligation introduces an energy barrier that slows the folding time to several hundred milliseconds. A great deal of evidence points to His 26 or His 33 as the ligand in unfolded horse heart cyt *c*.[2,3,11] Nevertheless, recent studies indicate that other bases (Lys[12] or N-terminus in yeast cyt *c*[13]) can act as ligands as well. We demonstrate here that ligand substitution at the heme can be slowed significantly when the iron center is replaced by Co(III), providing a closer look at the folding kinetics and the ligands in the unfolded form of this protein.

Octahedral Co(III)-complexes (with strong-field ligands) have a special place in transition metal chemistry. These complexes exhibit extremely slow ligand substitution rates due to their low-spin d^6 electronic configuration.[14,15] The inertness of these complexes (along with Cr(III)-complexes) have made it possible to study the kinetics of ligand-substitution processes and resulted in our current understanding of dissociative-substitution mechanisms in transition metal complexes.[14,15]

It is partly due to this inertness that nature has not utilized cobalt as widely as iron or copper, for instance.[16] Until very recently, the only known cobalt-containing catalytic systems have been vitamin B_{12}[17,18] and nitrile hydratase[19]. Even with the new additions to the list (methionine aminopeptidase, prolidase, glucose isomerase, methylmalonyl-CoA carboxytransferase, aldehyde decarbonylase, lysine-2,3-aminomutase, and bromoperoxidase),[20] the number of known cobalt-proteins are slightly more than a handful. The substitution of cobalt for other metals in proteins has, nevertheless, been a popular tool in bioinorganic chemistry for mechanistic and spectroscopic studies.[16] For example, coboglobins (Co-hemo- and myoglobin) have been used to understand dioxygen binding in heme proteins,[21-23] while cobalt substitution for spectroscopically silent (Zn(II)) or paramagnetic metal ions (Fe(III)) has allowed the characterization of active sites (absorption and EPR spectroscopy)[24,25] and protein structures (NMR),[26] respectively.

Our work represents the first example in which the inertness of Co(III) is utilized to understand an important biological process, namely protein folding. As it will be shown in this chapter, the slow folding kinetics of Co(III)-cyt *c* have allowed the convenient study of protein dynamics with a variety of spectroscopic techniques, including electronic absorption, circular dichroism (CD), fluorescence and NMR spectroscopy. These investigations have revealed previously unresolved folding pathways involving Lys- and His-misligated populations of unfolded molecules, as well as extremely long-lived folding intermediates that should be amenable to structural characterization. The relevance of these findings to the folding of the native protein is strongly supported by the fact that Co-cyt *c* retains the native structure and metal coordination, as indicated by spectroscopic and X-ray diffraction studies.

Materials and Methods

General

Horse, tuna and yeast cyt *c* were purchased from Sigma. All protein solutions were prepared with purified water (Millipore Nanopure system) and buffered to pH 7.0 with 50 mM sodium phosphate unless otherwise noted. Guanidine hydrochloride (GuHCl) (United States Biochemical) and urea (Aldrich) were of the highest purity available. UV-visible and CD spectra were collected with Hewlett Packard 8452A and Aviv 62A DS spectrometers, respectively, both of which are equipped with temperature control units. Fluorescence measurements were made with a Hitachi F-4500 spectrophotometer. Protein concentrations were estimated using $\varepsilon_{426} \approx 106{,}000$ $M^{-1}cm^{-1}$.[34,35]

Synthesis of Co-cyt *c* and its derivatives

Horse, tuna and yeast Co-cyt *c* and their dansyl-, homoarginine- and Pt(terpy)-derivatives were prepared according to established protocols with minor modifications. See Appendix B for full details about synthesis, purification and characterization.

Crystallization horse and tuna Co-cyt *c*

All solutions for crystallization were prepared by mixing appropriate amounts of two stock solutions: Stock solution A was 0.75 M NaCl and 0.1 M NaP_i (pH 6.0), while Stock solution B contained saturated $(NH_4)_2SO_4$ (~ 4 M) in addition to 0.75 M NaCl and 0.1 M NaP_i (pH 6.0). Tuna and horse Co-cyt *c* crystals were grown at room temperature in sitting or hanging drops. Prior to setting up crystallization wells, the protein solutions were concentrated and exchanged into Stock solution A using Centricon or Microcon centrifuge filtration units (MW-cutoff 10,000 amu). The reservoir solution was 500 μL of 70 – 75% (for tuna) or 85 – 95% (for horse) saturated $(NH_4)_2SO_4$, 0.75 M NaCl and 0.1 M NaP_i, and the drops were 2 μl of 4 – 10 mM protein and 2 μl reservoir solution. Rod-shaped tuna Co-cyt *c* crystals appeared within a day and were fully grown in 2 – 3 days (dimensions ~ 1 × 0.1 × 0.1 mm^3) (Figure 3.1). At high ammonium sulfate concentrations (≥ 80%), tuna Co-cyt *c* crystals were visibly smaller, yet they retained the rod-shaped morphology. Horse Co-cyt *c*, in contrast to the tuna protein, was very sluggish to nucleate; it took two months for crystals to appear. These crystals were quite large (2 × 0.5 × 0.5 mm^3), yet contained many surface defects. Small pieces had to be broken off these large "chunks" for diffraction experiments. These crystals diffracted to 1.5 Å, but a

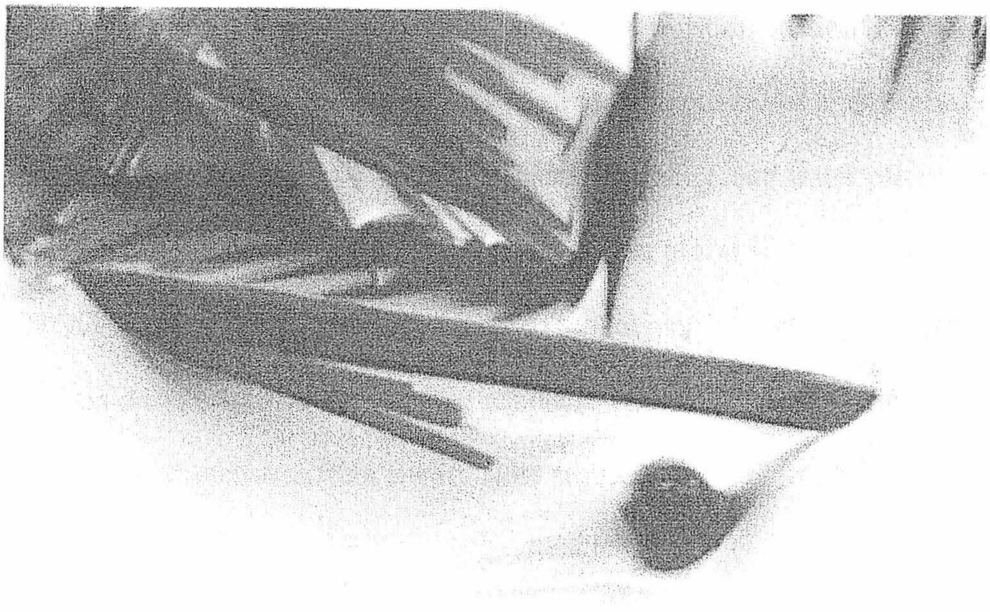

Figure 3.1. Tuna Co-cyt *c* crystals grown at ~ 75% saturated ammonium sulfate, 0.75 M sodium chloride and 50 mM sodium phosphate (pH 6.0). The large crystal is ca. 1.5 mm long.

symmetry group could not be assigned (due to apparent twinning in the crystals). Horse Co-cyt *c* crystals could thus not be used for structure determination.

Structure determination of tuna Co-cyt *c* by X-ray diffraction

X-ray diffraction data were collected at 100 K using an R-Axis IV imaging plate area detector and monochromatized Cu-Kα radiation (1.54 Å) produced by a Rigaku RU 200 rotating anode generator operated at 50 kV and 100 mA. The structure of Co-cyt *c* was determined at 1.5-Å resolution by refinement of a model from isomorphous crystals (space group $P4_3$) of tuna heart cyt *c* (PDB:3CYT)[27] against diffraction data using DENZO[28] (Table 3.1). Rigid-body, simulated-annealing, positional and thermal refinement with CNS,[29] amidst rounds of manual rebuilding, and water placement with XFIT[30] produced the final models. The Ramachandran plot was calculated with PROCHECK.[31] We have not attempted to model multiple sidechain conformations into electron densities for several surface residues. While this resulted in higher R-factors, the overall statistics were nevertheless satisfactory.

Equilibrium unfolding experiments

Horse, tuna and yeast Co-cyt *c* as well as the corresponding iron proteins were unfolded with GuHCl. Initially, stock solutions of different [GuHCl] (ranging from 0 to 8.0 M) and 50 mM NaP_i were prepared, and their pH was adjusted to 7, by adding appropriate amounts of concentrated NaOH. Each solution for unfolding experiments contained 600 – 1000 μl of one these GuHCl-stock solutions and 10 – 20 μl of Co-cyt *c* stock solution (~ 1 mM) buffered at pH 7. The final protein concentration in the solutions was 5-10 μM. Each denaturation curve consisted of at least 15 data points.

Table 3.1. X-ray data collection and refinement statistics for tuna Co-cyt *c* structure.

Residues	103 + 1 Heme
Waters	367
Unit cell dimensions (Å)	74.175 × 74.175 × 35.561
No. of monomers / unit cell	2
Symmetry group	$P4_3$
Resolution (Å)	30.0–1.5
X-ray wavelength (Å)	1.54
No. of measurements	66114
No. of unique reflections	28430
Completeness (%)	90.5 (91.6)[#]
$\langle I / \sigma I \rangle$[†]	27.8 (6.4)[#]
R_{sym}[‡] (%)	8.4 (29.0)[#]
R[§] (%)	22.2
Free R[II] (%)	24.8
Rms Bnd[¶] (Å)	0.016
Rms Ang[¶] (°)	1.36
Average temperature factor ($Å^2$)	
All protein	13.85
Main chain atoms	12.27
Sidechain atoms	12.82
Heme atoms	8.74
Water molecules	22.31
Ramachandran plot (%)	
Residues in most favored regions	93.6
Residues in add.l allowed regions	5.2
Residues in generously allowed regions	1.2
Residues in disallowed regions	0.0
Metal–ligand bond distances (Å)	
His 18	2.03 (2.00)*
Met 80	2.38 (2.27)*

[†] intensity signal to noise ratio. [#] Numbers in parentheses correspond to values in the highest-resolution shell. [‡] $R_{sym} = \Sigma\Sigma_j | I_j - \langle I \rangle | / \Sigma\Sigma_j | I_j |$. [§] $R = \Sigma || F_{obs} | - | F_{calc} || / \Sigma | F_{obs} |$ for all reflections (no σ cutoff). [II] Free R calculated against 8% of the reflections removed at random. [¶] Root mean square deviations from bond and angle restraints. * Fe(III)-only cyt *c* (PDB:3CYT).

These solutions were allowed to equilibrate overnight (at least 8 hours) at room temperature before spectroscopic measurements.

The unfolding of Co-cyt *c* was followed by changes in 428-nm or 422-nm absorption, 228-nm circular dichroism and 350-nm tryptophan emission. GuHCl-concentrations in the samples were determined (after spectroscopic measurements) by using the empirical relationship between the concentration of GuHCl and the refractive index of GuHCl solutions:[32]

$$[\mathrm{GuHCl}] = 57.147(\Delta\mathrm{N}) + 38.68(\Delta\mathrm{N})^2 - 91.60(\Delta\mathrm{N})^3 \qquad (1)$$

where ΔN is the difference between the refractive index of the solution and the refractive index of a 50 mM $\mathrm{NaP_i}$ solution (≈ 1.3342). Refractive indices were measured with a Milton Roy Abbe-3L Refractometer.

Construction of denaturation curves (adapted from the Ph.D. thesis by Gary A. Mines)

The denaturation curves were constructed with the assumption that the unfolding of Co-cyt *c* is a two-state process, i.e., each sample contains only the folded protein and the unfolded protein and no other species:

$$\chi_u + \chi_f = 1 \qquad (2)$$

where χ_u and χ_f are the fraction of unfolded and folded protein, respectively. The absorption, CD or fluorescence amplitude, y, is equal to the sum of the individual contributions of the folded and unfolded proteins:

$$y = \chi_u y_u + \chi_f y_f \qquad (3)$$

Combining Equations 2 and 3 yields:

$$\chi_u = \frac{y - y_f}{y_u - y_f} \qquad (4)$$

The pre- and post unfolding transition data are defined using a second assumption (as it is traditionally done) that y_u *and* y_f vary linearly with denaturant concentration:

$$y_u = m_u[\mathrm{GuHCl}] + b_u \qquad (5)$$

$$y_f = m_f[\mathrm{GuHCl}] + b_f \qquad (6)$$

m is the slope and *b* is the y-intercept. Denaturation curves are generated using Equations 4, 5 and 6, which can then be fit (by Kaleidagraph) using the following expression:

$$\chi_u = \frac{1}{1 - \left(\dfrac{m_D([\mathrm{GuHCl}]_{1/2} - [\mathrm{GuHCl}])}{RT} \right)} \qquad (7)$$

where $[\mathrm{GuHCl}]_{1/2}$ is the denaturation midpoint, and m_D is the slope relating the free energy of folding and [GuHCl]:[33]

$$\Delta G_f = \Delta G_f^{\circ} + m_D[\mathrm{GuHCl}] \qquad (8)$$

where ΔG_f° is the folding free energy at [GuHCl] = 0. Equation 8 is derived by using the two-state approximation for unfolding, where $\chi_u = 1/(1+K_f)$ and $\Delta G_f^{\circ} = RT\ln K_f$. It follows that the folding free energy $\Delta G_f^{\circ} = m_D[\mathrm{GuHCl}]_{1/2}$.

pH titrations of unfolded Co-cyt *c*

The pH-dependent equilibria for axial coordination in unfolded Co-cyt *c* (tuna and horse) were followed by changes in the Soret absorption. The samples were prepared from a 4 M GuHCl stock solution. The pH of this solution was varied by the addition of small amounts (negligible compared to the volume of the stock solution) of concentrated NaOH or HCl between pH 2 and 11. At ≥ 15 different pH values, 1 ml aliquots were withdrawn and added a small amount (~ 10 μl) of concentrated protein stock solution in order to give a Co-cyt *c* concentration of 5 to 10 μM. The solutions were allowed to equilibrate at least 8 hours before spectroscopic measurements. The pH's were rechecked following these measurements. The data were fit by nonlinear least squares methods using Kaleidagraph to the equation:

$$Abs_{pH} = \frac{Abs_{pH2} + Abs_{pH8}n(pK_a - pH)}{1 + 10^{n(pK_a - pH)}}$$

where n is the number of protons involved and pK_a is the midpoint of the transition.

Kinetics of cyanide binding to unfolded Co-cyt *c*

CN^--binding to horse Co-cyt *c* was monitored by the increase (decrease) in Soret absorbance at 430 nm (422 nm). A 1 ml-solution of ~ 5 μM unfolded protein in 4.5 M GuHCl (pH 7) was added 100 μl of 0.6 M NaCN solution (pH 7) with a Hamilton syringe. Kinetics data acquisition was started immediately after the addition of CN^--solution. The kinetics run spanned 40,000 seconds with 800 equally spaced data points. The pH of the solution was checked after the data acquisition and was found to be 7.7. This pH value indicates that the concentration of free cyanide (pK_a ~ 9.2) in the solution was slightly less than 60 mM.

Folding kinetics

Folding kinetics of Co-cyt *c* were monitored by changes in Soret absorbance, circular dichroism at 228 nm and tryptophan fluorescence at 350 nm. The folding reaction was initiated by the manual dilution of an unfolded protein solution in concentrated denaturant. The starting solutions were 10 – 50 μM protein (depending on the extent of dilution for initiating folding), ≥ 3.8 M GuHCl for horse and tuna Co-cyt *c*, and ≥ 2 M GuHCl for the yeast (typically at pH 7). These GuHCl concentrations ensured that ≥ 99% of the protein was unfolded. The solutions were allowed to equilibrate at room temperature for 10 min to 5 days. In order to trigger folding, the desired volume of a 50 mM NaP_i solution (pH 7) was added with a Hamilton syringe and the solution was quickly mixed by repeated suction and release with a Pasteur pipette. Resulting solutions were 5 – 15 μM protein and 0.4 – 2.0 M GuHCl (0.4 – 0.8 M GuHCl for yeast Co-cyt *c* experiments). The kinetics data acquisition was started immediately thereafter. A typical acquisition time (at room temperature) was 40,000 seconds, with each data point taken every 50 or 100 seconds. Longer (shorter) acquisition times were necessary at low (high) temperatures. The solutions were stirred with a magnetic bar throughout the kinetics run. The sample cell was sealed with Parafilm to prevent solvent evaporation so as to ensure that the protein concentration remained constant over the long course of these experiments. pH's and refractive indices of the solutions were determined after the folding reaction was complete. Folding kinetics were fit by Kinfit (Matlab version) written by Dr. Jay Winkler.

NMR spectroscopy of horse Co-cyt *c*

^{1}H-NMR spectra were acquired on a Varian Unity Plus 600-MHz spectrometer equipped with a Nalorac inverse probe with a self-shielded *z* gradient. Water suppression was achieved with presaturation during relaxation delay. The spectra were processed with VNMR (Varian). All samples were prepared in 90:10 H_2O / D_2O and 50 mM NaP_i at pH 7. The protein concentration in the samples was typically 1 mM or higher. Folding kinetics experiments were carried out at 4 or 10° C. Samples for kinetics measurements initially contained 0.3 – 20 mM protein in 4 M GuHCl. These solutions were allowed to equilibrate for at least 10 min at room temperature in an NMR tube; to initiate folding, an appropriate volume of NaP_i buffer solution (prepared in 90:10 H_2O / D_2O and cooled in an icebath) was added with a Pasteur pipette. The final GuHCl concentration was 0.4, 0.8 or 2.0 M. The sample tube was immediately placed in the NMR spectrometer. Data acquisition was started after the temperature in the sample chamber reached equilibrium and the D_2O signal was locked (total duration $\approx 3 - 5$ min). Prior to the kinetics run, the NMR magnet was tuned and shimmed using a sample that contained the same GuHCl concentration as the final folding solution, so as to minimize the preparation time before data acquisition. For folding kinetics measurements, a macro written by Dr. Scott Ross was used that allowed 1D-^{1}H NMR spectra (1024 – 2048 transients each) to be acquired at increasing intervals over a span of up to 5 days. Another macro was used to extract the time course of NMR signal amplitudes at selected proton resonances. These data were processed with Kaleidagraph.

Results and Discussion

Spectral characterization of folded and unfolded Co-cyt *c*

The absorption spectra of tuna- and yeast Co-cyt *c* are identical to that of the horse protein, which was reported previously,[34,35] indicating that the metal coordination is the same (Figure 3.2 A). The Soret-band maximum is at 427 nm ($\varepsilon \approx 106{,}000$ $M^{-1}cm^{-1}$), and the Q-bands peak at 534 ($\varepsilon \approx 8{,}500$ $M^{-1}cm^{-1}$) and 568 nm ($\varepsilon \approx 5{,}700$ $M^{-1}cm^{-1}$).[34] The far-UV CD spectrum of Co-cyt *c* is very similar to that of the Fe-protein and has the characteristic minima at 208 and 222 nm of a largely α-helical structure (Figure 3.2 B).

Unfolded Co-cyt *c* (Co-cyt c_u) has a far-UV CD spectrum that suggests a random-coil conformation. The Trp 59-fluorescence, fully quenched by energy transfer to the heme in the folded protein, has considerable intensity in the unfolded form, indicating loss of compact tertiary structure (Figure 3.2 C). Unfolding of Co-cyt *c* is also accompanied by blue shifts in the absorption spectrum attributable to ligand substitution, with the Soret band peaking at 422 nm, and the Q-bands at 564 and 530 nm.

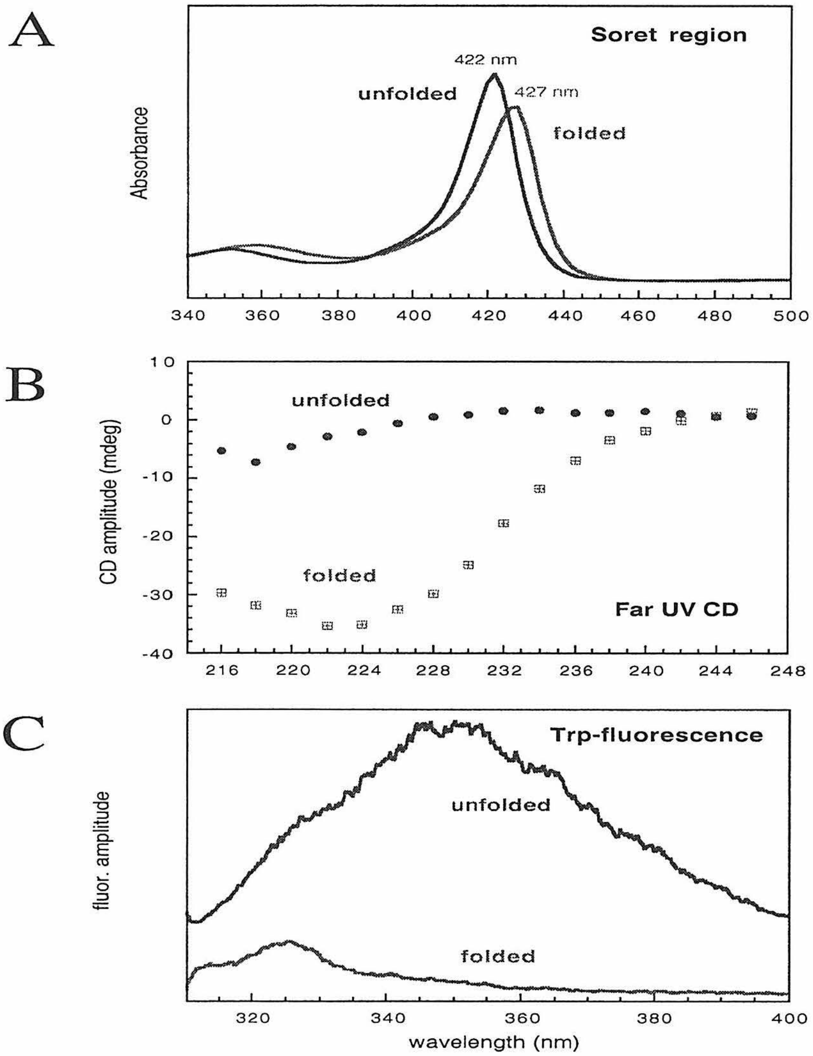

Figure 3.2. UV-vis-, CD- and fluorescence spectral changes upon the unfolding of Co-cyt *c*.

Structural characterization of Co-cyt *c*

^{1}H-NMR spectroscopy

The proton-NMR spectrum (270 MHz) of the diamagnetic Co(III)-cyt *c* (horse) has been previously reported,[26] and it is very similar to that of the isoelectronic Fe(II)-cyt *c*. The high degree of chemical shift dispersion and sharp resonance peaks in our 600-MHz spectrum indicate that Co-cyt *c* is highly-structured and well-ordered (Figure 3.3), in accordance with the α-helical far-UV signature. Also noteworthy are the Met 80-

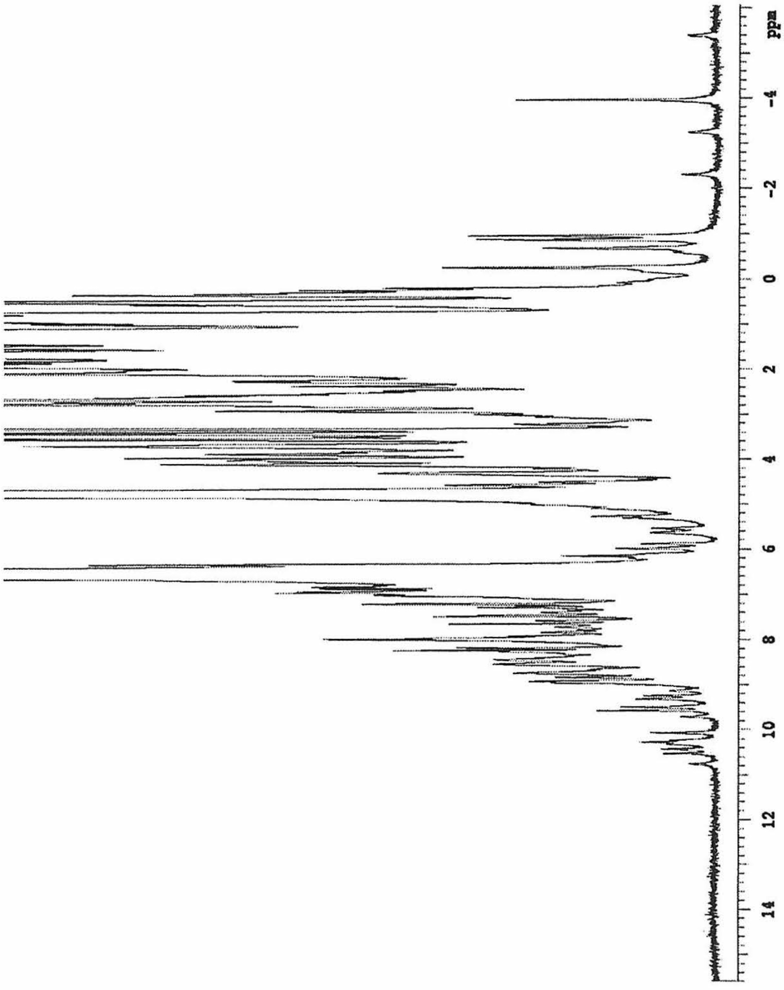

Figure 3.3. 1D-proton-NMR of horse Co-cyt *c* (in 0.8 M GuHCl, pH 7, 25° C). The broad peaks centered at ~ 5 and ~ 7 ppm are due to water and GuHCl protons, respectively.

proton resonances at –2.10 (γ-CH), –3.00 (β-CH_3), –3.78 (CH_3) and -5.15 (γ–CH) ppm) that are shifted significantly upfield due the porphyrin ring currents;[26] these low-frequency resonances provide good evidence that Met-80 is coordinated to the metal center in Co-cyt *c*.

X-ray crystallography

The structure of tuna-Co cyt *c* was determined at 1.5 Å resolution. The structure is virtually identical to that of the Fe(III)-protein ($RMSD_{C\alpha}$ = 0.22 Å) (Figure 3.4).[27,36] The final model has good stereochemistry ($RMSD_{bond} \leq$ 0.016 Å, $RMSD_{angle} \leq$ 1.36°), with most residues (93.6%) falling in the most favored regions in the Ramachandran plot (Table 3.1). The His 18-Met 80 axial coordination of the metal is also preserved in Co-cyt *c* (Figure 3.4), although these bonds ($d_{\text{Met 80-Co(III)}}$ = 2.38 Å, $d_{\text{His 18-Co(III)}}$ = 2.03 Å) are slightly longer compared to the Fe-protein ($d_{\text{Met 80-Fe(III)}}$ = 2.27 Å, $d_{\text{His 18-Fe(III)}}$ = 2.00 Å).[27] Metal-$N_{pyrrole}$ distances in Co-cyt *c* (Co-N_A, N_B, N_C and N_D are 2.03, 1.99, 2.01 and 2.03 Å) are on average shorter than those in the native protein (2.02, 2.03, 2.14 and 2.11 Å).

Stability of Co-cyt *c*

The denaturation curves and the folding free energies of for horse-, tuna- and yeast Co-cyt *c* are shown in Figure 3.5 and the accompanying Table 3.2. The denaturation curves were constructed by monitoring changes in the far-UV CD spectrum, as well as in the Soret absorption and Trp 59 fluorescence. In all cases, the folding-unfolding equilibrium can be adequately described by a two-state model. Also, shown in Table 4.2 are the denaturation midpoints and folding free energies for the corresponding

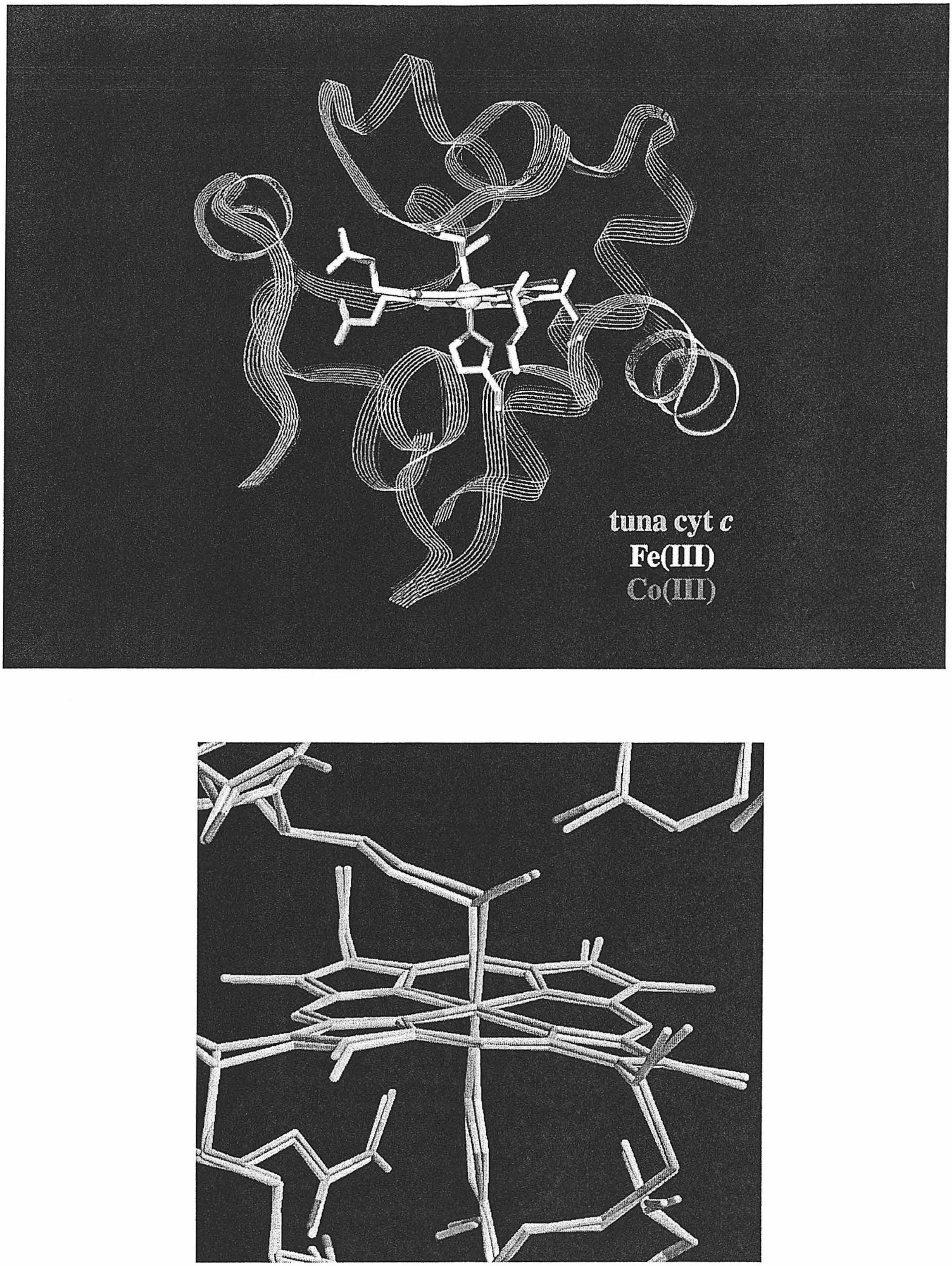

Figure 3.4. X-ray crystal structure of tuna Co-cyt *c* superimposed on Fe-cyt *c* structure (PDB ID:3CYT). **(top)** whole structure; **(bottom)** heme region (Co-cyt *c* atoms are multi-colored).

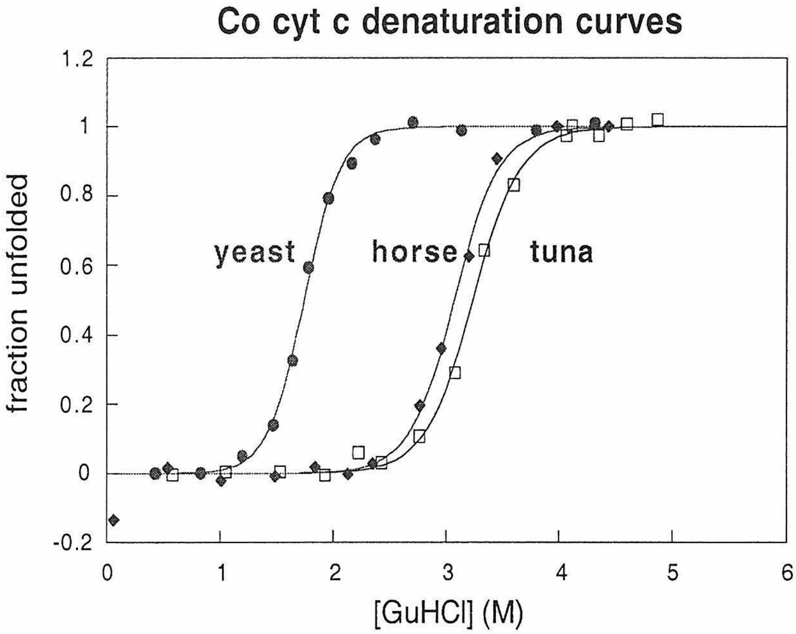

Comparison of folding free energies (denaturation midpoint ([GuHCl], M))

	yeast	**horse**	**tuna**
Co(III) cyt *c*	6.1 kcal/mol	9.9 kcal/mol	9.8 kcal/mol
	(1.75 M)	(3.0 M)	(3.25 M)
Fe(III) cyt *c*	4.6 kcal/mol	9.0 kcal/mol	9.4 kcal/mol
	(1.3 M)	(2.8 M)	(2.9 M)

Figure 3.5. Denaturation curves for horse-, tuna- and yeast Co-cyt *c* determined by CD spectroscopic measurements.

Table 3.2. Folding free energies and denaturation midpoints for horse-, tuna- and yeast Co(III)- and Fe(III)-cyt *c*.

Fe-proteins. In all three cases, Co-cyt *c* is ~ 1 kcal/mol more stable, which we attribute to a stronger bond between Met 80 and the metal.

Folding kinetics of Co-cyt *c* monitored by UV-vis and CD spectroscopy

Folding of horse and tuna Co-cyt *c* was initiated by the manual dilution of a concentrated denaturant solution (≥ 3.8 M to ≤ 2M GuHCl). UV-visible absorption, CD and fluorescence spectroscopy were employed to monitor the dynamics of Co(III)-ligand substitution, secondary structure and tertiary structure formation, respectively. In all cases, the folding reaction follows biexponential kinetics (Figure 3.6). Note: Due to the

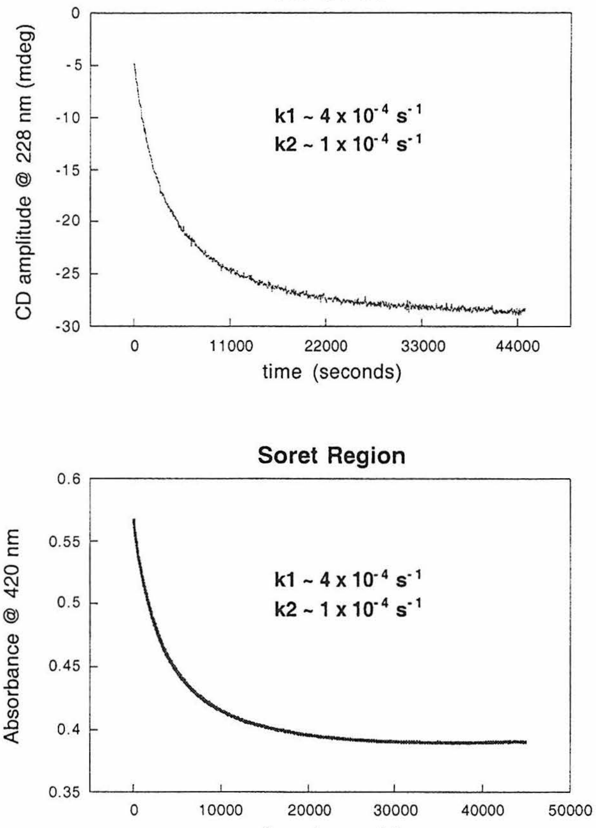

Figure 3.6. Co-cyt *c* (horse) folding kinetics monitored by CD- (**top**) and UV-vis spectroscopy (**bottom**) (final [GuHCl] = 2.0 M, 25° C, 10 min unfolding).

uncertainties in the sample temperature in fluorescence measurements, they are not reported here. The rates and relative amplitudes of the two phases agree within error for UV-vis and CD spectroscopic measurements (although varying degrees of signal change are observed during the mixing deadtime), confirming previous findings (Chapter 2) that backbone movements during the folding of cyt *c* are strongly coupled to ligand substitution processes on the iron center.

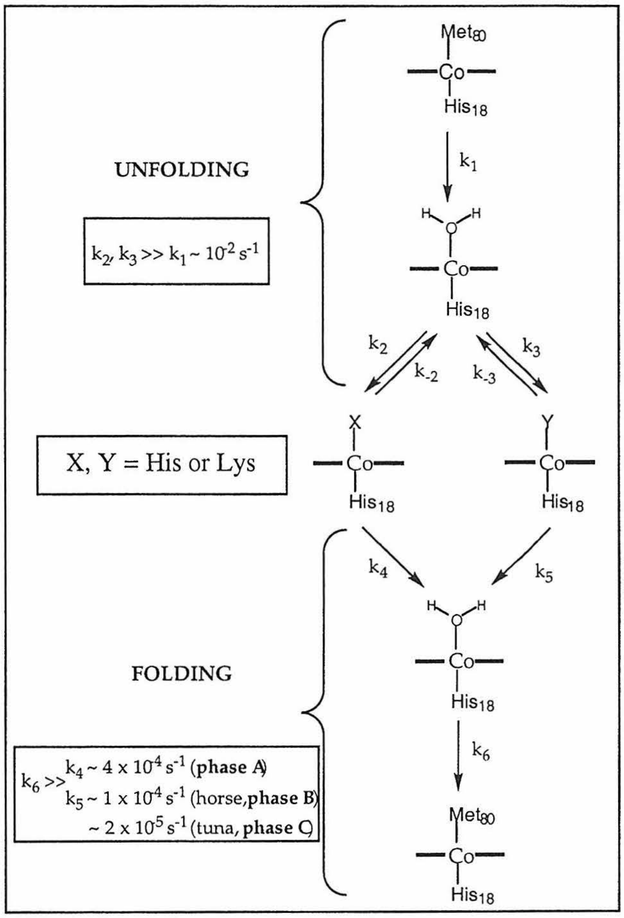

Figure 3.7. Proposed mechanism for ligand substitution events during Co-cyt *c* (un)folding. Rate constants were determined from kinetics measured by time-resolved UV-vis (k_1) and CD (k_4, k_5) spectroscopy.

Figure 3.7 and Table 3.3 summarize folding rates and amplitudes of the observed kinetics phases as monitored by CD spectroscopy. Misligated Co-cyt c_u folds much more slowly than Fe-cyt c_u, owing to the high activation barrier for Co(III)-ligand dissociation. This activation barrier could be eliminated by replacing the non-native axial ligand (X or Y in Figure 3.7) by an exogenous ligand, such as CN^- (Figure 3.8). Indeed, upon treating the unfolded protein with CN^-, folding of horse Co(III)-cyt *c* was complete within the deadtime of manual mixing (~ 5 s) as observed by CD spectroscopy (Figure 3.8). The CN^--group is not displaced by S(Met 80) upon folding due to the

	Phase A		Phase B		Phase C	
	tn	**hh**	**tn**	**hh**	**tn**	**hh**
5 min	95 %	53 %	---	47%	5 %	---
10 min	90 %	51 %	---	49 %	10 %	---
12 h	70 %	35 %	---	65 %	30 %	---
3 days	65 %	25 %	---	75 %	35 %	---

Table 3.3. Amplitudes of folding phases in tuna (tn) and horse (hh) Co-cyt *c* after various incubation times for unfolding.

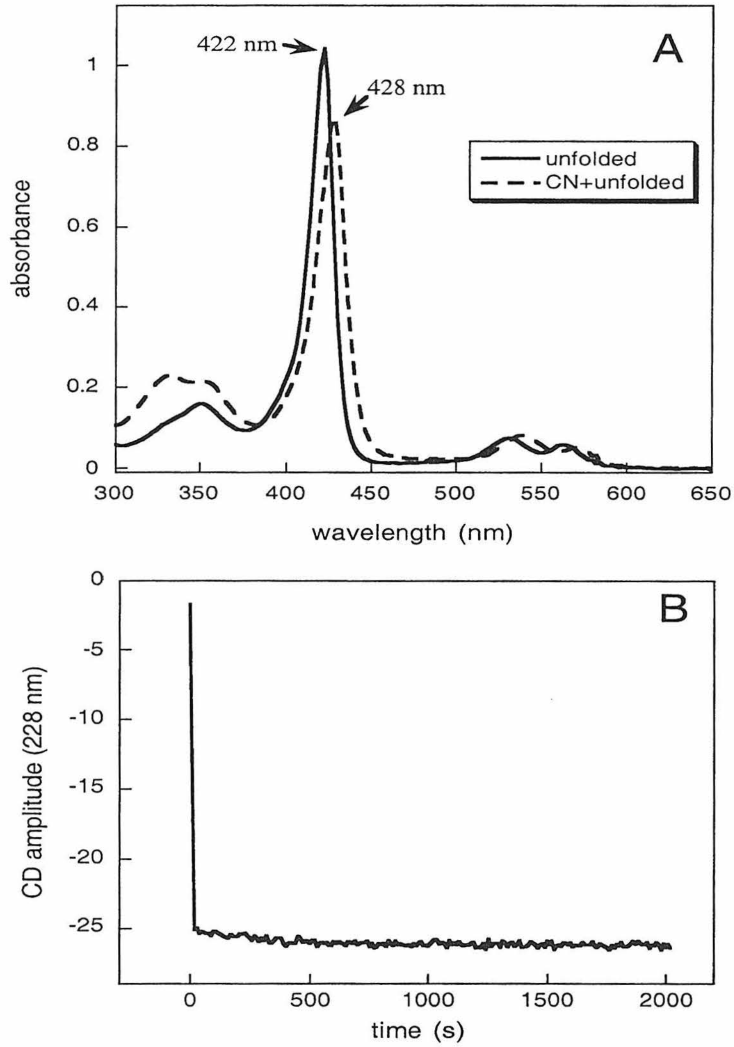

Figure 3.8. (**A**) Absorption spectrum of free (—) and CN^--bound (---) unfolded Co-cyt *c* (in 4 M GuHCl). (**B**) Refolding kinetics of CN-Co-cyt *c*. The initial drop in CD amplitude takes place within 5-10 seconds. The far-UV CD spectrum of the resulting species is identical to that of the folded protein.

stability of the Co(III)-CN⁻ bond. This, however, does not impede with the formation of the secondary and the tertiary structure of cyt *c*, as evidenced by the helical structure of CN-Co-cyt *c* (CD measurements) and supported by the native-like structure of CN-Met80Ala cyt *c* (NMR).[37]

The rate constants for Co-cyt c_u folding are independent of pH between pH 5 and 7.5, consistent with a dissociative mechanism where protonation of the leaving group follows the rate-limiting step. The folding kinetics are strongly dependent on temperature. The Arrhenius plots for the two phases reveal an activation energy of ~ 21 kcal/mol (Figure 3.9), considerably higher than that for the dissociation of His 33 from Fe(III) in denatured horse cyt *c* (16.8 kcal/mol).[11]

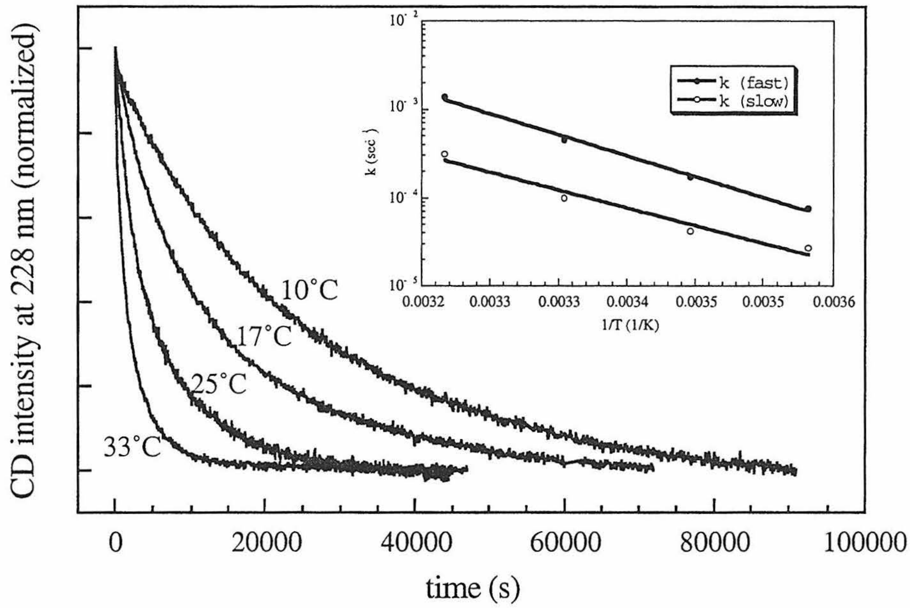

Figure 3.9. Temperature dependence of Co-cyt *c* (horse) folding kinetics (final [GuHCl] = 2.0 M. **(Inset)** Arrhenius plot for the two kinetics phases. For the fast phase: $\Delta H^{\ddagger} = 21.2$ kcal/mol, $\Delta S^{\ddagger} = -2.1$ cal/mol.K; for the slow phase: $\Delta H^{\ddagger} = 20.2$ kcal/M, $\Delta S^{\ddagger} = -8.1$ cal/mol.K.

The relative amplitudes of the two folding phases of Co-cyt *c* are strongly dependent on the duration of unfolding. In horse Co-cyt *c*, the amplitude of the faster phase (phase A: ~ $4 \times 10^{-4}s^{-1}$) decreases from 50% (after 10 min of unfolding) to 25% (after three days of unfolding) in favor of a slower phase (phase B: ~ $1 \times 10^{-4}s^{-1}$) (Figure 3.10 and Table 3.3). Similarly, while tuna Co-cyt *c* folding kinetics are essentially monoexponential after 5 min of unfolding, a slow phase (phase C) grows in and reaches ~ 35 % of the total amplitude after 3 days of unfolding (Figure 3.10 and Table 3.3). These findings indicate that ligand substitution during Co-cyt *c* unfolding also is sluggish, enabling investigation of nonequilibrium populations of unfolded species. (Note: Due to the small rate constant for Phase C (~ $2 \times 10^{-5}\,s^{-1}$), we have not been able to monitor its whole time course. Consequently, there are significant uncertainties in this rate constant and the amplitude of Phase C).

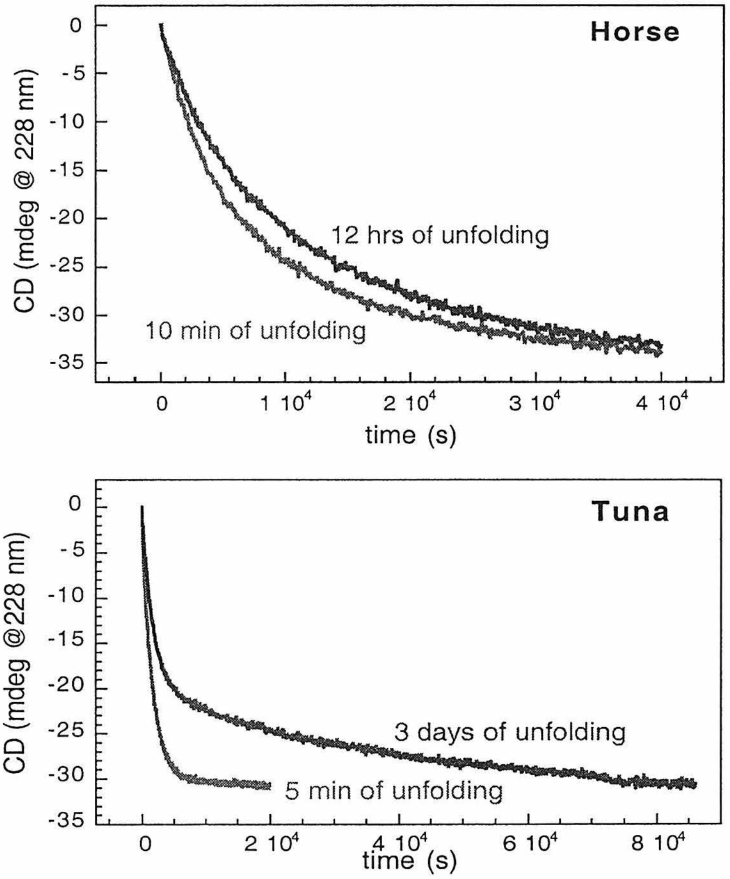

Figure 3.10. Dependence of Co-cyt *c* folding kinetics (monitored by CD spectroscopy) on the duration of unfolding; **(top)** horse Co-cyt *c*; **(bottom)** tuna Co-cyt *c* (final [GuHCl] = 2.0 M, 25° C).

We attribute the biphasic folding kinetics of Co-cyt *c* to the presence of two differently misligated unfolded protein populations (Figure 3.7). CN^- binding to unfolded Co-cyt *c* also follows biexponential kinetics that occur on a similarly slow timescale as folding (Figure 3.11). This observation supports the view that the biphasic folding kinetics of Co-cyt *c* are not due to a complex folding mechanism but to two species that fold independently with simple exponential kinetics. Moreover, the relative rates of the two CN^--binding phases are similar to those observed for folding (fast phase rate: slow phase rate = 4:1), providing further evidence that in both reactions the rate-limiting step is the dissociation of the nonnative axial ligand. The presence of multiple misligated forms of unfolded cyt *c* has previously been suggested by pH-jump studies.[11] However, parallel folding of these unfolded states has not been directly observed, probably because of the temporal proximity of Fe(III) ligand substitution to other folding processes. By temporally separating the ligand-substitution-coupled folding from (ligand-substitution

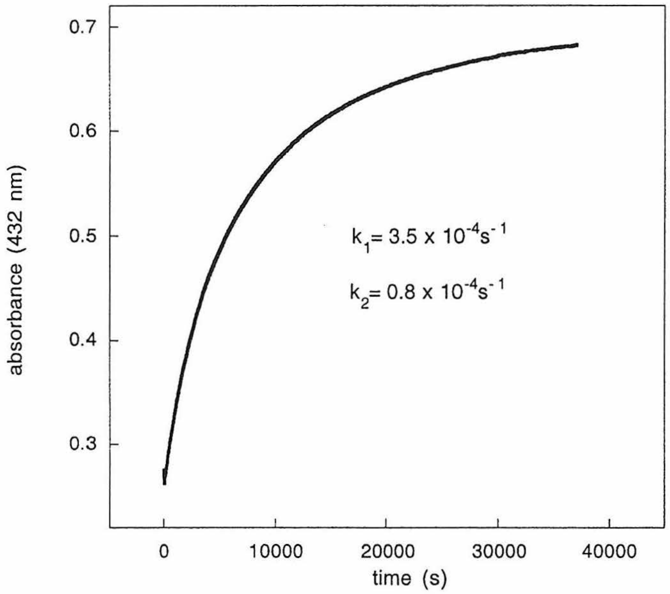

Figure 3.11. Kinetics of CN^- binding to unfolded Co-cyt *c* (12 h of unfolding, [GuHCl] = 4.0 M, [Co-cyt *c*] ~ 5 μM, $[CN^-]$ ~ 50 mM).

independent) backbone dynamics in the Co(III) protein, we have been able to directly detect two discrete cyt *c* folding pathways.

Identity of ligands in unfolded Co-cyt *c*

Comparison of tuna and horse Co-cyt c_u folding kinetics (Figure 3.12) suggests the probable identity of the ligands in the unfolded protein. Especially revealing is the absence of phase B in the tuna Co-cyt c_u kinetics; the composition and the structure[36,38] of tuna- and horse cyt *c* are essentially identical (85% sequence identity), but the tuna protein lacks His 33. Therefore, we assign phase B to the His 33-ligated population. Phase B appears to be due to the thermodynamically preferred ligand in horse Co-cyt c_u, in accordance with the assignment of His 33 as the predominant ligand in the unfolded iron protein.[11]

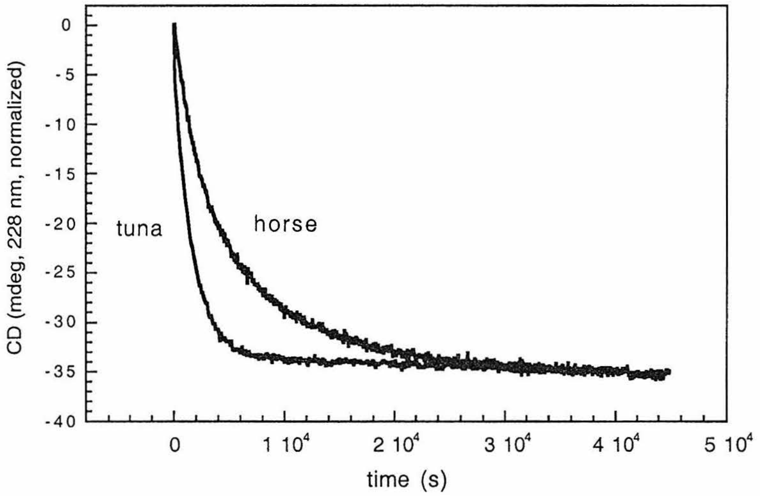

Figure 3.12. Comparison of the folding kinetics of tuna and horse Co-cyt *c* (10 min of unfolding, pH 6.5, 2.0 M GuHCl, 25° C).

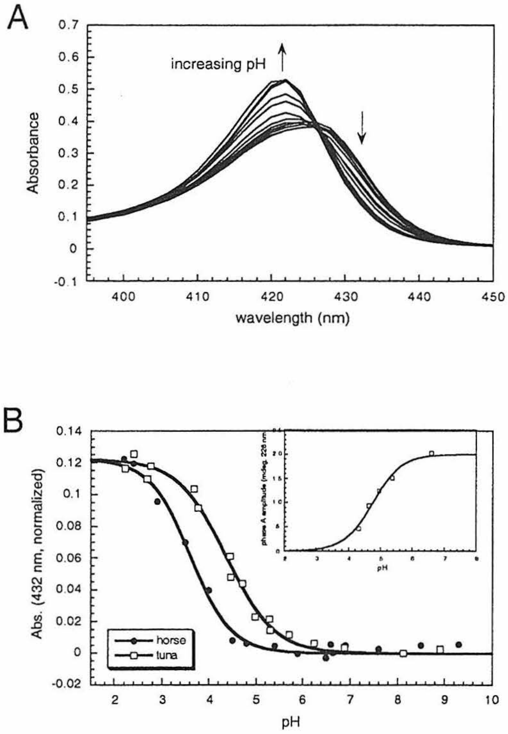

Figure 3.13. pH dependence of axial coordination in unfolded Co-cyt *c*. **(A)** pH-dependent changes in the Soret band of tuna Co-cyt c_u ([GuHCl] = 4.0 M). **(B)** Soret absorption (432 nm) in unfolded tuna and horse Co-cyt *c* as a function of pH. **(Inset)** Phase A amplitude (CD, 228 nm) of tuna Co-cyt *c* as a function of pH.

We also have examined the absorption spectra of horse- and tuna Co-cyt c_u as a function of pH. In both species, the pH titration reveals a dominant transition with a pK_a in the range 3 to 5 (3.6 for horse; 4.4 for tuna), attributable to the (de)protonation of the axial ligand (Figure 3.13). Furthermore, the amplitude of phase A is pH-dependent with a transition midpoint of ~ 4.6 (Figure 3.13 B inset). Based on the assignment of His 33 as the predominant ligand in horse Co-cyt *c*, we conclude that the pK_a of Co(III)-bound histidine (Co(III)-His) in Co-cyt c_u is ~ 3.6. We reasoned that it was unlikely that His 26 is sufficiently perturbed in the unfolded protein to exhibit a pK_a of 4.6. Consequently, we initially ascribed phase A to a Lys-misligated form, which should have a higher pK_a than

Co(III)-His. It is important to note here that in both horse and tuna cyt *c*, the N-terminal amino group is acetylated and thus unable to coordinate.

In order to unambiguously determine if a Lys is indeed involved in misligation, we chemically modified all Lys residues in horse- (19 lysines) and tuna- (16 lysines) Co-cyt *c* into homoarginines (see Appendix B), which are expected to be poor metal-ligands in aqueous solution. This modification yields a protein (Har-Co-cyt *c*) that retains the overall charge and stability of the unmodified protein. The folding of horse Har-Co-cyt *c* follows biexponential kinetics that are essentially identical

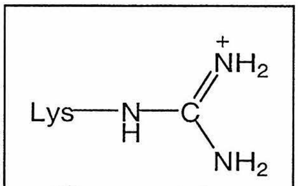

Homoarginine

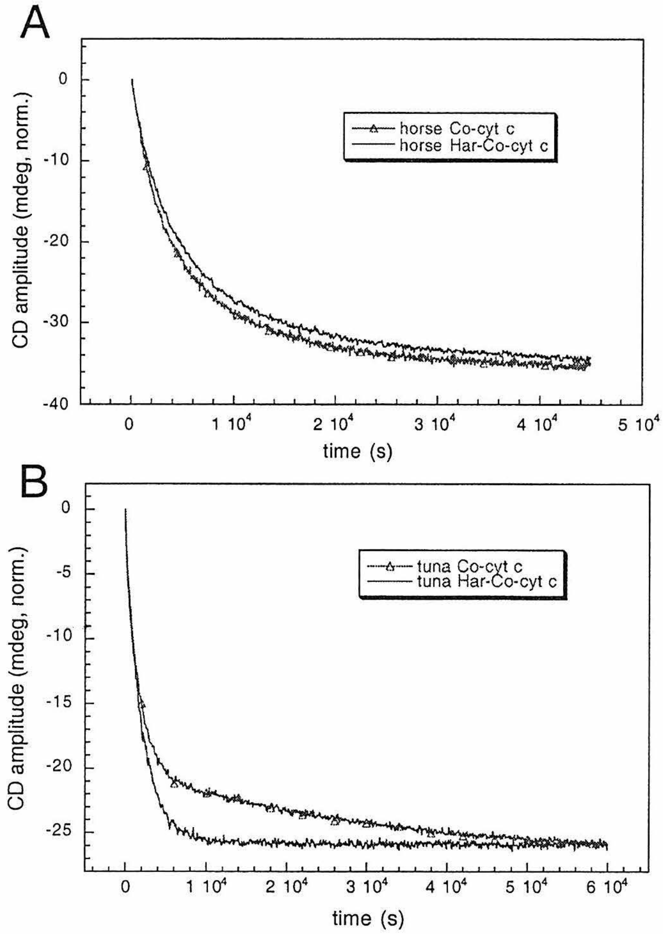

Figure 3.14. Comparison of the folding kinetics of Co-cyt *c* and Har-Co-cyt *c*. **(A)** Horse Co-cyt *c* (final [GuHCl] = 2.0 M,10 min unfolding, 25° C), **(B)** Tuna Co-cyt *c* (final [GuHCl] = 2.0 M, 2 day unfolding, 25° C).

to those of the unmodified protein with slightly slower rates (~ 1.5 fold), but similar relative amplitudes (Figure 3.14 A). On the other hand, the folding of tuna Har-Co-cyt *c* lacks Phase C and has monoexponential kinetics even after 2 days of unfolding (Figure 3.14 B). These findings provide strong evidence that histidines dominate misligation in unfolded cyt *c*, but in their absence, lysines are also involved. We conclude that Phase A and Phase B are due to His 26- and His 33-misligation, respectively, and Phase C results from a Lys residue (Figure 3.7). The identity of this residue remains undetermined due to the large number of lysines in cyt *c*.

Apparently, His 26 ligation in horse Co-cyt c_u is significantly destabilized compared to His 33 ligation (by 0.8 pH units). This could be due to the combined effect of smaller on-rate and a larger off-rate in the His 26-Co(III) binding equilibrium (see Figure 3.15 for the reaction scheme and simulated kinetics). The equal population of His 26 and His 33-misligated species in Co-cyt *c* in the initial stages (5 min) of unfolding suggest that the on-rates for His 26 and His 33 are similar (Figure 3.15). It follows from the relative equilibrium populations (His 33: His 26 ≈ 3:1 after 3 days unfolding) that the off-rate for His 26 should be 3 times faster than that for His 33. This is in perfect agreement with the 3 – 4 fold faster folding rate for the His 26-misligated protein (Phase A), which is also limited by the off-rate of His 26. The destabilization of His-26 ligation relative to His-33 ligation is presumably due to the shorter distance between the former and the heme group: the distance for an extended chain between His 26 and His 18 (ligated to the heme) is ~ 29 Å compared to ~ 54 Å for His 33.[11] This shorter distance may result in unfavorable steric interactions and an entropic penalty when His 26 is coordinated to the metal center.

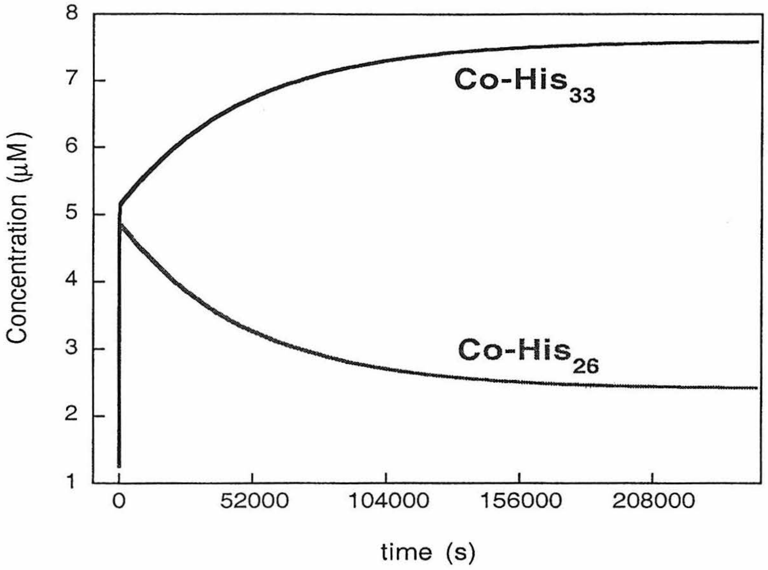

1) $Co(H_2O)His_{26}{}^{+}His_{33}{}^{+} \underset{k_{-1}\cdot[H^{+}]}{\overset{k_1}{\rightleftharpoons}} Co(H_2O)His_{26}His_{33}$

2) $Co(H_2O)His_{26}His_{33} \underset{k_{off,\ His\ 33}}{\overset{k_{on,\ His\ 33}}{\rightleftharpoons}} Co(His_{33})$

3) $Co(H_2O)His_{26}His_{33} \underset{k_{off,\ His\ 26}}{\overset{k_{on,\ His\ 26}}{\rightleftharpoons}} Co(His_{26})$

$-\log(k_1/k_{-1}) = 6.5 = pK_a$ of free histidine

$-\log(k_{on,\ His\ 33}/k_{off,\ His\ 33}) = -\log(10^{-2}/10^{-5}) = -3 = pK$ of His_{33} binding to Co(III)

$-\log(k_{on,\ His\ 26}/k_{off,\ His\ 26}) = -\log(10^{-2}/3\times10^{-5}) = -2.5 = pK$ of His_{26} binding to Co(III)

$$\left.\begin{array}{l}[Co(H_2O)His_{26}{}^{+}His_{33}{}^{+}]_0 = 2.4\times10^{-6}\,M\\ [Co(H_2O)His_{26}His_{33}]_0 = 7.6\times10^{-6}\,M\\ [Co(His)]_0 = 0\,M\end{array}\right\}\ \text{total concentration} = 10\times10^{-6}\,M$$

Figure 3.15. (top) Simulated kinetics of ligand exchange during horse Co-cyt *c* unfolding. **(bottom)** Reaction scheme and parameters used for the kinetics simulation. The species in parentheses indicate axial ligands to Co(III) and "+" indicates protonated species. The forward and backward rates for reaction 1 were set high ($\geq 10^{6.5}$) in order to accommodate fast (de)pronation equilibria and to temporally separate them from reactions 2 and 3. The rates for reactions 2 and 3 were best guesses to fit observed unfolding kinetics. The simulation was run with Chemical Kinetics Simulator (IBM).

Detection of a long-lived folding intermediate of Co-cyt *c*

Previous studies have revealed that formation of some secondary structure occurs before the ligand substitution processes that lead to Fe-cyt *c* folding.[39,40] At neutral pH and low [GuHCl], folding intermediates are trapped long enough to be studied by pulsed H/D exchange NMR.[3,41] These intermediates contain native-like features, such as the C- and N-terminal helices that dock against each other. The ability of these helices to form despite misligation has been attributed to the large separation between His 26 and 33 and the termini. Accordingly, when horse Co-cyt *c* is refolded at low [GuHCl] (≤ 0.8 M), we observe a large decrease in the far-UV CD amplitude (≤ 40% of total amplitude) within the deadtime of manual mixing (~ 5 s), consistent with the formation of a helical intermediate (Figure 3.16). This intermediate, especially at low temperature, persists for hours without significant change (Figure 3.16). During tuna Co-cyt *c* folding a similar intermediate is also observed under the same conditions, but to a lesser extent. This observation can be explained by the replacement of His 33 misligation with Lys-misligation in tuna Co-cyt *c*. Since several Lys residues are located within or near the termini, heme ligation by any of them should preclude the formation and docking of the terminal helices.

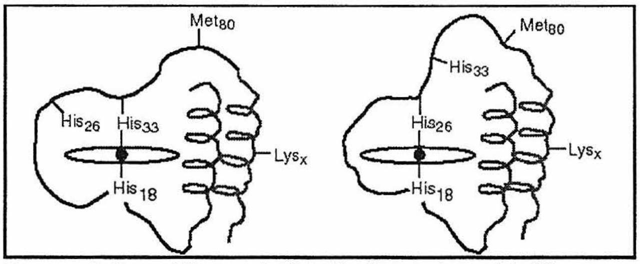

Proposed C- and N-terminal helix formation with His-misligation

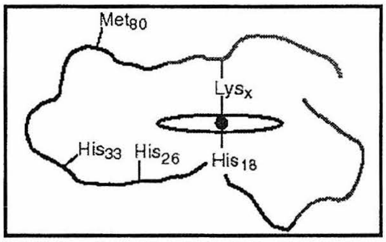

Hypothetical lysine-misligation

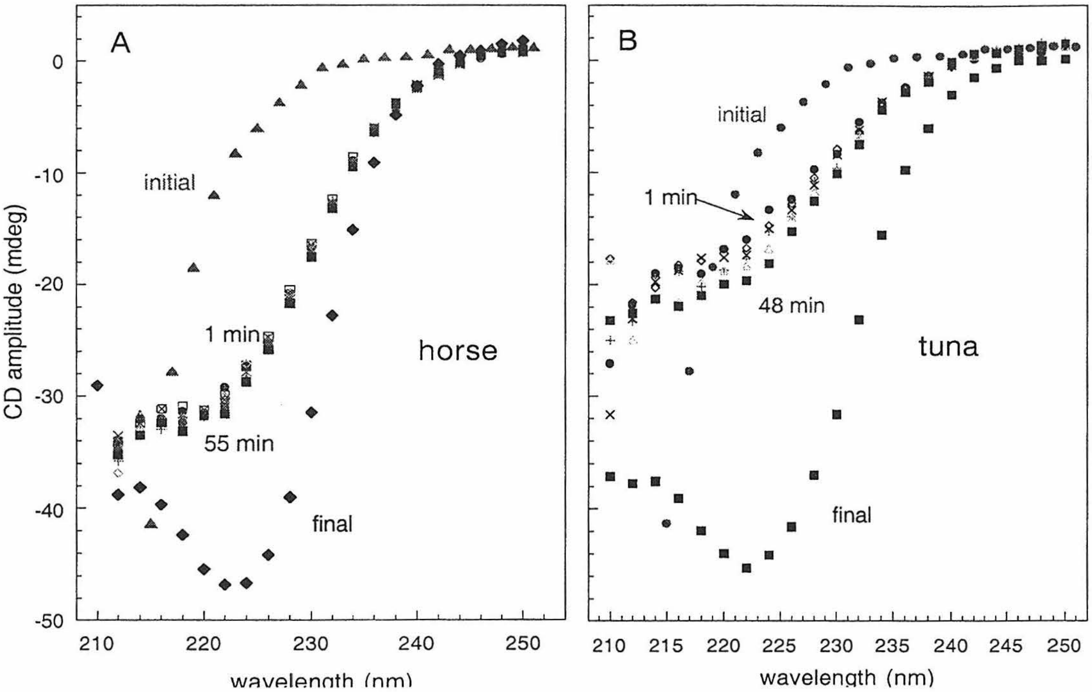

Figure 3.16. Far-UV CD spectra of Co-cyt *c* species (**A**, horse; **B**, tuna) formed during refolding in 0.4 M GuHCl (7° C). Immediately after the initiation of the horse Co-cyt *c* folding reaction (~ 1 min), a long-lived intermediate with some α-helical content is formed. The degree of helicity under the same conditions is considerably less for the tuna protein.

Real-time NMR monitoring of Co-cyt *c* folding kinetics

NMR spectroscopy offers a distinct advantage over other spectroscopic methods in that it enables the monitoring folding and unfolding reactions at the level of individual residues. It is therefore ideally suited to map out folding surfaces or energy landscapes that are defined by ensembles of unfolded and partially-folded structures that exist at different stages of the folding reaction.[42] Pulsed H/D exchange NMR studies, in particular, have been useful in structurally characterizing folding intermediates by way of analyzing the distribution of protein sites that are protected form hydrogen-exchange.[3,39-41] There has been a recent interest in following protein dynamics (folding, enzyme kinetics, etc.) by real-time NMR, i.e., under nonequilibrium conditions.[42] These experiments involve the sequential accumulation of spectra following the initiation of a reaction. However, even a 1D-NMR spectrum may take on the order of seconds in the best case scenario, putting most folding reactions beyond the realm of real-time NMR. We have seen that Co(III)-cyt *c* folding can take on the order of days to be complete, which makes it an ideal target to investigate by NMR spectroscopy.

We have followed Co-cyt *c* (horse) folding by NMR at low temperatures (≤ 10° C) in order to increase the available time window. The unfolded protein displays an NMR spectrum characteristic of a random coil: the resonances are relatively sharp and not dispersed (Figure 3.17).[43] The upfield signals due to the Met 80-sidechain protons seen in the spectrum of the folded protein[26] (Figure 3.3) are also absent, consistent with the loss of this ligand. As the protein refolds, chemical shift dispersion becomes apparent and the upfield-peaks due to the Met 80 protons appear (Figure 3.18). However, the extent of

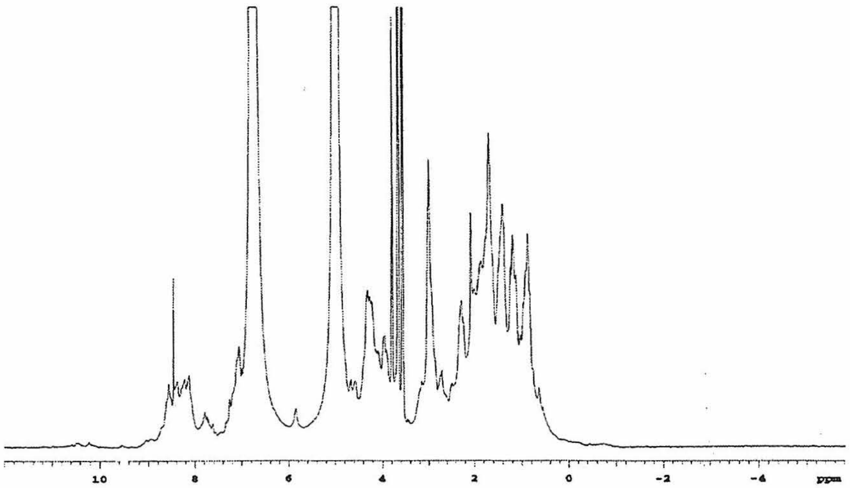

Figure 3.17. 1D-proton-NMR spectrum of unfolded (obtained 5 min after the initiation of folding) horse Co-cyt *c* (4° C, ~ 0.3 mM protein, 0.4 M GuHCl). Broad peaks centered at ~ 5 and ~ 7 ppm are due to water and GuHCl protons, respectively. Sharp peaks at ~ 3.7 and ~ 8.4 ppm are due to organic impurities.

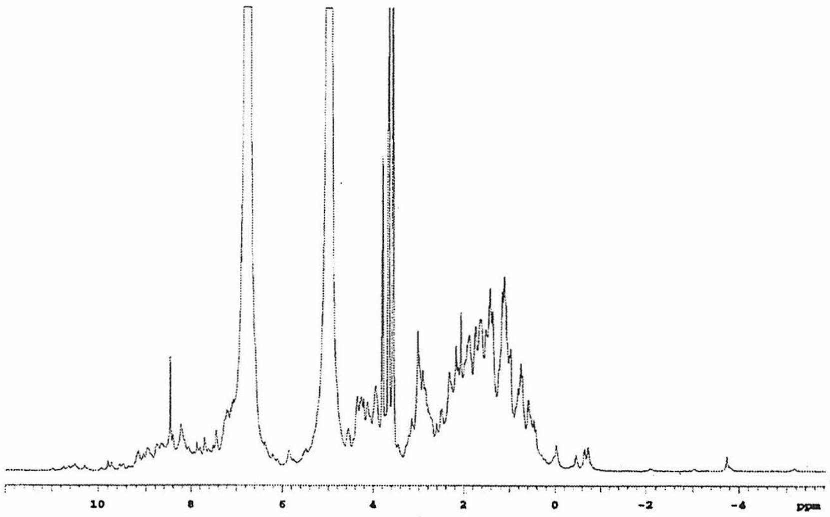

Figure 3.18. 1D-proton-NMR spectrum of refolded horse Co-cyt *c* (4° C, ~ 0.3 mM protein, 0.4 M GuHCl). Broad peaks centered at ~ 5 and ~ 7 ppm are due to water and GuHCl protons, respectively. Sharp peaks at ~ 3.7 and ~ 8.4 ppm are due to organic impurities.

dispersion for the refolded protein and the Met-80 peak amplitudes are significantly smaller than those for the native protein. The FPLC of the refolded product reveals, in addition to some amount of correctly folded protein, species of lower mobility which are not fully structured (as characterized by CD- and NMR-spectroscopy). Moreover, the kinetics of refolding monitored by the Met-80 CH_3 resonance at 3.78 ppm are significantly slower than those followed by CD spectroscopy (Figure 3.19). We attribute these observations to aggregation or other (unknown) bimolecular processes that become operational at high concentrations used for NMR spectroscopy ($\geq$ 0.3 mM); these processes lead to slower folding and the formation of misfolded species (note: no insoluble aggregates is formed during the folding reaction). In accordance with hypothesis, we have found that at higher protein concentrations, the amount of misfolded species increases as indicated by the NMR spectrum of the refolded species (less dispersion and satellites for the Met-80 resonances; see Figure 3.19) and FPLC chromatograms (higher ratio of misfolded protein: native-like protein) (Figure 3.20).

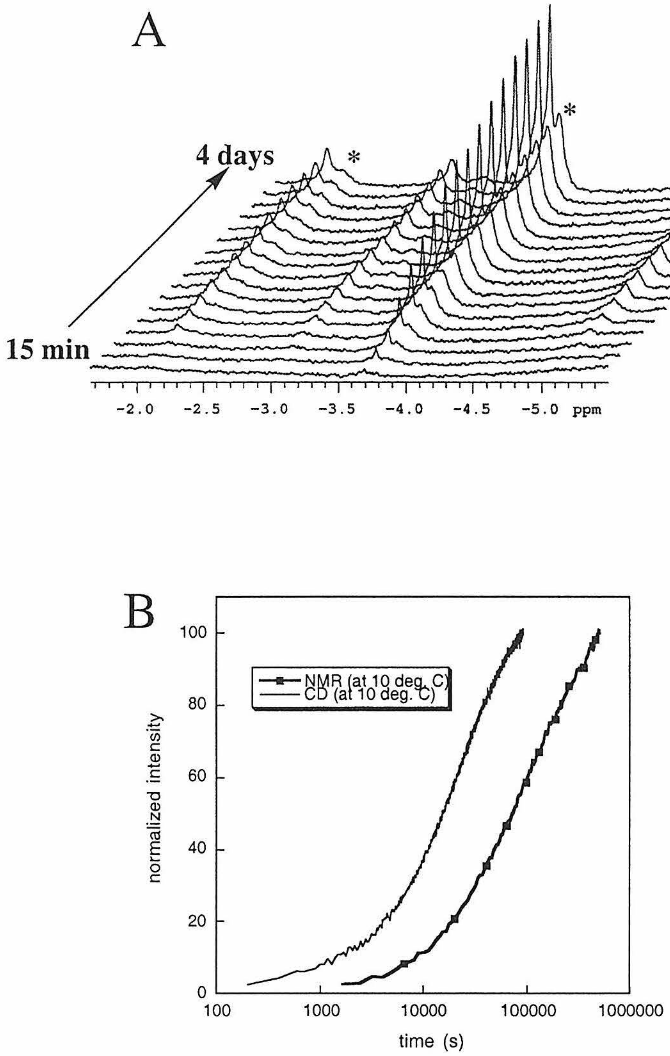

Figure 3.19. Evolution of Met80-sidechain proton resonances during Co-cyt *c* (horse) folding (**A**) and the corresponding kinetics trace (**B**, monitored at –3.78 ppm). The folding kinetics monitored by NMR are significantly slower than those monitored by CD spectroscopy under similar conditions (0.4 M GuHCl, 10° C). This is attributed to bimolecular processes (e.g., aggregation) that become significant at high protein concentrations (in this NMR run: [Co-cyt c]$_{\text{final}}$= 1.3 mM) and decelerate the folding reaction. These processes also result in the formation of misfolded species. One such species has distinct Met 80-proton resonances (at -2.2, -3.2, -3.9 and –5 ppm), two of which are labeled with asterisks.

We have also sought evidence for the α-helical folding intermediate observed with CD-spectroscopy (Figure 3.16). Because of its long lifetime, this intermediate is ideally suited for structural characterization by NMR spectroscopy. An examination of the horse Co-cyt *c* 1D-NMR spectrum obtained immediately after the initiation of refolding does, however, not reveal any sign of a structured intermediate. The amide region of the spectrum, for example, is devoid of chemical shift dispersion (Figure 3.21). Nevertheless, the amide peaks are quite broad, raising the possibility of a molten globular intermediate that has a fluxional secondary structure.[43] It is also quite likely that the breadth of these resonances is simply due to the heterogeneity of the sample which contains a mixture of folded, misfolded and unfolded species.

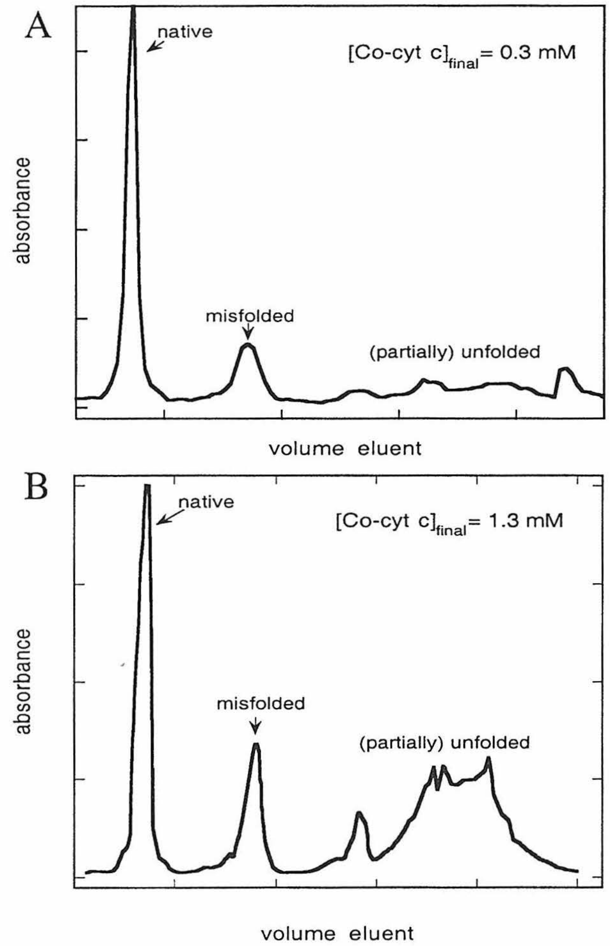

Figure 3.20. FPLC traces of refolded Co-cyt *c* from NMR-kinetics experiments. **(A)** [Co-cyt *c*]$_{final}$ = 0.3 mM under refolding conditions; **(B)** [Co-cyt *c*]$_{final}$ = 1.3 mM under refolding conditions. In addition to the correctly folded protein (characterized by CD and UV-vis spectroscopy), which elutes at 0.25 M NaCl, there are species that appear to be misfolded or partially unfolded. While the misfolded species has close to native-like CD- and UV-vis spectra and slightly shifted Met 80-proton NMR resonances (see Figure 3.18), the species that elute later have considerably less α-helicity. The relative amount of these partially unfolded species increases when the protein concentration is raised.

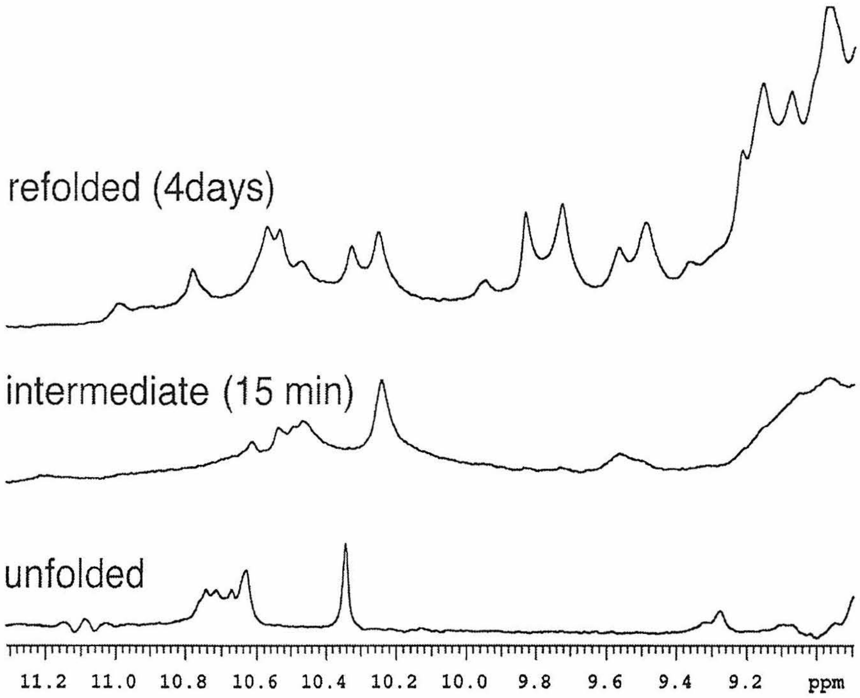

Figure 3.21. Amide-region NMR spectra of various horse Co-cyt *c* species formed during folding (0.4 M GuHCl, 1.3 mM Co-cyt *c*, 4° C). The intermediate species does not appear to have a compact structure as indicated by the lack of chemical shift dispersion.

Conclusions

The inertness of low-spin Co(III) complexes played a crucial role in the development of mechanistic models for octahedral substitution reactions.[14,15] This property of Co(III) has allowed us to elucidate the ligand substitutions that are strongly coupled to the folding and unfolding of cyt *c*. We have also detected a very long-lived folding intermediate that is trapped owing to the increased energy barrier to folding in the Co-substituted protein. Our approach opens new avenues for studying the folding dynamics of other proteins whose structures depend upon polypeptide coordination to one or more metal centers.

References

(1) Babul, J.; Stellwagen, E. *Biochemistry* **1972**, *11*, 1195-1200.

(2) Muthukrishnan, K.; Nall, B. T. *Biochemistry* **1991**, *30*, 4706-4710.

(3) Elöve, G. A.; Bhuyan, A. K.; Roder, H. *Biochemistry* **1994**, *33*, 6925-6935.

(4) Yeh, S.-R.; Han, S.; Rousseau, D. L. *Acc. Chem. Res.* **1998**, *31*, 727-736.

(5) Yeh, S.-R.; Rousseau, D. L. *Nat. Struct. Biol.* **1998**, *5*, 222-227.

(6) Telford, J. R.; Wittung-Stafshede, P.; Gray, H. B.; Winkler, J. R. *Acc. Chem. Res.* **1998**, *31*, 755-763.

(7) Telford, J. R.; Tezcan, F. A.; Gray, H. B.; Winkler, J. R. *Biochemistry* **1999**, *38*, 1944-1949.

(8) Shastry, M. C. R.; Sauder, J. M.; Roder, H. *Acc. Chem. Res.* **1998**, *31*, 717-725.

(9) Jones, C. M.; Henry, E. R.; Hu, Y.; Chan, C. K.; Luck, S. D.; Bhuyan, A.; Roder, H.; Hofrichter, J.; Eaton, W. A. *Proc. Natl. Acad. Sci. USA.* **1993**, *90*, 11860-11864.

(10) Hagen, S. J.; Carswell, C. W.; Sjolander, E. M. *J. Mol. Biol.* **2001**, *305*, 1161-1171.

(11) Colón, W.; Wakem, L. P.; Sherman, F.; Roder, H. *Biochemistry* **1997**, *36*, 12535-12541.

(12) Russell, B. S.; Melenkivitz, R.; Bren, K. L. *Proc. Natl. Acad. Sci. USA.* **2000**, *97*, 8312-8317.

(13) Hammack, B.; Godbole, S.; Bowler, B. E. *J. Mol. Biol.* **1998**, *275*, 719-724.

(14) Basolo, F.; Pearson, R. G. *Mechanisms of Inorganic Reactions*; John Wiley and Sons: New York, 1967.

(15) Langford, C. H.; Gray, H. B. *Ligand Substitution Processes*; W. A. Benjamin: Reading, 1966.

(16) Lippard, S. J.; Berg, J. M. *Principles of Bioinorganic Chemistry*; University Science Books: Mill Valley, CA, 1994.

(17) Pratt, J. M. *Inorganic Chemistry of Vitamin* B_{12}; Academic Press: London, 1972.

(18) Halpern, J. *Science* **1985**, *227*, 869-875.

(19) Kobayashi, M.; Shimizu, S. *Nat. Biotechnol.* **1998**, *16*, 733-736.

(20) Kobayashi, M.; Shimizu, S. *Eur. J. Biochem.* **1999**, *261*, 1-9.

(21) Dickinson, L. C.; Chien, J. C. W. *J. Biol. Chem.* **1973**, *248*, 5005-5011.

(22) Yonetani, T.; Yamamoto, H.; Woodrow, G. V. *J. Biol. Chem.* **1974**, *249*, 682-690.

(23) Yonetani, T.; Kayne, F. J.; Yonetani, T. *J. Biol. Chem.* **1974**, *249*, 691-698.

(24) Bertini, I.; Luchinat, C. In *Bioinorganic Chemistry*; Bertini, I., Gray, H. B., Lippard, S. J., Valentine, J. S., Eds.; University Science Books: Mill Valley, CA, 1994.

(25) Bertini, I.; Luchinat, C. *Adv. Inorg. Biochem.* **1984**, *6*, 71.

(26) Moore, G. R.; Williams, R. J. P.; Chien, J. C. W.; Dickinson, L. C. *J. Inorg. Biochem.* **1980**, *12*, 1-15.

(27) Takano, T.; Dickerson, R. E. *Proc. Natl. Acad. Sci. USA* **1980**, *77*, 6371.

(28) Otwinowski, Z.; Minor, W. *Methods Enzymol.* **1997**, *276*, 307-326.

(29) Brünger, A. T.; Adams, P. D.; Clore, G. M.; DeLano, W. L.; Gros, P.; Grosse-Kunstleve, R. W.; Jiang, J. S.; Kuszewski, J.; Nilges, M.; Pannu, N. S.; Read, R. J.; Rice,

L. M.; Simonson, T.; Warren, G. L. *Acta Crystallogr. Sect. D-Biol. Crystallogr.* **1998**, *54*, 905-921.

(30) McRee, D. *J. Mol. Graphics* **1992**, *10*, 44-46.

(31) Laskowski, R. A.; Macarthur, M. W.; Moss, D. S.; Thornton, J. M. *J. Appl. Crystallogr.* **1993**, *26*, 283-291.

(32) Nozaki, Y. *Methods Enzymol.* **1972**, *26*, 43-50.

(33) Pace, N. C.; Shirley, B. A.; Thomson, J. A. In *Protein Structure: A Practical Approach*; Creighton, T. F., Ed.; IRL Press: Oxford, 1990; pp 311-330.

(34) Dickinson, L. C.; Chien, J. C. W. *Biochemistry* **1975**, *14*, 3526-3534.

(35) Dickinson, L. C.; Chien, J. C. W. *Biochemistry* **1975**, *14*, 3534-3541.

(36) Swanson, R.; Trus, B. L.; Mandel, N.; Mandel, G.; Kallai, O. B.; Dickerson, R. E. *J. Biol. Chem.* **1977**, *252*, 759-775.

(37) Banci, L.; Bertini, I.; Bren, K. L.; Gray, H. B.; Sompornpisut, P.; Turano, P. *Biochemistry* **1995**, *34*, 11385-11398.

(38) Bushnell, G. W.; Louie, G. V.; Brayer, G. D. *J. Mol. Biol.* **1990**, *214*, 585-595.

(39) Elöve, G. A.; Chaffotte, A. F.; Roder, H.; Goldberg, M. E. *Biochemistry* **1992**, *31*, 6876-6883.

(40) Sosnick, T. R.; Mayne, L.; Englander, S. W. *Proteins* **1996**, *24*, 413-426.

(41) Roder, H.; Elöve, G. A.; Englander, S. W. *Nature* **1988**, *335*, 700-704.

(42) van Nuland, N. A. J.; Forge, V.; J., B.; Dobson, C. M. *Acc. Chem. Res.* **1998**, *31*, 773-780.

(43) Dahiyat, B. I.; Mayo, S. L. *Proc. Natl. Acad. Sci. USA* **1997**, *94*, 10172-10177.

Chapter 4

Electron Tunneling in Protein Crystals*.

Electron Transfer Kinetics between Zn- and Fe-cyt *c* in a Crystal Lattice

---

* Adapted from Tezcan, F. A; Crane, B.R; Winkler, J. R.; Gray, H. B. *Proc. Natl. Acad. Sci. USA* **2001**, *98*, 5002-5006. All phases of this work were carried out in collaboration with Dr. Brian Crane.

Introduction

Long-range electron tunneling is an integral part of many biological processes, most notably respiration and photosynthesis.[1] Tunneling can occur over distances as long as 20 Å in a matter of microseconds. This efficiency is provided by proteins, which not only present a low dielectric medium for redox centers so as to lower their reorganization energy, but also provide a chemical bond framework that mediates electronic coupling.[1]

Extensive experimental and theoretical investigations have elucidated the role of polypeptide structure in facilitating electron tunneling through proteins.[1-9] Most of the definitive work has centered on molecules with fixed donor-acceptor distances and orientations, such as proteins covalently modified with redox-active units [1-3] or proteins that contain both donors and acceptors.[4,5] This work has established that the dependence of rate on distance is exponential,[1,2,8,9] as expected for a tunneling reaction,[6] with decay constants in the 1.0 – 1.2 Å^{-1} range.[1,2,9] It is likely, therefore, that the redox centers in these proteins are electronically coupled through the chemical-bond framework of the intervening medium.[1-4,6,7]

Electron transfer (ET) *between* proteins is less well understood, as it involves at least three steps: association of the donor and acceptor; electron tunneling within the donor-acceptor complex; and dissociation of the oxidized and reduced products.[10-12] Since the dynamics of the first and the third steps obscure the electron tunneling reaction, many studies have focused on the ET properties of stable protein-protein complexes formed under low ionic strength conditions in solution; examples include complexes formed between cytochrome *c* (cyt *c*) and cytochrome *c* peroxidase (CcP),[3,11] cyt *c* and cytochrome *f*,[13] and myoglobin and cytochrome b_5.[14] It has been difficult to interpret the results, however, as neither the donor-acceptor docking geometries nor the conformations of these complexes are known.[15] Conversely, the crystal structures of several protein-protein complexes have been determined, yet these may not correspond to the structures formed in solution.[16-18] *Tunneling kinetics and structure have to be investigated under the same conditions to understand electronic coupling between proteins.*[19]

A protein crystal containing photoactivatable donors and acceptors at specific lattice sites is an ideal medium for investigating the dependence of tunneling rates on structure. In the crystal lattice of tuna cytochrome *c* (cyt *c*),[20,21] chains of cyt *c* molecules form helices with 24.1 Å separation between neighboring metal centers (Figure 4.1). Tunneling timetables predict that activationless ET over this distance in a protein can take place in the millisecond time range.[22] All other metal-metal distances in the lattice are greater than 30 Å, with estimated electron tunneling times that are at least three orders of magnitude slower. Thus, the heme groups can be treated as randomly ordered in a one-dimensional chain, separated by identical protein and solvent media. By doping Zn-cyt *c* (isomorphous with Fe-cyt *c*) into this lattice, interprotein ET reactions can be triggered by laser excitation, as illustrated in Scheme 1. The triplet state of Zn-cyt *c* (*Zn-cyt *c*) is generated in high yield with 550- or 580-nm excitation (**R1**). This highly reducing excited state ($E_0 \approx -0.8$ V) reacts with Fe(III)-cyt *c* ($E_0 \approx 0.25$ V) to generate Fe(II)-cyt *c* and the Zn-cyt *c* cation radical, Zn-cyt c^+ ($E_0 \approx 0.9$ V) (**R2**).[23]

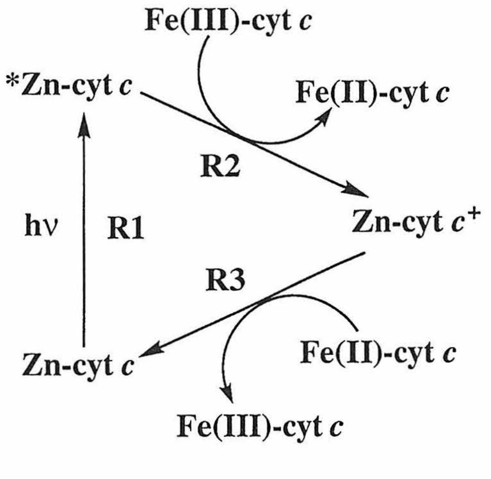

Scheme 1

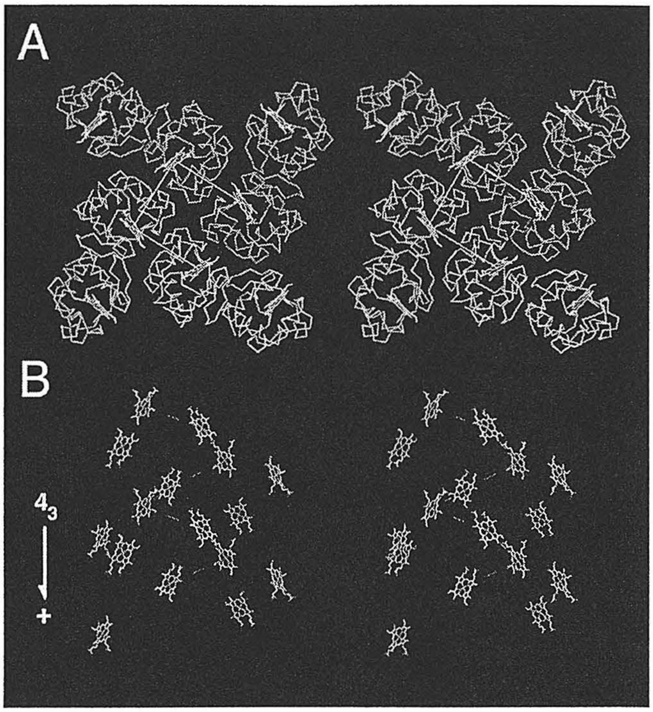

Figure 4.1. Stereoviews of tuna cyt *c* crystal lattice (space group $P4_3$). The asymmetric unit contains two molecules, with one related to a 4_3 axis at the unit cell origin and the other related to a second 4_3 axis at the unit cell center. The two screw axes run anti-parallel to each other and are related by a pseudo-twofold axis directed along the *ab* diagonal. This packing produces a 24.1 Å separation between the metal centers of adjacent molecules (Mol_i and Mol_{i+1}) within each screw axis. **(A)** View down the $P4_3$ axis. Different colors indicate pairs of cyt *c* molecules in the same asymmetric unit. White lines connect the iron centers that are separated by 24.1 Å. **(B)** View of heme orientation along the $P4_3$ axis. Broken lines connect the hemes that are involved in ET reactions.

In a dark reaction, Zn-cyt c^+ and Fe(II)-cyt *c* recombine to yield the ground-state species (**R3**).

We have successfully measured and analyzed the kinetics of ET (Reactions **R2** and **R3**) between native and Zn-substituted tuna cytochrome *c* (cyt *c*) molecules in crystals. We have determined the structure of the Zn:Fe-cyt *c* cocrystals to 1.5 Å resolution, which has allowed an accurate description of the relative donor-acceptor geometries, and the protein and solvent medium separating them. We have found that the ET-rates in cyt *c* crystals closely match those for through-protein ET over similar donor-acceptor separations, confirming that van der Waals interactions and water-mediated hydrogen bonds can be effective coupling elements for electron tunneling across a protein-protein interface.

Materials and Methods

Preparation of Zn-cyt *c*

Tuna cyt *c* was purchased from Sigma. Zn-substituted cyt *c* was prepared following the protocols used for Co-cyt *c*, which can be found in Appendix B. Zn-cyt *c* is light-sensitive and degrades completely in a few hours. Therefore, it was always kept away from room light unless it was deaerated. Purification of Zn-cyt *c* was accomplished by cation-exchange (Mono S) FPLC (Figure 4.2) running an NaCl gradient similar to that

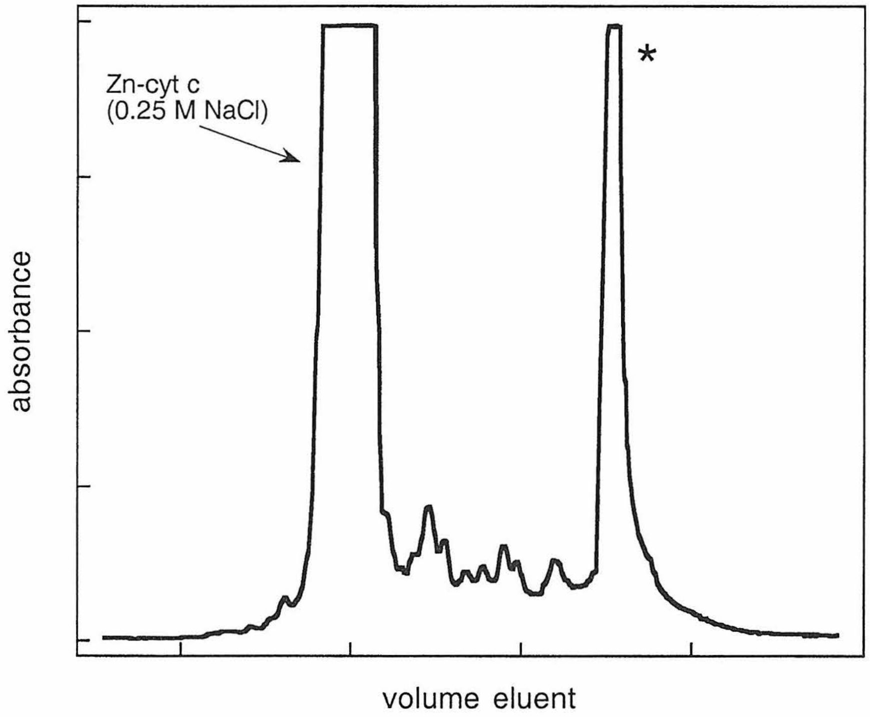

Figure 4.2. FPLC trace for the purification of tuna Zn-cyt *c*. The desired product elutes at ~ 0.25 M NaCl. There is a large amount of impurities, including species marked with an asterisk, which only becomes mobile upon treatment with 1 M NaOH.

used for Co-cyt *c* purification (see Appendix B). The pure product elutes at 0.25 M NaCl. Zn-cyt *c* was characterized by absorption- (Soret maximum at 424 nm and Q-bands at 550 and 584 nm) and electrospray mass spectroscopy (MW = 12038 amu) (Figure 4.3). The concentration of Zn-cyt *c* solutions was estimated using $\varepsilon_{424} \approx 200{,}000\ M^{-1}cm^{-1}$.

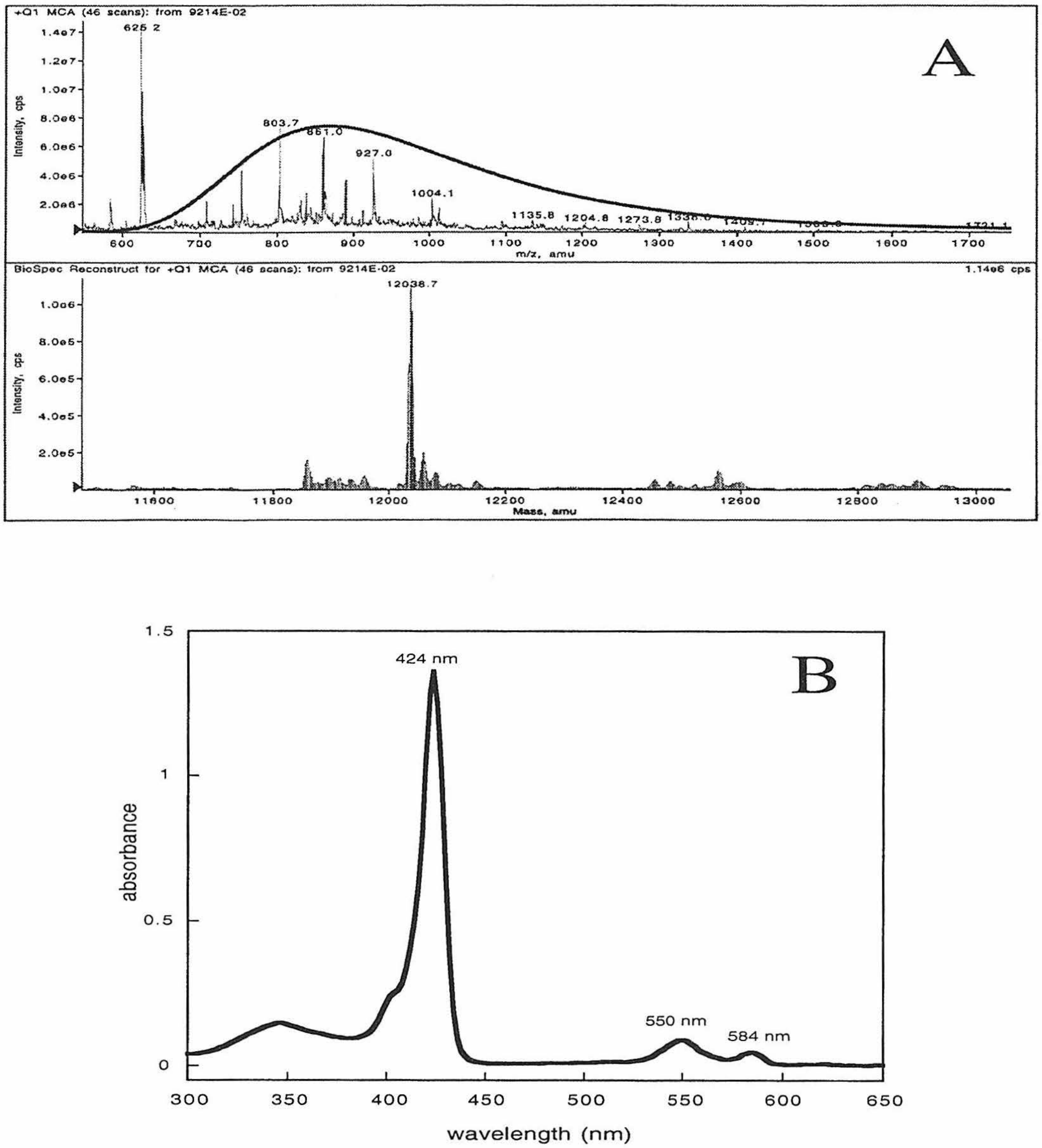

Figure 4.3. Electrospray mass- (**A**) and UV-vis (**B**) spectra of tuna Zn-cyt *c*.

Cocrystallization of Zn:Fe- and Zn:Co-cyt *c*

All solutions for crystallization were prepared by mixing appropriate amounts of two stock solutions: Stock Solution A was 0.75 M NaCl and 0.1 M NaP_i (pH 6.0), while Stock Solution B contained saturated $(NH_4)SO_4$ (~ 4 M), in addition to 0.75 M NaCl and 0.1 M NaP_i (pH 6.0). Prior to setting up crystallization wells, the protein solutions were concentrated and exchanged into Stock Solution A using Centricon or Microcon centrifuge filtration units (MW-cutoff 10,000 amu). Zn:Fe(III)-cyt *c*, Zn:Fe(II)-cyt *c* and Zn:Co(III)-cyt *c* cocrystals were grown at room temperature in sitting or hanging drops. Zn:Fe(II)-cyt *c* crystals were grown aneorobically in a tent using deaerated solutions; the protein solution was also deaerated and reduced with dithionite. The reservoir solution for all species contained 500 μL of 70 – 85% concentrated $(NH_4)_2SO_4$, 0.75 M NaCl and 0.1 M NaP_i (pH 6.0), and the drops were 2 μl reservoir solution and 2 μl of 4 –10 mM protein, where the composition of the protein ranged from 3 Fe(or Co)-cyt *c*:1 Zn-cyt *c* to 1 Fe(or Co)-cyt *c*:3 Zn-cyt *c*. Crystal growth is governed by the Fe- or Co-protein, which nucleates rapidly (few hours) to produce large rod-shaped crystals (500 × 50 × 50 μm), rather than the Zn-protein, which crystallizes slowly (> 2 weeks) in higher ammonium sulfate concentrations (~ 85%) to give bundles of thin needles (500 × 5 × 5 μm) (Figure 4.4). Generally, if the ratio of Fe-(or Co) to Zn-cyt *c* was unity or greater, diffraction quality crystals were obtained within a couple of days.

Cocrystallization was confirmed by UV-vis (Figure 4.5) or X-ray absorption measurements (Figure 4.6) done directly on the crystals, or indirectly by the UV-vis spectra of crystals dissolved in a minimal amount of water. For the latter, the crystal was first placed in an 85% saturated ammonium sulfate solution to wash away the

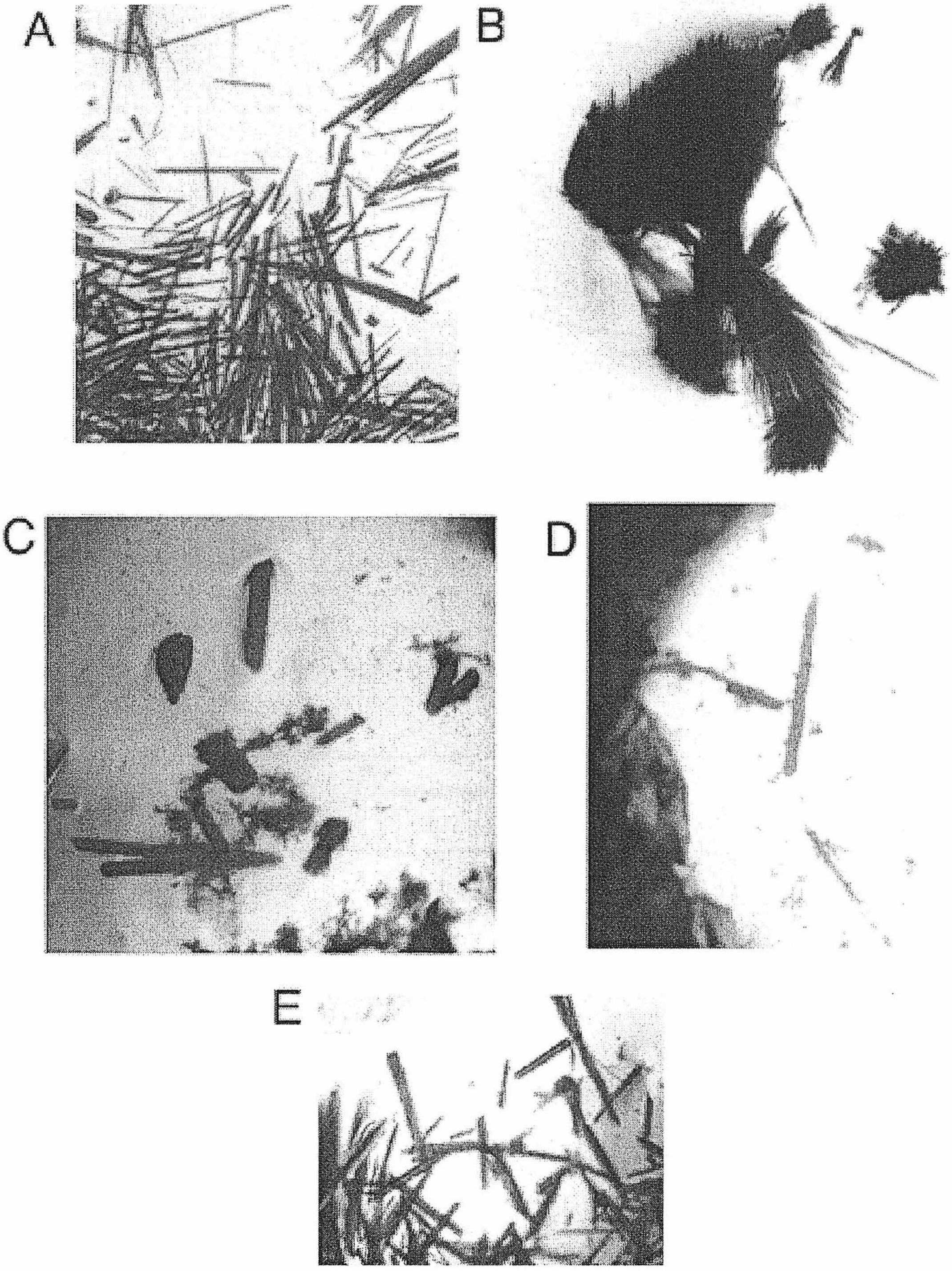

Figure 4.4. Tuna cyt *c* crystals. **(A)** Fe-cyt *c*, **(B)** Zn-cyt *c*, **(C)** 2Fe:1Zn-cyt *c*, **(D)** 1Fe:1Zn-cyt *c*, **(E)** 2Co:1Zn-cyt *c*.

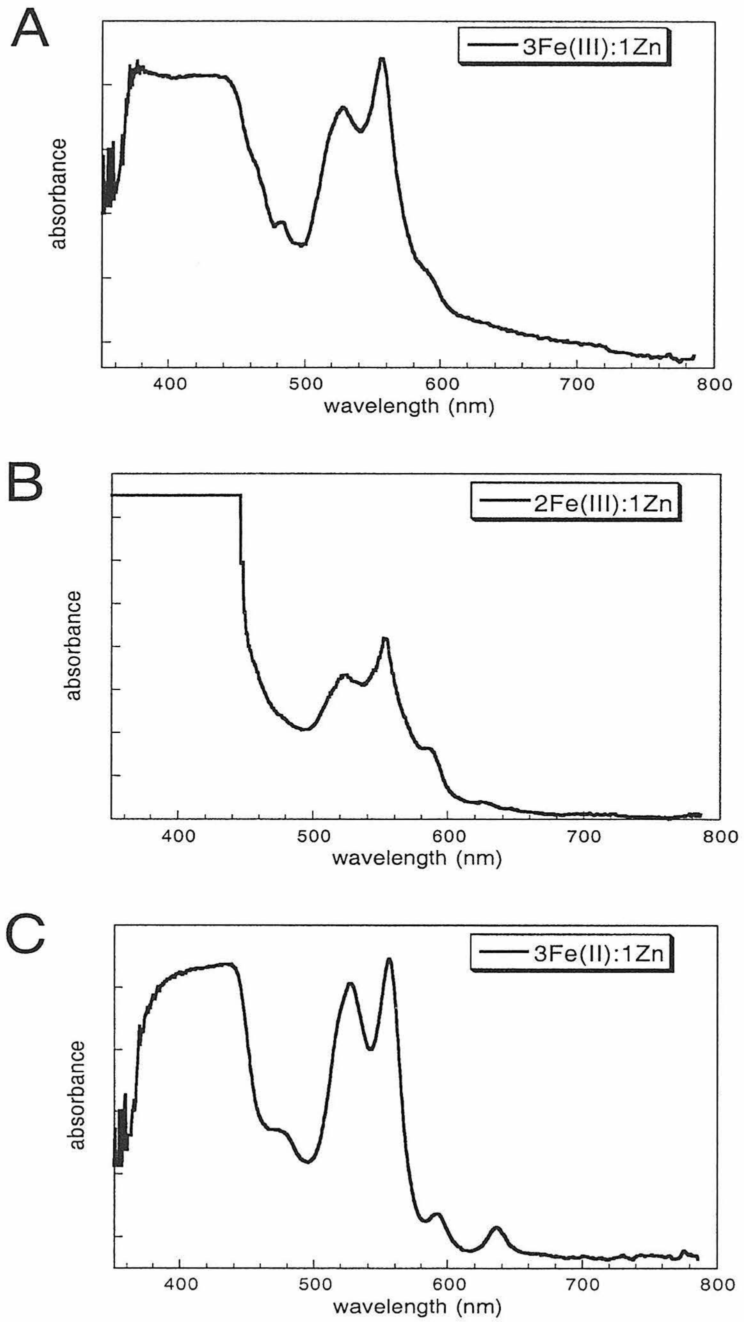

Figure 4.5. Absorption spectra of Zn:Fe-cyt *c* cocrystals. **(A)** 3Fe(III):1Zn, **(B)** 2Fe(III):1Zn, **(C)** 3Fe(II):1Zn. Q-band features for Zn-cyt *c* and Fe-cyt *c* (AcMet adduct of AcMP8) can be found in Figures 4.3 and 1.13, respectively. The absorption band at 630 nm in **C** is seen in some crystals and attributed to an impurity of unknown identity. Y-axes could not be normalized due to different amounts of scattered light in each crystal.

2Fe:1Zn-cyt c

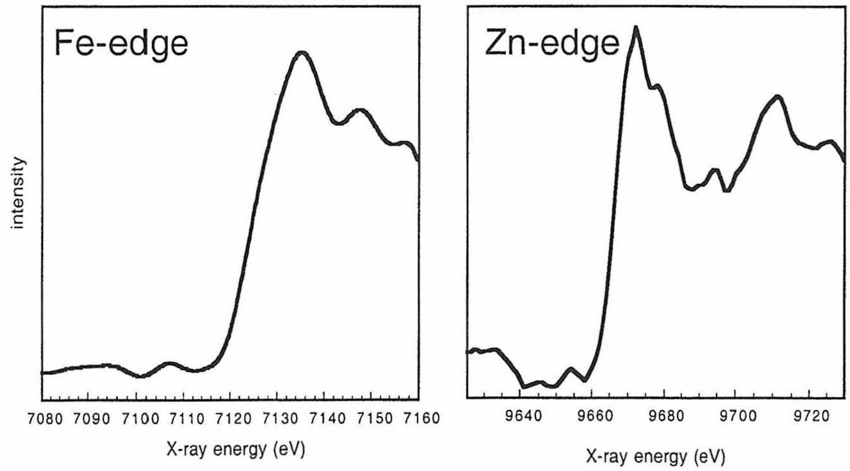

1Fe:1Zn-cyt c

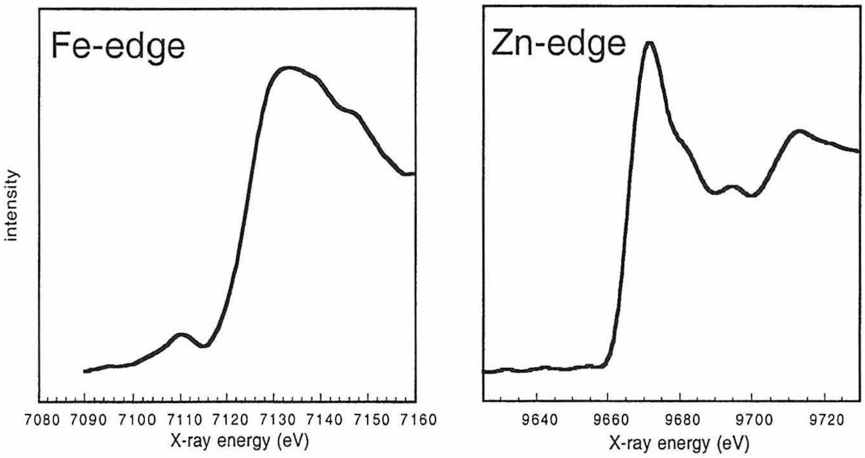

Figure 4.6. X-ray absorption spectra of Fe:Zn-cyt *c* cocrystals in the Fe and Zn K-edge regions. **(top)** 2Fe:1Zn-cyt *c*, **(bottom)** 1Fe:1Zn-cyt *c*.

protein that has not incorporated into the crystals. UV-vis spectroscopic measurements on the crystals were performed using a microspectrophotometer setup with a diode array detector (Ocean Optics PC1000) interfaced to a PC. The data were processed with Spectraware 2.0. X-ray absorption (fluorescence) spectroscopy was done at Beamline 9-2 at the Stanford Synchrotron Radiation Laboratories (SSRL). The data were processed using *Choochme*, a program available at SSRL BL 9-2 workstations.

Structure determination of Zn:Fe-cyt *c* by X-ray diffraction

X-ray diffraction data were collected at 100 K using an R-Axis IV imaging plate area detector and monochromatized Cu-Kα radiation (1.54 Å) produced by a Rigaku RU 200 rotating anode generator operated at 50 kV and 100 mA, or at SSRL beamline 9-2 (1.28 Å) equipped with a CCD detector. The structures of Fe:Zn-cyt *c* cocrystals were determined by refinement of a model from isomorphous crystals (space group $P4_3$) of tuna heart cyt *c* (PDB:3CYT)[21] against diffraction data using DENZO[24] (Table 4.1). Rigid-body, simulated-annealing, positional and thermal refinement with CNS,[25] amidst rounds of manual rebuilding, and water placement with XFIT[26] produced the final models. The Ramachandran plot was calculated with PROCHECK.[27] Superimposed, non-interacting Fe- and Zn-porphyrins were simultaneously refined for each of the two cyt *c* molecules in the unit cell. Stereochemical restraints were removed from the heme axial ligand bonds in the later stages of refinement. Fe:Zn occupancies were defined using multiwavelength anomalous diffraction data collected at the Stanford Synchrotron Radiation Laboratory BL-92 on crystals grown out of 2Fe:1Zn and 1Fe:2Zn solution stoichiometries. For each crystal, metal occupancy refinement with MADPHSREF[28] was carried out against data sets collected at four energies (7124, 7135, 9666 and 9671 eV) chosen to accentuate both the absorptive and dispersive components of Fe and Zn anomalous scattering.

Table 4.1. X-ray data collection, refinement and metal occupancy statistics for tuna Fe:Zn-cyt *c* structures.

[*]Approximate stoichiometry of the crystallization solution. [†]intensity signal to noise ratio. [‡]$R_{sym} = \Sigma\Sigma_j | I_j - \langle I \rangle | / \Sigma\Sigma_j | I_j |$. [§] $R = \Sigma || F_{obs}| - |F_{calc}|| / \Sigma | F_{obs}|$ for all reflections (no σ cutoff). [‖]Free R calculated against 8% of the reflections removed at random. [¶]Root mean square deviations from bond and angle restraints. [**]Relative occupancies of Fe and Zn as determined by multiwavelength anomalous diffraction experiments. For 2Fe:1Zn, different crystals were used for structure and metal occupancy determinations. Values are averages of the two molecules in the asymmetric unit. [††]Fe(III)-only cyt *c* (PDB:3CYT). [‡‡]The increase in the Met 80 bond length with increasing Zn-occupancy indicates that for Zn-only cyt *c*, $d_{\text{Met 80}} \geq 2.50$ Å.

Stoichiometry[*]	**2Fe:1Zn**	**1Fe:2Zn**
Residues	103 + 1 Heme	103 + 1 Heme
Waters	488	488
Unit cell dimensions (Å)	74.18×74.18×35.54	74.36×74.36×35.70
No. of monomers / unit cell	2	2
Symmetry group	$P4_3$	$P4_3$
Resolution (Å)	30.0–1.5	30–2.0
X-ray wavelength (Å)	1.54	1.28
No. of measurements	61451	19049
No. of unique reflections	27877	11058
Completeness (%)	89.0 (68.4)	81.7 (78.2)
$\langle I / \sigma I \rangle$[†]	19.3 (3.5)	17.1 (8.7)
R_{sym}[‡] (%)	6.6 (23.2)	6.2 (13.0)
R[§] (%)	22.9	22.0
Free R[II] (%)	25.1	24.4
Rms Bnd[¶] (Å)	0.008	0.008
Rms Ang[¶] (°)	1.4	1.4
Fe:Zn occupancy[**]	0.68:0.32	0.39:0.61
Average temperature factor (Å^2)		
All protein	14.28	19.99
Main chain atoms	12.58	18.08
Sidechain atoms	12.74	18.12
Heme atoms	9.57	16.12
Water molecules	23.46	29.98
Ramachandran plot (%)		
Residues in most favored regions	93.0	90.7
Residues in add.l allowed regions	5.8	8.1
Residues in generously allowed regions	1.2	1.2
Residues in disallowed regions	0.0	1.2
Metal–ligand bond distances (Å)		
His 18	(2.00)[††] 2.00	2.00
Met 80	(2.27)[††] 2.44	2.50[‡‡]

Kinetics of electron transfer in Zn:Fe- and Zn:Co-cyt *c* cocrystals monitored by transient absorption spectroscopy

Sample preparation

Crystals for transient absorption experiments were mounted and sealed inside 1 × 1 mm quartz capillaries (Figure 4.7) in an anaerobic tent to prevent oxidative photodegradation of Zn-cyt *c*. If crystals were grown outside the tent, they were soaked in deaerated solutions for at least two days prior to kinetics measurements. Once deaerated, the crystals were resistant to photodegradation indefinitely. Prior to crystal mounting in the tent, one end of each quartz capillary was flame-sealed using a Bunsen burner. In order to facilitate handling in the tent, the capillary was attached to the surface of a glass slide using a small amount of clay (Figure 4.7). To mount the crystals, the upper half of the capillary (opposite from the sealed end) was filled with the crystallization solution all the way to the top using a small (0.3 – 0.5 mm diameter tip) glass pipette. Desired crystals were picked up with the tip of a micropipettor and released onto the top of the solution in the capillary. The capillary was then set upright to allow the crystals to sink to

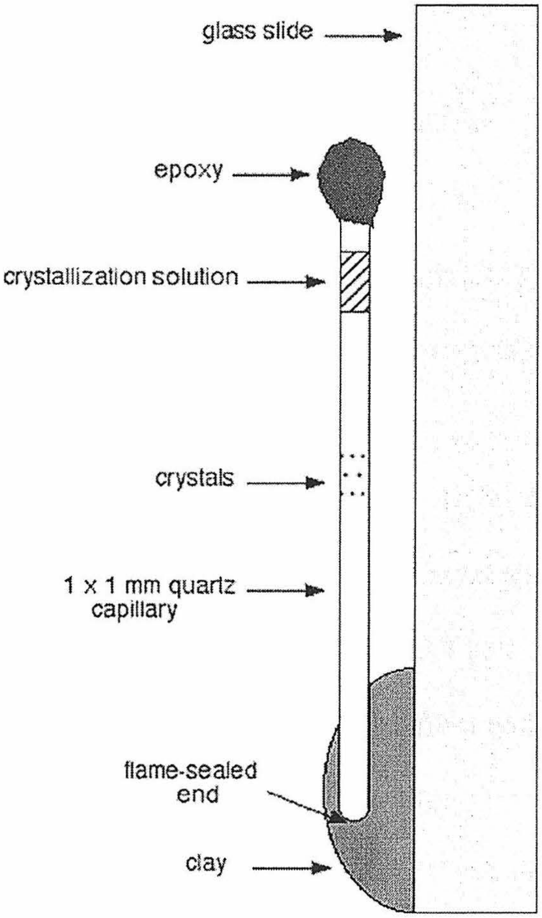

Figure 4.7. Illustration of the crystal mounting setup for transient absorption experiments.

the bottom of the solution. The crystallization solution was then carefully removed from the capillary first with the glass pipette and then a paper wick (Important note: Thorough removal of the solvent from around the crystals is necessary to prevent laser damage to the sample). The paper wick was also used to position the crystals (which are now in the middle of the capillary) onto the sides and away from the corners of the capillary, and to cluster them together as much as possible. Finally, a small amount of crystallization solution was added to the top of the capillary to avoid the desiccation of the crystals, followed by the sealing of the open end with epoxy (Figure 4.7).

Data collection

The transient absorption setup consisted of a Xe-arc lamp probe light source (Oriel 6263, 75 W), to reflecting objectives (Ealing, ×15 / 0.28) to focus (~ 20 μm diameter at the crystal sample) and collect the probe light, and a Nd:YAG pumped OPO laser (Spectra Physics) as the pump light source (Figure 4.8). 550 or 580-nm output from the OPO was used for the excitation of Zn-cyt *c* Q-bands. The excitation beam propagated colinearly with the probe light and focused onto the crystals (~ 100 –150 μM diameter at the sample). The probe and excitation beams were aligned using a metal plate with a small pinhole (~ 0.2 mm diameter). The excitation energy ranged from 0.4 to 9 mJ/pulse at the sample. The collected probe light was directed with an optical fiber and focused onto the aperture of an ISA monochromator (0.1 m) coupled to a 9-stage Hamamatsu photomultiplier tube (PMT). The PMT output was digitized (Sony/Tektronix digitizer RTD 710, 1 MΩ) and processed on a PC using a LabView program written by Dr. Brian Crane. The data were fit using a nonlinear least-squares fitting program

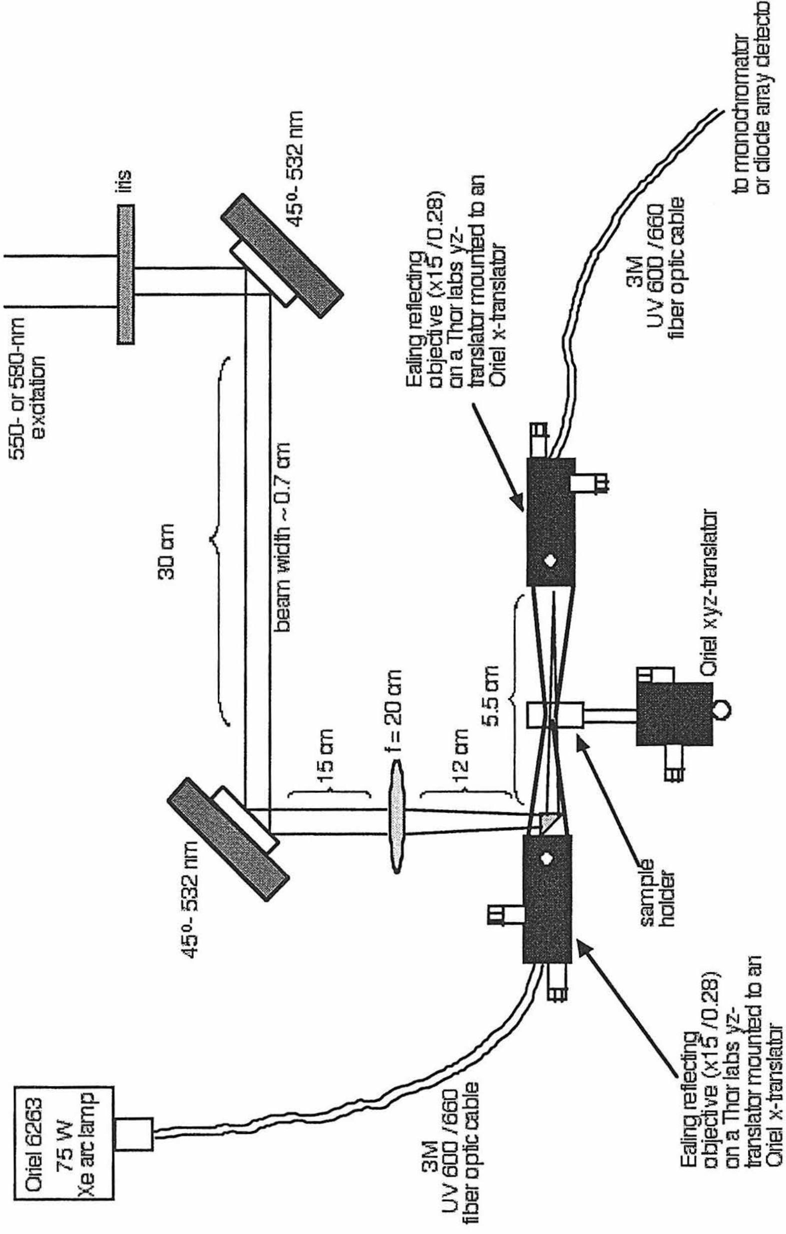

Figure 4.8. Sketch of the BILRC single-crystal transient absorption spectroscopy setup (not drawn to scale).

(Kinfit, Matlab version) written by Dr. Jay Winkler. Large crystals (≥ 50 μm (width) × 50 μm (depth)) consistently exhibited reproducible kinetics. When only smaller crystals were available, they were clustered together in order to minimize stray probe light. Generally, no visible damage to crystals by laser excitation was observed even at high pulse energies (≥ 4 mJ). Owing to the intense absorption of *Zn-cyt *c* or Zn-cyt c^+, extensive signal averaging was not necessary (≤ 25 shots at 470 nm and 675 nm). When monitoring fast kinetics (at 675 nm), a 15 or 100 kΩ terminator was used to shorten the digitizer response time. In those cases, more signal averaging (≥ 100 shots) was necessary due to increased noise.

Kinetics of electron transfer between Zn-cyt *c* and Fe-cyt *c* in solution

The kinetics of electron transfer between Zn-cyt *c* and Fe-cyt *c* (horse) in solution were measured using the transient absorption (TA) spectroscopy setup described in Chapter 2 (550-nm excitation). Horse Zn-cyt *c* was prepared following the protocol used for tuna Zn-cyt *c*. Samples were 10 μM Zn-cyt *c* and 125 to 1000 μM Fe(III)-cyt *c* in μ 0.1 M NaP_i buffer. They were thoroughly deaearated using repeated evacuation and Ar-fill cycles. *Zn-cyt *c* emission and Zn-cyt c^+ absorption were monitored at 470 and 675 nm, respectively. TA data were fit using Kinfit. The forward ET rate (reaction **R2** in Scheme 1) is equal to the slope in the plot of *Zn-cyt *c*-decay rate vs. Fe(III)-cyt *c* concentration (Equation 3):

$$*Zncytc \xrightarrow{k_1} Zncytc \qquad (1)$$

$$*Zncytc + Fe(III)cytc \xrightarrow{k_{R2}} Zncytc^+ + Fe(II)cytc \qquad (2)$$

$$k_{obs} = k_1 + k_{R2}[Fe(III)cytc] \qquad (3)$$

R2 generates equimolar amounts of Zn-cyt c^+ and Fe(II)-cyt *c*, which react to give ground-state species (**R3**) (Equation 4). The bimolecular rate for this is equal to the slope of 1/[Zn-cyt c^+] vs. time plot (Equation 6):

$$Zncytc^+ + Fe(II)cytc \xrightarrow{k_{R3}} Zncytc + Fe(III)cytc \qquad (4)$$

$$-\frac{d[Zncytc^+]}{dt} = k_{R3}[Zncytc^+][Fe(II)cytc] = k_{R3}[Zncytc^+]^2 \qquad (5)$$

Integration of (4) yields:

$$\frac{1}{[Zncytc^+]_t} = \frac{1}{[Zncytc^+]_0} + k_{R3}t \qquad (6)$$

The time course of [Zn-cyt c^+] was followed at 675 nm, where $\Delta\varepsilon_{\text{Zn-cyt } c+ - \text{Zn-cyt } c} \approx 13{,}000$ $M^{-1}cm^{-1}$(Figure 4.9).[23]

Results

Structural characterization of Zn:Fe-cyt *c* cocrystals by X-ray diffraction

The structures of 1Zn:2Fe- and 2Zn:1Fe-cyt *c* were determined at 1.5 Å and 2.0 Å resolution, respectively (Table 4.1). The structures are virtually identical to that of the native protein ($RMSD_{C\alpha}$ = 0.23 and 0.24 Å).[20,21] The final models have good stereochemistry ($RMSD_{bond} \leq$ 0.008 Å, $RMSD_{angle} \leq$ 1.4°), with most residues (93.0 and 90.7%) falling in the most favored regions in the Ramachandran plot (Table 4.1). It appears that His 18-Met 80 axial coordination of the metal is preserved in Zn-cyt *c*. As the occupancy of Zn-cyt *c* in the cocrystals is raised from 32% to 61%, the average $d_{\text{Met 80-metal}}$ increases from 2.44 Å to 2.50 Å, while $d_{\text{His 18-metal}}$ stays constant at 2.00 Å. This indicates that for Zn-only cyt *c*, $d_{\text{His 18-Zn}}$ = 2.00 Å and $d_{\text{Met 80-Zn}} \geq$ 2.50 Å.

Electron transfer kinetics in Zn:Fe-cyt *c* cocrystals

We initially looked for ET by measuring the decay kinetics of *Zn-cyt *c* using transient absorption spectroscopy. *Zn-cyt *c* has intense absorption in the 450 – 500-nm range, whereas the ground-state molecule does not (Figure 4.9). In pure Zn-cyt *c* crystals, the excited-state decay could be fit satisfactorily to a monoexponential function with a rate constant of ~ 80 s^{-1} (= k_{int}, intrinsic decay rate constant), similar to that measured in solution (Figure 4.10 A),[23] although a better fit is obtained with a biexponential function, yielding two rate constants, 380 s^{-1} (20%) and 70 s^{-1} (80%). We attribute the fast phase

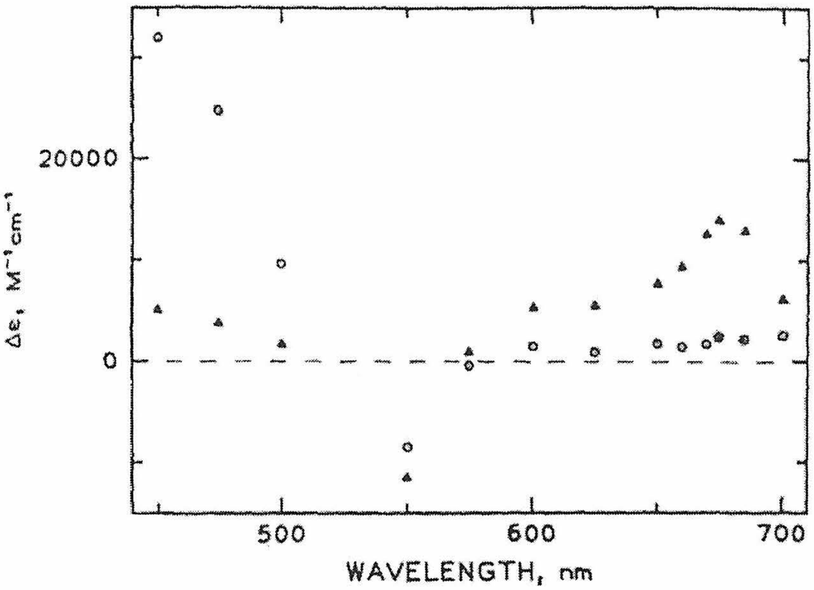

Figure 4.9. Molar difference spectra of *Zn-cyt *c* / Zn-cyt *c* (o) and Zn-cyt c^+ / Zn-cyt *c* (Δ). Adapted from Elias et al., *J. Am. Chem. Soc.* **1988**, *110*, 429-434.

to triplet-triplet energy transfer between neighboring Zn-cyt *c* molecules in the crystal lattice. Zemel and Hoffman reported fast *Zn-porphyrin decay at high pulse energies attributable to triplet-triplet energy transfer between the metal centers in the α- and β-subunits of Zn-hemoglobin (24.1 Å metal-metal separation).[29] In accordance with this observation, we have found that the amplitude of the fast decay channel in pure Zn-cyt *c* crystals grew with increasing pulse energy, reaching 35% at 9 mJ/pulse (Figure 4.11). At the typical pulse energies (< 800 μJ) employed in our experiments, however, this amplitude never exceeded 20%.

In Fe(III):Zn-cyt *c* cocrystals, the *Zn-cyt *c* decay is considerably faster than that in pure Zn-cyt *c* crystals and can only be described by a biexponential fit (Figure 5.10 A). We assign the fast phase ($k_{fast} = 400 \pm 100$ s^{-1}) to ET from *Zn-cyt *c* to Fe(III)-cyt *c* (**R2**), where the electron tunneling rate ($k_{ET} = k_{fast} - k_{int}$) is 320 s^{-1}. The slower phase ($k_{slow} = 70 \pm 20$ s^{-1}) closely matches the intrinsic decay of *Zn-cyt *c*, consistent with a distribution of

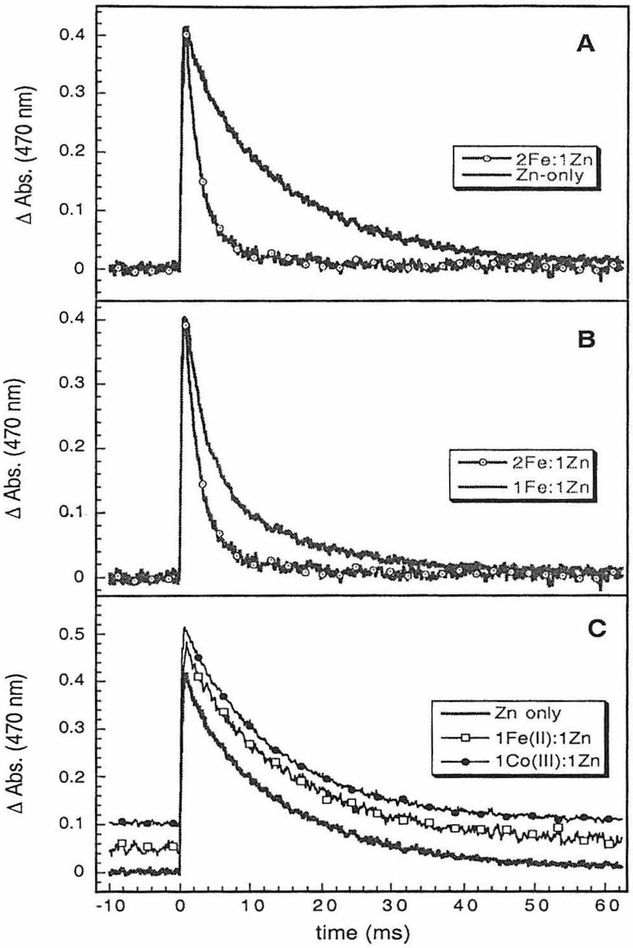

Figure 4.10. *Zn-cyt *c* decay kinetics monitored at 470 nm. Δ absorbances are normalized. **(A)** Pure Zn-cyt *c* (green); 2Fe(III):1Zn-cyt *c* (red). **(B)** 2Fe(III):1Zn-cyt *c* (red); 1Fe(III):1Zn-cyt *c* (purple). **(C)** Pure Zn-cyt *c* (green); Fe(II):Zn-cyt *c* (black); Co(III):Zn-cyt *c* (blue). The second and third traces are offset for clarity.

cyt *c* molecules in the crystals, which would allow a fraction of Zn-cyt *c* molecules to be adjacent to only two other Zn-molecules and hence decay without undergoing an ET process. Accordingly, the amplitude of the slow phase grows relative to the fast phase as the Zn-cyt *c* fraction in the cocrystals increases; for the 2Fe(III):1Zn-cyt *c* crystals, the fast phase amplitude is ~ 90% of the total, whereas it is 65% for the1Fe(III):1Zn-cyt *c* crystals (Figure 4.10 B). No power dependence of the excited-state decay was observed in Fe(III):Zn-cyt *c* cocrystals (Figure 4.11 B), indicating that the contribution of triplet-triplet energy transfer to the fast decay kinetics was negligible. On the other hand, in Zn-

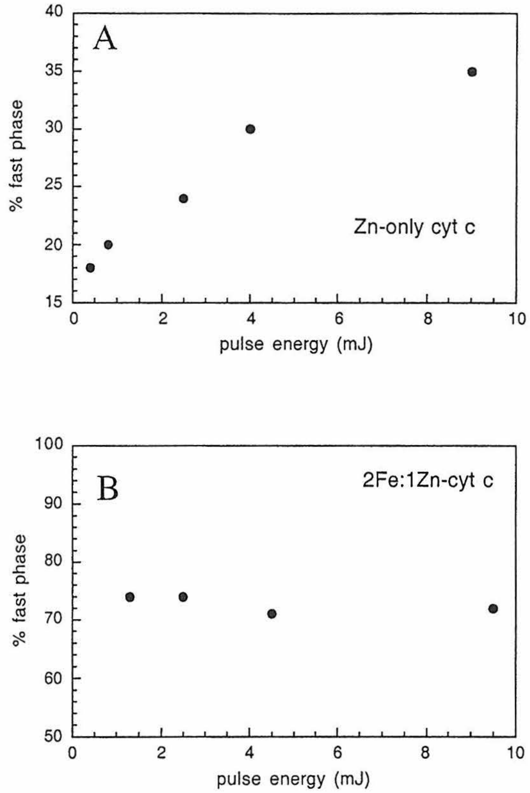

Figure 4.11. Dependence of the fast phase amplitude (in 470 nm TA kinetics) on the excitation energy. **(A)** Zn-only cyt *c*, **(B)** 2Fe:1Zn-cyt *c*. The increase in fast phase amplitude in Zn-only crystals with increasing energy is consistent with triplet-triplet energy transfer between neighboring Zn-cyt *c* molecules in crystals.

only cyt *c* crystals, where energy transfer is significant, the fast phase amplitude grows with increasing excitation power (Figure 4.11 A).

In parallel with the amplitude, the rate constant for the fast phase in the cocrystals also grows (from 350 s^{-1} for 1Fe:2Zn-cyt *c* up to 510 s^{-1} with 2Fe:1Zn-cyt *c* cocrystals) as the relative Fe(III)-cyt *c* concentration is increased. This observation is consistent with an increase in the fraction of Zn-cyt *c* molecules adjacent to two Fe-cyt *c* molecules (instead of one), whose excited-state decay rate ($k_{fast,2}$) should be faster by k_{ET} ($k_{fast,2} \approx 2 k_{ET} + k_{int}$). Although the observed decay kinetics should be described by a triexponential function, it has not been possible to extract statistically significant values of k_{fast} and $k_{fast,2}$

from fits to the single-crystal ET kinetics. Instead, increasing contributions from $k_{fast,2}$ leads to larger values for the k_{fast} component in the biexponential fits.

While the quenching of *Zn-cyt *c* decay in Zn:Fe(III)-cyt *c* cocrystals is good evidence for ET, it does not provide absolute proof. Due to strong absorption by Fe(III)-cyt *c* in the 520 – 620-nm range and the intense Zn-cyt *c* fluorescence, Förster energy transfer may be operative, giving rise to rapid *Zn-cyt *c* decay. As controls, we examined Fe(II):Zn-cyt *c* and Co(III):Zn-cyt *c* cocrystals. Fe(II)- and Co(III)-cyt *c* have similar absorption spectra as the Fe(III)-protein, thus the extent of Förster energy transfer in these cocrystals should be comparable to that in Zn:Fe(III)-cyt *c* cocrystals. On the other hand, ET in the former case is thermodynamically disfavored, and in the latter there is a large barrier, owing to a high Co(III/II) reorganization energy (> 2.4 eV).[30] We found that *Zn-cyt *c* decay in both cases was slow and monoexponential, with rate constants (68 s^{-1} for Fe(II) and 78 s^{-1} for Co(III)) that are essentially the same as those observed in pure Zn-cyt *c* crystals (Figure 4.10 C). This finding indicates that the quenching of *Zn-cyt *c* decay in Zn:Fe(III)-cyt *c* cocrystals is most likely due to ET.

The search for ET products proved to be difficult: first, absorbance measurements in the Soret region are precluded in crystals ([protein] ≈ 75 mM), owing to high extinction coefficients ($abs_{424} \approx 65$ for a 50 μm thick crystal); second, Fe(II)-cyt *c* formation in the Q-band region is difficult to monitor, as the isosbestic point for Zn-cyt *c* and *Zn-cyt *c* (540 nm) coincides with that for Fe(II)- and Fe(III)-cyt *c*. Our efforts to detect Zn-cyt c^+ were successful, because in the deep red region of the spectrum the molar absorbance of this cation radical greatly exceeds that of *Zn-cyt *c* (Figure 4.9).[23] The transient kinetics probed at 675 nm reveal a prompt absorbance increase due to *Zn-

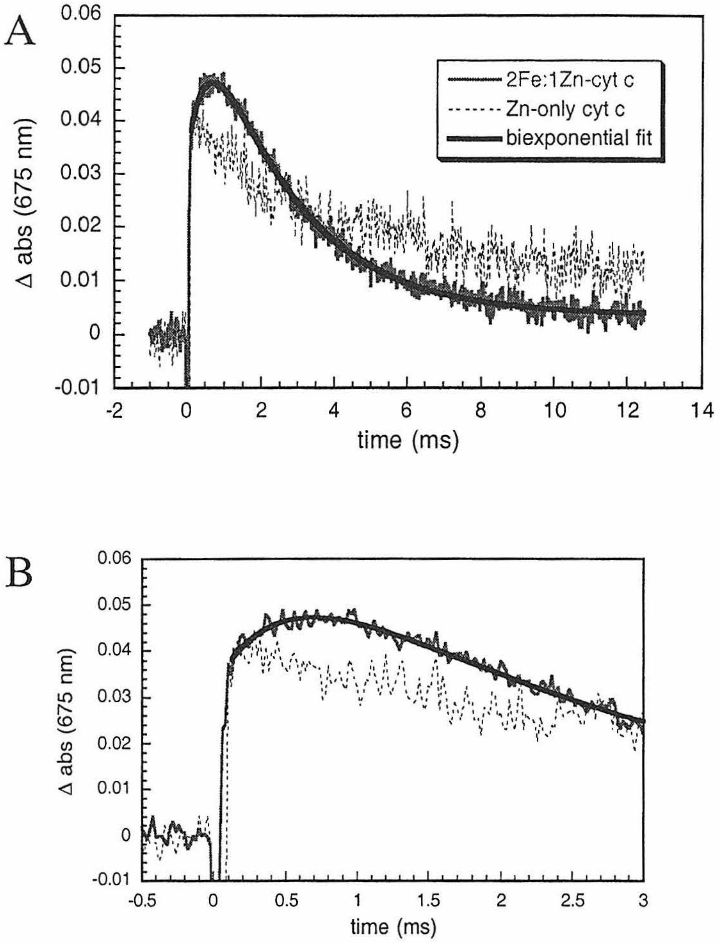

Figure 4.12. Transient absorption (675 nm) kinetics. **(A)** The signal rise in pure Zn-cyt *c* crystals (blue-dotted) is instantaneous due to the generation of the triplet excited state,*Zn-cyt *c*; in 2Fe:1Zn-cyt *c* cocrystals (red-solid), there is an additional rise attributable to the Zn-porphyrin cation radical, Zn-cyt c^+. The negative signal following the laser flash results from *Zn-cyt *c* fluorescence. **(B)** A view of early TA kinetics from 2Fe:1Zn-cyt *c* cocrystals showing the rounded feature.

cyt *c* formation, followed by a slower rise corresponding to production of Zn-cyt c^+ (Figure 4.12). The time constant for the subsequent decay of the 675 nm absorbance matches that measured at 470 nm (Figure 4.10), indicating that charge recombination (**R3**) is faster than charge separation (**R2**). A biexponential fit to the 675-nm data yields the following rate constants: 400 ± 100 s^{-1} ($k_{ET} = 320\ s^{-1}$) for **R2**; and 2000 ± 500 s^{-1} for **R3**. The finding that **R3** ($\Delta G \approx -0.65$ eV) is faster than **R2** ($\Delta G \approx -1.05$ eV) despite an apparently lower driving force has been observed previously in other Zn-porphyrin systems.[31] We believe that this discrepancy is most likely due to uncertainties in the redox potentials of *Zn-cyt *c* and Zn-cyt c^+, although there may also be differences in donor-acceptor coupling in **R2** and **R3**.

Kinetics of electron transfer between Zn- and Fe(III)-cyt *c* in solution

We have investigated the kinetics of electron transfer between Zn- and Fe(III)-cyt *c* (horse) in solution (μ 0.1 M) using transient absorption spectroscopy. In analogy to the measurements in crystals, ET was monitored by changes in *Zn-cyt *c* and Zn-cyt c^+ absorbances at 470 and 675 nm, respectively. As expected under pseudo-first order conditions, the decay rate of *Zn-cyt *c* grows linearly with increasing Fe(III)-cyt *c* concentration (Equation 3 and Figure 4.13 A). The analysis of *Zn-cyt *c*-decay yields a

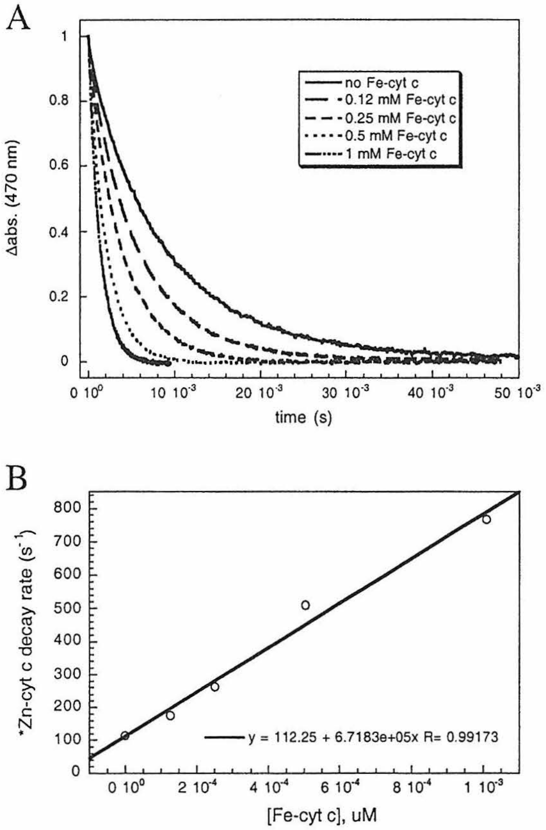

Figure 4.13. Quenching of *Zn-cyt *c* (horse) by Fe(III)-cyt *c* (horse) in solution under pseudo-first order conditions (μ 0.1 M). **(A)** Transient absorption traces, **(B)** Stern-Volmer plot. The higher-than-expected decay rate of *Zn-cyt *c* (110 $M^{-1}s^{-1}$) at [Fe-cyt *c*] = 0 is possibly due to the presence of impurities resulting from the photodegradation of Zn-cyt *c*.

bimolecular rate constant of 7 ± 1 x 10^5 $M^{-1}s^{-1}$for the forward ET reaction (**R2**) (Figure 4.13 B). In comparison, the self-exchange rate ($\Delta G^\circ = 0$ eV) of horse Fe-cyt *c* at a similar ionic strength (μ 0.12 M) is 5.4×10^3 s^{-1}.[32] Charge recombination (**R3**) involves the reaction of equimolar concentrations of Zn-cyt c^+ and Fe(II)-cyt *c*. The rate constant for this reaction is obtained from the slope of the 1/[Zn-cyt c^+] vs. time plot (Figure 4.14), where [Zn-cyt c^+] can be calculated using $\Delta\varepsilon_{675(\text{Zn-cyt } c+ - \text{ Zn-cyt } c)} \approx 13{,}000$ $M^{-1}cm^{-1}$ (Figure 4.9).[23] As seen in crystals, the charge recombination rate constant, 1.0 (2) $\times 10^7$ $M^{-1}s^{-1}$, is approximately tenfold faster than that for the forward ET, indicating

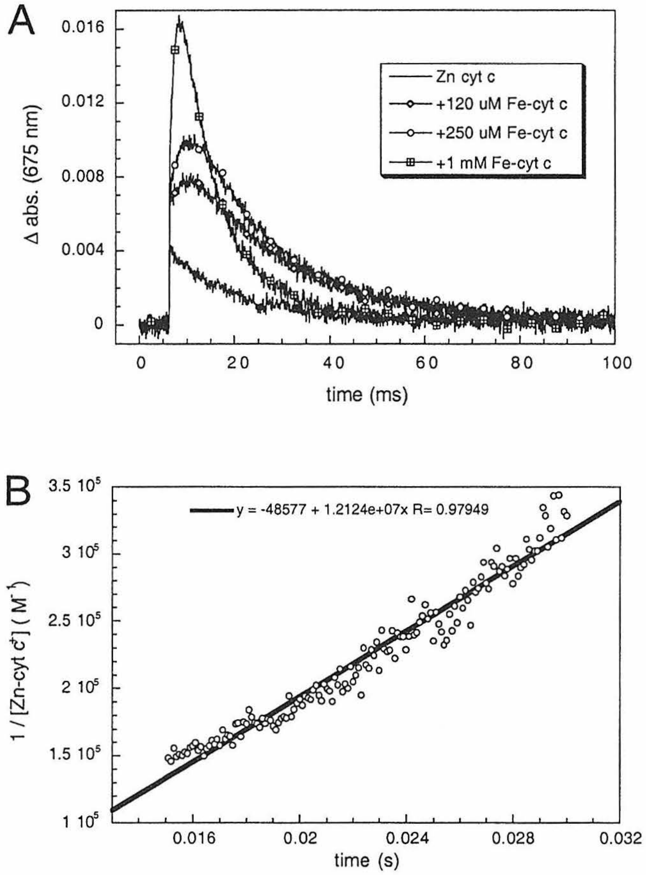

Figure 4.14. **(A)** Solution kinetics of Zn-cyt c^+ formation and decay monitored at 675 nm. The yield and the rate of Zn-cyt c^+ formation, as well its decay, increases as [Fe(III)-cyt *c*] concentration is increased. **(B)** 1/[Zn-cyt c^+] vs. time plot ([Fe(III)-cyt *c*] = 250 μM), whose slope yields the rate constant for the charge recombination reaction according to Equation 5. The plot was started at 15 μs, when *Zn-cyt *c* has almost completely decayed (see Figure 4.13 B).

that the activation free energy in crystals does not differ significantly from that in solution. According to semiclassical theory, the activation free energy, $\Delta G^{\ddagger}$, is equal to $-(\Delta G^{o} + \lambda)^{2}/4\lambda$, where λ is the nuclear reorganization energy for the reaction and ΔG^{o} is the driving force.[1] While compensating variations in ΔG^{o} and λ (simultaneous increase or decrease in both parameters) could result in similar $\Delta G^{\ddagger}$ values in crystals and solution, it is more likely that they do not vary.

Discussion

Rapid relay of electrons by redox enzymes necessarily involves short-lived, weakly bound protein-protein complexes. The recognition sites between proteins in such complexes tend to be smaller (<1200 Å^2) and include more water molecules than the interfaces between subunits in oligomeric proteins.[33] In fact, the protein-protein interface between the natural redox partners cyt *c* and cytochrome *c* peroxidase (CcP) (770 Å^2)[34] is very small compared to other interfaces; there are 17 van der Waals contacts, 13 water molecules (two of which form bridging hydrogen bonds across the interface), but only one direct hydrogen bond bridging the two proteins. The interprotein interactions in crystals of tuna cyt *c* are similar (Figure 4.15): 760 Å^2 of surface area is buried in an interface with 31 van der Waals contacts, 16 water molecules (3 bridging), and one direct hydrogen bond. In addition, a heme vinyl group makes direct contacts across the interface in both the cyt *c* -cyt *c* and the CcP-cyt *c* complexes. Electron tunneling across hydrogen bonded interfaces is well established; hydrogen bonds have been shown to provide electronic coupling comparable to σ-bonded frameworks.[35-37] Similarly, coupling across one or two water molecules (< 5 Å) should not be much weaker than that over a

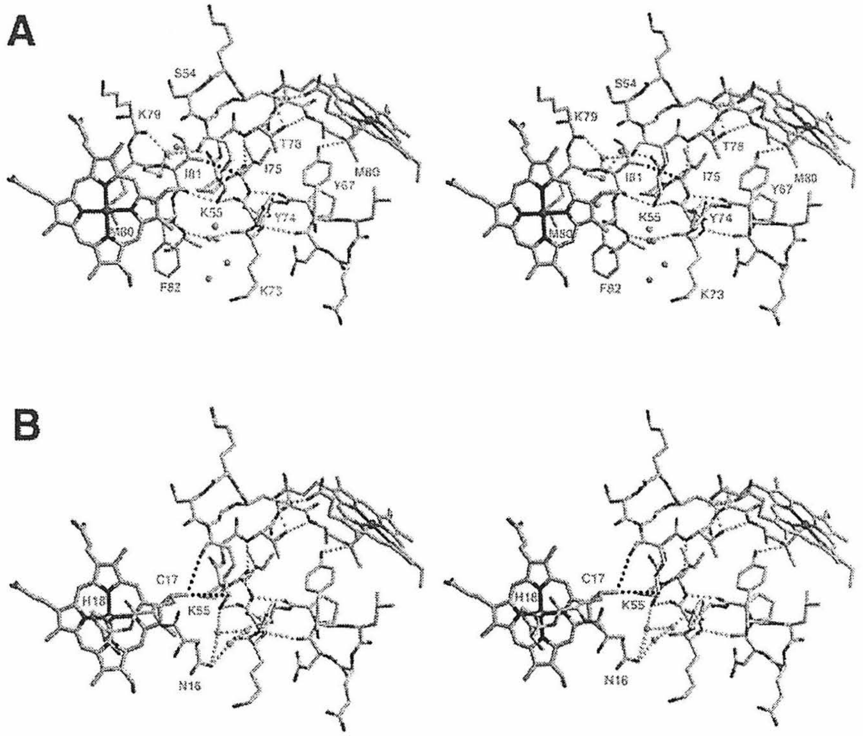

Figure 4.15. Stereoview of heme groups in Zn:Fe-cyt *c* cocrystals (brown) and the intervening protein and solvent medium. Blue spheres indicate water molecules in the protein-protein interface region. Selected hydrogen bonds and short van der Waals contacts are depicted as yellow and black traces, respectively. Residues belonging to different proteins are colored in green and gray. Residues below **(A)** and above **(B)** the heme plane on the left-hand side are shown separately. The sidechain and main-chain atoms of 14 residues on each molecule participate in the interface, burying 400 Å of solvent accessible surface area on Mol$_i$ and 360 Å on Mol$_{i+1}$. Close contacts in the interface include those between Ile 81$_i$ and Ile 75$_{I+1}$, and the heme vinyl$_i$ and Lys 55$_{i+1}$. The sidechain of Lys 55$_{i+1}$ and the peptide carbonyl of Ile 81$_I$ form the only direct protein-protein hydrogen bond. Water-bridged hydrogen bonds link the main-chain of Phe 82$_i$ to that of Lys 73$_{i+1}$, the sidechain of Asp 16$_i$ to that of Lys 55$_{i+1}$, and the main chain of Ile 81$_i$ to both the main-chain and sidechain of Lys 55$_{i+1}$. Furthermore, a series of two or more water molecules mediate additional hydrogen bonds between interfacial residues.

comparable distance of peptide (Figure 4.16).[38] We have found that the interprotein ET rates for **R2** and **R3** fall well within the range that has been established for Ru-proteins with similar donor-acceptor separations (intraprotein ET) (Figure 4.16),[22,38,39] indicating that small protein-protein interfaces, such as that between Zn-cyt *c* and Fe-cyt *c*, are quite effective in mediating redox reactions.

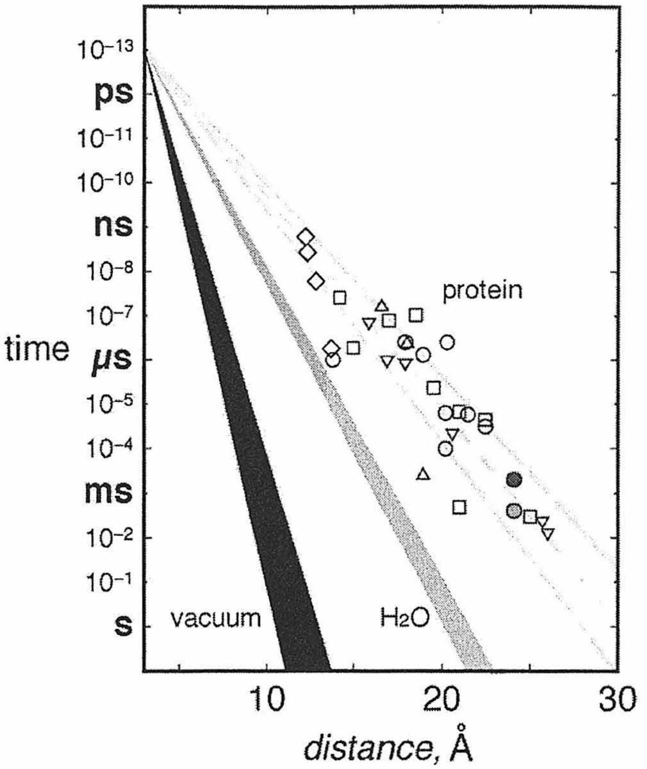

Figure 4.16. Electron tunneling timetable in Ru-modified proteins (open symbols), water (blue, β = 1.61 – 1.75 $Å^{-1}$) and vacuum (dark blue, β = 3.0 – 4.0 $Å^{-1}$) (adapted from Ponce et al., *J. Am. Chem. Soc.* **2000**, *122*, 8187-8191). Most coupling-limited electron tunneling times in proteins (cytochrome *c* (o); azurin (∇); cytochrome b_{562} ( ); myoglobin (Δ); high-potential iron-sulfur protein (◊)) fall in the 1.0-1.2 $Å^{-1}$ wedge (pale blue solid lines; average β of 1.1 $Å^{-1}$ is the pale blue dashed line). Colored circles (*Zn-cyt *c* → Fe(III)-cyt *c*, green; Fe(II)-cyt *c* → Zn-cyt c^{+}, red) are interprotein ET time constants.

It is universally believed the surface topology and charge distribution of a redox protein are crucial in its recognition of other proteins and proper docking.[11,40] Yet, it is not known whether nature has selected for surface residues also on the basis of their ability to promote efficient electronic coupling across interfaces. Our findings offer an insight into this question. The protein-protein docking geometry observed in the crystals of cyt *c* is not relevant for its biological redox reactions. In fact, cyt *c* is thought to interact with its natural redox partners, such as CcP[11,40] and cytochrome bc_1 complex,[41] through the positively charged, Lys-rich surface patch surrounding its exposed heme

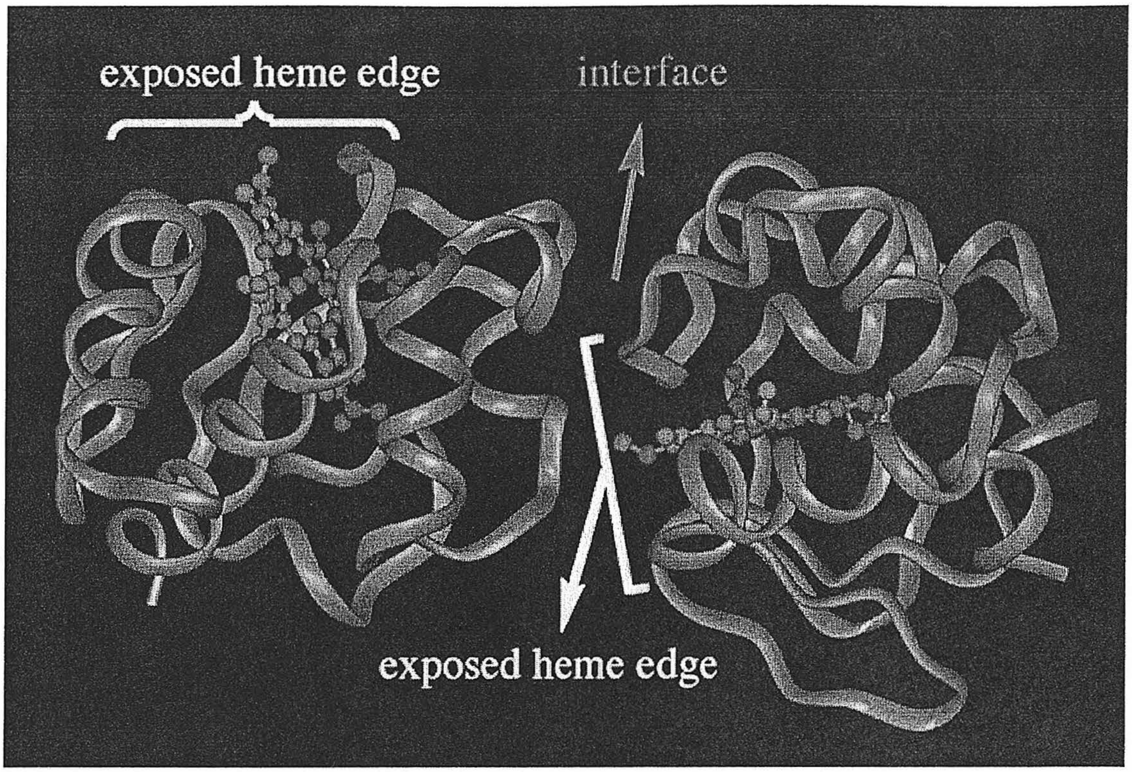

Figure 4.17. Relative orientation of cyt *c* molecules involved in electron transfer in the crystal lattice.

edge. While one molecule in the cyt *c*-cyt *c* complex contributes part of this patch to the interface, the other molecule has its exposed heme edge oriented away from it (Figure 4.17). The fact that a non-biological interface can support efficient electronic tunneling provides strong evidence that the selection of surface residues is primarily based on recognition and docking.

Conclusions

Crystal lattices offer a unique environment where molecules are held in fixed and structurally-definable orientations. This molecular order, absent in the solution phase, provides great advantages in manipulating chemical reactions, as well as studying their mechanisms.[42] Especially in the field of organic chemistry, there has been a growing interest in using crystals to achieve stereo- and regioselective synthesis, and obtaining structural information on the progress of reactions.[43-45] By integrating photosensitizers into protein crystals we have extended the scope of crystal-phase chemistry to proteins. The employment of Zn-porphyrin redox photochemistry is especially well-suited for investigations of interprotein electron tunneling in heme proteins.

The applications of this methodology could extend well beyond the bounds of interprotein ET kinetics. Zn-cyt *c* should be an excellent optical trigger for time-resolved X-ray crystallography, a technique that requires rapid and efficient initiation of a reaction throughout the X-ray beam cross-section in the sample.[46,47] The long-lived, strongly reducing triplet excited state ($\phi_{\mathrm{triplet}} = 0.9$)[48] of Zn-cyt *c* leads to high quantum yields for ET ($\phi_{\mathrm{ET}} \approx 0.8$ in our system).[49] Introduction of Zn-porphyrins thus creates opportunities to probe redox-induced structural changes and catalytic intermediates in protein crystals.

References

(1) Gray, H. B.; Winkler, J. R. (1996) *Annu. Rev. Biochem.* **65**, 537-561; Winkler, J. R., DiBilio, A. J., Farrow, N. A., Richards, J. H.; Gray, H. B. (1999) *Pure Appl. Chem.* **71**, 1753-1764; Winkler, J. R. (2000) *Curr. Op. Chem. Biol.* **4**, 192-198.

(2) Langen, R.; Chang, I.-J.; Germanas, J. P.; Richards, J. H.; Winkler, J. R.; Gray, H. B. *Science* **1995**, *268*, 1733-1735.

(3) Mei, H.; Wang, K.; Peffer, N.; Weatherly, G.; S., C. D.; Miller, M.; Pielak, G. J.; Durham, B.; Millett, F. *Biochemistry* **1999**, *38*, 6846-6854.

(4) Farver, O.; Pecht, I. *JBIC* **1997**, *2*, 387-392.

(5) Dick, L. A.; Malfant, I.; Kuila, D.; Nebolsky, S.; Nocek, J. M.; Hoffman, B. M.; Ratner, M. A. *J. Am. Chem. Soc.* **1998**, *120*, 11401-11407.

(6) Beratan, D. N., Betts, J. N.; Onuchic, J. N. (1991) *Science* **252**, 1285-1288; Onuchic, J. N., Beratan, D. N., Winkler, J. R.; Gray, H. B. (1992) *Annu. Rev. Biophys. Biomol. Struct.* **21,** 349-377; Beratan, D. N.; Skourtis, S. S. (1998) *Curr. Op. Chem. Biol.* **2,** 235-243.

(7) Daizadeh, I.; Gehlen, J. N.; Stuchebrukhov, A. A. *J. Chem. Phys.* **1997**, *106*, 5658-5666.

(8) Moser, C. C.; Keske, J. M.; Warncke, K.; Farid, R. S.; Dutton, P. L. *Nature* **1992,** *355*, 796-802.

(9) Williams, R. J. P. *JBIC* **1997**, *2*, 373-377.

(10) McLendon, G.; Hake, R. *Chem. Rev.* **1992**, *92*, 481-490.

(11) Nocek, J. M.; Zhou, J. S.; De Forest, S.; Priyadarshy, S.; Beratan, D. N.; Onuchic, J. N.; Hoffman, B. M. *Chem. Rev.* **1996**, *96*, 2459-2489.

(12) Davidson, V. L. *Acc. Chem. Res.* **2000**, *33*, 87-93.

(13) Pletneva, E. V.; Fulton, D. B.; Kohzuma, T.; Kostic, N. M. *J. Am. Chem. Soc.* **2000**, *122*, 1034-1046.

(14) Liang, Z. X.; Nocek, J. M.; Kurnikov, I. V.; Beratan, D. N.; Hoffman, B. M. *Journal of the American Chemical Society* **2000**, *122*, 3552-3553.

(15) The crystal structures of several multidomain proteins, such as cytochrome c oxidase (Iwata et al., *Nature* **1995**, *376*, 660-669; Tsukihara, et al., *Science* **1996,** *272*, 1136-1144), flavocytochrome b_2 (Xia, Z.-X; Mathews, F. S., *J. Mol. Biol.* **1990,** *212*, 837-863), Mg/Fe hemoglobin (Kuila et al., *J. Am. Chem. Soc.* **1991,** *113*, 6520-6526),

and FMN-cytochrome P450BM-3 (Sevrioukova, I. F.; Hazzard, J. T.; Tollin, G.; Poulos, T. L., *J. Biol. Chem.* **1999,** *274*, 36097-36106) have been determined at high resolution; intersubunit ET kinetics in these proteins have also been investigated extensively. These multidomain proteins are distinct from protein-protein complexes because the intersubunit interactions in the former are much more extensive and lead to tight association.

(16) Pelletier, H.; Kraut, J. *Science* **1992**, *258*, 1748-1755.

(17) Chen, L.; Durley, R. C. E.; Mathews, F. S.; Davidson, V. L. *Science* **1994**, *264*, 86-90.

(18) Sevrioukova, I. F.; Li, H.; Zhang, H.; Peterson, J. A.; Poulos, T. L. *Proc. Natl. Acad. Sci. USA* **1999**, *96*, 1863-1868.

(19) Feher and colleagues have measured the kinetics of photoinduced ET between the photosynthetic reaction center and cyt c_2 (*R. sphaeroides*) complexed in crystals (Adir et al., *Biochemistry* **1996,** *35,* 2535-2547. However, the low resolution (3.5 Å) of this structure and poor cyt c_2 electron density did not allow a precise definition of the polypeptide and solvent medium between the electron donor (cyt c_2 heme) and the acceptor (bacteriochlorophyll dimer).

(20) Swanson, R.; Trus, B. L.; Mandel, N.; Kallai, O. B.; Dickerson, R. E. *J. Biol. Chem.* **1977**, *257*, 759-775.

(21) Takano, T.; Dickerson, R. E. *Proc. Natl. Acad. Sci. USA* **1980**, *77*, 6371.

(22) Gray, H. B.; Winkler, J. R. *Annu. Rev. Biochem.* **1996**, *65*, 537-561.

(23) Elias, H.; Chou, M. H.; Winkler, J. R. *J. Am. Chem. Soc.* **1988**, *110*, 429-434.

(24) Otwinowski, Z.; Minor, W. *Methods Enzymol.* **1997**, *276*, 307-326.

(25) Brünger, A. T.; Adams, P. D.; Clore, G. M.; DeLano, W. L.; Gros, P.; Grosse-Kunstleve, R. W.; Jiang, J. S.; Kuszewski, J.; Nilges, M.; Pannu, N. S.; Read, R. J.; Rice, L. M.; Simonson, T.; Warren, G. L. *Acta Crystallogr. Sect. D-Biol. Crystallogr.* **1998**, *54*, 905-921.

(26) McRee, D. *J. Mol. Graphics* **1992**, *10*, 44-46.

(27) Laskowski, R. A.; Macarthur, M. W.; Moss, D. S.; Thornton, J. M. *J. Appl. Crystallogr.* **1993**, *26*, 283-291.

(28) Crane, B. R.; Getzoff, E. D. *Acta Crystallogr. D* **1997**, *53*, 23-40.

(29) Zemel, H.; Hoffman, B. M. *J. Am. Chem. Soc.* **1981**, *103*, 1192-1201.

(30) Sun, J.; Su, C.; Wishart, J. F. *Inorg. Chem.* **1996**, *35*, 5893-5901.

(31) Liang, N.; Kang, C. H.; Ho, P. S.; Margoliash, E.; Hoffman, B. M. *J. Am. Chem. Soc.* **1986**, *108*, 4665-4666.

(32) Dixon, D. W.; Hong, X.; Woehler, S. E. *Biophys. J.* **1989**, *56*, 339-351.

(33) Lo Conte, L.; Chothia, C.; Janin, J. *J. Mol. Biol.* **1999**, *285*, 2177-2198.

(34) Connolly, M. L. *Science* **1983**, *221*, 709-713.

(35) de Rege, P. J. F.; Williams, S. A.; Therien, M. J. *Science* **1995**, *269*, 1409-1413.

(36) Kirby, J. P.; Roberts, J. A.; Nocera, D. G. *J. Am. Chem. Soc.* **1997**, *119*, 9230-9236.

(37) Yang, J.; Seneviratne, D.; Arbatin, G.; Andersson, A. M.; Curtis, J. C. *J. Am. Chem. Soc.* **1997**, *119*, 5329-5336.

(38) Ponce, A.; Gray, H. B.; Winkler, J. R. *J. Am. Chem. Soc.* **2000**, *122*, 8187-8191.

(39) This comparison was made with the assumption that the driving forces, ΔG^o, for R2 and R3 are close to the activationless limit, where ΔG^o equals the reorganization

energy, λ ($\lambda_{\text{cyt c}} \approx 1$ eV). In any case, our values are lower limits for activationless ET due to the parabolic dependence of ET rate on driving force.

(40) Northrup, S. H. In *Cytochrome c: A Multidisciplinary Approach*; Scott, R. A., Mauk, A. G., Eds.; University Science Books: Sausalito, 1996; pp 543-570.

(41) Tian, H.; Sadoski, R.; Zhang, L.; Yu, C.-A.; Yu, L.; Durham, B.; Millett, F. *J. Biol. Chem.* **2000**, *275*, 9587-9595.

(42) Schmidt, G. J. M. *Pure Appl. Chem.* **1971**, *27*, 647.

(43) Kim, J. H.; Hubig, S. M.; Klindeman, S. V.; Kochi, J. K. *J. Am. Chem. Soc.* **2000**, *122*, in press.

(44) Kodani, T.; Matsuda, K.; Yamada, T.; Kobatake, S.; Irie, M. *J. Am. Chem. Soc.* **2000**, *122*, 9631.

(45) Garcia-Garibay, M. A.; Shin, S.; Sanrame, C. N. *Tetrahedron* **2000**, *56*, 6729.

(46) Ren, Z.; Bourgeois, D.; Helliwell, J. R.; Moffat, K.; Srajer, V.; Stoddard, B. L. *J. Synchotron Rad.* **1999**, *6*, 891-917.

(47) Schlichting, I. *Acc. Chem. Res.* **2000**, *33*, 532-538.

(48) Dixit, B. P. S. N.; Moy, V. T.; Vanderkooi, J. M. *Biochemistry* **1984**, *23*, 2103-2107.

(49) $\phi_{ET} = (k_{ET}/(k_{ET} + k_{int}) = 320\ s^{-1} / 400\ s^{-1} = 0.8$, where $k_{int}$is the intrinsic decay rate of *Zn-cyt *c*.

Appendix A

Photodisproportionation of $Ru(bpy)_3^{2+}$. Reduction of cyt *c* and MP8 by $Ru(bpy)_3^{1+}$

As illustrated in Figure 3.4, we have used $Ru(bpy)_3^{2+}$-redox photochemistry to initiate the folding of cyt *c*. The most important advantages that $Ru(bpy)_3^{2+}$ provides in this context are its strongly reducing ($E_o = -0.84$ V) MLCT-excited state, and the reversibility of its photochemistry that allows extensive signal averaging (T. Pascher, J.P. Chesick, J. R. Winkler, H. B. Gray, *Science*, **271**, 1558 – 1560). The excited state species ($*Ru(bpy)_3^{2+}$) has a lifetime of 600 ns, implying that electron transfer to oxidized, unfolded cyt *c* has to be achieved within this timescale. $*Ru(bpy)_3^{2+}$ is quenched by unfolded Fe(III)-cyt *c* with a rate constant of ~ 10^9 $M^{-1}s^{-1}$ (Figure A.1).

During folding experiments using $Ru(bpy)_3^{2+}$ as a photoreductant, we observed a kinetics phase with a time-constant of ~ 10 μs (Figure A.2). We initially attributed this phase to a ligand-substitution process coupled to folding, as any spectral change due to reduction was assumed to occur within a microsecond. Interestingly, the kinetics of this phase were dependent on protein concentration, which is not consistent with a folding process (folding of cyt *c* is unimolecular). The Stern-Volmer plot for this phase exhibits a linear concentration dependence, yielding a bimolecular rate constant of ~ 10^9 $M^{-1}s^{-1}$(Figure A.3). Moreover, a similar concentration-dependent phase was also observed with the imidazole-adduct of AcMP8 (Figures A.3, A.4 and A.5), which cannot undergo folding and thus is not subject to folding-coupled ligand substitution processes. Upon careful examination of the transient absorption spectra, it became clear that the changes were consistent with secondary reduction of cyt *c* via an unknown reductant. We suspected that this reductant may be $Ru(bpy)_3^{1+}$ ($E_o = -1.25$ V), generated by the disproportionation of $*Ru(bpy)_3^{2+}$.

$$2 * Ru(bpy)_3^{2+} \xrightarrow{k_{disprop.}} Ru(bpy)_3^{1+} + Ru(bpy)_3^{3+}$$

Due to the bimolecular nature of this reaction, the decay of $^*\mathrm{Ru(bpy)}_3^{2}$ can no longer be described by a mono-exponential function, especially at high concentrations. This is exactly what we have observed (Figure A.6): while at low $[^*\mathrm{Ru(bpy)}_3^{2}]$ the luminescence can be satisfactorily fit to a single exponent, significant deviations are apparent at high $[^*\mathrm{Ru(bpy)}_3^{2}]$. Following reactions and rate expression can be used to describe the decay of $^*\mathrm{Ru(bpy)}_3^{2}$:

$$^*\mathrm{Ru(bpy)}_3^{2+} \xrightarrow{k_1} \mathrm{Ru(bpy)}_3^{2+}$$

$$2\ ^*\mathrm{Ru(bpy)}_3^{2+} \xrightarrow{k_2} \mathrm{Ru(bpy)}_3^{1+}\ \mathrm{Ru(bpy)}_3^{3+}$$

$$\frac{-d[^*\mathrm{Ru(bpy)}_3^{2+}]}{dt} = k_1\,[^*\mathrm{Ru(bpy)}_3^{2+}] + k_2\,[^*\mathrm{Ru(bpy)}_3^{2+}]^2$$

This rate equation can be integrated to yield (from "Chemical Kinetics and Reaction Mechanisms" by J. H. Espenson, 2nd Edition, 1995, pp 34 – 35, McGraw Hill):

$$[^*Ru^{2+}]_t = \frac{k_1[^*Ru^{2+}]_o e^{-(k_1 t)}}{k_1 + k_2[^*Ru^{2+}]_o[1 - e^{-(k_1 t)}]}$$

The luminescence decays at high $[^*\mathrm{Ru(bpy)}_3^{2+}]$ are indeed perfectly described by this expression (Figure A.7), yielding $k_1 = 1.45 \times 10^6\ \mathrm{s}^{-1}$ (= intrinsic decay rate) and $k_2 = 2 \times 10^9\ \mathrm{s}^{-1}$ (= rate of disproportionation).

The simultaneous generation of Ru(I) and Ru(III) species as a result of $^*\mathrm{Ru(bpy)}_3^{2+}$-disproportionation is apparent in the multi-wavelength transient absorption spectra. Features in the spectrum collected 5 μs after excitation (Figure A.8) match closely with those obtained when the Ru(I)-Ru(II) (Figure A.9) and Ru(III)-Ru(II) (Figure A.10) difference spectra are added. Moreover, we also observe the amplitude of the secondary reduction phase diminish as the excitation intensity is reduced (consistent with a lower [*Ru(bpy)$_3^{2}$]$_0$), while the rate constant stays the same, as expected under the pseudo-first order conditions (at constant [cyt *c*]) (Figure A.11).

In 1977, Creutz and Sutin reported “vestiges” of Inverted-Region ET behavior in the excited-state reactions of Ru-polypyridyl complexes (C. Creutz, N. Sutin, *J. Am. Chem. Soc*, **1977**, *99*, 241 – 243). It was pointed out in a footnote that, in preliminary experiments, an upper limit of 10^7 $M^{-1}s^{-1}$ ($\mu > 0.5$ M) was observed for the rate constant for *Ru(bpy)$_3^{2+}$ disproportionation, which should (and appears to) clearly lie deep in the inverted region, given the high exergonicity ($\Delta G = -1.7$ eV) and low reorganization energy ($\lambda < 0.5$ eV) for this reaction. In comparison, similar ET reactions between *Ru(bpy)$_3^{2+}$ and various metal-polypyridyl complexes ($\Delta G = 0.7 - 2.0$ eV) proceed at ~ 10^9 $M^{-1}s^{-1}$ (same study). Our measurements show, however, that the *Ru(bpy)$_3^{2+}$ disproportionation reaction actually proceeds at diffusion-limited rates (> 10^9 $M^{-1}s^{-1}$ at $\mu > 3.5$ M; > 5×10^8 $M^{-1}s^{-1}$ at $\mu = 0.05$ M). Such leveling of electron tunneling at (close to) activationless rates in the inverted region has been observed before (see, for example, Mines et al., *J. Am. Chem. Soc.*, **1996**, *118*, 1961–1965). This leveling effect has been attributed to the formation of electronically excited ET products, which results in a lower effective driving force, pulling the reaction out of the inverted region. It seems quite likely that such a reaction manifold due to low lying Ru(I)(bpy)$_3$ MLCT states could be operational in the disproportionation of *Ru(bpy)$_3^{2+}$.

Note: Materials and methods are described in figure captions.

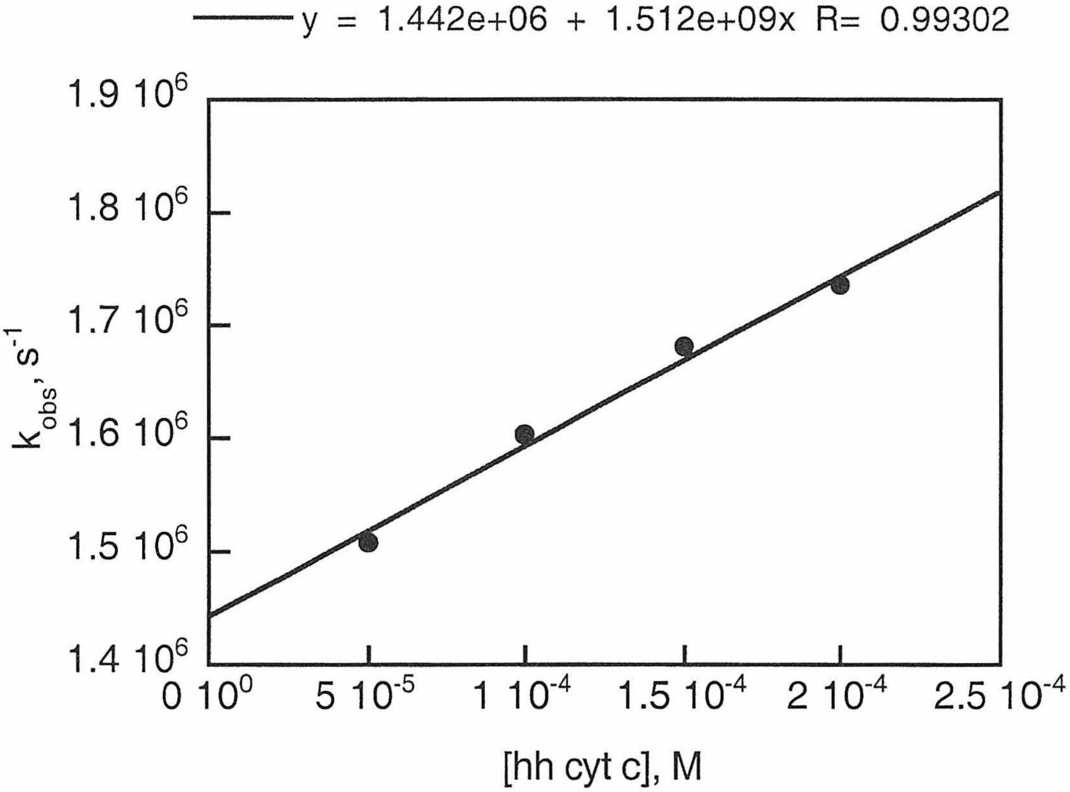

Figure A.1. Dependence of $*\mathrm{Ru(bpy)}_3^{2+}$ luminescence decay rate constant on [unfolded cyt *c*]. The samples were 50 – 200 μM horse heart cyt *c*, 250 μM $\mathrm{Ru(bpy)}_3^{2+}$, 3.2 M GuHCl , and 50 mM $\mathrm{NaP_i}$ (pH 7). Luminescence was measured at 650 nm using a 1 mm-pathlength quartz cell and the transient absorption setup described in Chapter 2. The samples were thoroughly deaerated prior to measurements. The 1.4×10^6 $\mathrm{M^{-1}s^{-1}}$-intercept is in excellent agreement with the intrinsic decay rate of $*\mathrm{Ru(bpy)}_3^{2+}$ in aqueous solution.

A

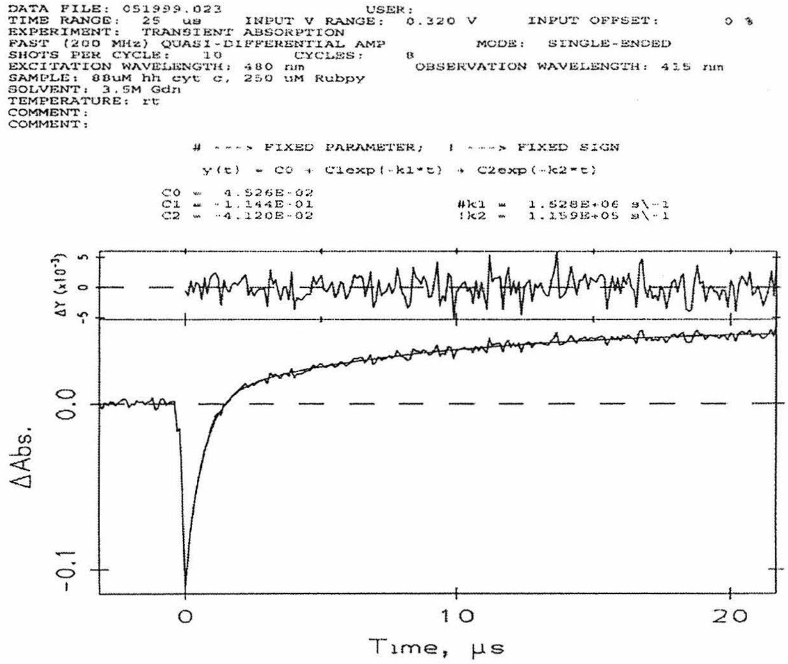

```
DATA FILE: 051999.023                    USER:
TIME RANGE:  25  us    INPUT V RANGE:  0.320 V     INPUT OFFSET:      0 %
EXPERIMENT:  TRANSIENT ABSORPTION
FAST (200 MHz) QUASI-DIFFERENTIAL AMP           MODE:  SINGLE-ENDED
SHOTS PER CYCLE:   10        CYCLES:     8
EXCITATION WAVELENGTH: 480 nm          OBSERVATION WAVELENGTH: 415 nm
SAMPLE: 88uM hh cyt c, 250 uM Rubpy
SOLVENT: 3.5M Gdn
TEMPERATURE: rt
COMMENT:
COMMENT:

          # ---> FIXED PARAMETER;   ! ---> FIXED SIGN

           y(t) = C0 + C1exp(-k1*t) + C2exp(-k2*t)

        C0 =  4.526E-02
        C1 = -1.144E-01                    #k1 =  1.528E+06 s\-1
        C2 = -4.120E-02                    !k2 =  1.159E+05 s\-1
```

B

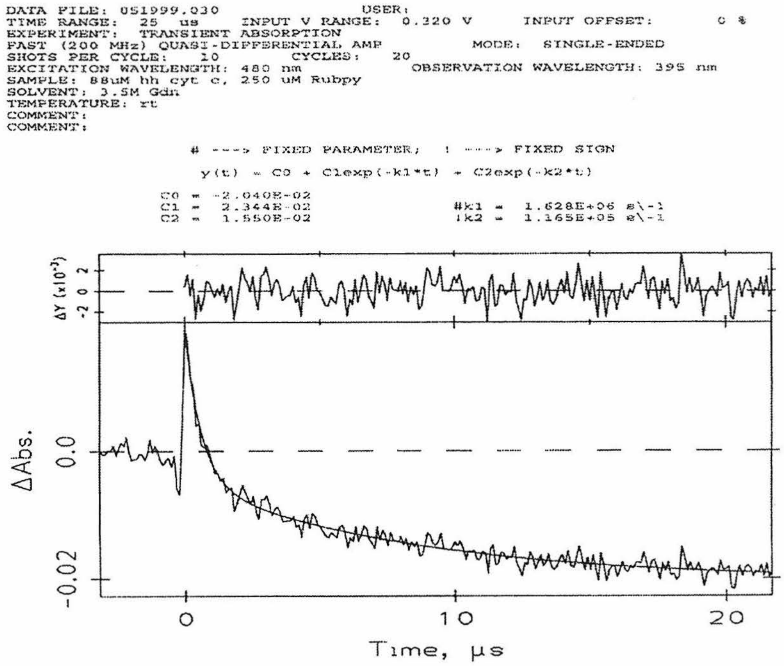

```
DATA FILE: 051999.030                    USER:
TIME RANGE:  25  us    INPUT V RANGE:  0.320 V     INPUT OFFSET:      0 %
EXPERIMENT:  TRANSIENT ABSORPTION
FAST (200 MHz) QUASI-DIFFERENTIAL AMP           MODE:  SINGLE-ENDED
SHOTS PER CYCLE:   10        CYCLES:    20
EXCITATION WAVELENGTH: 480 nm          OBSERVATION WAVELENGTH: 395 nm
SAMPLE: 88uM hh cyt c, 250 uM Rubpy
SOLVENT: 3.5M Gdn
TEMPERATURE: rt
COMMENT:
COMMENT:

          # ---> FIXED PARAMETER;   ! ---> FIXED SIGN

           y(t) = C0 + C1exp(-k1*t) + C2exp(-k2*t)

        C0 = -2.040E-02
        C1 =  2.344E-02                    #k1 =  1.628E+06 s\-1
        C2 =  1.550E-02                    !k2 =  1.165E+05 s\-1
```

Figure A.2. Transient absorption spectra showing the secondary reduction of cyt *c* by Ru(bpy)$_3^{1+}$. The samples were 88 µM cyt *c*, 250 µM *Ru(bpy)$_3^{2+}$, 3.5 M GuHCl and 50 mM NaP$_i$. The spectra were collected at 415 (**A**) and 395 nm (**B**) using 480-nm excitation (Coumarin 480 dye). The fast phase (1.6 × 10^6 s^{-1}) and the slow phase (1.2 × 10^5 s^{-1}) are due to *Ru(bpy)$_3^{2+}$ decay and the secondary reduction process, respectively.

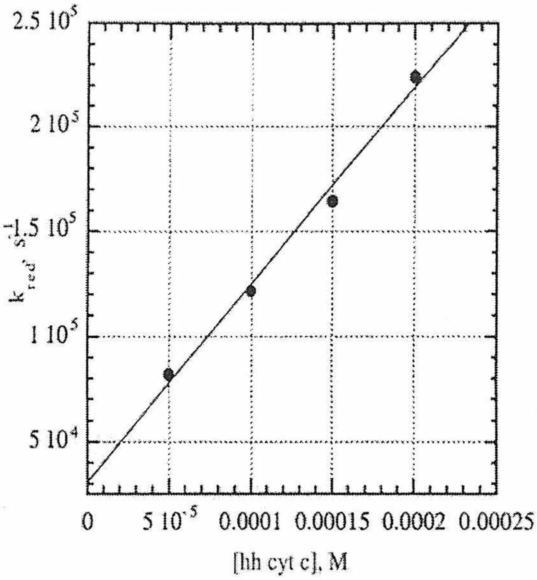

$k_{red} = 3.1{*}10^{4}\ s^{-1} + 9.399{*}10^{8}\ M^{-1}s^{-1}\ [\text{cyt c}]$

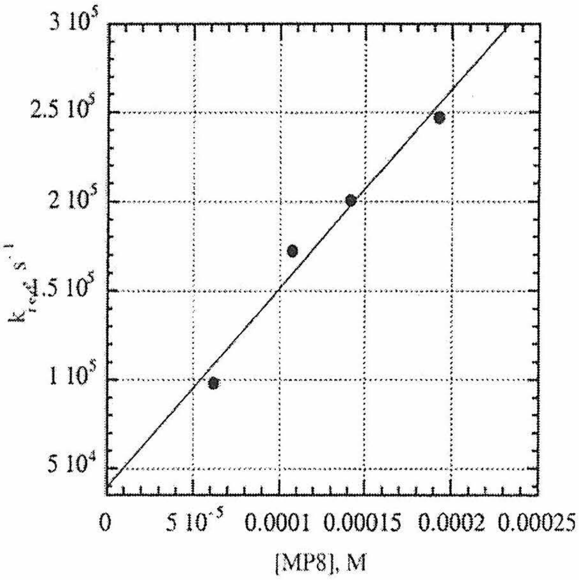

$k_{red} = 3.9{*}10^{4}\ s^{-1} + 1.153{*}10^{9}\ M^{-1}s^{-1}\ [\text{MP8}]$

Figure A.3. Dependence of the secondary reduction rate constant on cyt *c* (**upper**) and AcMP8 (**lower**) concentration.

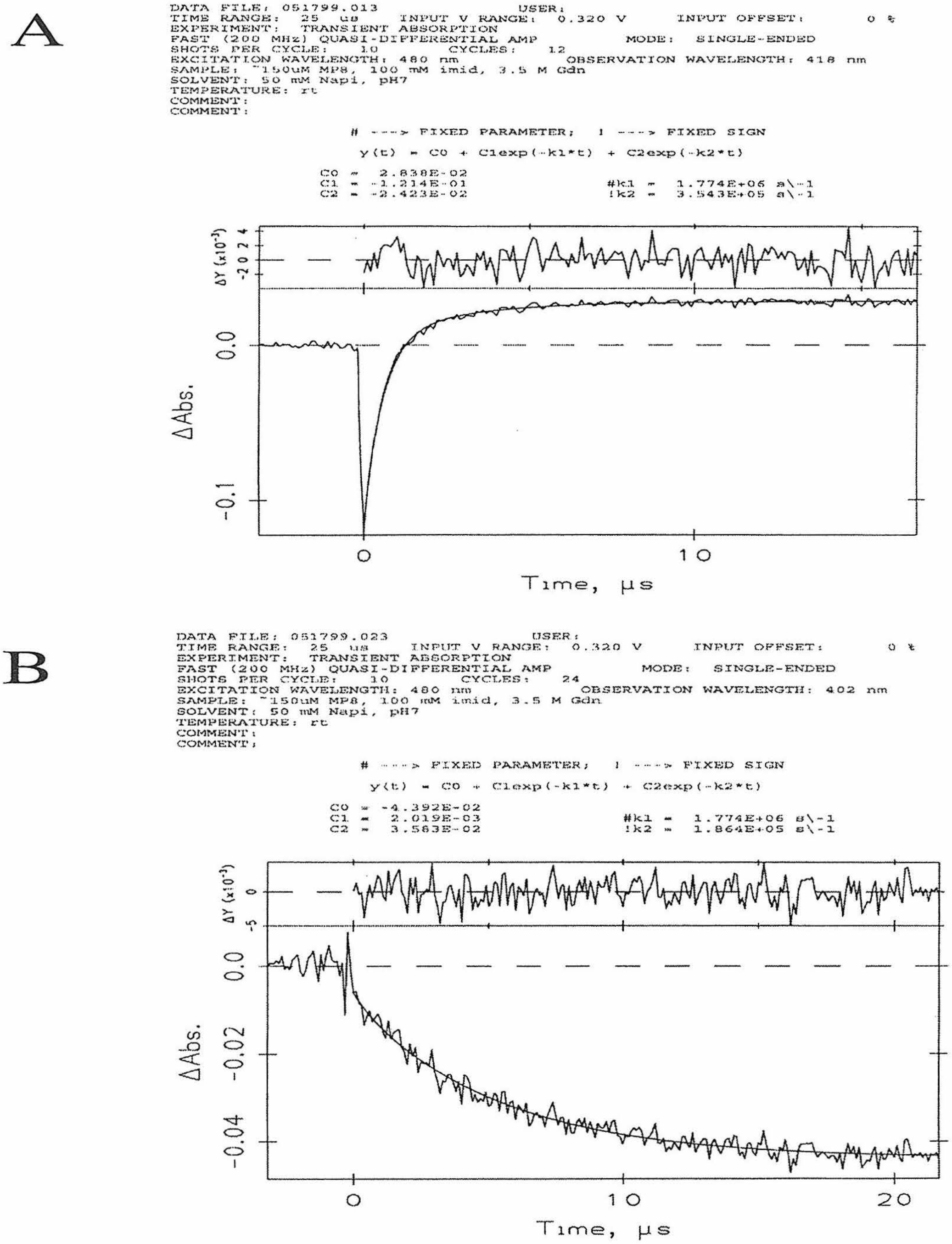

A

```
DATA FILE: 051799.013                    USER:
TIME RANGE:  25  us    INPUT V RANGE:  0.320 V      INPUT OFFSET:        0 %
EXPERIMENT:  TRANSIENT ABSORPTION
FAST (200 MHz) QUASI-DIFFERENTIAL AMP            MODE:  SINGLE-ENDED
SHOTS PER CYCLE:   10        CYCLES:   12
EXCITATION WAVELENGTH: 480 nm           OBSERVATION WAVELENGTH: 418 nm
SAMPLE: ~150uM MP8, 100 mM imid, 3.5 M Gdn
SOLVENT: 50 mM Napi, pH7
TEMPERATURE: rt
COMMENT:
COMMENT:

               # ---> FIXED PARAMETER;  ! ---> FIXED SIGN

                y(t) = C0 + C1exp(-k1*t) + C2exp(-k2*t)

            C0 =  2.838E-02
            C1 = -1.214E-01                    #k1 =  1.774E+06 s\-1
            C2 = -2.423E-02                    !k2 =  3.543E+05 s\-1
```

B

```
DATA FILE: 051799.023                    USER:
TIME RANGE:  25  us    INPUT V RANGE:  0.320 V      INPUT OFFSET:        0 %
EXPERIMENT:  TRANSIENT ABSORPTION
FAST (200 MHz) QUASI-DIFFERENTIAL AMP            MODE:  SINGLE-ENDED
SHOTS PER CYCLE:   10        CYCLES:   24
EXCITATION WAVELENGTH: 480 nm           OBSERVATION WAVELENGTH: 402 nm
SAMPLE: ~150uM MP8, 100 mM imid, 3.5 M Gdn
SOLVENT: 50 mM Napi, pH7
TEMPERATURE: rt
COMMENT:
COMMENT:

               # ---> FIXED PARAMETER;  ! ---> FIXED SIGN

                y(t) = C0 + C1exp(-k1*t) + C2exp(-k2*t)

            C0 = -4.392E-02
            C1 =  2.019E-03                    #k1 =  1.774E+06 s\-1
            C2 =  3.583E-02                    !k2 =  1.864E+05 s\-1
```

Figure A.4. Transient absorption spectra showing the secondary reduction of (imid)AcMP8 by $Ru(bpy)_3^{1+}$. The samples were 150 μM AcMP8, 100 μM imidazole, 250 μM $*Ru(bpy)_3^{2+}$, 3.5 M GuHCl and 50 mM NaP_i. The spectra were collected at 418 (**A**) and 402 nm (**B**). The fast phase (1.7×10^6 s^{-1}) and the slow phase (~ 2×10^5 s^{-1}) are due to $*Ru(bpy)_3^{2+}$ decay and the secondary reduction process, respectively.

A

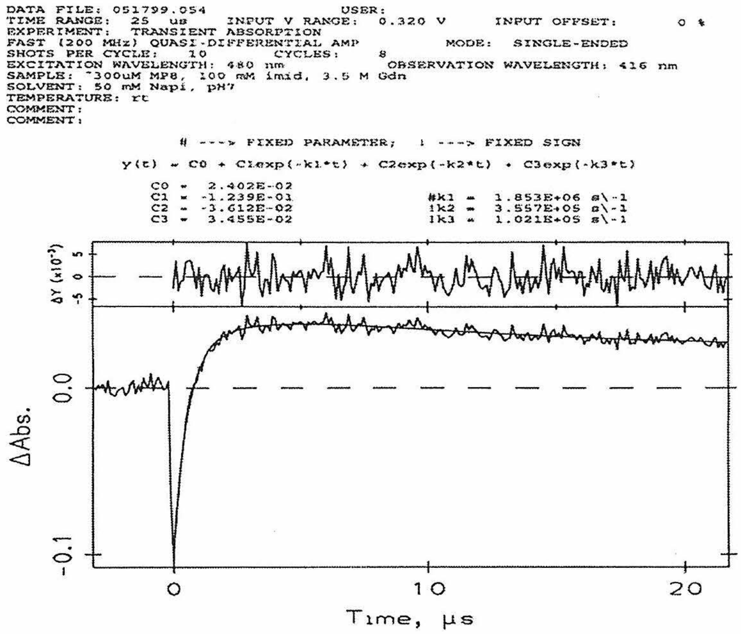

```
DATA FILE: 051799.054                    USER:
TIME RANGE:   25  us    INPUT V RANGE:   0.320 V     INPUT OFFSET:        0 %
EXPERIMENT:   TRANSIENT ABSORPTION
FAST (200 MHz) QUASI-DIFFERENTIAL AMP           MODE:   SINGLE-ENDED
SHOTS PER CYCLE:    10        CYCLES:     8
EXCITATION WAVELENGTH: 480 nm          OBSERVATION WAVELENGTH: 416 nm
SAMPLE: ~300uM MP8, 100 mM imid, 3.5 M Gdn
SOLVENT: 50 mM Napi, pH7
TEMPERATURE: rt
COMMENT:
COMMENT:

            # ---> FIXED PARAMETER;   ! ---> FIXED SIGN

     y(t) = C0 + C1exp(-k1*t) + C2exp(-k2*t) + C3exp(-k3*t)

          C0 =  2.402E-02
          C1 = -1.239E-01                      #k1 =  1.853E+06 s\-1
          C2 = -3.612E-02                      !k2 =  3.557E+05 s\-1
          C3 =  3.455E-02                      !k3 =  1.021E+05 s\-1
```

B

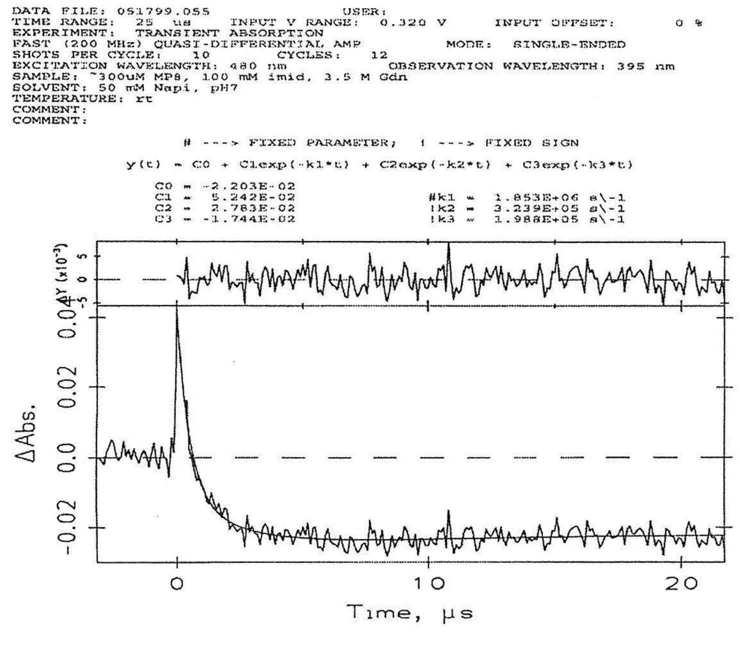

```
DATA FILE: 051799.055                    USER:
TIME RANGE:   25  us    INPUT V RANGE:   0.320 V     INPUT OFFSET:        0 %
EXPERIMENT:   TRANSIENT ABSORPTION
FAST (200 MHz) QUASI-DIFFERENTIAL AMP           MODE:   SINGLE-ENDED
SHOTS PER CYCLE:    10        CYCLES:    12
EXCITATION WAVELENGTH: 480 nm          OBSERVATION WAVELENGTH: 395 nm
SAMPLE: ~300uM MP8, 100 mM imid, 3.5 M Gdn
SOLVENT: 50 mM Napi, pH7
TEMPERATURE: rt
COMMENT:
COMMENT:

            # ---> FIXED PARAMETER;   ! ---> FIXED SIGN

     y(t) = C0 + C1exp(-k1*t) + C2exp(-k2*t) + C3exp(-k3*t)

          C0 = -2.203E-02
          C1 =  5.242E-02                      #k1 =  1.853E+06 s\-1
          C2 =  2.783E-02                      !k2 =  3.239E+05 s\-1
          C3 = -1.744E-02                      !k3 =  1.988E+05 s\-1
```

Figure A.5. Transient absorption spectra showing the secondary reduction of (imid)AcMP8 at high [(imid)AcMP8]. The samples were 300 μM AcMP8, 100 μM imidazole, 250 μM *Ru(bpy)$_3^{2+}$, 3.5 M GuHCl and 50 mM NaP$_i$. The spectra were collected at 416 (**A**) and 395 nm (**B**). The secondary reduction is now about twice as fast (3.5 × 10^5 s^{-1}) as that with 150 μM AcMP8 (Figure A.4). The reoxidation of AcMP8 by Ru(III)-species (1 × 10^5 s^{-1}) is also visible.

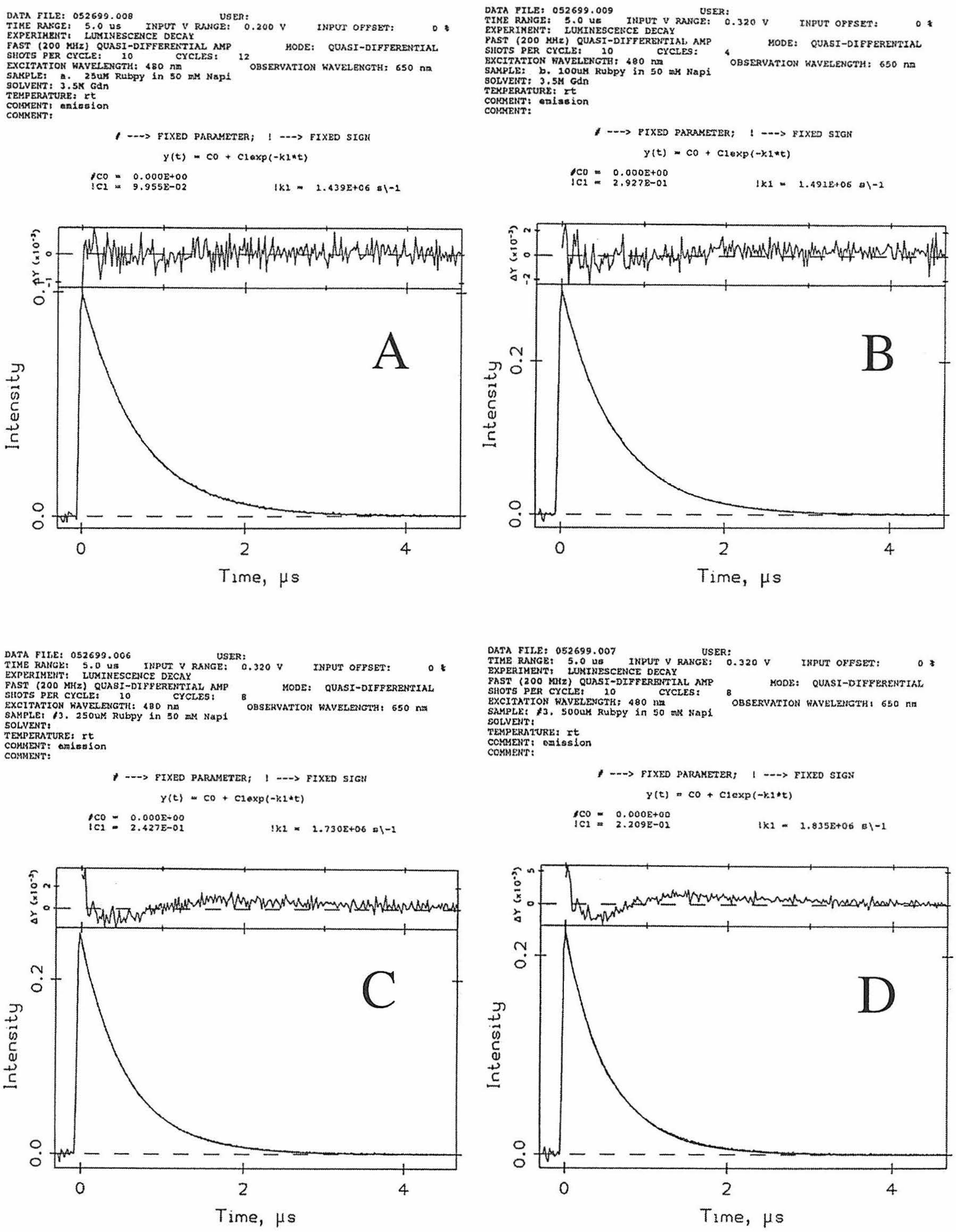

```
DATA FILE: 052699.008             USER:
TIME RANGE:  5.0 us    INPUT V RANGE:  0.200 V     INPUT OFFSET:      0 %
EXPERIMENT:  LUMINESCENCE DECAY
FAST (200 MHz) QUASI-DIFFERENTIAL AMP         MODE:  QUASI-DIFFERENTIAL
SHOTS PER CYCLE:   10       CYCLES:   12
EXCITATION WAVELENGTH: 480 nm           OBSERVATION WAVELENGTH: 650 nm
SAMPLE:  a.  25uM Rubpy in 50 mM Napi
SOLVENT: 3.5M Gdn
TEMPERATURE: rt
COMMENT: emission
COMMENT:

              # ---> FIXED PARAMETER;  ! ---> FIXED SIGN

                    y(t) = C0 + C1exp(-k1*t)

          #C0 =  0.000E+00
          !C1 =  9.955E-02                  !k1 =  1.439E+06 s\-1
```

```
DATA FILE: 052699.009             USER:
TIME RANGE:  5.0 us    INPUT V RANGE:  0.320 V     INPUT OFFSET:      0 %
EXPERIMENT:  LUMINESCENCE DECAY
FAST (200 MHz) QUASI-DIFFERENTIAL AMP         MODE:  QUASI-DIFFERENTIAL
SHOTS PER CYCLE:   10       CYCLES:    4
EXCITATION WAVELENGTH: 480 nm           OBSERVATION WAVELENGTH: 650 nm
SAMPLE:  b. 100uM Rubpy in 50 mM Napi
SOLVENT: 3.5M Gdn
TEMPERATURE: rt
COMMENT: emission
COMMENT:

              # ---> FIXED PARAMETER;  ! ---> FIXED SIGN

                    y(t) = C0 + C1exp(-k1*t)

          #C0 =  0.000E+00
          !C1 =  2.927E-01                  !k1 =  1.491E+06 s\-1
```

```
DATA FILE: 052699.006             USER:
TIME RANGE:  5.0 us    INPUT V RANGE:  0.320 V     INPUT OFFSET:      0 %
EXPERIMENT:  LUMINESCENCE DECAY
FAST (200 MHz) QUASI-DIFFERENTIAL AMP         MODE:  QUASI-DIFFERENTIAL
SHOTS PER CYCLE:   10       CYCLES:    8
EXCITATION WAVELENGTH: 480 nm           OBSERVATION WAVELENGTH: 650 nm
SAMPLE: #3. 250uM Rubpy in 50 mM Napi
SOLVENT:
TEMPERATURE: rt
COMMENT: emission
COMMENT:

              # ---> FIXED PARAMETER;  ! ---> FIXED SIGN

                    y(t) = C0 + C1exp(-k1*t)

          #C0 =  0.000E+00
          !C1 =  2.427E-01                  !k1 =  1.730E+06 s\-1
```

```
DATA FILE: 052699.007             USER:
TIME RANGE:  5.0 us    INPUT V RANGE:  0.320 V     INPUT OFFSET:      0 %
EXPERIMENT:  LUMINESCENCE DECAY
FAST (200 MHz) QUASI-DIFFERENTIAL AMP         MODE:  QUASI-DIFFERENTIAL
SHOTS PER CYCLE:   10       CYCLES:    8
EXCITATION WAVELENGTH; 480 nm           OBSERVATION WAVELENGTH: 650 nm
SAMPLE: #3. 500uM Rubpy in 50 mM Napi
SOLVENT:
TEMPERATURE: rt
COMMENT: emission
COMMENT:

              # ---> FIXED PARAMETER;  ! ---> FIXED SIGN

                    y(t) = C0 + C1exp(-k1*t)

          #C0 =  0.000E+00
          !C1 =  2.209E-01                  !k1 =  1.835E+06 s\-1
```

Figure A.6. Concentration dependence of *Ru(bpy)$_3^{2+}$-luminescence in the absence of cyt *c* or AcMP8. **(A)** 25 µM, **(B)** 100 µM, **(C)** 250 µM, **(D)** 500 µM. At high concentrations, the decay can no longer be described by a monoexponential function.

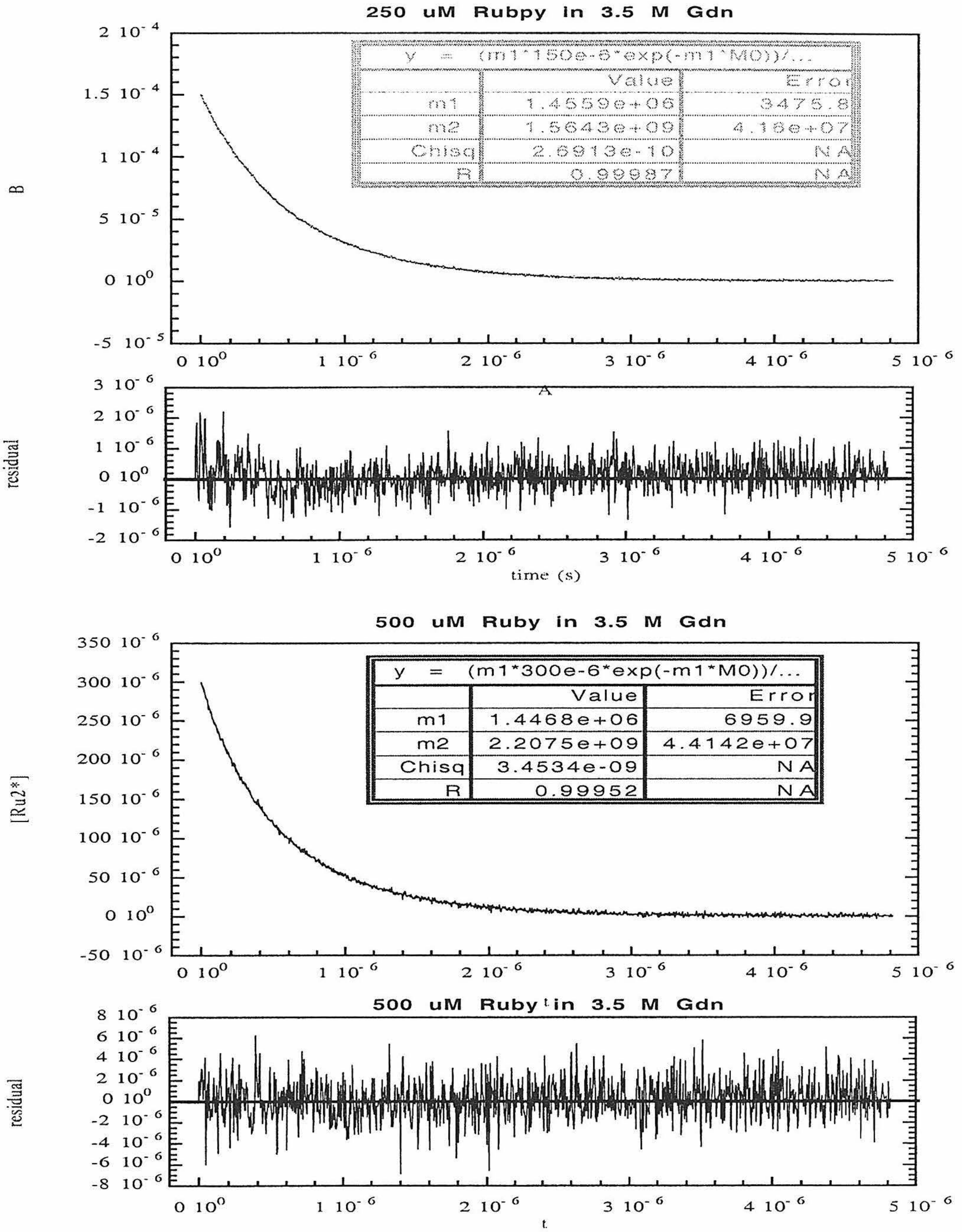

Figure A.7. Luminescence decay of 250 μM (upper) and 500 μM (lower) $^*Ru(bpy)_3^{2+}$. Decays can be satisfactorily fit when the $^*Ru(bpy)_3^{2+}$-disproportionation reaction is taken into account. Variables m1 (1.45 × 10^6) and m2 (~ 2 × 10^9) correspond to the intrinsic decay and the disproportionation rates of $^*Ru(bpy)_3^{2+}$, respectively.

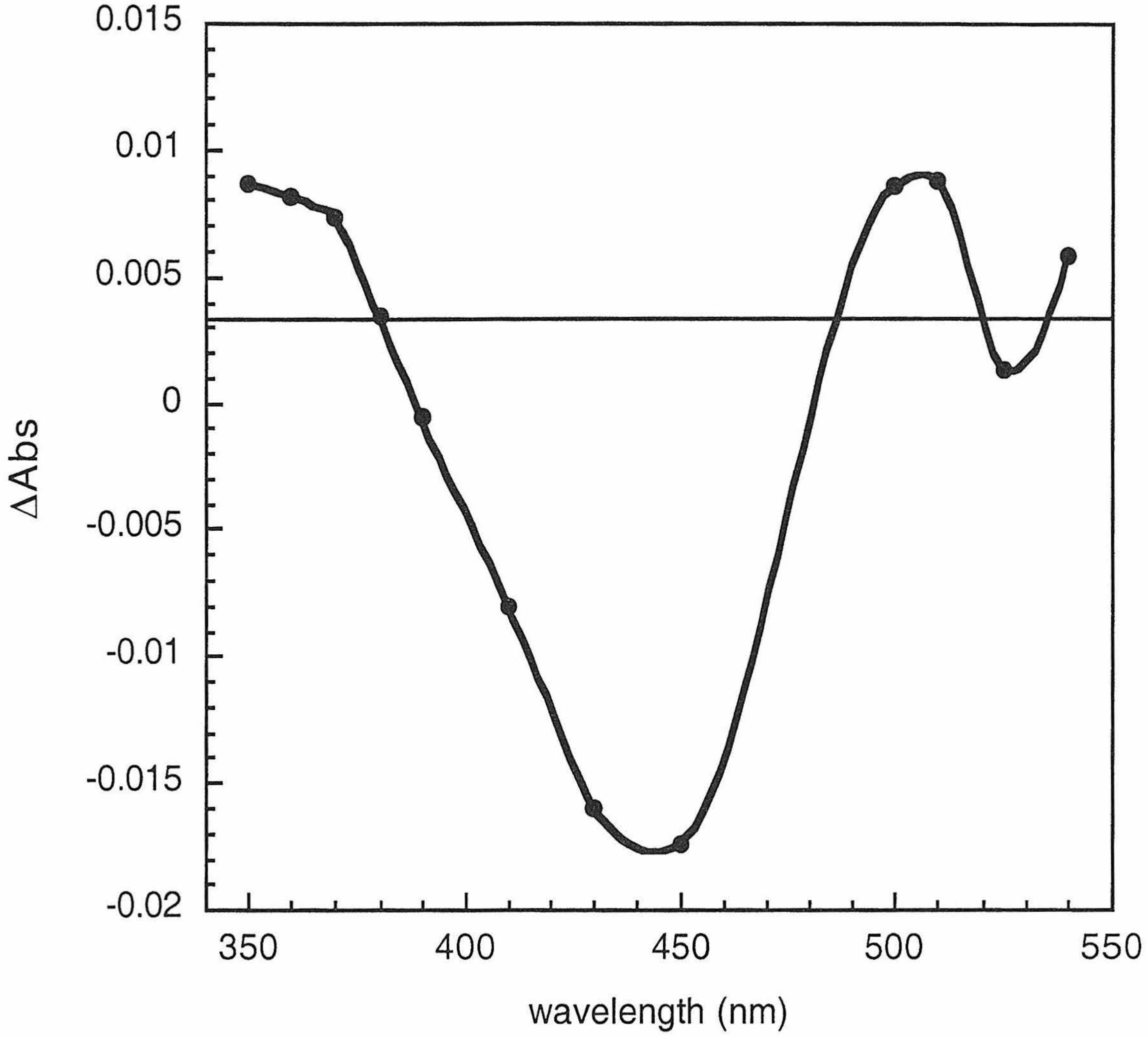

Figure A.8. Multi-wavelength transient absorption spectrum of $Ru(bpy)_3^{2+}$ at 5 μs following excitation. The sample was 250 μM $Ru(bpy)_3^{2+}$ and 3.5 M GuHCl. The increase in absorption at ~ 500 nm is due solely to the generation of Ru(I)-species, whereas both Ru(I) and Ru(III)-species contribute to the large decrease at 450 nm (see A.9 and A.10).

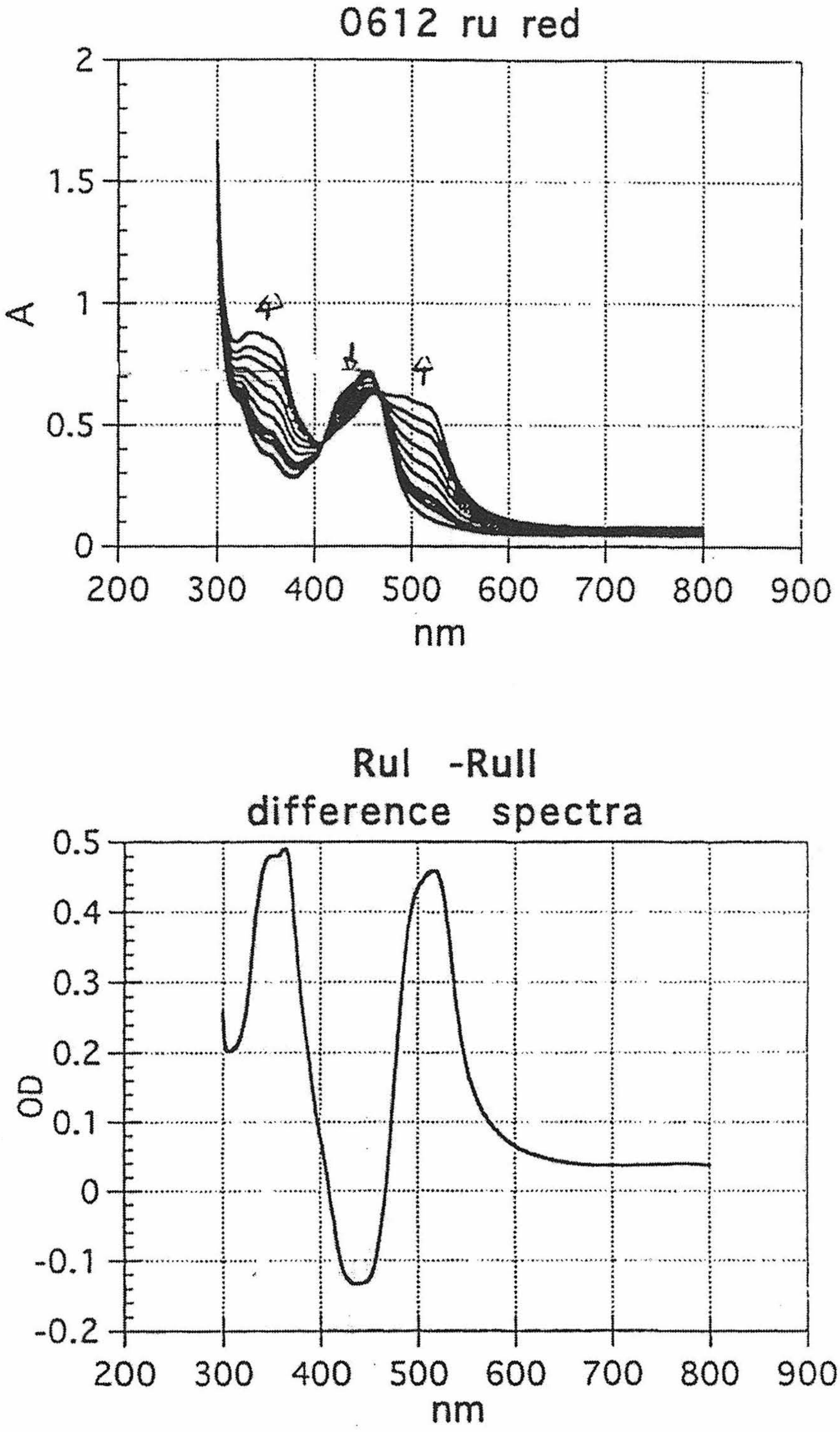

Figure A.9. Spectroelectrochemistry of $Ru(bpy)_3^{2+}$ (top) and the Ru(I)-Ru(II) difference spectrum (bottom) (courtesy of Chad Immoos, UC Irvine). Arrows indicate the direction of spectral changes associated with Ru(I) generation.

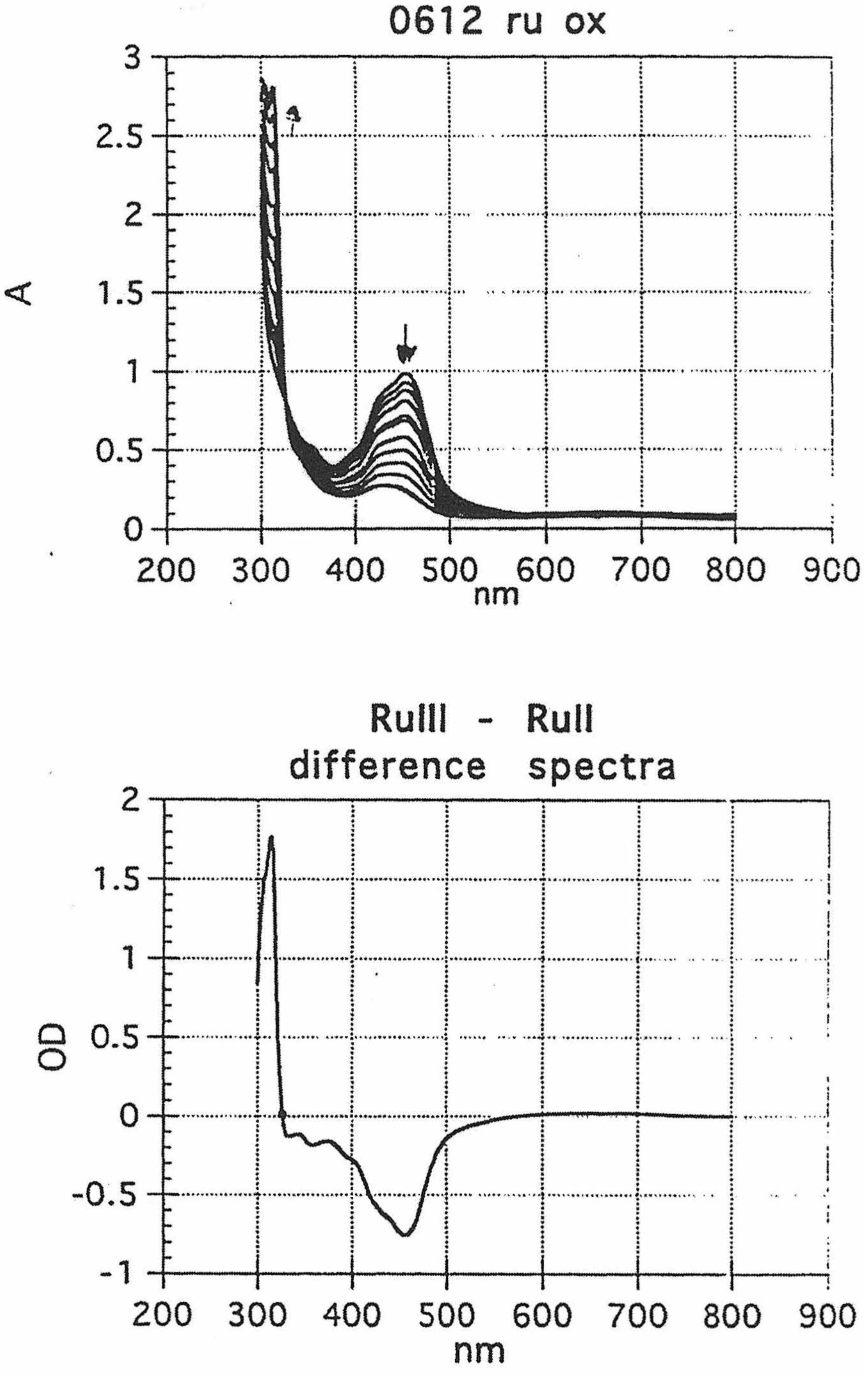

Figure A.10. Spectroelectrochemistry of $Ru(bpy)_3^{2+}$ and the Ru(III)–Ru(II) difference spectrum (courtesy of Chad Immoos, UC Irvine). Arrows indicate the direction of spectral changes associated with Ru(III) generation.

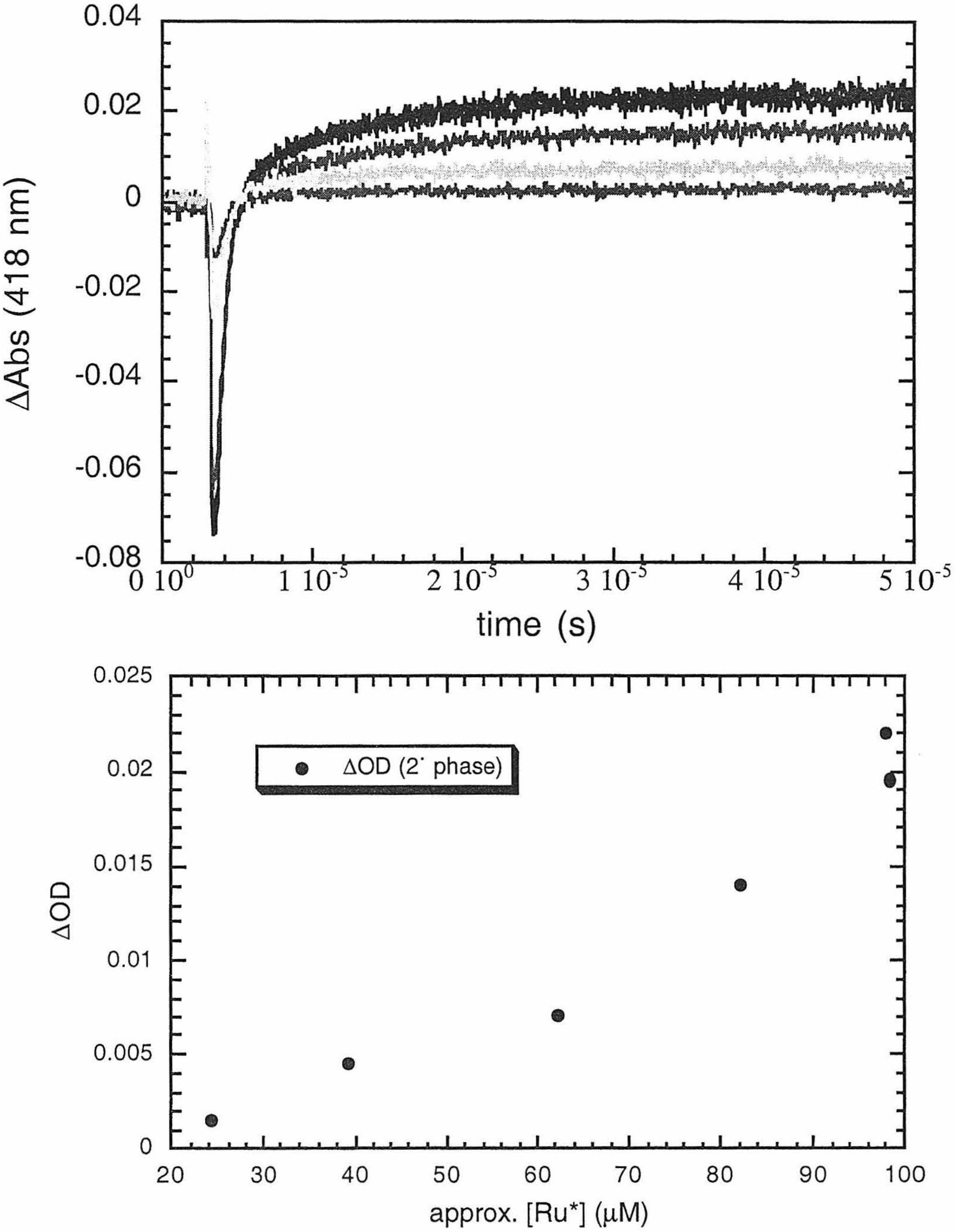

Figure A.11. Dependence of the secondary reduction phase amplitude (at 418 nm) on excitation (480 nm) intensity. The sample is 250 μM unfolded cyt *c*, and 250 μM $Ru(bpy)_3^{2+}$. The light intensity was attenuated using cross-polarizers. The rate constant for the secondary reduction phase (1.5×10^5 s^{-1}) is independent of light intensity.

Appendix B

Preparation of Co-cyt *c* and its Derivatives

Preparation of Co-cyt *c*

Co-cyt *c* was synthesized according to established procedure (Dickinson, L. C.; Chien, J. C. *Biochemistry* **1975**, *14*, 3526 – 3534) with minor modifications. In a typical preparation, 200 mg of horse, tuna or yeast cyt *c* was placed under vacuum for at least 2 hours to minimize the water content. The desiccated protein was submitted to the Beckman Institute Peptide Facility (John Racs) in a Teflon tube specially designed for use with the Teflon line in that facility. Extra care was taken to place all material at the bottom of the tube, as the lyophilized protein easily sticks on the walls during transfer. The protein was treated for 5 min at 80 K with just enough anhydrous HF to cover the protein. In this period, the color of the protein turns from red-brown to purple, indicating the extraction of iron to yield metal-free cyt *c* (porphyrin cyt *c*). At this point the tube was covered with aluminum foil, as porphyrin cyt *c* is light-sensitive, and vacuum was applied for 30 min to 1 hour to eliminate unreacted HF. From this point on, the protein was strictly kept away from light and at 4° C until cobalt was inserted. Porphyrin cyt *c* (at this point, a gelatinous mass) was dissolved in a minimal amount (~ 10 ml) of 50 mM sodium acetate buffer (pH 5) while still in the Teflon tube. The absorption spectrum of porphyrin cyt *c* exhibits a Soret band with a maximum at 404 nm and four Q-bands characteristic of free-base porphyrin species (Figure B.1A). Any fluoride salts in the protein solution were eliminated by repeated dilution (with NaOAc buffer) and concentration using an Amicon stirred cell (YM 10 membrane). For the complete removal of salts and other impurities, protein was then run down a G25-Sephadex column (75 cm length, 5 cm diameter) using the same buffer. While the published protocol reports the presence of denatured or aggregated material, we have not rigorously attempted to purify porphyrin cyt *c* at this stage (Note: especially in horse cyt *c* preparations, a significant amount of red colored material remained on the column even after several column-volumes of eluent). All of the collected material (~ 50 ml) was dialyzed overnight against 5 liters of 10 mM NaP_i buffer (pH 7.4) using a dialysis tubing (Spectrapor) with a MW-cutoff of 3000 amu. The protein was then concentrated ~ 10-fold (down to 5 ml) using an Amicon stirred cell or a Centriprep (MW cutoff 10,000 amu. $CoCl_2$ (Aldrich) was then added in 20 – 50-fold molar excess over porphyrin cyt *c*, whose concentration was estimated using $\varepsilon_{404\,\mathrm{nm}} \approx 150{,}000\ \mathrm{M^{-1}cm^{-1}}$. The pH of the solution was adjusted to 4 with glacial acetic acid. The metallation reaction was allowed to proceed at 50° C in a water bath protected from room light. Depending on the protein concentration, the reaction was complete within 2 – 5 hours, yielding burgundy-colored Co cyt *c* (Figure B.1B).

Purification of Co-cyt *c*

The reaction solution was exchanged into 50 mM NaP_i buffer (Buffer A, pH 7) using an Amicon stirred cell or Centriprep. The protein was purified by FPLC (Pharmacia) using a cation exchange column (Mono S 16/10 or 10/10) against an NaCl gradient (Buffer B = Buffer A + 1 M NaCl). Buffers A and B also contained 1 mM dithiothreitol (DTT) when purifying yeast Co-cyt *c* in order to prevent protein dimerization through Cys102. In a typical run, the protein was loaded onto the column using a 10-ml Superloop and washed with 20 ml of Buffer A using a flow rate of 5 ml/min (or 2.5 ml/min with Mono S 10/10). An NaCl-gradient was then run at the same flow rate, typically up to 0.4 – 0.5 M NaCl over the course of 100 (Mono S 10/10) or 150 ml (Mono S 16/10). Horse, tuna and yeast Co-cyt *c* eluted at ~ 0.25, 0.35 and 0.48 M

NaCl, respectively (Figure B.2). Probably due to its lower stability, the yeast protein contained significantly more impurities than horse and tuna Co-cyt *c*, therefore requiring multiple (2 – 3) FPLC runs. In all cases, significant amounts aggregated or denatured protein material remained bound to the top of the column. While some of this material eluted at 1 M NaCl, most of it could only be solubilized using 1 M NaOH. The purity of the Co-cyt *c* was confirmed by matrix-assisted laser desorption- (MALDI) or electrospray mass spectroscopy at the Beckman Institute Peptide and Protein Microanalytical Laboratories. The masses for horse, tuna and yeast Co-cyt *c* were ~ 12360, 12030 and 12710 amu (all ± 5 amu), respectively (Figure B.3).

Chemical modification of Co-cyt *c*

<u>Modification of yeast Co-cyt *c* with a dansyl-fluorophore at Cys 102</u>

FPLC-purified yeast Co-cyt *c* was treated with 10 mM DTT overnight (to break intermolecular disulfide bonds), which was then removed by running the solution down a PD-10 gel filtration column (Pharmacia) or by exchange into water using an Amicon stirred cell. This concentrated protein solution was added 50-fold excess 5-((((2-iodoacetyl)amino)ethyl)amino)naphthalene-1-sulfonic acid (IAEDANS) (Molecular Probes), which is a thiol-specific derivative of the dansyl-fluorophore. The pH was adjusted to 7 and the reaction was allowed to run overnight at room temperature. After unreacted IAEDANS was eliminated by several washes with 50 mM NaP$_i$ (Buffer A) using Centriprep (MW-cutoff 10,000 amu), the product was purified using the previously described FPLC protocol (see

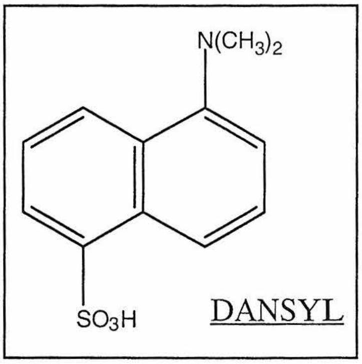

preceding section). The dansylated Co-cyt *c* eluted at lower [NaCl] (~ 0.40 M) than unmodified yeast Co-cyt *c* (Figure B.4), as expected from the negatively charged sulfonate group of the dansyl fluorophore. Attachment of the dansyl group on the protein was confirmed by the orange emission of the solution upon UV-excitation. The MALDI mass spectrum revealed a peak at 13008 amu, in accordance with the additional mass from the fluorophore (Figure B.4). Dansyl-Co cyt *c* appears to be somewhat unstable; even at 4° C some protein was observed to precipitate over two weeks.

Guanidination of surface lysines in horse and tuna Co-cyt *c* with methylisourea

The surface lysine residues in tuna or horse Co-cyt *c*, which are implicated in misligation in unfolded cyt *c*, were transformed into homoarginines using published protocols (Russell, B. S.; Melenkivitz, R.; Bren, K. L. *Proc. Natl. Acad. Sci. USA* **2000**, *97*, 8312 – 8317). FPLC-purified Co-cyt *c* was concentrated to ~ 1 mM and incubated with 0.5 M *o*-methylisourea hydrogen sulfate (MIU) (Aldrich) for 5 days at pH 11.0 and 4° C under constant stirring (Note: with tuna Co-cyt *c*, we have found that the inclusion of 4 M GuHCl in the reaction solution was also necessary for all lysine residues to be modified). A considerable amount of the protein precipitated out of the solution over this period. To eliminate the precipitated protein, the reaction solution was run down a PD-10 column using 50 mM NaP_i buffer (pH 7). After complete exchange into the same buffer using Centriprep (MW-cutoff 10,000), the protein was purified using the previously described FPLC protocols. MIU-modified horse and tuna Co-cyt *c* (Har-Co-cyt *c*) eluted at ~ 0.35 M and 0.40 M NaCl, respectively (Figures B.5

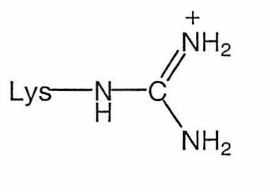

HOMOARGININE

and B.6), with main products having masses of 13159 and 12702 amu (Figures B.5 and B.6). These values indicate that all lysines (19 and 16) were successfully modified (each modification adds 42 amu). Comparison of the chemical denaturation curves for Co-cyt *c* and Har-Co-cyt *c* (horse) indicate that the conversion of lysines into homoarginines do not affect the protein stability (Figure B.7).

Modification of surface histidines in horse Co-cyt *c* with [Pt(terpy)]Cl

The surface histidines in horse (His 26 and 33) Co-cyt *c* were modified with [Pt(terpy)Cl]Cl according to standard literature preparation (Brothers, H. M.; Kostic, N. M. *Inorg. Chem.* **1988**, *27*, 1761 – 1767). 1-2 mM protein in 0.1 M sodium acetate buffer (pH 5) was treated with two – threefold excess [Pt(terpy)Cl]Cl (Aldrich) for 3 days at room temperature. Following exchange into Buffer A (50 mM NaP_i, pH 7), the protein was purified by FPLC, where the singly and doubly modified proteins eluted at 0.30 and 0.45 M NaCl respectively (Figure B.8). The extent of the modification could be quantitated from the 342-nm band due to the Pt-complex ($\varepsilon_{342} \sim 14{,}600\ M^{-1}cm^{-1}$) (Figure B.8). The Pt-adducts, however, were found to be very unstable, dissociating within a couple days. They could also not withstand MALDI or electrospray mass spectroscopic conditions (Figure B.8).

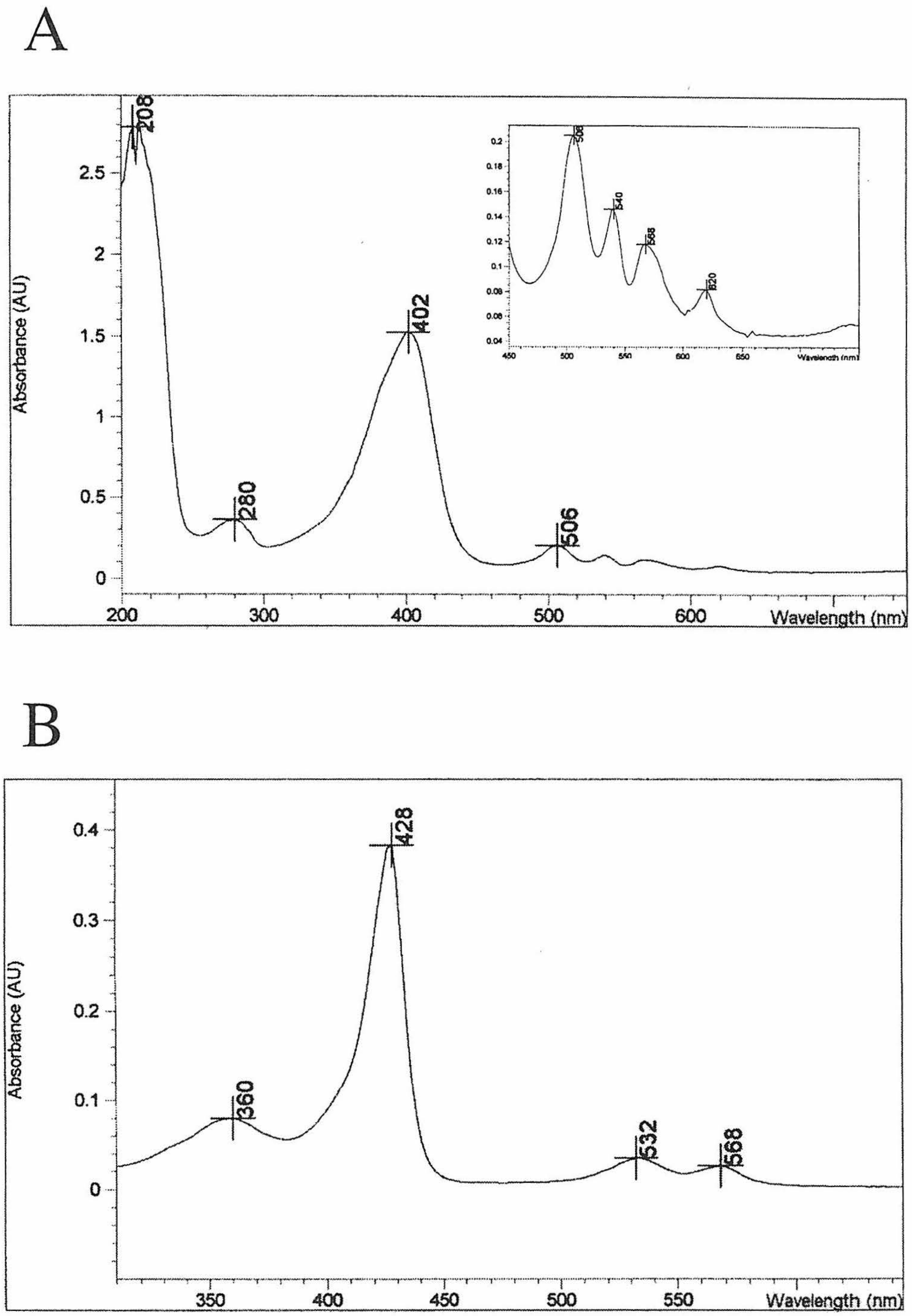

Figure B.1. UV-vis spectra of porphyrin-cyt *c* (**A**) and Co-cyt *c* (**B**).

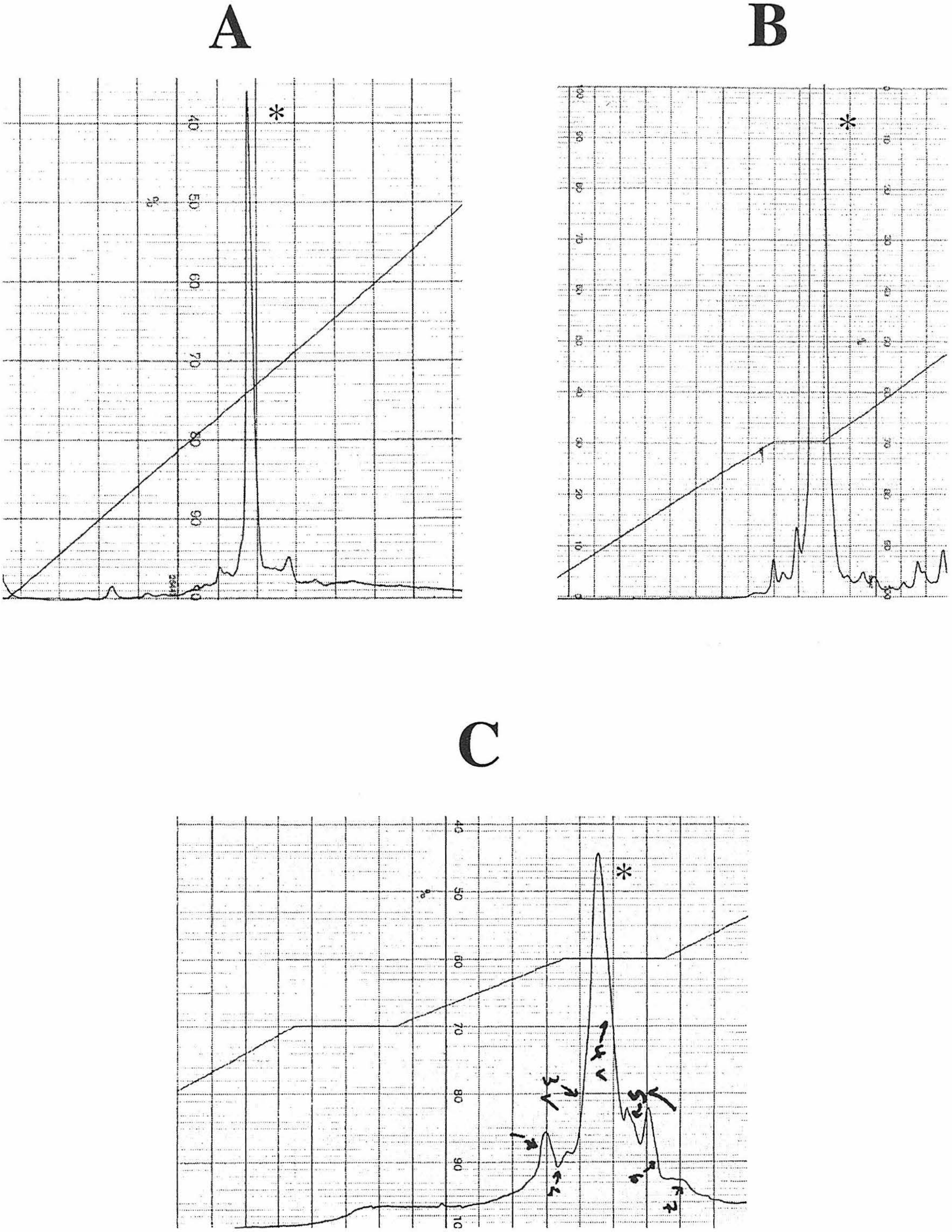

Figure B.2. FPLC chromatograms of horse- (**A**), tuna- (**B**) and yeast- (**C**) Co-cyt *c*. Desired products are marked with an asterisk. Sloped lines indicate the Buffer B gradient.

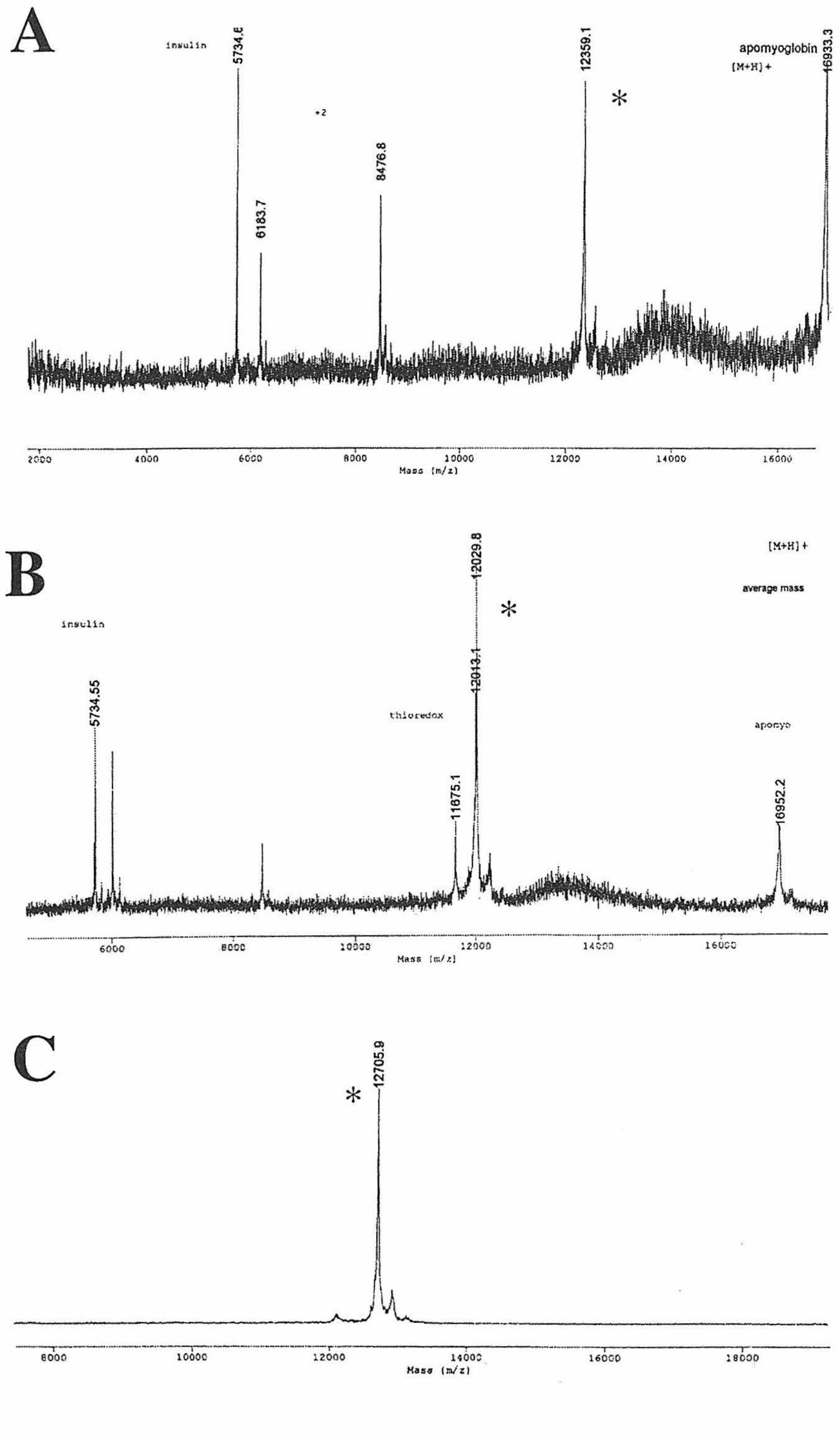

Figure B.3. MALDI mass spectra of horse- (**A**), tuna- (**B**), and yeast- (**C**) Co-cyt *c*. Desired products are marked with an asterisk.

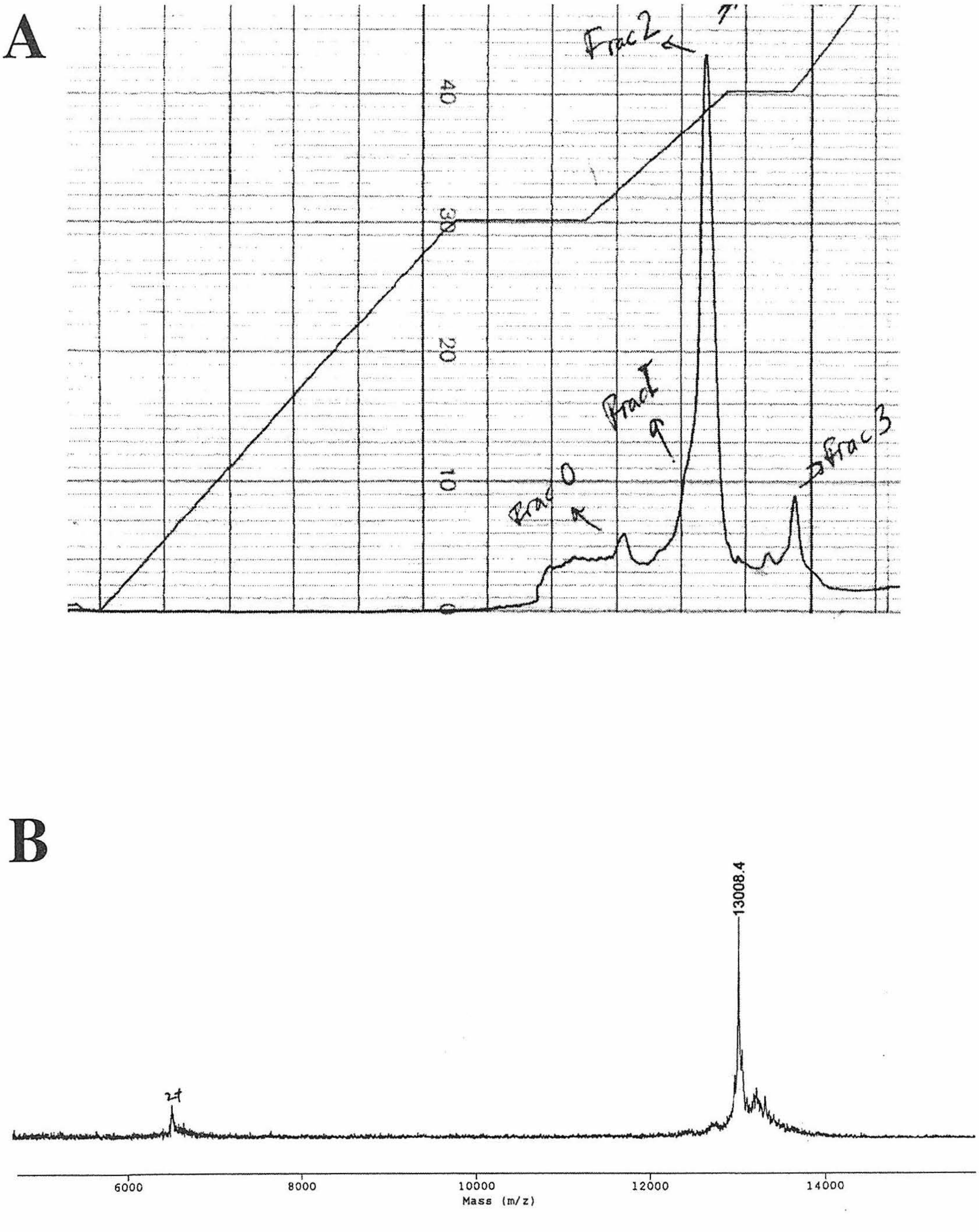

Figure B.4. FPLC chromatogram of dansyl-Co cyt *c* **(A)** and MALDI mass spectrum of the purified product **(B)** (which is labeled “Frac 2”).

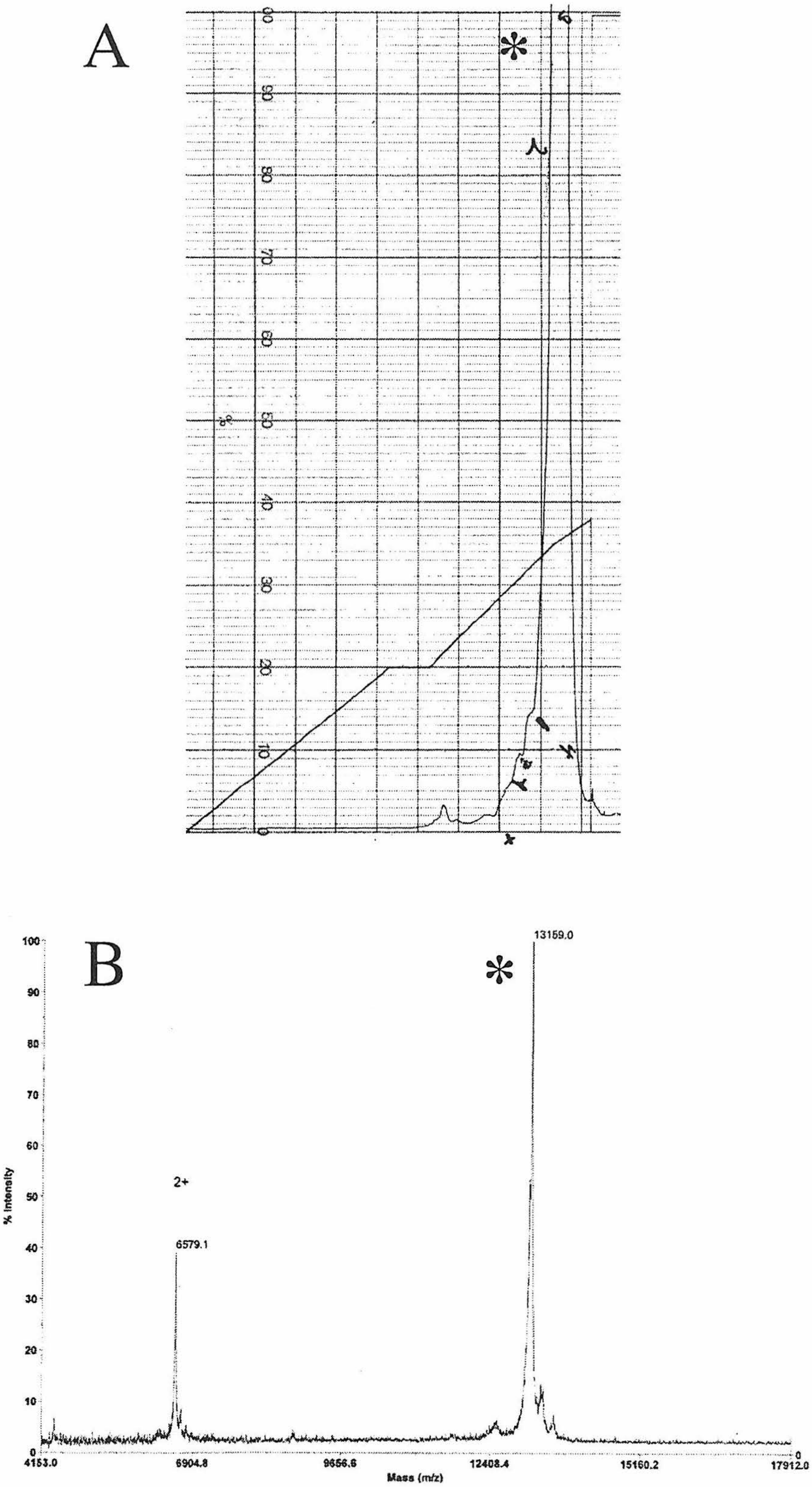

Figure B.5. FPLC chromatogram (**A**) and MALDI mass spectrum (**B**) of methylisourea-treated horse Co-cyt *c*. Peaks marked with an asterisk indicate the desired product.

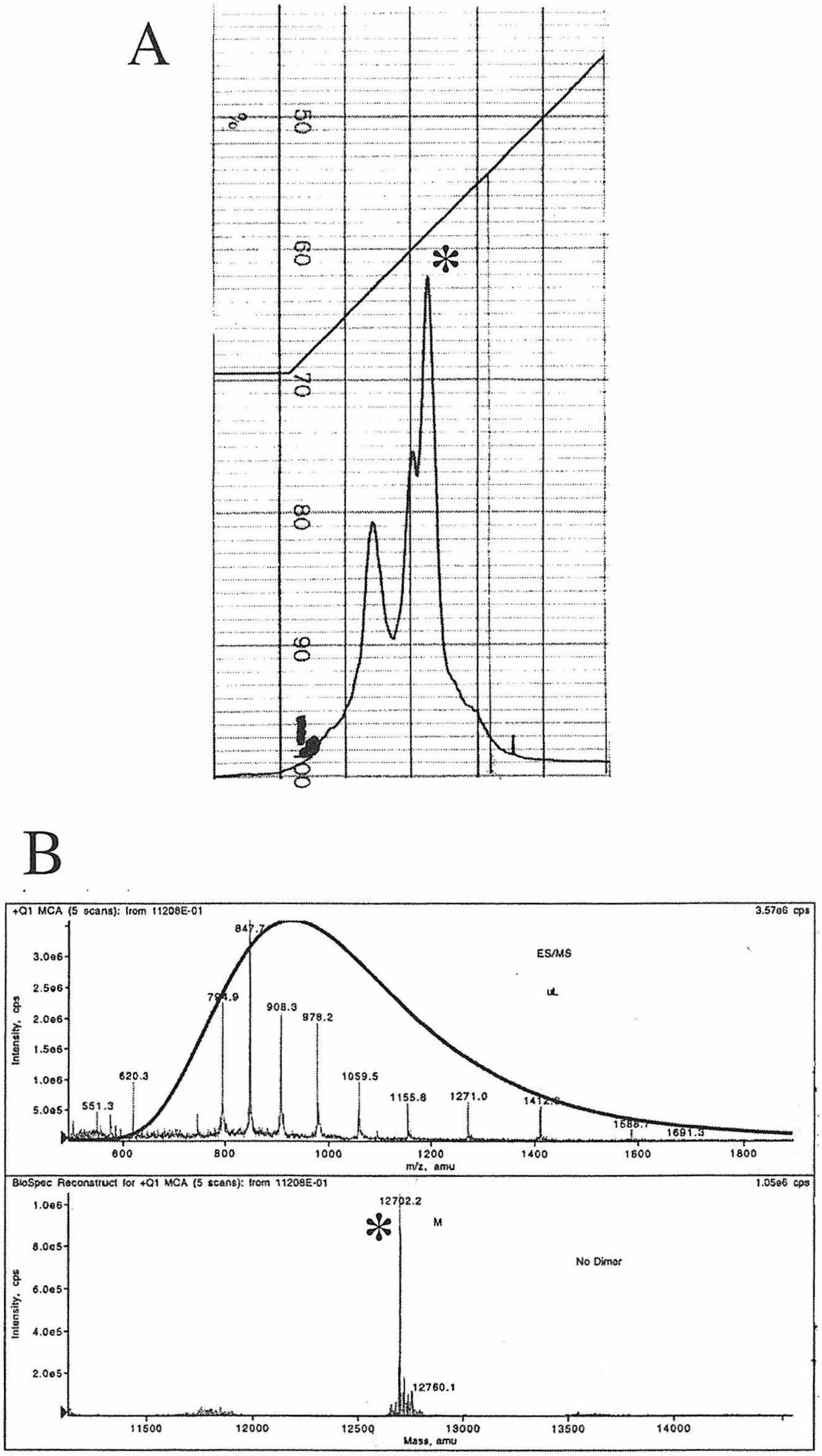

Figure B.6. FPLC chromatogram (**A**) and electrospray mass spectrum (**B**) of methyliosurea-treated tuna Co-cyt *c*. Peaks marked with an asterisk indicate the desired product.

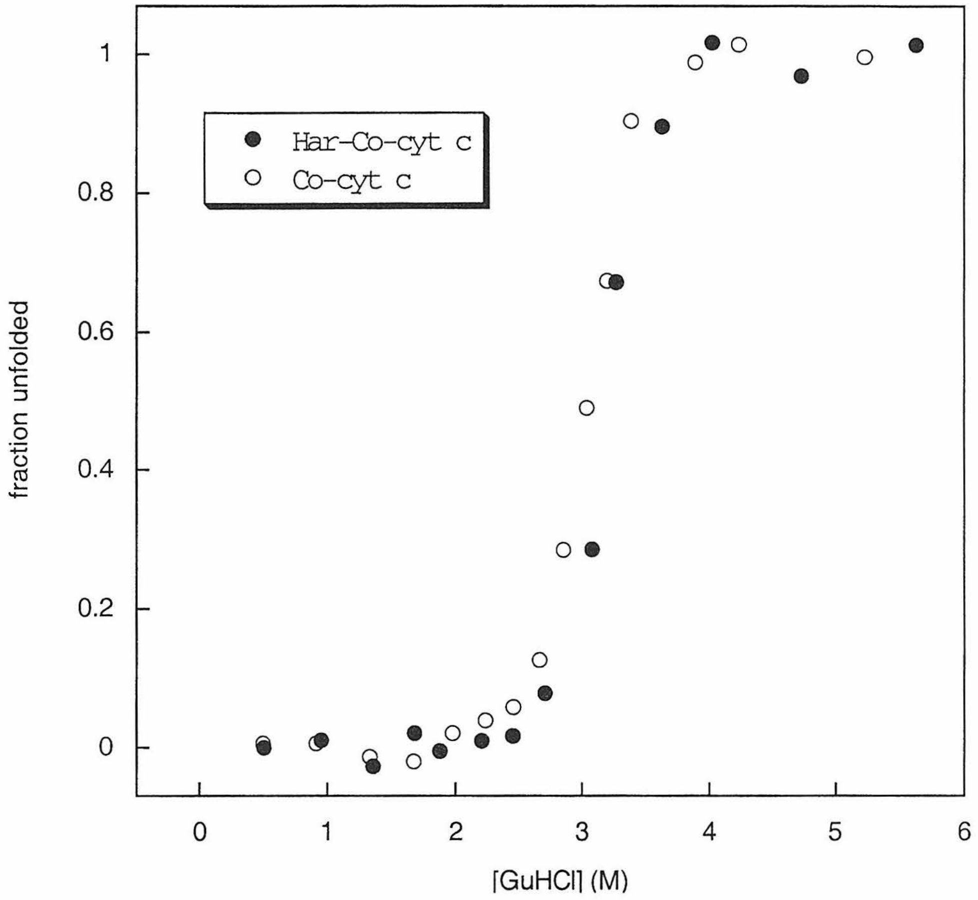

Figure B.7. Denaturation curves for Co-cyt *c* and Har-Co-cyt *c* from horse (determined by changes in 422-nm absorption). The denaturation midpoint for Har-Co-cyt *c* is 3.2 M GuHCl.

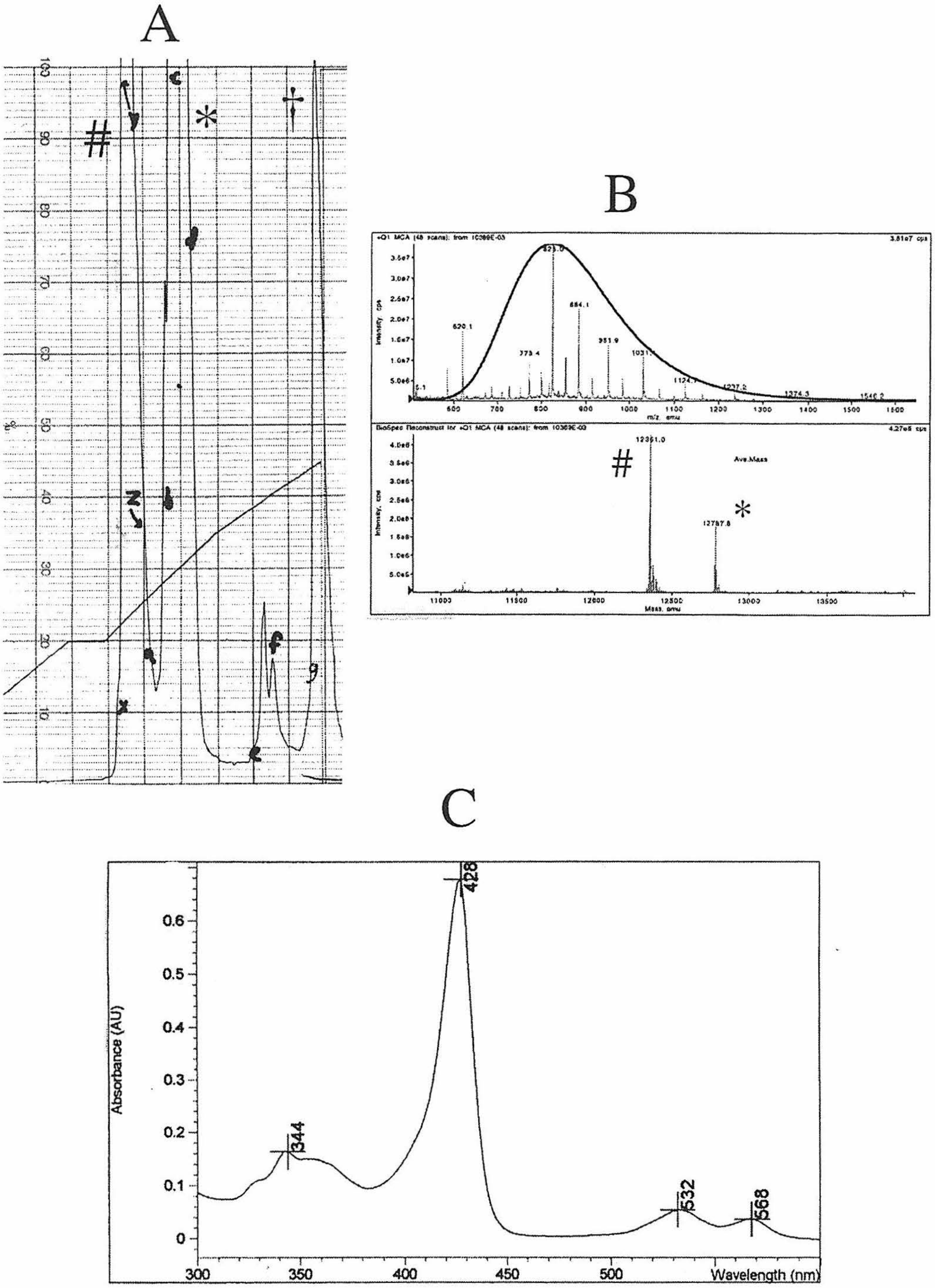

Figure B.8. FPLC chromatogram (**A**), electrospray mass spectrum (**B**) and UV-vis spectrum for Pt(terpy)-modified horse Co-cyt *c*. #, *, and † indicate unmodified, singly-modified, and doubly-modified species. For the mass spectrum, an aliquot from the singly-modified FPLC peak was used. Apparently the Pt(terpy)-adduct is not stable, as the main peak in the mass spectrum is that of the unmodified protein.

Appendix C

Miscellaneous Properties of Metal-Subsituted Cytochromes *c*

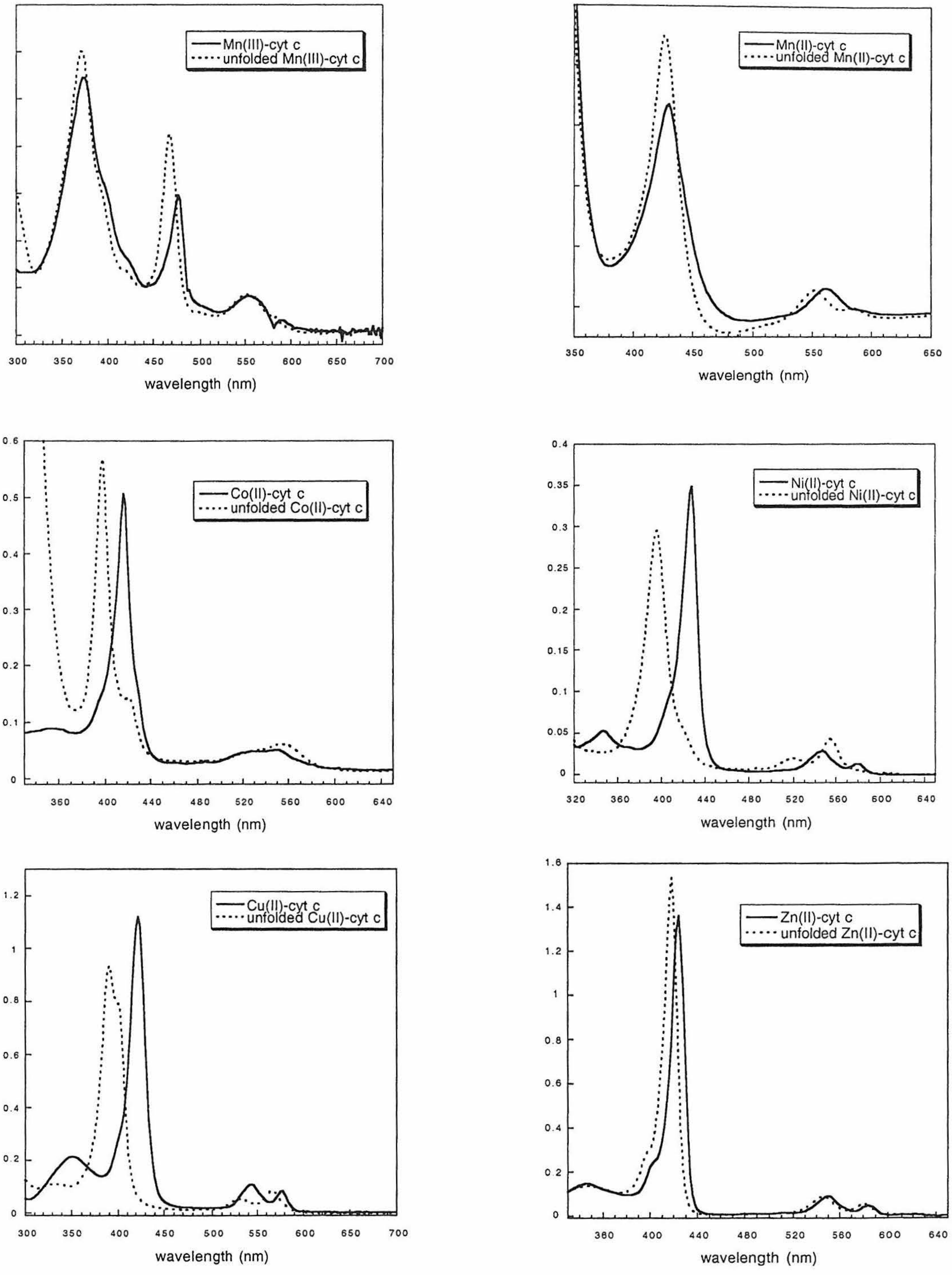

Figure C1. UV-vis spectra of folded and unfolded metal-substituted cytochromes *c*. Mn-, Ni-, and Cu-cyt *c* were synthesized and purified using the protocols described in Appendix B. Mn(II)- andCo(II)-cyt *c* were obtained using excess dithionite under anaerobic conditions. Cu-cyt *c* is involved in a monomer↔dimer equilibrium in the unfolded state; the monomeric form has a Soret peak at 402 nm and the dimeric form at 390 nm.

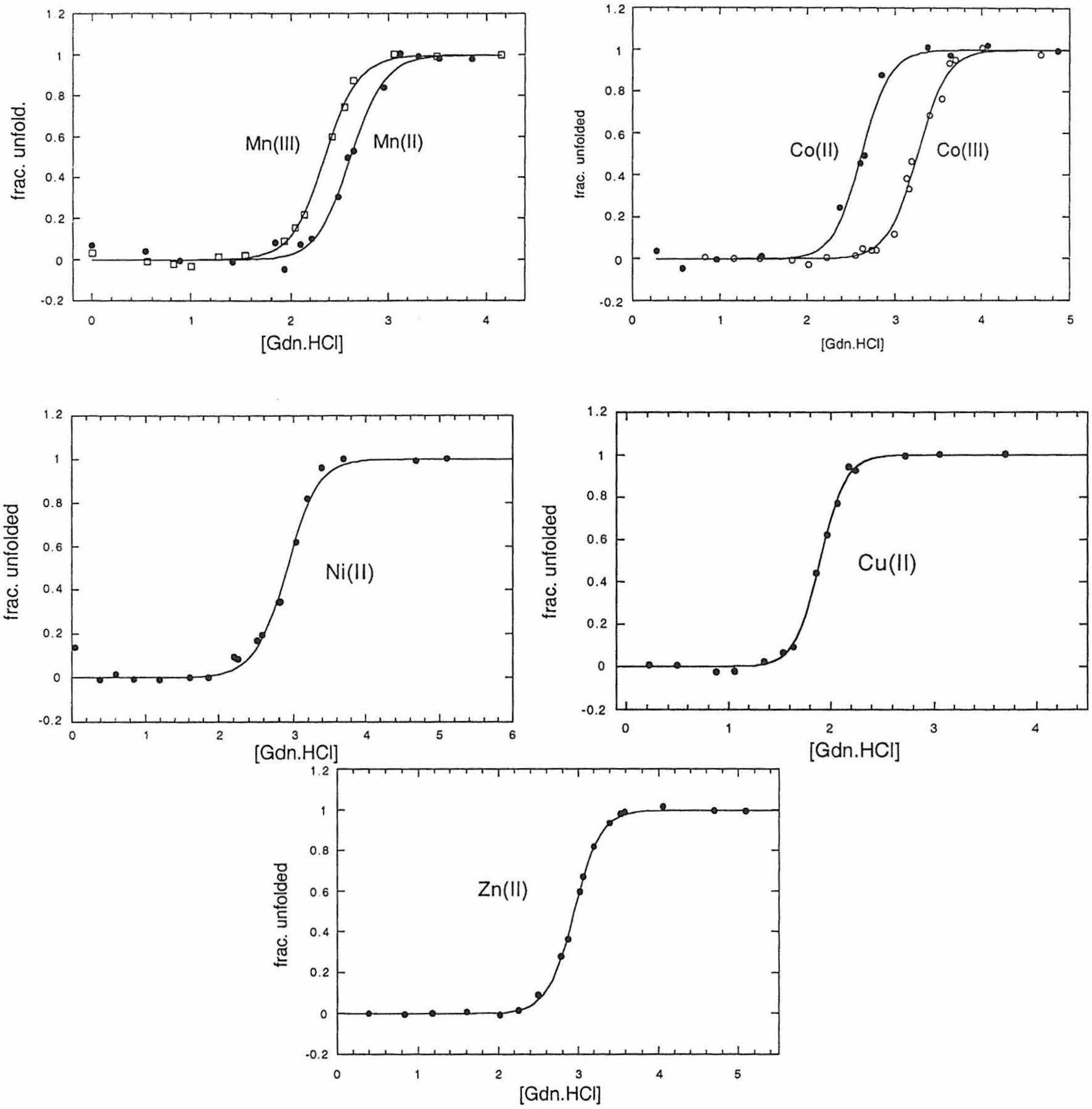

$[\mathrm{GdnHCl}]_m$ (M)= 2.6 (Mn^{2+}), 2.35 (Mn^{3+}), 2.6 (Co^{2+}), 3.1 (Co^{3+}),
2.9 (Ni^{2+}), 1.9 (Cu^{2+}), 2.9 (Zn^{2+})

m_d (kcal/M.mol)=3.4(Mn^{2+}), 3.3 (Mn^{3+}), 3.3 (Co^{2+}), 3.3 (Co^{3+}),
3.5 (Ni^{2+}), 4.6 (Cu^{2+}), 3.5 (Zn^{2+})

Figure C2. Unfolding curves for metal-substituted cyt *c*'s and corresponding parameters.

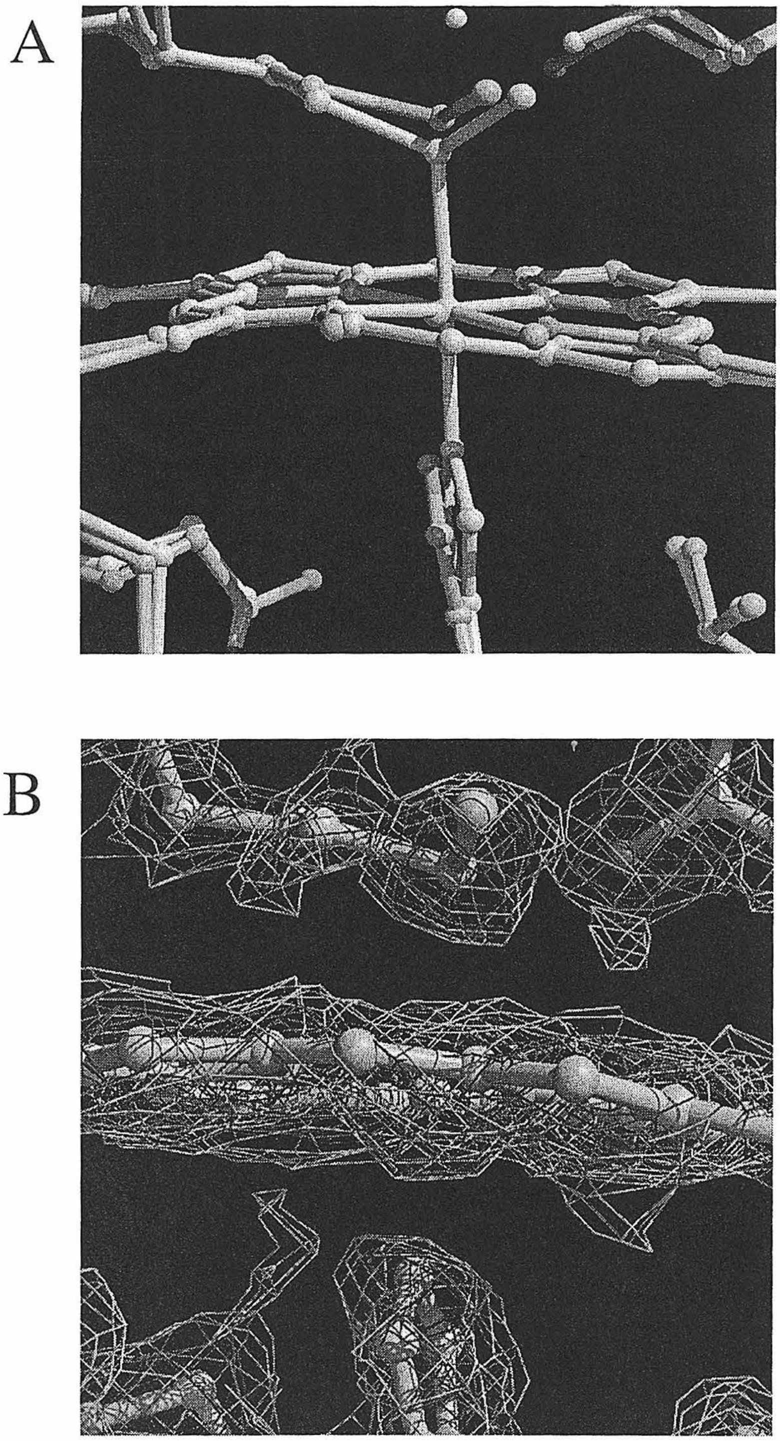

Figure C3. Heme region in the crystal structure of tuna Mn(III)-cyt *c*. Mn-cyt *c* was crystallized according to the same protocol used for Co-cyt *c* crystallization. Diffraction quality crystals (2 molecules per asymmetric unit, $P4_3$ space group, 74.24×74.24×35.65 Å^3) were obtained at 85% saturated ammonium sulfate. The structure was determined as described in Chapters 3 and 4 to a resolution of 1.5 Å; structure refinement was stopped at R=0.235 and R_{free}=0.260. (**A**) Mn-cyt *c* (multi-colored) superimposed on Fe(III)-cyt *c* (white) (PDB ID:3CYT). Mn-pyrrole nitrogen bonds are ~2.02 Å long (similar to those in the Fe-protein), while the axial bonds are significantly elongated (Mn-S(Met 80)≈2.85 Å (vs. 2.27Å), Mn-N(His 18)≈2.18 Å (vs. 2.00Å)) due to the high-spin nature of Mn(III). (**B**) $2F_o$-F_c electron density map (blue, 1σ; magenta, 2σ), suggesting that the Met 80 sidechain may have some mobility.